UNIVERSITY OF CAPE TOWN
IYUNIVESITHI YASEKAPA • UNIVERSITEIT VAN KAAPSTAD

Development of image based crack measurements, to investigate delamination in different weave Fibre Reinforced Polymers

ABRAAR HARNEKAR

Thesis presented for degree of:

Msc (Eng) in the Department of Mechanical Engineering

Faculty of Engineering and Built Environment

University of Cape Town (UCT)

2019

Blast Impact and Survivability Research Unit

Plagiarism Declaration

I, Abraar Harnekar, hereby:

1. grant the University of Cape Town free license to reproduce the above thesis in whole or in part, for the purpose of research;
2. declare that:
   - I have used the IEEE convention for citation and referencing. Each significant contribution to, and quotation in, this report/project from the work(s) of other people has been attributed and has been cited and referenced.
   - the above thesis is my own unaided work, both in concept and execution, and that apart from the normal guidance from my supervisor, I have received no assistance apart from that explicitly stated in the Acknowledgements.
   - This thesis/dissertation has been submitted to the Turnitin module (or equivalent similarity and originality checking software) and I confirm that my supervisor has seen my report and any concerns revealed by such have been resolved with my supervisor."

I am now presenting the thesis for examination for the degree of Msc (Eng) in Mechanical Engineering.

Signed by candidate

Abraar Harnekar

23 April 2019

Abstract

This project investigates the delamination dependence of fibre reinforced polymers, of different weave patterns, using an image-based crack measurement method.

Glass fibre reinforce polymer (FRP) with three different weave pattern namely Unidirectional, Plain weave and Twill weave patterns were manufactured using the infusion process. Waterjet cutting was used to cut the panels to produce the test specimens. The Double Cantilever Beam (DCB) test was used to measure the Mode I fracture toughness, following the standardised test method ASTM D5528.

DCB tests requires two hinge blocks to be bonded to the specimens and is conducted using the Zwick machine which actively measures force and opening displacement. In order to calculate the fracture toughness from a DCB test, the crack length must be measured. An image-based crack measurement method was developed, using still images that were extracted from a digital video of the DCB experiment.

The image-base method involved scripting a MATLAB file to detect the specimen surface as edges. The specimen was painted white and the test had a black background. This caused a sharp change in intensity which made the specimen edge easier to detect. The detection algorithm only catered for accuracy and not speed.

A series of tests were conducted to verify the detection algorithm, of which included designing an Ultrasound Wedge device. The Wedge device was used to emulate a DCB tests in a static position whereby an Ultrasound Thickness Tester was used to obtain and verify the position of the crack tip obtained by the algorithm.

DCB tests showed that the Twill weave specimens had the greatest resistance to delamination, while the Unidirectional weave offered the least resistance to delamination. The Plain weave pattern was inconclusive due to the large variation between the Plain weave specimens.

Acknowledgements

In the name of Allah, the Most Beneficent, the most Merciful. Firstly, I would like to thank the Lord Almighty for helping me find the strength get to the current position I find myself in.

Of the many people, the author would like to express his gratitude to the following people for their support and guidance during the project.

- To my parents (Abba and Mummy) and siblings (At'har, Shafeeqah and Badrunnisa) for all their help, support and guidance they have given me to help aid me to complete this project.
- My supervisor Dr Reuben Govender for his advice and guidance he has given throughout the project
- Associate professor Chris von Klemperer for his help and guidance during my time spent in the UCT composite Labs
- To Penny Park-Ross for the help and assistance during the time spent in the CME labs
- To Dirk Findeis for his advice as to which NDT method I should use.
- To Mr Pierre Smith and the UCT workshop for their help with manufacturing my drawing components.
- To my many friends that has helped me throughout my two-year period. Of which some I would like to single out specifically:
    - Muhsin Osman, Richard Ferreira, Zaynulabiedeen Ebrahim and Imad Khan for their help and company in the composite laboratory when manufacturing the composite panels.
    - Nabeel Gool, Mohammed Siddique Parker, Altaaf Harnaker, Shabbir Esmail, Aaron Graham and Rendi Khobo for their help and input regarding my detection algorithm**.**
    - Samiksha Naidoo, Mushin Osman, Oliva Govender, Henakshi Joysuree, Sahil Dadah, Anjana Yodaiken, Younos Mohamed, Ayesha Jacobs and Miguel Garcia Naude for their help with proof reading this report and or their coding data collection.

  A special mention should go to Olivia, Henakshi, Mushin, Zaynulabiedeen and Muhammed Tootla for all their support and company they have given me during my stressful time of my master's degree. No words can describe how extremely grateful I am for everything they have done for me.

Table of Contents

List of Figures

List of Tables

Nomenclature

Interlaminar fracture Theory and Testing

Symbols	Units	Description
K	$MPa.m^{0.5}$	Stress Intensity Factor
K_C	$MPa.m^{0.5}$	Critical fracture toughness
σ_f	MPa	Applied Stress
a	mm	crack length
G	kJ	Strain Energy Release Rate
G_C	kJ	Critical Strain Energy Release Rate
P	N	Applied force
C	$M.N^{-1}$	Compliance
b	mm	Width of specimen
E	GPa	Youngs Modulus
t	mm	Thickness of specimen
δ	mm	Load point displacement (crack opening displacement)
Δ	mm	crack length correction Factor
G_{IC}	kJ	Critical Strain Energy Release Rate of Mode I

Image Analysis

Symbols	Description
$I(x,y)$	Edge Intensity value of image at (x,y)
M	Magnitude of Gradient Intensity
θ	Gradient Direction
G_x	Sobel Operator in x direction
G_y	Sobel Operator in y direction
$G_S\ (x,y)$	Gradient Intensity of Sobel operator

MATLAB crack detection algorithm

Symbols	Description
x_0, y_0	Start point x & y
θ	Sweep Angle
x_1, y_2	End Points x & y
L	length of one line
x_m, y_m	Middle point x & y between (x_0, y_0) & (x_1, y_1)

Abbreviations

Symbols	Description
DCB	Double Cantilever Beam
ENF	End Notch Flexure
MMB	Mixed Mode Bending
UD	Unidirectional
MD	Multidirectional
US	Ultrasound
CP	Crossing Points
ASTM	American Society for Testing and Materials
FRP	Fibre Reinforced Polymer
GSM	Grams per square meter
MSDS	Material Safety Data Sheets
MBT	Modified Beam Theory
CC	Compliance Calibration
DIP	Digital Image Processing

1. Introduction

A composite material is formed when two or more materials are combined to form a new material, with improved properties such as a high strength to weight ratio. Fibre reinforced polymers (FRP) are a composite material consisting of layers of fibres (plies), embedded in a polymer matrix. An FRP structure is made by layering several plies to achieve the desired thickness [1] .

Delamination (separation of plies) is a mode of failure which can occur in FRP whereby the plies separate, either due to a manufacturing defects or external loading. Delamination significantly reduces the stiffness and strength of the FRP [2]. As an internal defect, delamination is not easily detected. An unmonitored delamination may propagate enough to cause sudden, catastrophic failure of a given structure. Linear Elastic Fracture Mechanics (LEFM) can be used to analyse crack initiation and growth, given loading, size of flaws and material properties such as fracture toughness[3]. One of the key parameters determined from delamination testing is fracture toughness, which is a measure of the resistance of the material to crack growth.

There are three modes of failure considered in Fracture Mechanics: tensile opening (Mode I), in plane shear (Mode II) and out of plane shear (Mode III). A summary of the modes of failures can be seen Figure 1-1.

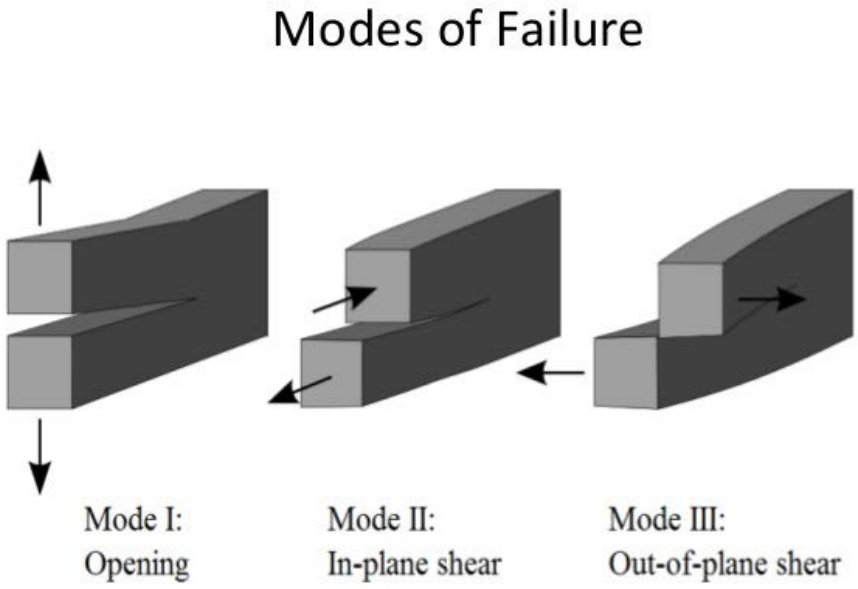

Figure 1-1: Different modes of failure [4]

According to Benzeggagh and Kenane [5] combination of Modes I and II are of interest, due to these naturally occurring in many real-world applications.

Colleagues in our research group, BISRU, have conducted extensive blast loading studies on glass-epoxy/vinyl ester FRP structures/sandwich panels [6], [7],[8], [9] and [10] . This project will be restricted to glass fibre reinforced epoxy panels, so that the material properties measured will be relevant to related blast loading studies.

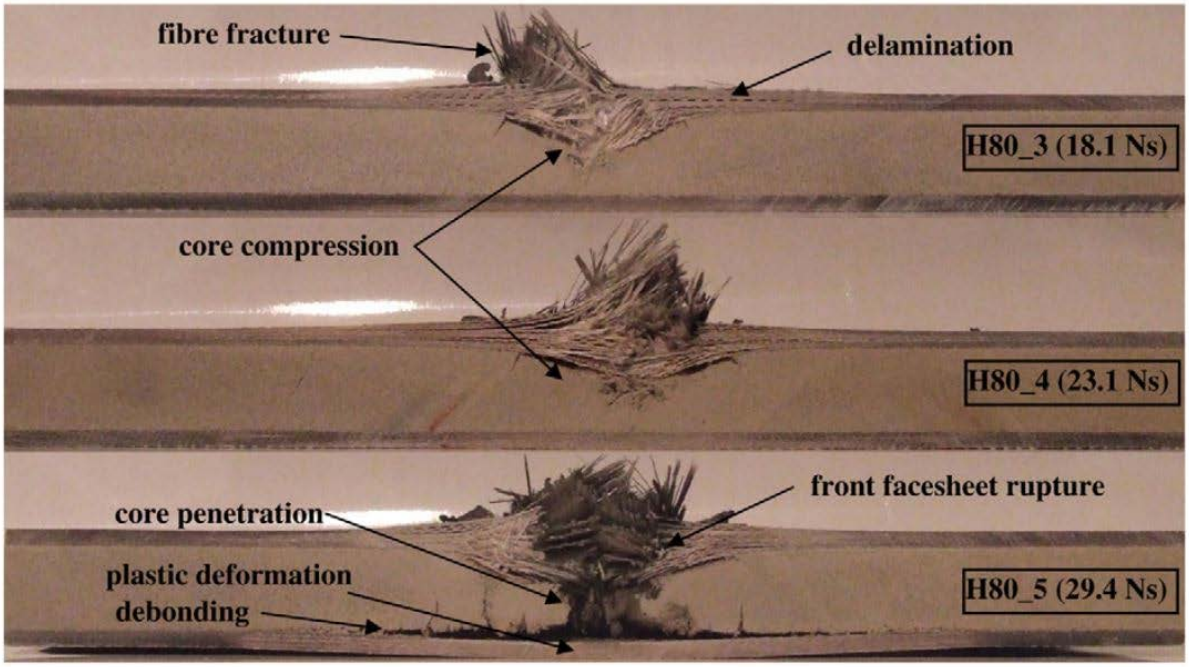

Figure 1-2: Delamination of selected sandwich panels after blast loading [10]

Delamination testing of selected sandwich panels was performed after blast loading was carried out by Langdon et al, which is illustrated in Figure 1-2. It can be seen that delamination occurs in both tension and shear (a mix of Mode I and II). By working with similar FRPs to those studied by Langdon et al, this project's material characterization will support the simulation of these experiments.

Standardised testing methods exist for measurement of fracture toughness in Mode I, Mode II and Mixed Mode I-II. Regardless of the fracture mode, delamination testing involves tracking the crack length and hence the crack growth. One way to obtain this is to use a travelling microscopes or NDT methods to follow the propagation. These methods can’t be used if delamination is tested via impact loading, because the crack grows much faster than the measurement can accommodate.

This project will investigate image-based crack measurements as an alternative technique to measure crack propagation, as it can be applied in scenarios where conventional methods aren't suitable such as high experimental rates, but experiments can be filmed with high speed cameras.

The primary research questions of this project are:

- Does the accuracy of image-based crack measurement compare acceptably with the methods required by the ASTM standards?
- Does the fracture toughness values at initiation and propagation depend on the different weave patterns being used under the given Modes of failures?
-

The objectives of this project are:

- To manufacture composite specimens for delamination testing
- To develop an image-based crack detection method for delamination tests, that requires minimum user input
- To validate the accuracy of the image-based crack detection against other accepted crack measurement methods such as Ultrasonic detection

  To perform delamination tests on a range of FRP weave patterns, using the tools above to facilitate crack measurement and calculation of G, in order to examine differences in crack growth for different weaves.

This project is also limited to the usage of three weave patterns namely, Unidirectional ($0°$), Plain Weave and Twill Weave whereby the Mode I fracture toughness values at initiation between these patterns will be compared. While other weave patterns are available, the local suppliers did not stock these in a similar areal weight to the patterns mentioned above.

2. Literature Review

2.1. Fibre reinforced polymers

Fibre reinforced polymers (FRP) consist of high strength fibres embedded in a polymer matrix [1], as shown in Figure 2-1. The fibres are the principle load carrying members, while the matrix keeps the fibres in the desired location and orientation.

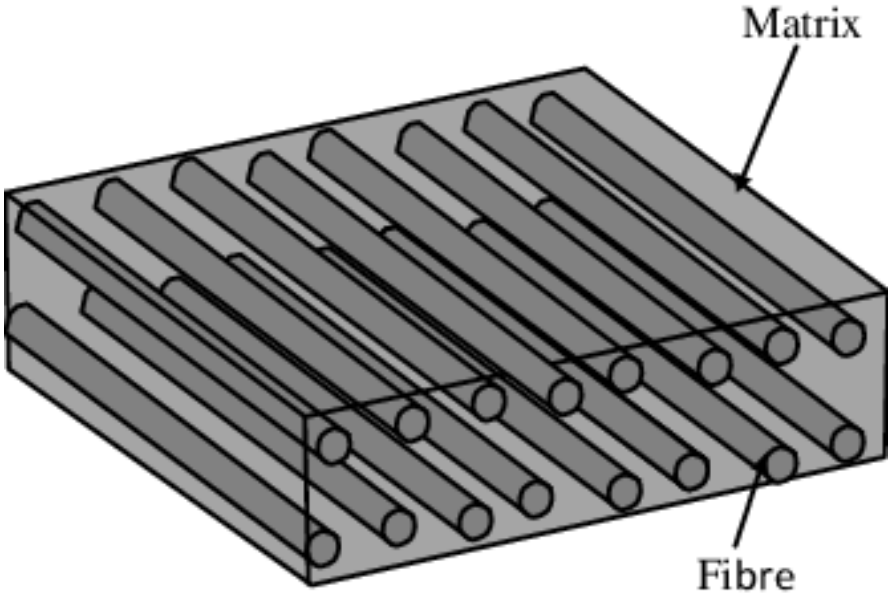

Figure 2-1: Example of a two-layer laminate [11]

Figure 2-1 shows an example of a two-layered Unidirectional (UD) laminate, whereby all the fibres are in one direction. A UD pattern can carry large loads parallel to the fibres but has very limited capacity for loading perpendicular to the fibres. A true UD is difficult to fabricate, as there is nothing to stop the fibres from falling apart. For practical purposes a few stiches are used to hold the fibres together as a fabric.

The main drawback of a UD pattern is that it can carry large loads parallel to the fibres but has very limited capacity for loads perpendicular to the fibres. This causes fabrication of UD to be difficult as the only thing holding the fibres together are a couple of stiches as shown in Figure 2-2. Without the stitching the fibres will fall apart.

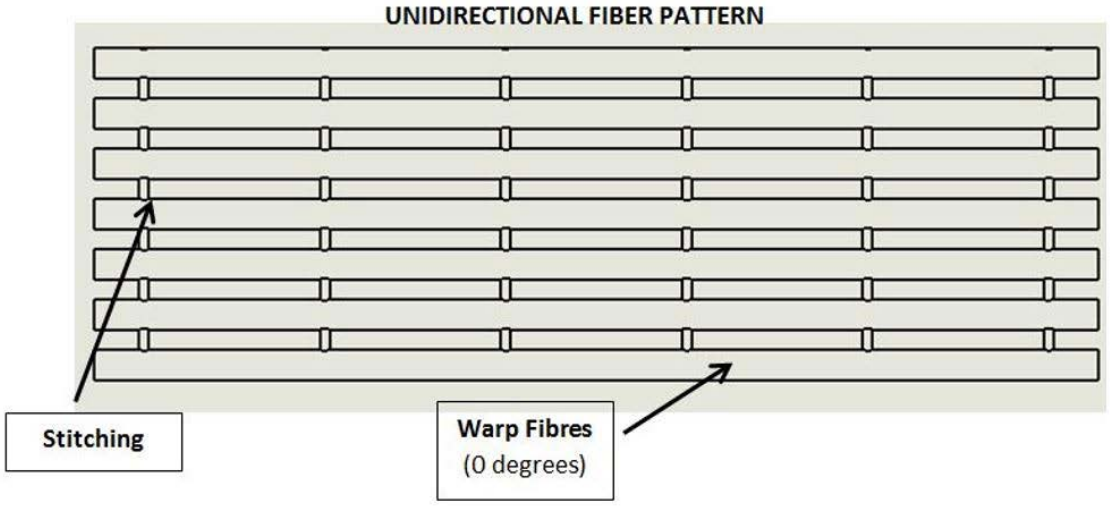

Figure 2-2 : Unidirectional pattern

To improve the strength and stiffness of a panel in both directions a multi-layered set-up is used whereby the layers are layered alternately from 0 to 90 degrees.

Alternatively, the fibres can be woven together to bring about different weave pattern FRP to aid in fabrication of the laminate.

2.1.1. Weave patterns

Each layer of fibre fabric consists of two types of fibres, namely the warp fibres (fibres running lengthwise in the material) and weft fibres (fibres running perpendicular to the weft fibres), shown in Figure 2-3. The weft fibres are woven over and under the warp fibres. Depending on how the fabric is woven together, different mechanical properties and drapability will arise.

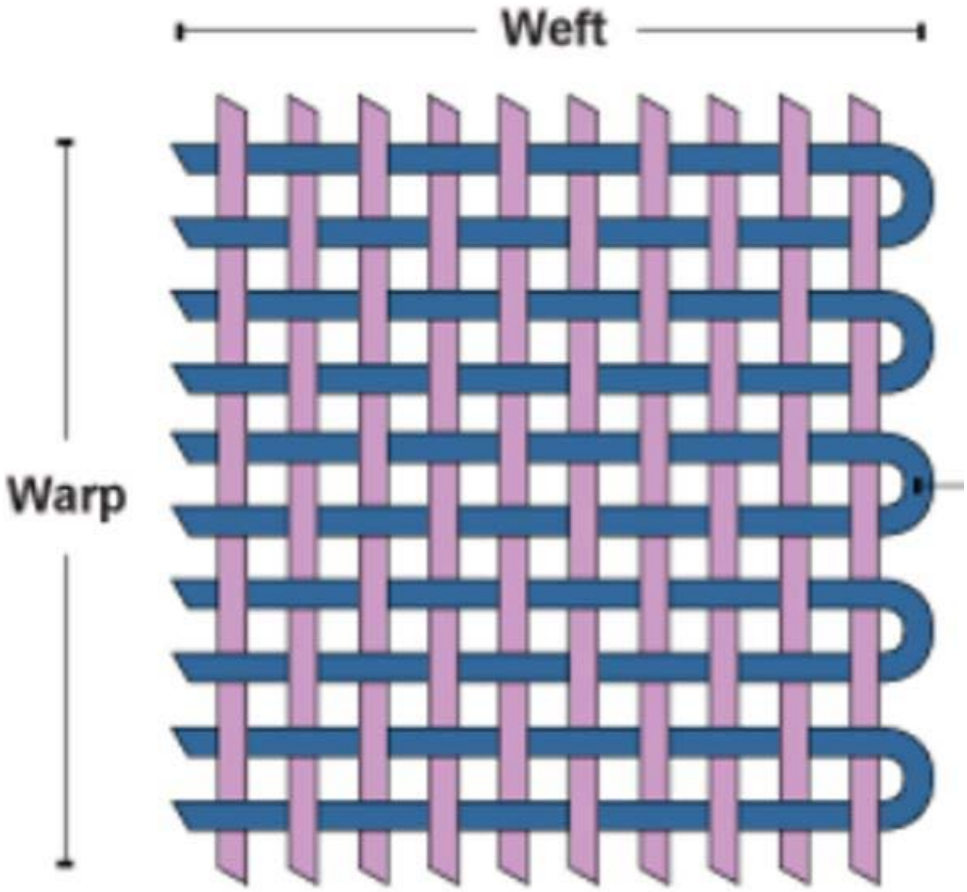

Figure 2-3: Typical construction of the fibres [12]

Further emphasis will be given to Plain and Twill weave pattern.

2.1.1.1. Plain weave pattern

This is one of the most commonly used weave pattern and is produced by weaving the weft fibres over and under one warp fibre. Thus, making the fibres interlace at every crossing [13]. Due to the crossing occurring at every crossing point, the Plain weave pattern is not easy to construct. Figure 2-4 shows the typical layout of a Plain weave pattern.

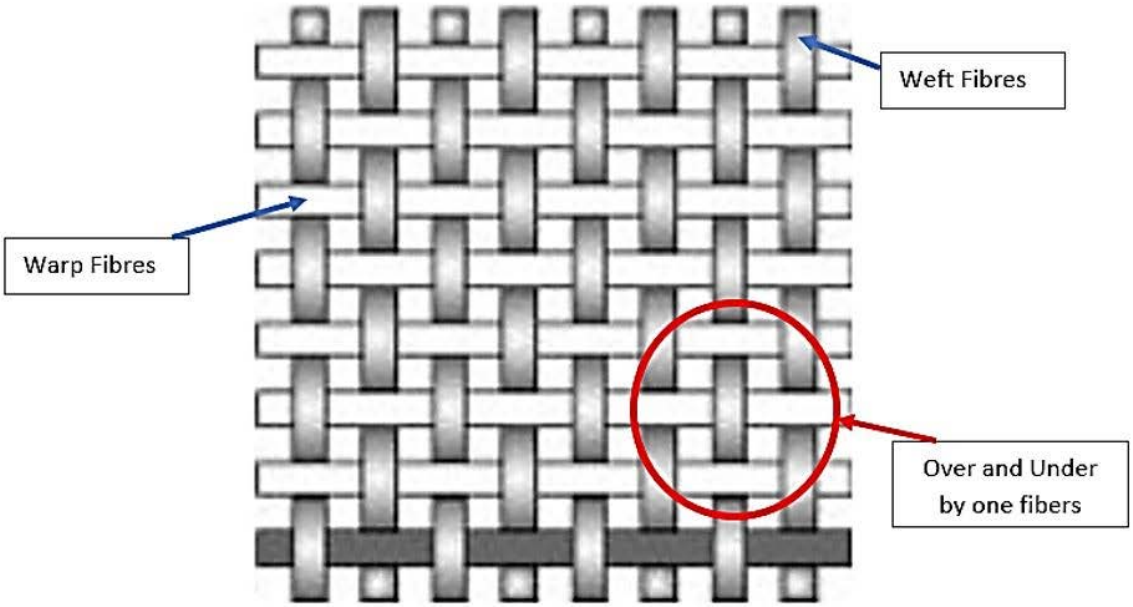

Figure 2-4: Plain weave pattern [14]

The advantage of a Plain weave is that it's very stable and gives rise to equal strength in both directions. The disadvantage is that the material is not easy to drape or conform to complex shapes [13], [14]. Plain weave also gives rise to low mechanical properties compared to other weave type patterns [14].

2.1.1.2. Twill weave pattern

A Twill weave pattern is produced by weaving the weft fibres over and under 2 or more warp fibres. For example, a 2 by 2 Twill weave pattern is whereby the warp and weft fibres are woven over and under by two fibres [13]. In a Twill weave pattern as shown in Figure 2-5, the adjacent fibres are offset by one [13] thus producing a diagonal like pattern in the fabric [12].

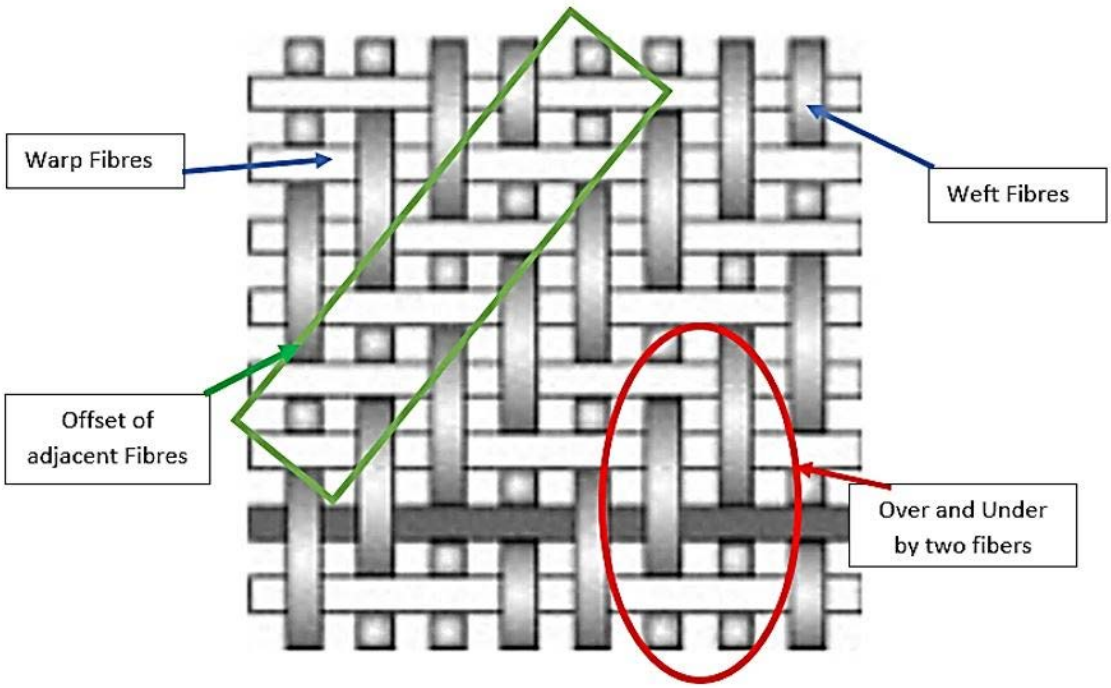

Figure 2-5: Twill weave pattern [14]

The advantage of a Twill weave pattern is that due to the offset of the fibres, the fabric is allowed to conform to complex shapes while still retaining the strength in both directions [13]. The mechanical properties of a Twill weave pattern is stronger as two or more fibres are bundled together before it's woven together [14].

2.2. Manufacturing methods

There are numerous ways to manufacture FRPs which include amongst others: Wet/Hand lay-up, Spray-Up, Infusion moulding and Filament Winding.

Due to the resources available at the department's Composites Manufacturing laboratory, only Wet/hand lay-up will be expanded on.

2.2.1. Wet/Hand Lay-up

Wet/Hand Lay-up, shown in Figure 2-6, is one of the simplest methods to learn and manufacture composite panels [15].

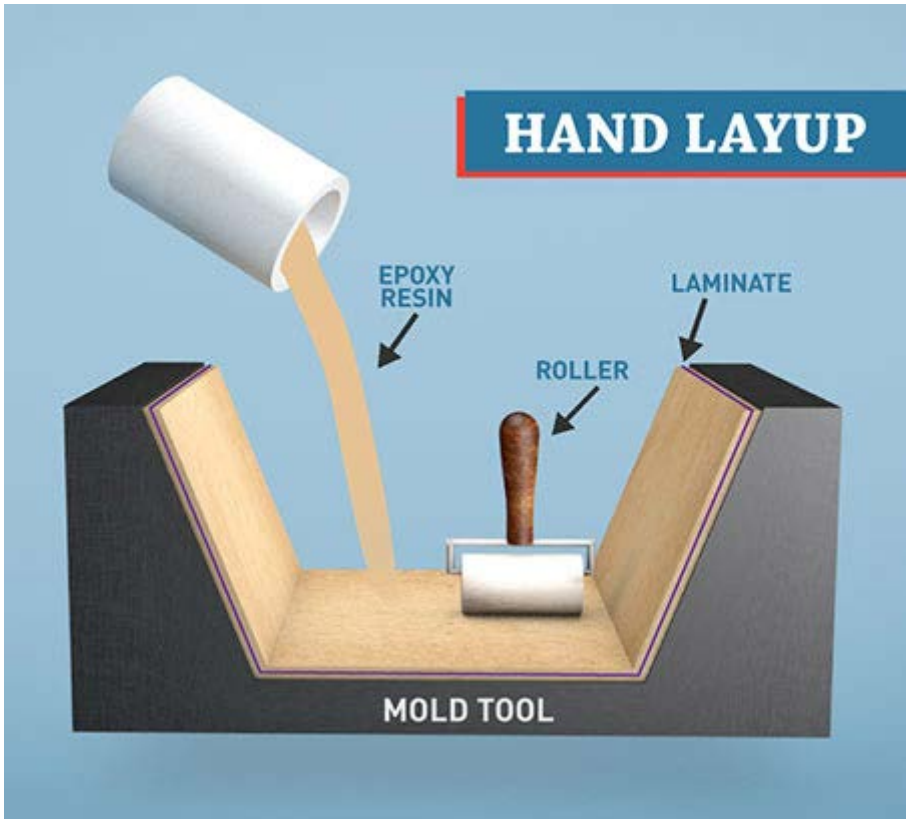

Figure 2-6: Wet/hand lay-up process [16]

The process involves using a liquid resin, mixed with a predetermined amount of hardener and applying it to the laid-out fibres. A roller/brush is used to evenly spread the resin across the fibreglass layers. This is done one layer at a time until the required thickness of the part is reached [17]. The part is left to cure at room temperature. A vacuum bag can be used to help consolidate the layers, by squeezing the fibres and resin against the mold. Post curing of the parts in an oven is done after demoulding to achieve the best mechanical properties of the materials.

2.2.2. Infusion Process

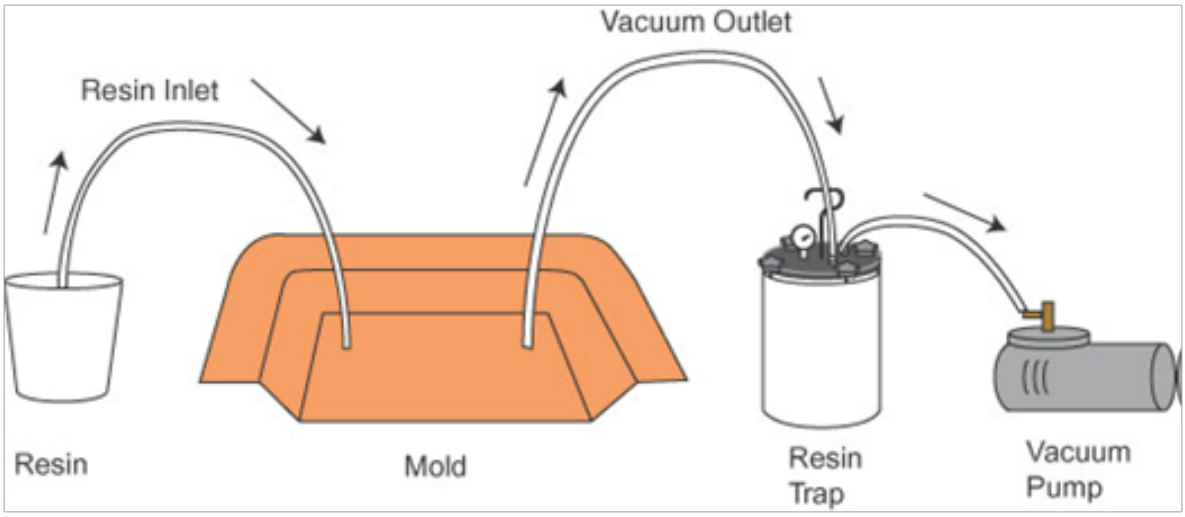

Figure 2-7: Infusion process [18]

Figure 2-7 shows the infusion process where vacuum is used to draw liquid resin into the mould. All the fibre material is stacked dry onto the mould table. A layer each of flow promotion (green flow) media and peel ply, is placed on either side of the stacked material. The green flow material is used to aid the resin to flow across the entire part, whereas the peel ply layers aid in demoulding the manufactured part.

The fibre stack is placed under vacuum to remove any voids or air pockets from the given part. The resin, mixed with the correct hardener ratio, is infused into the parts using a vacuum pump. The part is cured before demoulding [19].

Note: Green flow and peel ply layers are used in both the infusion and wet/hand layup process

2.3. Interlaminar fracture theory and testing

Failure due to fracture in brittle materials such as FRPs does not depend purely on the applied stress or strain, but also needs to consider the presence of defects and uncertainties in the loading. Fracture mechanics theory assumes the presence of a crack, and relates the crack geometry, the material's resistance to crack growth (fracture toughness) and the applied stress to determine whether the crack will propagate, leading to fracture [20].

The two main approaches to measure fracture toughness area is the stress intensity and energy-based approaches.

The stress intensity factor K is calculated from the applied stress σ_f and current crack length a:

$$K = \sigma_f \sqrt{\pi a} \tag{2.1}$$

If the stress intensity factor K exceeds the critical fracture toughness K_c, the crack will grow. Fracture toughness K_c is considered to be a fundamental material property.

For anisotropic materials such as FRPs, it is more convenient to work with the strain energy release rate G. Strain energy release rate is calculated from the applied force P, specimen width b, the compliance C and current crack length a :

$$G = \frac{P^2}{2b}\frac{dC}{da} \tag{2.2}$$

G is analogous to K, and if G exceeds some critical strain energy release rate G_c, the crack will propagate. For a linear, isotropic material, G may be calculated from K and the Young's Modulus E:

$$G = \frac{K^2}{E} \tag{2.3}$$

The relationship between G and K becomes more complicated for anisotropic materials. As it is much easier to work with global forces and displacements for FRP specimens, than the non-trivial stress field around the crack tip which is required to calculate K, fracture analysis in FRPs tends to work with G. Because of the relationship between K and G, the terms fracture toughness and strain energy release rate are often used interchangeably – in this document, any reference to the term 'fracture toughness' implies G_c.

2.3.1. Crack initiation and fracture toughness

According to [21], crack initiation is defined by one of three methods. These include taking the G values from

- the position of deviation from non-linearity from the force-displacement curves generated when the test is conducted
- the maximum load of the force-displacement curve
- Or the position where delamination is visually seen during the test under a microscope.

Figure 2-8 shows the three-method used to obtain the G value for crack initiation.

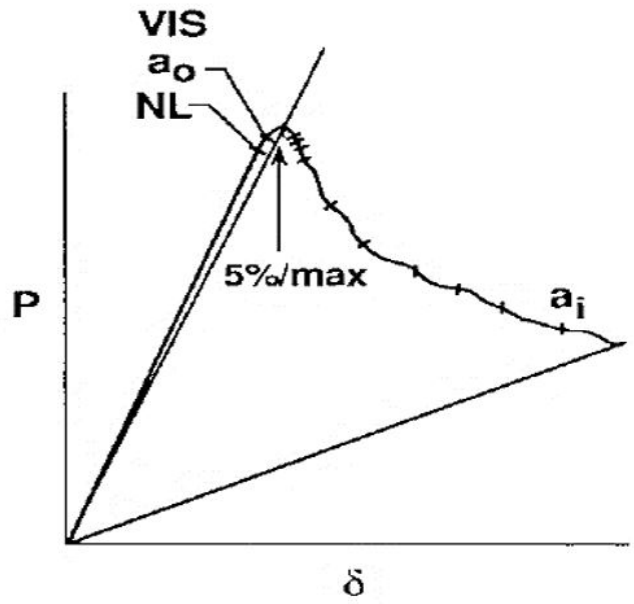

Figure 2-8: Load displacement curves showing possible crack initiation points.

With the crack initiation known, the crack propagates which in turns gives rise to a delamination resistance curve, (R – curve, Mode "X" fracture toughness vs crack length) shown in Figure 2-9. "X" referring to a specific mode type and crack length to the position of the crack with respect to a known origin/reference line.

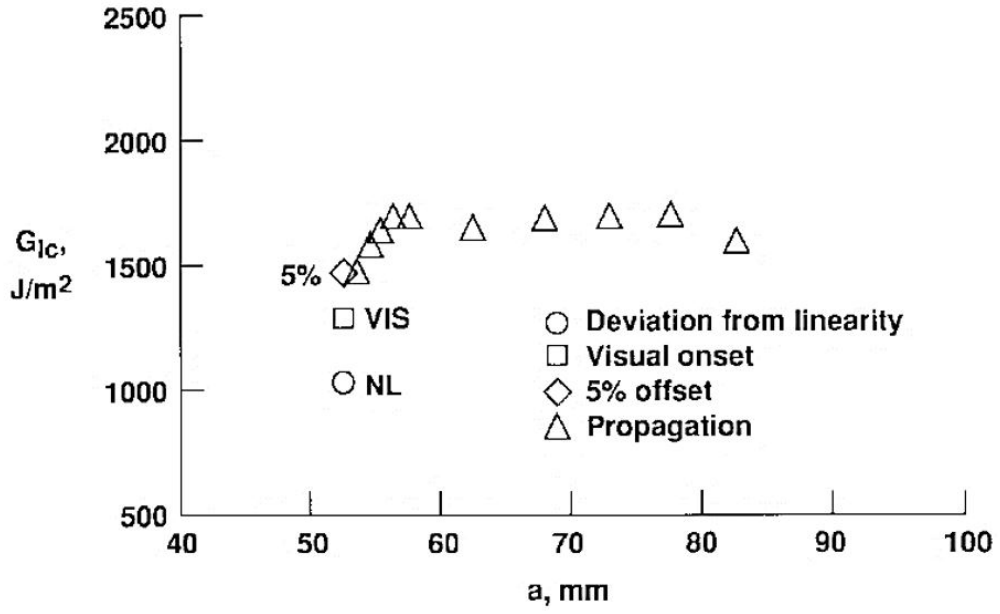

Figure 2-9:Example of a Delamination Resistance Curve [21]

As the crack propagates, the G value begins to increase, which is usually due to fibre bridging [22]. After the fibre bridging zone length, the G value tends to stabilize.

Parameters which affect the fracture toughness values and hence the R-curves includes the fibre directions, stacking sequences, mode mixities, crack length, type of resin and FRP being used [22]**.**

Davies presented a summary of different testing devices and methods for measuring interlaminar fracture toughness in 1998 [23], which was updated and refined by [24].

2.3.2. Mode I – Pure tensile

Mode I fracture toughness is that of pure tensile opening. For FRPs, the Mode I fracture toughness test is known as the Double Cantilever Beam (DCB) and is documented in "ASTM D5528 - Standard Test Method for Mode I Interlaminar fracture toughness of Unidirectional Fibre-Reinforced Polymer Matrix Composites [21]."

The DCB consists of a rectangular, uniform thickness specimen which contains a non-adhesive insert in the mid plane of the specimen, shown in Figure 2-10. This will act as the delamination initiator. Hinge (Loading) Blocks are attached to the specimen via an adhesive, typically an epoxy. A force is applied to the blocks which opens the specimen up at a constant rate by controlling the opening displacement or crosshead movements. The force and delamination lengths are recorded. The Mode I fracture toughness,G_I is calculated using the Modified Beam Theory (MBT) or the Compliance Calibration (CC) method. It should be noted that the MBT method is recommended as it yields the most conservatives G_I values [21].

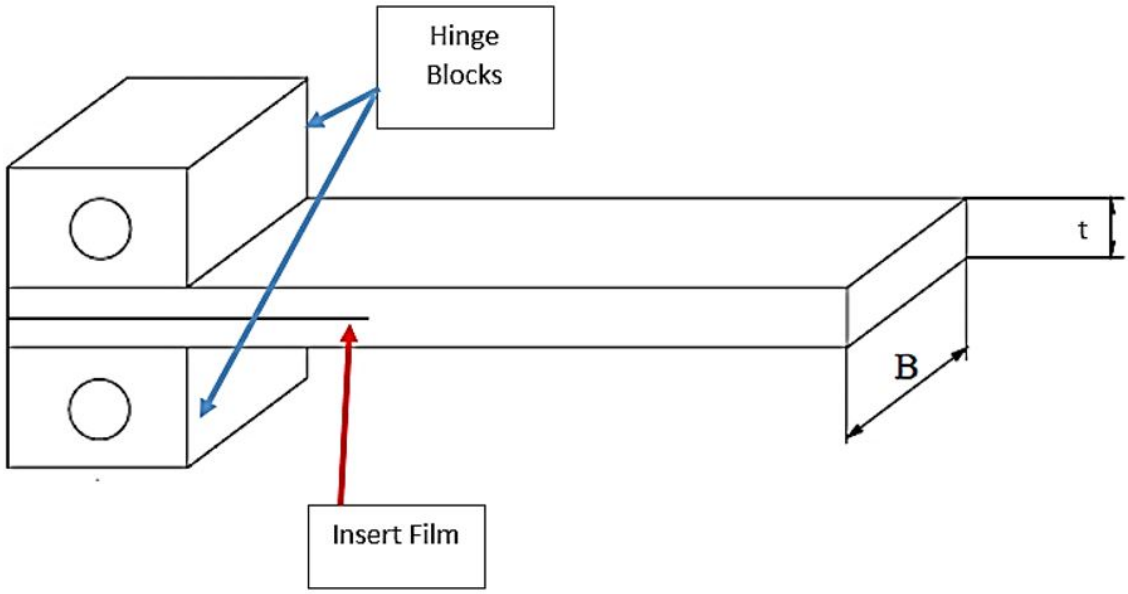

Figure 2-10: DCB set-up

By applying classical beam theory and assuming that the DCB arms are fully built in cantilevers which meet at the crack tip, it can be shown that the strain release rate for Mode I (G_I) can be expressed as [21]:

$$G_I = \frac{3P\delta}{2ba} \tag{2.4}$$

Whereby:

P = Load (N), δ = Load point displacement (mm), b = specimen width (mm), and a = delamination length (mm).

However, the arms of the DCB specimen don't behave as perfectly built in cantilevers - there is some rotation at the delamination front. A correction factor is used to correct this rotation by treating the delamination length to be slightly longer than what it actually is.

$$a = a + |\Delta| \tag{2.5}$$

Whereby Δ can be determined by generating a least square plot of the cube root of compliance $C^{\frac{1}{3}}$, as a function of delamination length as can be seen in Figure 2-11, where the compliance C is taken as $\frac{\delta}{P}$.

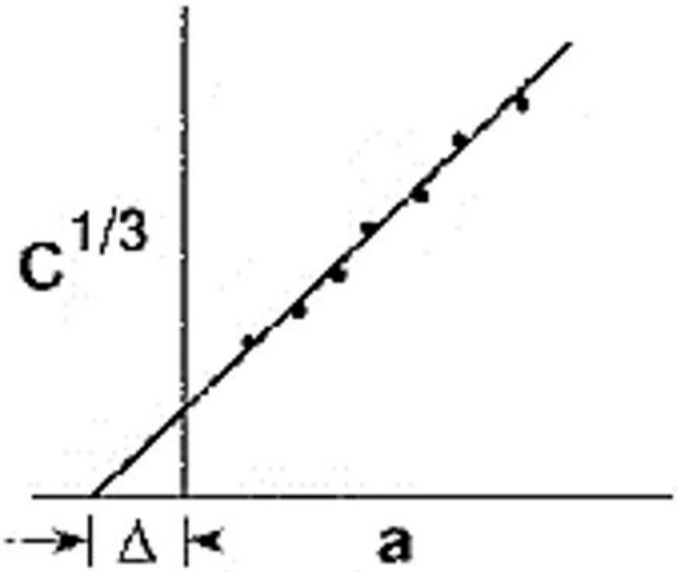

Figure 2-11: Graph depicting correction factor

The fracture toughness value for Mode I using MBT can now be calculated using as accordance to ASTMD5528 [21]:

$$G_I = \frac{3P\delta}{2b(a + |\Delta|)} \tag{2.6}$$

2.3.3. Mode II

Mode II fracture toughness is that of pure shear (known as sliding shear). The Mode II fracture toughness test is known as the End Notched Flexure (ENF) and is reported in “ASTM D7905/D7905M − 14 - Standard Test Method for Determination of the Mode II Interlaminar fracture toughness of Unidirectional Fibre-Reinforced Polymer Matrix Composites” [25].
Just like the DCB, the ENF specimen is also a rectangular specimen of uniform thickness with a non-adhesive insert at its mid-plane. The specimen is loaded with a 3-point bend test as indicated in Figure 2-12. Due to the 3-point flexure, the crack propagates into a highly stressed region, which leads to a more rapid crack growth. Hence the delamination growth is not stable. A record of applied force vs centre roller displacement is recorded.

The Mode II fracture toughness values are determined using the CC method [25]. Due to the nature of the crack propagation being unstable, only the crack initiation values are taken as the resistance to delamination for pure Mode II is not reliable [24].

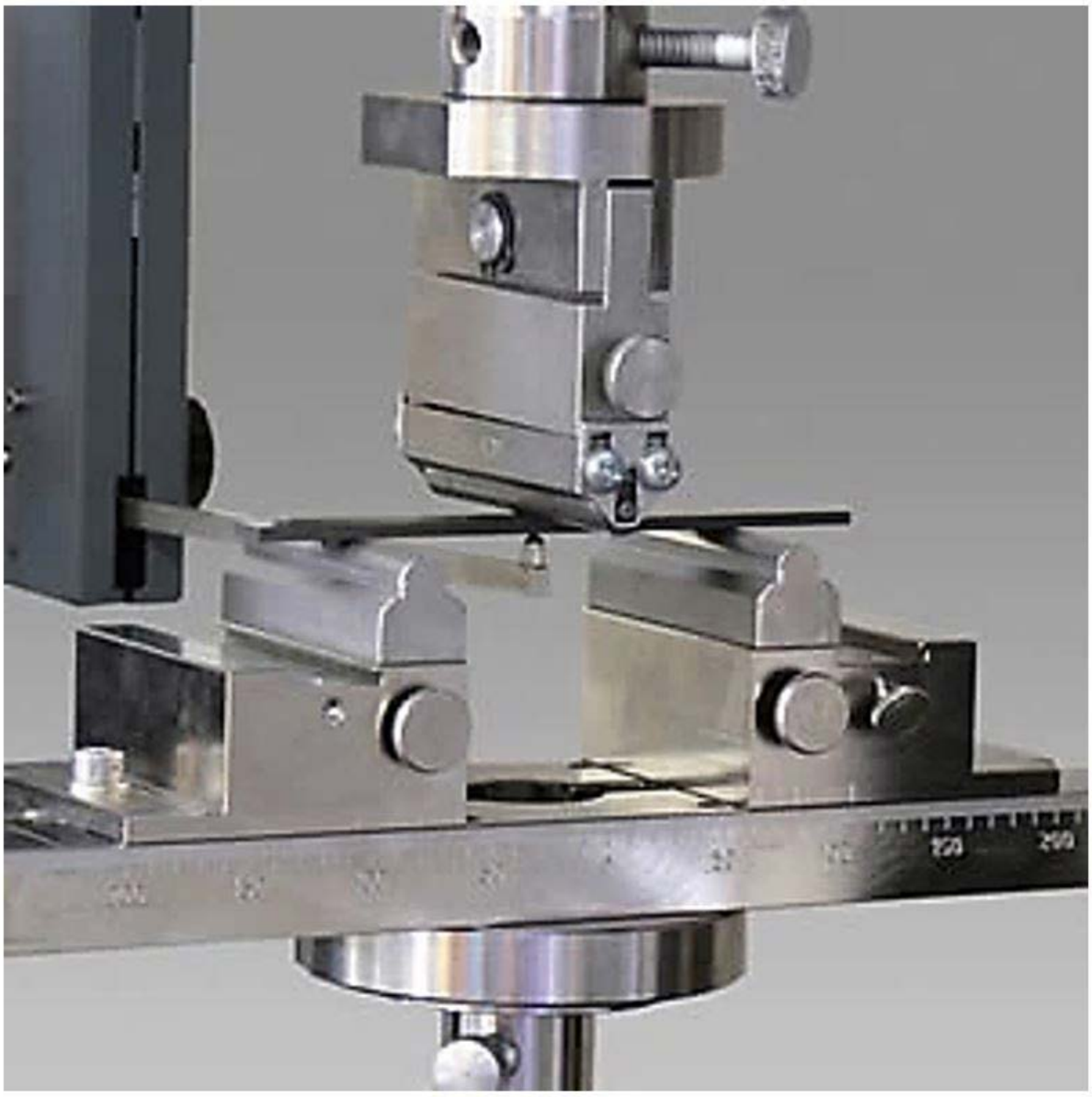

Figure 2-12: Setup of the ENF test fixture [26]

2.3.4. Mixed Mode I/II

Mixed Mode I/II fracture toughness combines-tensile and shear loading. The Mixed Mode I/II fracture toughness test is known as the Mixed Mode Bending (MMB) and is reported in “ASTM D6671 Standard Test Method for Mixed Mode I-Mode II Interlaminar fracture toughness of Unidirectional Fibre Reinforced Polymer Matrix Composites ” [27].

The MMB apparatus consists of a lever and a base. The base holds the specimen stationary whereas the lever loads the specimen. The lever is attached to a roller which acts as a fulcrum and thus when a load is applied, the tabs opens the specimen up as a Mode I specimen, while the specimen simultaneously experiences the shear stresses associated with three-point bend loading as a Mode II specimen.

Just as the DCB and ENF, the specimens are of rectangular uniform thickness. The length of the lever can be adjusted, which gives rise to different mode ratios between Mode I and II.

The applied load vs opening displacement is recorded and stored digitally. The fracture toughness values for the mode mixture are calculated from the critical loads from the load displacement curve [27].

Figure 2-13 shows the setup of an MMB fixture:

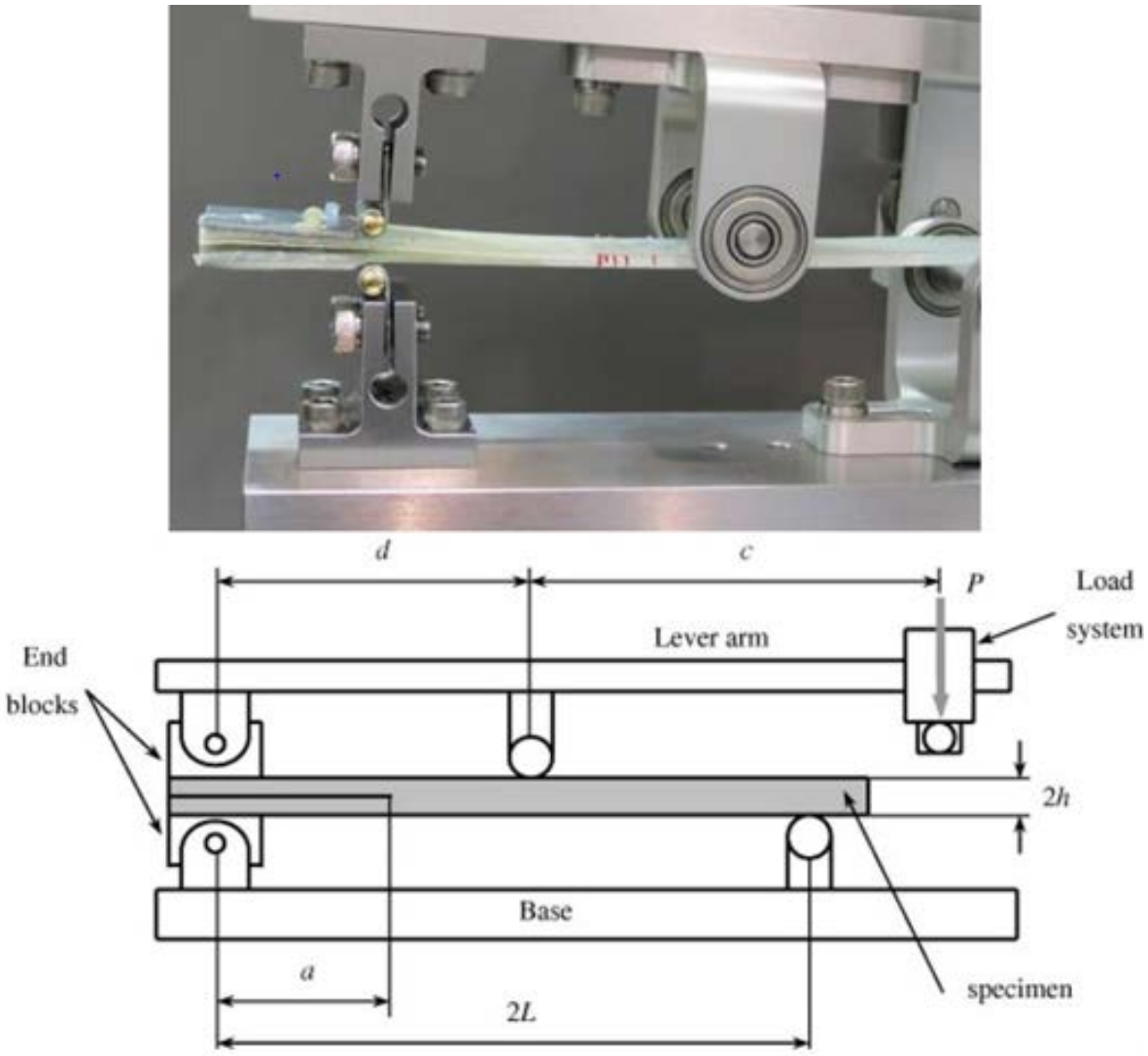

Figure 2-13: Setup of the MMB fixtures [27], [28]

2.3.5. Selected publications on glass fibre reinforced epoxy of Mode I fracture.

There are many publications in the literature for delamination testing of glass-epoxy FRP, of which only a portion is discussed here. It should be noted that ASTM D5528, the standard for DCB was drafted and standardized for UD FRPs (not strictly including woven FRPs).

Thus, the results of UD are considered as more reliable [3] compared to that of Multidirectional (MD) fabrics. Most applications make use of Multidirectional fibres, resulting in a need to standardize test methods for MD fabrics. The difficulty in standardizing these methods are because the orientations between plies of MD are different and thus crack propagation may not be stable.

A major difficulty in measuring fracture toughness in MD is that specimen has a tendency for intralaminar cracking and delamination between neighboring plies [29]. According to [2], the Mode I G_I for MD is 3 to 4 times as much as UD due to this intra-ply delamination.

As stated before the fracture toughness values are dependent on fibre direction and stacking sequence, hygro-thermal condition, mode mixity, crack length, weave and resin toughening.Sticthing can be seen as a form of weave strengthening. S Solaimurugan et al. examines glass woven with stitching across the thickness of the specimen. It can be seen that the a G_I value is 20 times stronger than without stitching [30]. These all produce different R resistance curves and in turn different G_I values.

A summary of various authors G_I values at various starter crack length taken from literature can be seen in Table 2-1 and Figure 2-14. It should be noted that these authors all made use of some sort of glass FRP under different conditions. The table included some of the thickness of specimens, material weight and epoxy used.

Table 2-1: Mode I comparison of literature values

		Variables					Mode I fracture toughness ($J.m^{-2}$)			
Authors (year)	**Reference List Number**	**Weave Pattern**	**Ply Layers**	**Areal Weight (GSM)**	**Thickness (mm)**	**Resin Type**	**Starter crack a = 35mm**	**Starter crack a = 45mm**	**Starter crack a = 50mm**	**Starter crack a = 55mm**
F. Ducept; Davies, P.; D. Gamby (1997)	[31]	UD	16	250		Epoxy	234		268	
M.M. Shokrieh; M. Heidari-Rarani (2011)	[2]	E-glass	24			epoxy	101.6			108.23
M.M. Shokrieh; A. Zeinedini; S.M. Ghoreishi (2017)	[22]	E-glass UD							194.46	
M.M. Shokrieh; M. Salamat-talab; M. Heidari-Rarani (2014)	[32]	E-Glass UD	24			Epoxy	80.56	87.68		85.31
M.Kenane (2009)	[3]	Prepreg E-glass			6	Epoxy			429	
M.Kenane; M.L. Benzeggagh (1997)	[33]	E-glass UD	16			Epoxy		118.02		
M.L. Benzeggagh; M. Kenane (1996)	[5]	E- glass			6			116.83		119.23
A.B. de Morais (2011)	[34]	GFRP UD			7					300
K. Saravanakumar, Nibras Farouk, V. Arumugam (2018)	[35]	GFRP UD		220		Epoxy			350	
J.D. Gunderson, John F. Brueck, Anthony J. Paris (2007)	[36]	GFRP UD			4.3	Epoxy				794
E. Triki, B. Zouari, F. Dammak (2016)	[37]	GFRP 0/90 MD			8	Epoxy			131	
F. Dharmawan, G. Simpson, I. Herszberg, S. John (2006)	[38]	GFRP Plain	18	800	4	Vinylester		121		
S.L. Bazhenov (1995)	[39]	E- glass Plain	24	200		Epoxy	142.5			

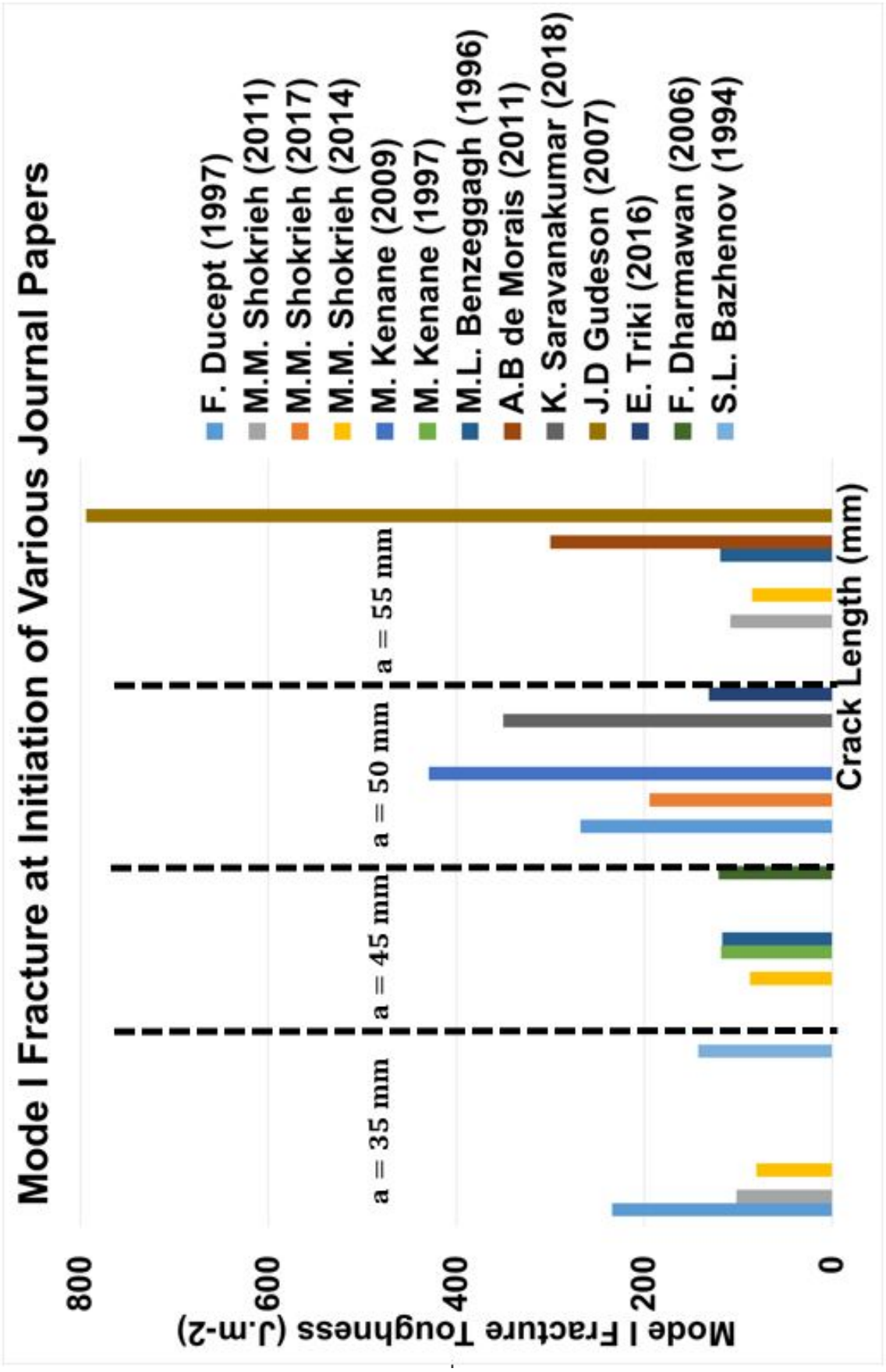

Figure 2-14: Graph showing Mode I critical energy release rate from selected literature

It can be seen that a slight change in any condition brings about a wide scatter between Mode I values among current literature.

2.4. Measuring crack propagation

To obtain the Mode I fracture toughness values (G_I) of an ASTM standardised fracture toughness test, the position of the crack tip at a given time is required. Based on the ASTM standards, these are done manually or visually during the tests at predetermined markers [40], [21]. The time, crack opening displacement and force required for the crack to reach the predetermined marker is recoded manually.

NDT techniques such as Ultrasonic crack detection, Shearography and Thermography can be used to help aid with detecting the position of the crack tip. Emphasis on the Ultrasonic NDT method will be further expanded on in Section 2.4.1.

2.4.1. Ultrasonic crack detection

The ultrasound device typically consists of a probe (transducer), which acts as a transmitter and a receiver, which has a display unit [41]. The transducer emits a particular sonic frequency, which is coupled with a liquid couplant, which allows the sound pass through a work piece. The sound waves travel through the part and then returns to the receiver. If there are defects present in a part, then the sound wave will reflect off the defect and return quicker, hence allowing the defect depth to be determined.

Advantages of ultrasound includes [42]:

- Good flaw detecting capabilities
- Good resolution on the display unit

Disadvantages includes [43]:

- Requires a smooth and flat surface
- Liquid couplant is required and therefore has the tendency to fill surface porosity, thus affecting the results obtained

2.4.2. Visual measurements of crack growth

Although measuring the crack tip manually produces reliable results, this process is extremely time consuming and is heavily based on the user's skills [44]. Due to the crack tip being periodically determined at every 5mm according to the ASTM standards, the crack length data is not continuous [45]. To obtain these values periodically, the user may need to pause the test, which prevents testing at higher rates.

Thus, a need arises to detect the position of the crack tip during the fracture toughness tests in a more automated way. By doing this, the time taken to determine the position of the crack tip reduces and a continuous crack length data can be found. This can be done using a Digital Image Processing (DIP) technique.

2.5. Crack measurements using image analysis.

There has been extensive research regarding detection of cracks using image analysis. Mohan and Poobal [46] critically reviewed 50 articles related to this topic using various camera and lighting equipment. For the purpose of the project only, visual camera-based images are used for the image analysis due to availability of the equipment. Other image analysis process includes infrared, microwave and electroluminescence.

Most crack detection algorithms work by either line or edge detection. To detect the crack as lines, the image needs to be processed in a way that a computational programme can read. This is done by creating a matrix for the images based on the pixel co-ordinates and intensity of that image.

An image can be represented as a function of form $f(x, y)$ from $\mathbb{R}^2 \longrightarrow \mathbb{R}$ where the intensity at any position of an image is given by the position (x, y) [47].

Each pixel value has an intensity value based on the colour of a given image. Due to the nature of the pictures being noisy, the images are usually enhanced using some form of filtering technique. The filters can be used in a way that can blur the background to remove noise (as indicated in [45]) or is used for edge enhancements (as can be seen in [48]).

2.5.1. Filtering of images

Filtering in the context of image processing, is a mathematical operation used on an image to transform that image to a new image, which enhances the original image. It is a neighbourhood operation in which the adjusted pixel intensity value of an output image is some function of pixel intensities of the neighbouring pixels of the input image [49], [50].

Filtering gives rise to smoothing, edge detection and morphology (Adapted from [51]). These are all techniques used to transform an image for image analysis. Edge detection will be further expanded on.

2.5.2. Edge detection

An edge detection is a filtering operation whereby the operation tries to locate sharp changes in intensity values or a large change in colour contrast between neighbouring pixel values [52].

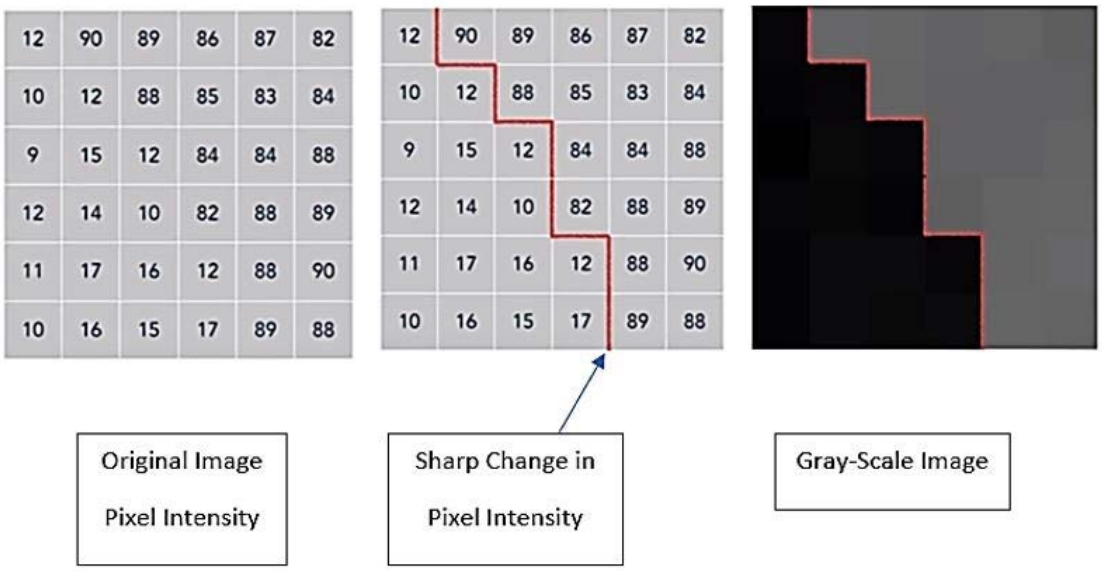

Figure 2-15: Depiction of an edge within an image

Figure 2-15 shows a grayscale image (on the far right) with corresponding pixels intensities on the far left. The edge, which corresponds to a sharp change in intensity, is indicated in red is in the middle.

There are two types of edge detection, namely the Gradient based method and Laplacian based method. It should be noted that only Gradient based method is being used in this project due to simplicity, hence will be expanded upon.

A Gradient based edge detection algorithm makes use of the derivative function, leading to the noise around the edges of an image will be amplified. Thus, a smoothing filtering process is used before the edge detection algorithm [52] to help reduce the noise effect.

A Gradient based method works on the assumption that an edge corresponds to a steep change in intensity value. As mentioned before an image is 2D function. By using this assumption, the edges of an image can be found by finding the derivative of the intensity values across the image. The edge in theory should be where the derivative of the intensity is maximum [53].

The local gradients can be estimated using the following approximation:

$$\frac{\partial f(x,y)}{\partial x} = \Delta x = \frac{f(x+dx,y) - f(x,y)}{dx} \tag{2.7}$$

$$\frac{\partial f(x,y)}{\partial y} = \Delta y = \frac{f(x,y+dy) - f(x,y)}{dy} \tag{2.8}$$

Where dx and dy is the distance along the x and y direction respectively. One can consider dx and dy as a pixel difference between two points, being the limiting case.

Figure 2-16 shows a sample of how the edge detection of a gradient operator is found for an edge along the x direction of an image. The image shows a black and white figure whereby the intensity changes from 0 to 255 along the edge. The edge is found when the gradient of the intensity is maximum which occurs when the second derivative crosses zero.

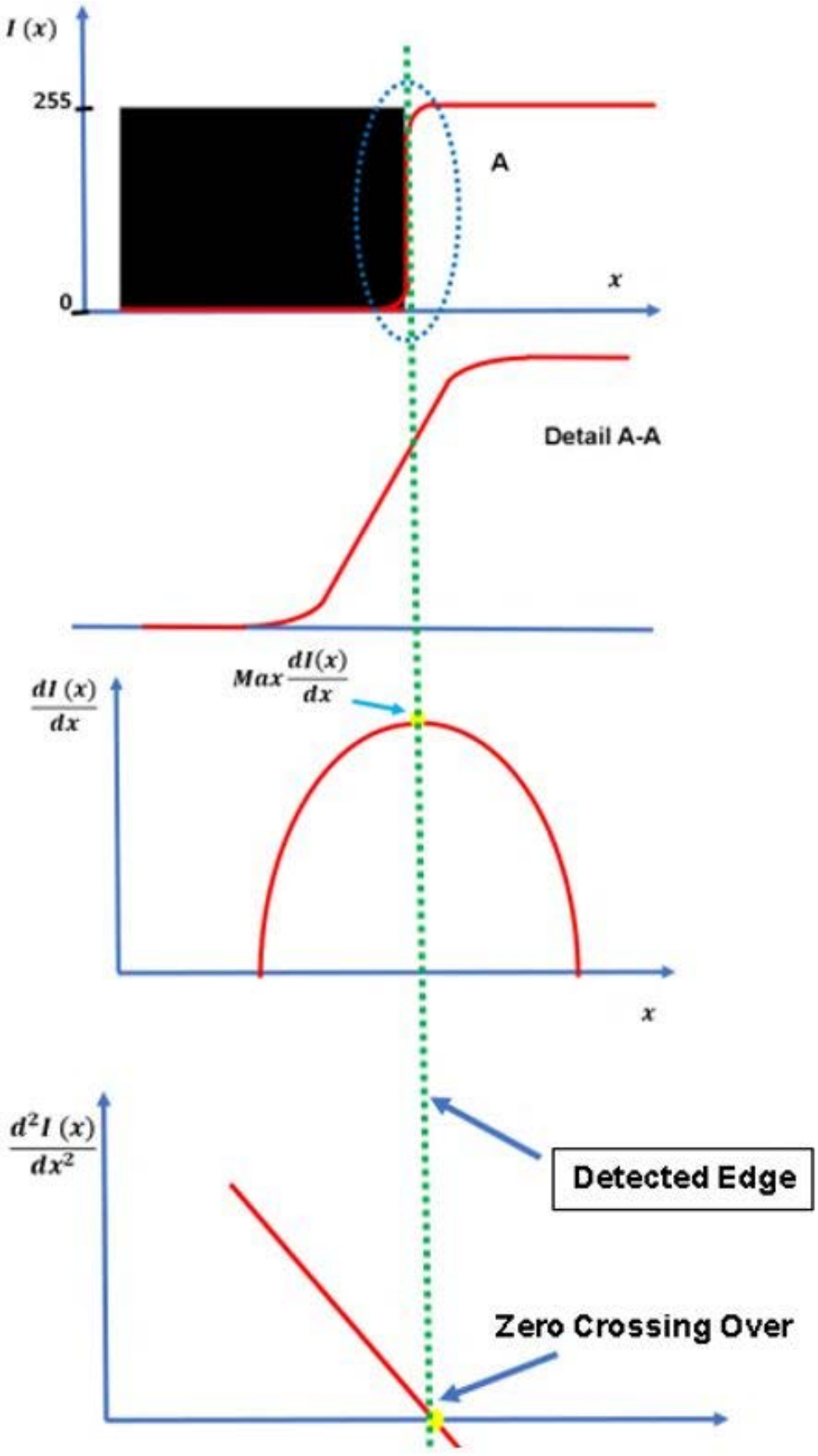

Figure 2-16: Edge detection of gradient operator in x direction

To detect the presence of a gradient discontinuity one can calculate size of the change of the gradient by taking the Pythagoras sum of Δx and Δy [53]:

$$M = \sqrt{(\Delta x)^2 + (\Delta y)^2} \tag{2.9}$$

Where M = the magnitude of the gradient

The direction of the gradient can be determined as:

$$\theta = \arctan\left(\frac{\Delta y}{\Delta x}\right) \tag{2.10}$$

Gradient based operation includes:

- Sobel edge detection
- Canny edge detection

2.5.2.1. Sobel edge detection

A Sobel edge detection is an operation that transforms an image by looking for all the edges within an image.

It makes use of two operation filters which acts as a convolution kernel. These kernels are used to detect the gradients of the edges. One operation detects all the horizontal edges (x direction) and the other detects the vertical edges (y direction) [52]. These convolution kernel can be expressed as

$$G_x = \begin{bmatrix} -1 & 0 & 1 \\ -2 & 0 & 2 \\ -1 & 0 & 1 \end{bmatrix} \tag{2.11}$$

$$G_y = \begin{bmatrix} 1 & 2 & 1 \\ 0 & 0 & 0 \\ -1 & -2 & -1 \end{bmatrix} \tag{2.12}$$

Whereby, G_x is Sobel operator in x direction and G_y is Sobel operator in y direction

The Sobel operator in the x-direction finds the difference between the column 1 and 3 by effectively subtracting the two. Thus, a vertical line is located where a sharp change occurs. Similarly, the Sobel operator in the y-direction locates the horizontal lines by subtracting row 1 from row 3.

To find the edges within the image, we take the Pythagoras sums in the x and y directions.

$$G(x,y) = \sqrt{G_x + G_y^2} \tag{2.13}$$

Given a threshold value, the Sobel operator only detects edges such that,

$$G_S(x,y) > \text{Threshold} \tag{2.14}$$

Whereby G_S is the gradient intensity value of a Sobel operator.

2.5.2.2. Canny edge detection

A Canny edge detector is a process which improves on an output image produced by a Sobel operator by getting rid of any unwanted edges. The Canny edge detection supresses the edges so that they are one pixel wide [54]. This is done by looking at every pixel of an image and checking to see if it's intensity a local maximum, in a given neighbourhood intensity. This will produce a sharp thin line as an edge which is also known as non-maximum suppression[55].

A double thresholding is used to give an indication as the strength of an edge that needs to be detected. Only edges above the upper threshold (maximumVal in Figure 2-17) value is considered as an edge and weak edges below the upper threshold is disregarded as an edge (Edge B in Figure 2-17) unless the edges are connected to its neighbouring pixel (Edge C in Figure 2-17 as its connected to edge A above the maximumVal). Edges below the lower threshold value are completely disregarded as edges [54]

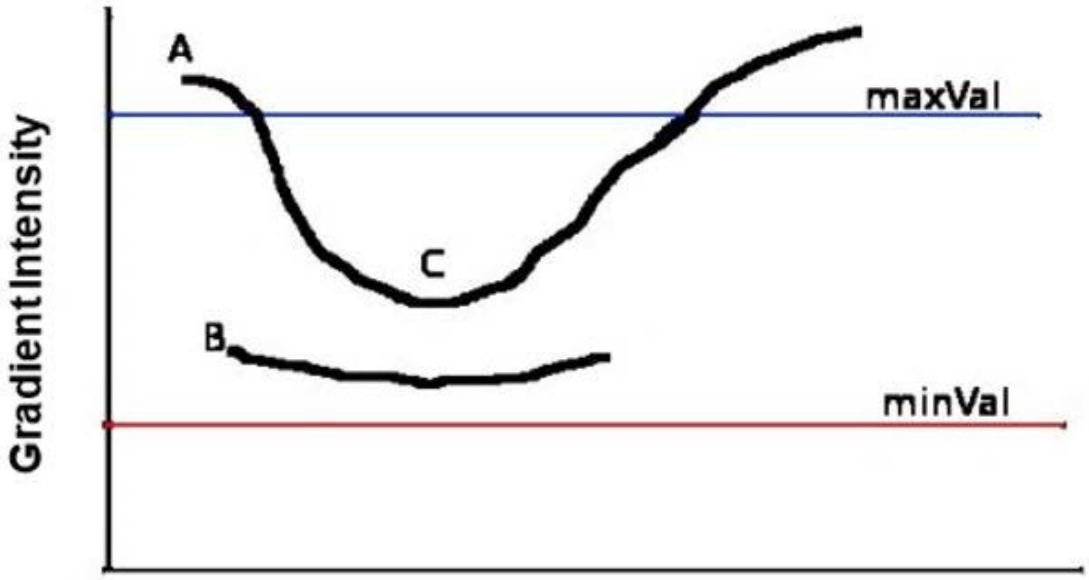

Figure 2-17: Double thresholding of canny edge detection [56]

2.6. Concluding remarks on literature

The literature in the sections above consists of the following:

- A summary of the different types of weaved FRPs used and the different manufacturing processes used to make the FRP panels.
- A brief summary of the theory of the interlaminar fracture toughness and the different standard testing methods used to measure fracture toughness.
- A summary of how an edge of an image is obtained.

This project will explore the effects of fracture toughness of woven fabrics for Mode I by means of an image-based method.

3. Experimental planning and DCB specimen manufacturing preparation

The following experimental plan shows what and why each method was used during this project

- Manufacturing materials used – Due to low cost, the glass fibre was used. Measuring fracture toughness for UD pattern is standardised in the ASTM standards. Thus, the UD pattern was chosen as a base material for this project. Based on the local supplier's availability, the 0/90 Plain weave and 2x2 Twill weave patterns were used to compare results with UD patterns.
- Composite panels – The two commonly used manufacturing methods used to manufacture composite in the Composite Lab is the wet layup and vacuum infusion process. Vacuum infusion was preferred to wet lay-up due to the size of the panels, and to reduce variation between panels due to operator error.
- Type of testing used - Due to its simplicity and time constraints, only the Mode I fracture toughness testing was conducted. The manufacturing panel was sized to produce at least 15 test specimens per panel. Each specimen required two hinge blocks to be bonded to one side of the specimen. This required the author to manufacture DCB Clamping Jigs.

The entire process of manufacturing the composite panels and the boding of the hinge blocks to obtain a testable DCB specimen is described in the sections 3.1 and sections 3.2

3.1. Manufacturing of Composite Panels

The vacuum infusion moulding process was used to manufacture the composite panels in the UCT Composites Lab.

3.1.1. Materials Needed for Infusion Process

The following materials were needed for the infusion process:

- Epoxy resin and hardener
- Fibre glass (dry fibres) - Material used for the composite panels
- Green flow - Layers used to promote resin flow through the composite panels
- Peel ply non-adhesive - Layers used to aid the de-moulding of the part
- Vacuum bag - Used to apply pressure and keep the part air-tight while under vacuum
- Feed pipes - Used to feed in resin and vacuum
- Tacky tape - Used to attach the vacuum bag onto the mould
- Ram wax - Used to prevent adhesion of the panels to the mould table

3.1.2. Reinforcing fibre materials

One of the aims of this project is to investigate the delamination effect of different weave patterns. For comparison purposes one would ideally want the areal weights of the different weave fabric to be constant. This was unfortunately not possible, due to the local supplier's limited stock. Based on the local supplier's stock range, similar areal weights were chosen, shown in Table 3-1 [57].

Table 3-1: Widths and areal weight selected for the different weave patterns

Pattern type	**Widths (mm)/LM**	**Weight (GSM)**
Unidirectional	500	250
Twill weave	1000	280
Plain weave	1300	200

To meet the ASTM requirements for the Mode I fracture toughness tests [21], the specimen dimension chosen was 160X25X4 mm. The insert length was chosen as 63mm.

Each weave pattern has a different ply thickness, which was provided by the supplier datasheet and confirmed by physical measurements. Based on the ply thicknesses, the number of layers needed for each panel was determined and is summarised in Table 3-2.

Table 3-2: Fabric thickness and number of layers for different weave patterns

Weaved pattern	Thickness of fabric (mm)	Layers needed for 4mm panel
Unidirectional	0.20	20
Twill weave	0.22	18
Plain weave	0.17	24

3.1.3. Preparing of the layers of panels

Each panel was oversized to ensure 15 specimens could be cut, making allowance for shrinkage and cutting. Figure 3-1 shows an example of a Plain weave panel.

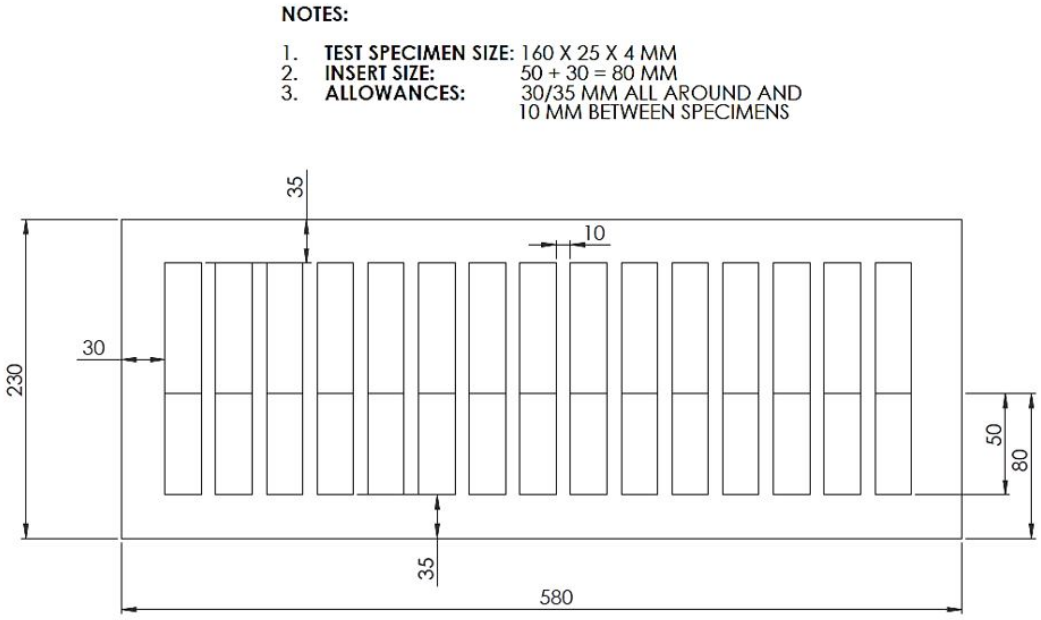

Figure 3-1: Oversizing of the Plain weave panel

Dimensions used for the materials of manufacturing processes can be seen in Appendix A.1

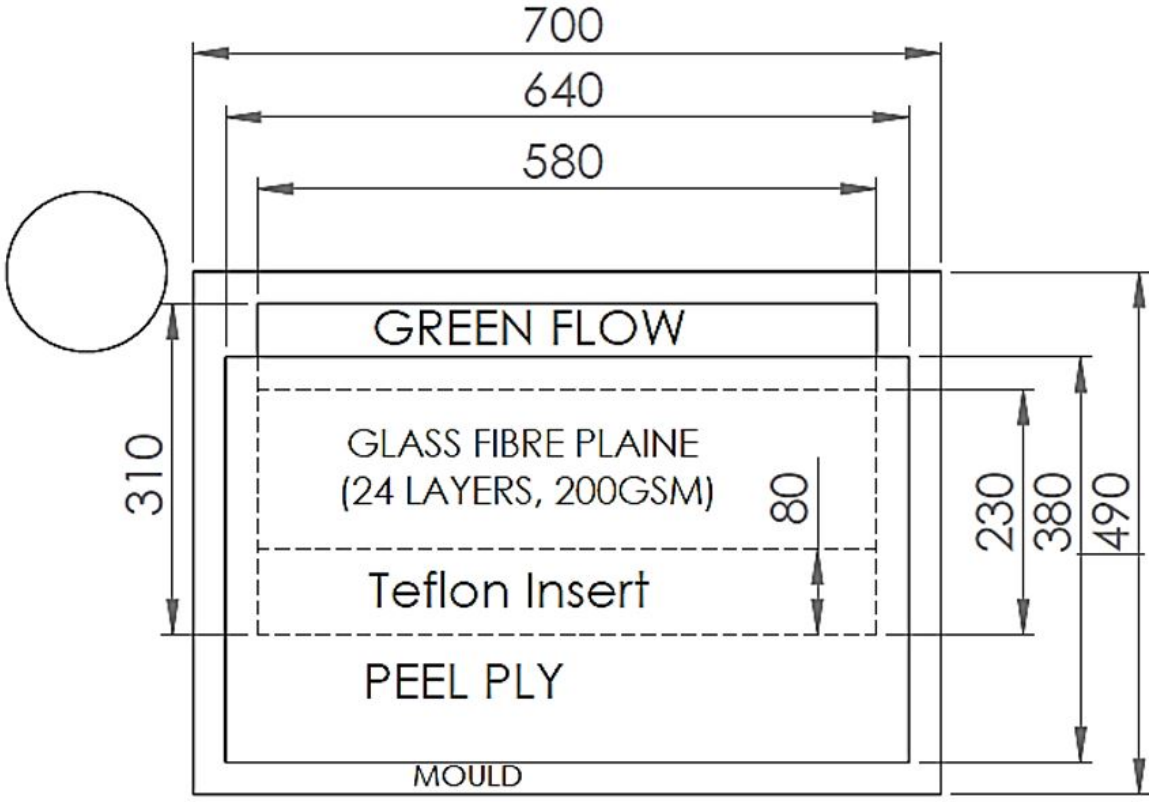

Figure 3-2: Lay-up of Plain weave panel

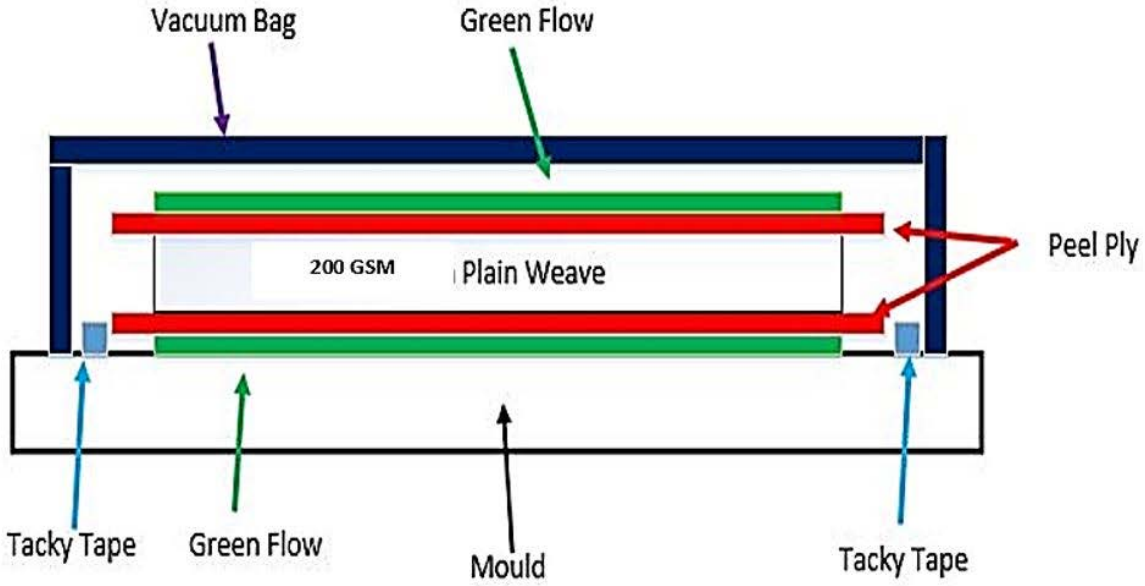

Figure 3-3: Side view of mould lay-up

Figure 3-2 and Figure 3-3 show the top and side views of the mould layout for the 200 GSM Plain weave. The Unidirectional and Twill weave patterns are laid up in a similar way.

Refer to Appendix for the preparation before the resin infusion and a detailed process of how the resin infusion was conducted.

3.1.4. Observations made after first batch of panel manufacturing

A few observations were made when manufacturing the different weave patterns. The UD pattern was manufactured first. It was evident that the resin flow rate was quite fast, and the resin reached the outlet port to the vacuum pump within 3 to 4 minutes. There was a concern that the resin had flowed rapidly over the surface plies but had not necessarily wetted the middle layers thoroughly.

It was understood that the resin flow rate needed to be slowed down for the next manufacturing batches (Plain and Twill weave patterns), to allow for more even wetting of the layers. Since the green flow layers are used to promote resin flow, the dimensions of the top layer of green flow for the Plain and Twill weave were reduced to compensate for the increased resin flow rate observed in the UD panels.

However, once the panels were manufactured it was observed that the resin flow rate is dependent on the type of pattern used. The time for the resin to reach the outlet pipe was slower for Twill and Plain weave patterns than the UD pattern and thus the reduction of the green flow was not needed.

By changing the sizes of the green flow, the panels were no longer symmetrical and thus there was an unwanted kink in the panels after the part was cured, shown in Figure 3-4. This is undesirable when testing as the flexural response of the specimens will no longer be uniform. This will indeed affect the results of the tests. However, this was corrected by manufacturing additional specimens in a second batch.

Figure 3-4: Unwanted kink of specimen

Future lay-ups of UD should keep a uniform green flow layer and the user should be prepared for a faster infusion process.

It was also noted that Plain weave required more resin than UD, whilst the Twill weave needed more than the Plain. This was to be expected, as the assumption was that the resin intake is directly proportion to the mass of the materials used for manufacturing processes.

3.2. Design aspects for Double Cantilever Beam testing

3.2.1. Clamping Jig – First iteration

For each DCB specimen, two Hinge Blocks need to be glued onto either side of one end of the specimen using the Spabond 340LV epoxy adhesive [58]. A Clamping Jig was manufactured to help alignment of the two holes of the hinge blocks, ensuring the specimen will fit easily in the DCB test fixtures on the Zwick machine and ensuring the specimen is loaded in pure tension without twisting.

Figure 3-5 shows how the holes are to be aligned.

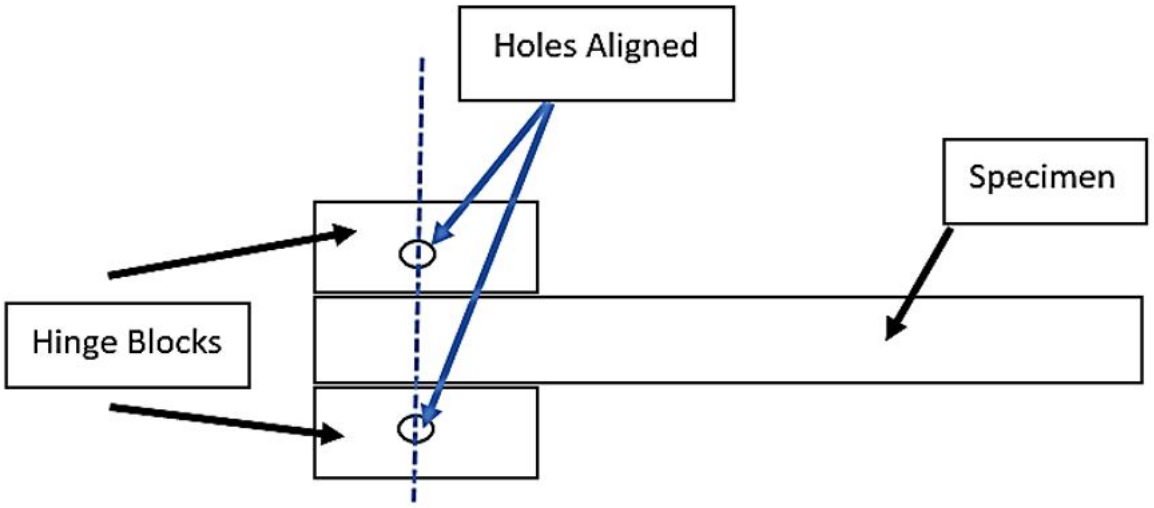

Figure 3-5: The way the holes needs to be aligned.

The Clamping Jig was designed using SolidWorks CAD software, and manufactured using an Ultimaker 2+ 3D printer. The Clamping Jig was assembled from three major components, including the Base, Tail and Pin Slider.

The full assembly instruction of the first Clamping Jig can be seen in Appendix C.1. The assembled Clamping Jig with the specimen can be seen in Figure 3-6

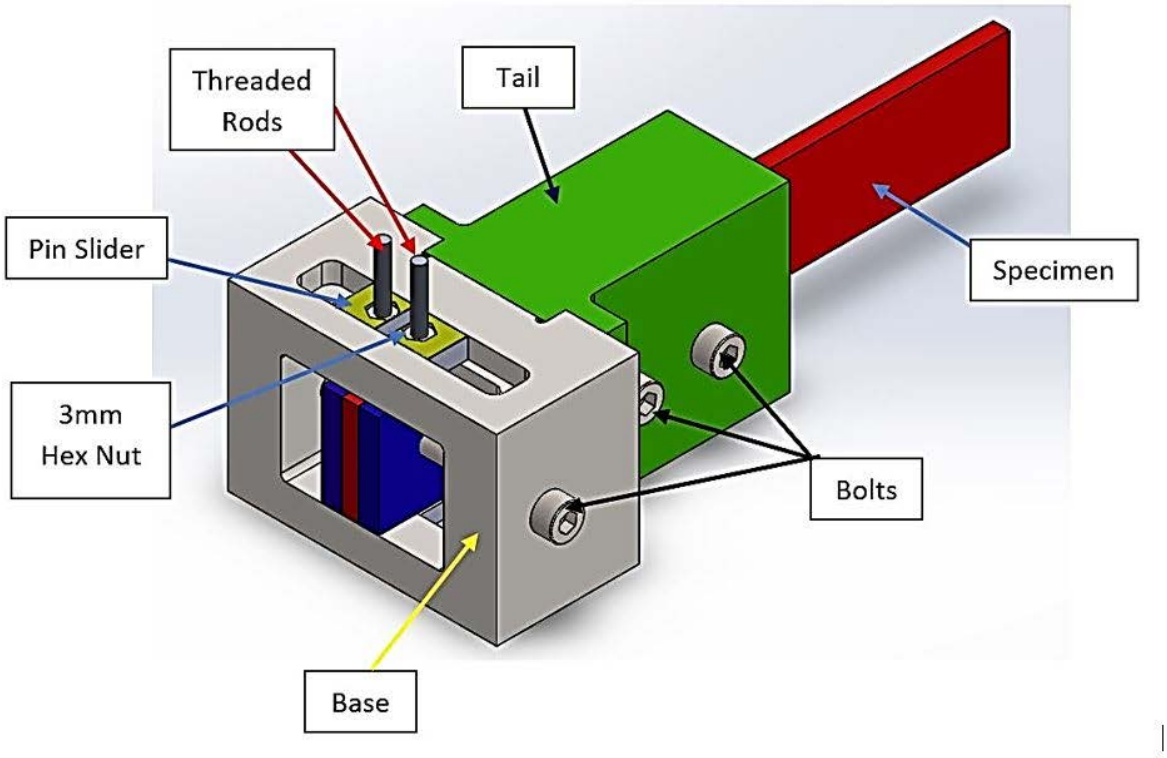

Figure 3-6: Assembled Clamping Jig and specimen

The Tail is attached to the Base using screws. The Pin Slider is inserted into the Base. The threaded rod is threaded into the nut which is placed into the Pin Sliders. The rod is also inserted through holes on the Hinge Blocks. The bolts are used to clamp the Hinge Blocks onto the specimens.

As mentioned earlier, these parts were modelled on Solidworks and then saved as an STL extension file, which was used to generate GCODE for the 3D printing machine. The filament material selected for the jig components was ABS. As the jig and specimens are placed in an oven at 40 to 45° to speed up the epoxy curing, the jig must be able to comfortably withstand these temperatures without softening or deforming. PLA, which is the other common 3D printing filament, has a glass transition temperature at 60°, which is rather close to the oven temperatures. ABS have its glass transition temperature at 105°, which comfortably exceeds the 40 to 45° anticipated.

Problems incurred with the first iteration:

- The top surface of the Base caused difficulty when positioning and clamping the hinge blocks due to the limited space of the design.
- The Tail and Base need not be 2 separate parts – By having them separate increases the amount of parts needed to be 3D printed

3.2.2. Clamping Jig - Second iteration

Based on the problems incurred from the first iteration the clamp design was redesigned to combine the Tail and Base into one part. The combined part in this case will be referred to as the Base. Figure 3-7 shows the redesign of the Base. The top surface remained open to allow the hinge blocks to easily assemble through the threaded rods.

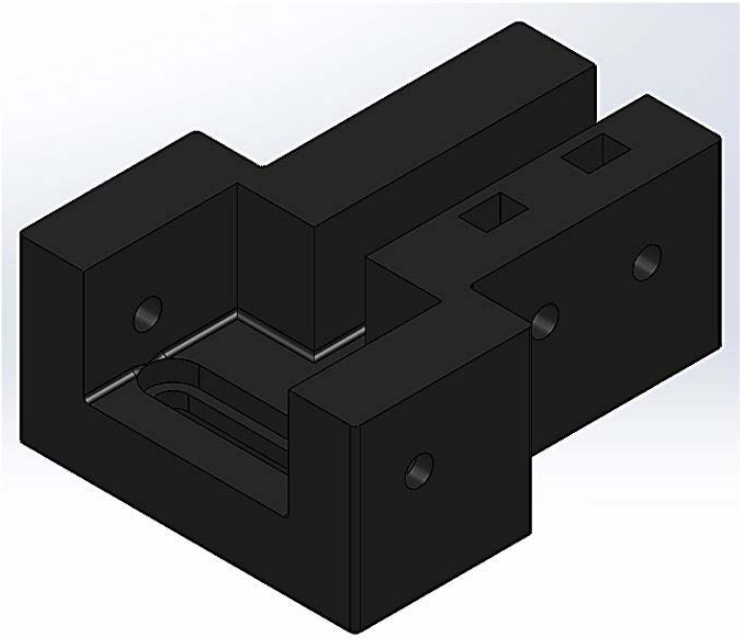

Figure 3-7: Second iteration of Base

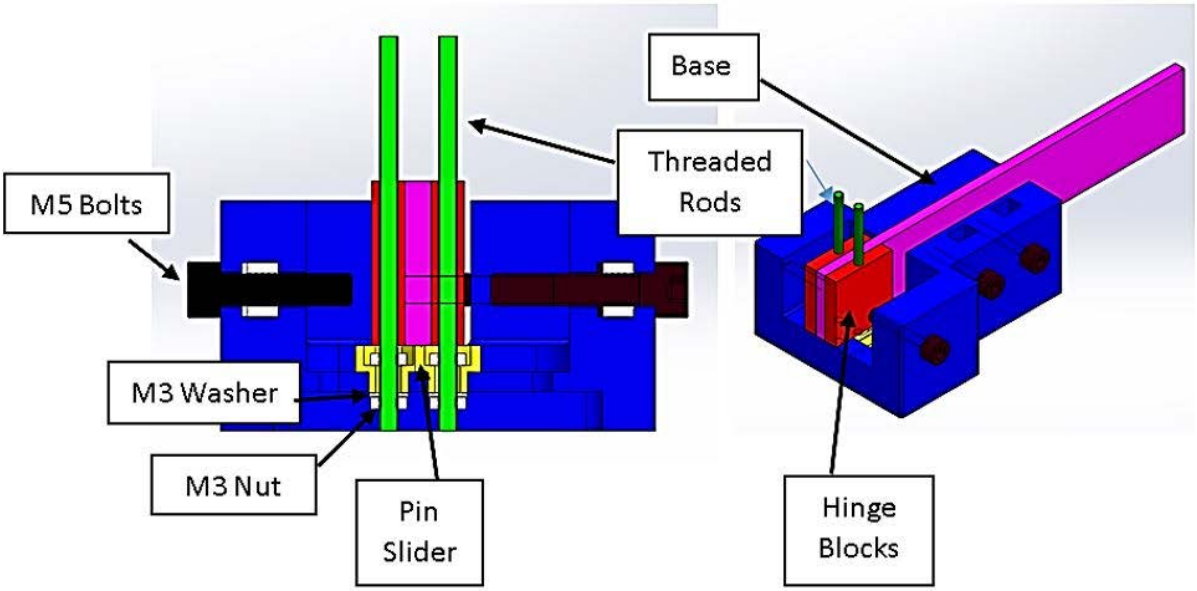

Figure 3-8: DCB assembled Clamping Jig

The assembly of the second iteration of the DBC fixture as shown in Figure 3-8 is assembled in a similar way to the first iteration. Considering the top surface is open, only 2 Pin Sliders was used. The Pin Slider was assembled in the same manner as the original Pin Slider. The threaded rod is inserted top down through the embedded nut on top of the first M3 nut of the Pin Slider. A washer and a M3 nut were used to tighten the threaded rod from the bottom up. This will secure the threaded rod within the slot. The hinge blocks were tightened towards the specimen using bolts and threaded through the embedded nut. Refer to Appendix C.2 to see the assembly instructions for the second iteration of the DCB Jig.

3.2.3. Gluing of hinge blocks

Hinge blocks were bonded to specimen by the following process:

- The bonding sides of the hinge blocks and specimens were degreased with Isopropanol. This ensures that the bonding area of the hinge blocks and specimen are clean, such that bonding of the components will take place.
- The ram wax is then applied to the Pin Slider slots. This is to allow the components to be easily removed once the bonding has occurred.
- Once the bonding area is cleaned up and the slots having a layer of ram wax, the hinge blocks are ready to be threaded into the Pin Slider via the threaded rod as seen in Figure 3-6.

The method of how the hinge blocks were attached to the specimen for the first and second DCB rig can be seen in Appendix D.1 and Appendix D.2 respectively.

3.2.4. Designing of DCB fixtures

In order to mount the DCB specimen on the Zwick machine for the fracture toughness test, it was necessary to design custom fixtures.

Two DCB fixtures were designed, namely:

- Top Hinge Block Holder
- Bottom Hinge Block Holder

The CAD designs of these fixtures can be seen in Appendix E

It should be noted that the slots have a clearance tolerance to make sure that the Hinge Blocks will rest onto the seat of the Hinge Blocks Holders.

4. Image-based crack measurements

The crack tip position is a vital parameter to calculate the critical strain energy release rate G. Each DCB fracture toughness test was recorded using a digital camera. By doing so, the position of the crack tip could be found using an image-based method. Image-based crack detection can be extended to higher speed tests, and less subject to operator error than manual visual readings during tests.

The video of the fracture toughness test was converted to a series of grayscale images, from which the detection algorithm could determine the crack tip position as a function of time. For each individual image, the detection algorithm would seek to identify the top and bottom crack surfaces as edge points (Refer to Figure 4-2).

As with most image processing methods, the edge detection criteria was related to the grayscale intensity of a pixel at a known position, $I(x, y)$, or the gradient of the intensity.

Once the points along the upper and lower crack edges were detected, polynomials (or other functions) were fit through these points. Either the intersection of the best-fit lines for the top and bottom crack surface or the last detected point was deemed to be the crack tip. Three different strategies for detecting the crack tip were investigated, with continuous refinement of the edge detection strategies and parameters:

- Angular Sweeping method
- Vertical Line method
- Crossing Point method

The aim of these detection algorithm is not to process the entire image for every frame as it is too time consuming. User inputs were used to crop the images to a small window within the frame to reduce computational time.

4.1. Angular Sweeping method

The Angular Sweeping method uses lines at different angles, with a common start point, which should be somewhere between the top and bottom crack surface within the crack opening region as indicated in Figure 4-2. The edge detection is performed along each line. Figure 4-1 shows the flow chart of the Angular Sweeping crack detection method.

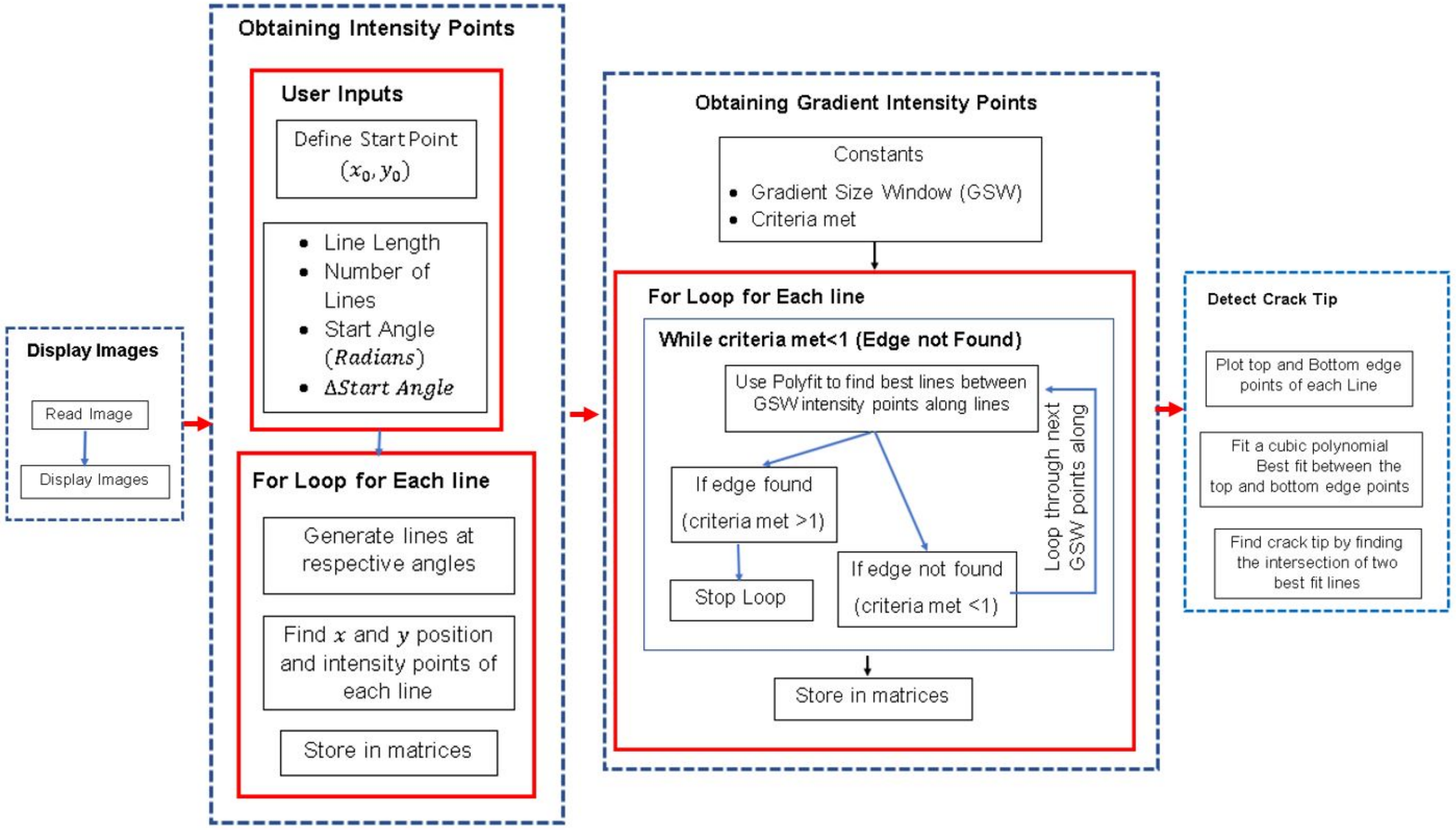

Figure 4-1: Flow chart showing the Angular Sweeping method

The DCB images were loaded into the MATLAB editor and a user input (x_0, y_0) was required somewhere within the crack opening region between the specimen opening (refer to Figure 4-3) to define the common start point.

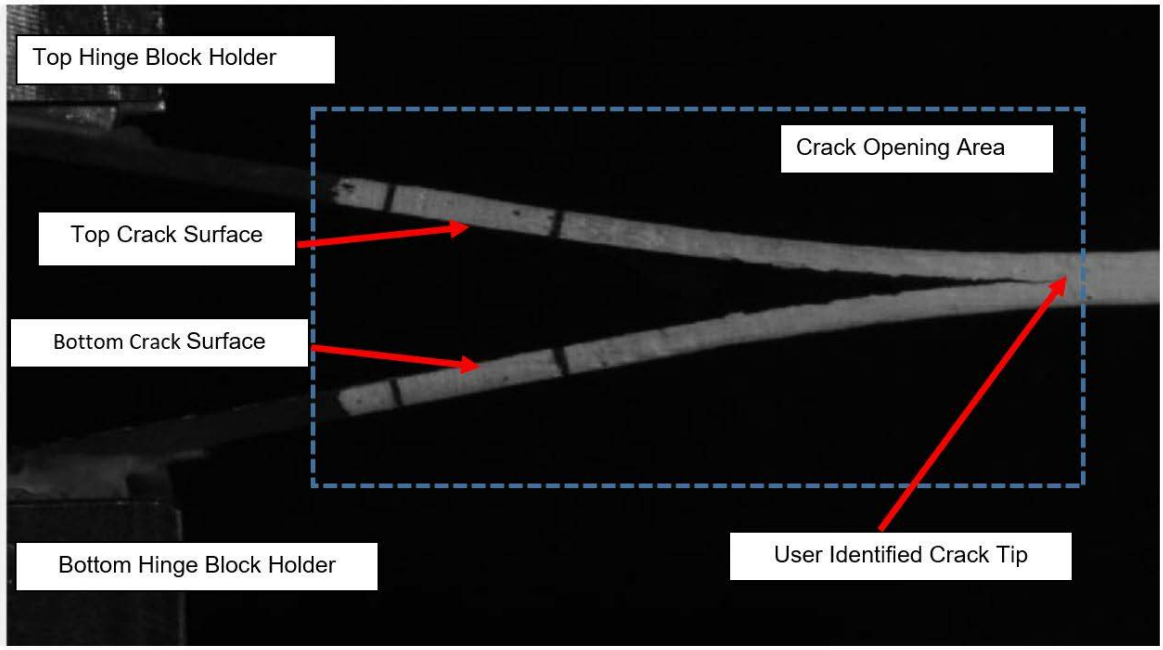

Figure 4-2: The crack opening area

The generated lines were formed from the starting point (x_0, y_0) to (x_1, y_1) at a known starting angle (θ), shown in Figure 4-3. The number of lines generated was chosen by the user. The $\Delta\theta$ value was chosen such that when the line sweeps were generated, the last line would be horizontal (green line in Figure 4-3, which is parallel to the starting point (x_0, y_0)).

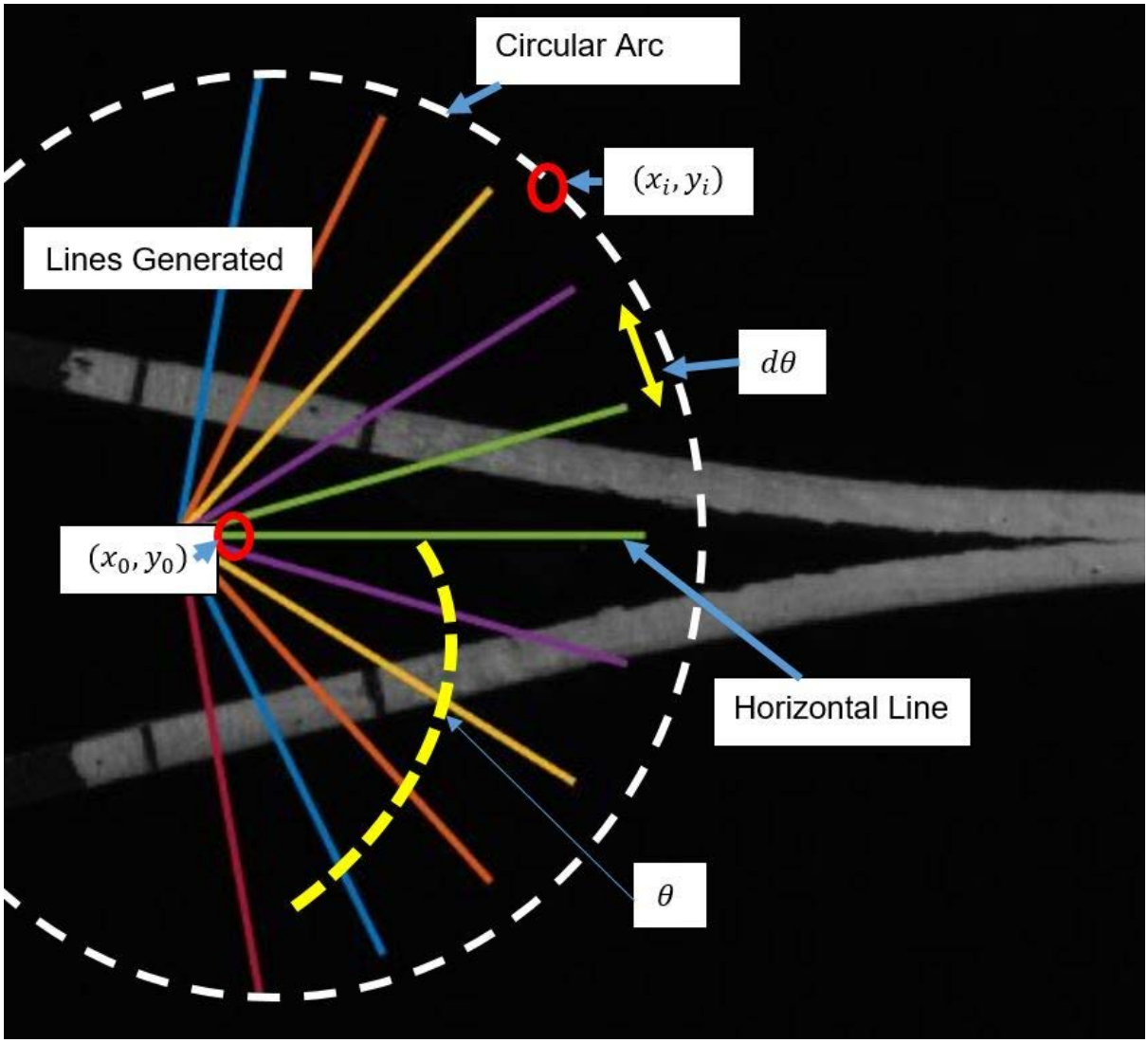

Figure 4-3: Lines swept along a circular arc

It is important to note that lines above the horizontal were intended to detect the top crack edge, and those below were intended to detect the lower crack edge.

The end point $(\mathrm{x}_1, \mathrm{y}_1)$ is along a circular arc. It is dependent on the length of the line L and can be derived from the combination of equations of a circle and the straight line:

$$\mathrm{x}_1 = \mathrm{x}_0 + \sqrt{\left(\frac{\mathrm{L}}{\tan\theta}\right)^2 + 1} \tag{4.1}$$

$$\mathrm{y}_1 = (\mathrm{x}_1 - \mathrm{x}_0) * \tan\theta + \mathrm{y}_0 \tag{4.2}$$

After incrementing θ to generate the full set of lines of length L, the built in MATLAB function "improfile" was used to determine intensity $(\mathrm{I}(\mathrm{x}, \mathrm{y}))$ at a given coordinate along each line.

In image processing, edges are detected by sharp changes to the pixel intensity, or the gradient thereof. The chosen starting point (x_0, y_0) was situated within a black region and the specimen was painted with a white layer of correction fluid. Thus, there was a sharp change in intensity value when the colour changed from black to white, corresponding to where the line intersected the top and bottom crack surfaces.

The simplest method to find the edge was to locate where the intensity along the line exceeded a specified threshold intensity.

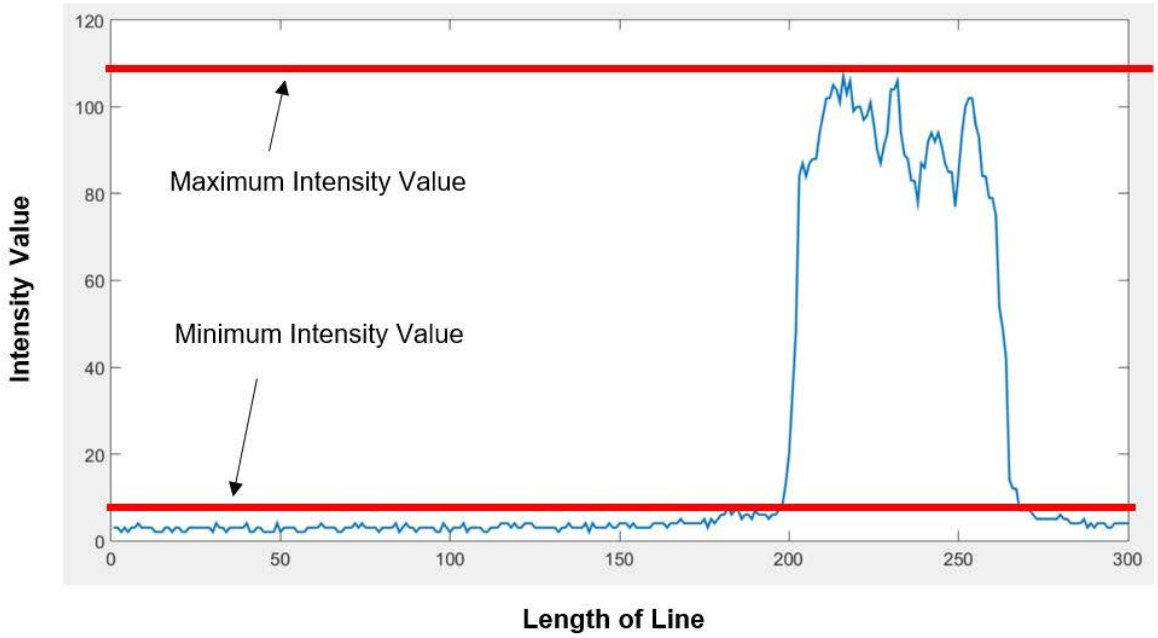

Figure 4-4: Graph showing pixel intensity of one line

Figure 4-4 shows a graph of the pixel intensity value along the length of one generated line. There is a sharp change in intensity values from 10 to 120, which corresponds to the dark to light transition at the upper crack surface. These were taken to be the minimum and maximum intensity values as a form of double thresholding to locate the edge points:

$$\text{Minimum intensity value} < \text{Edge thresholding points} < \text{Maximum intensity value} \tag{4.3}$$

To further refine the edge points, a gradient operator was used in addition to the thresholding. Refer to Figure 4-5 for the graph of the gradient intensity values along the length of one line.

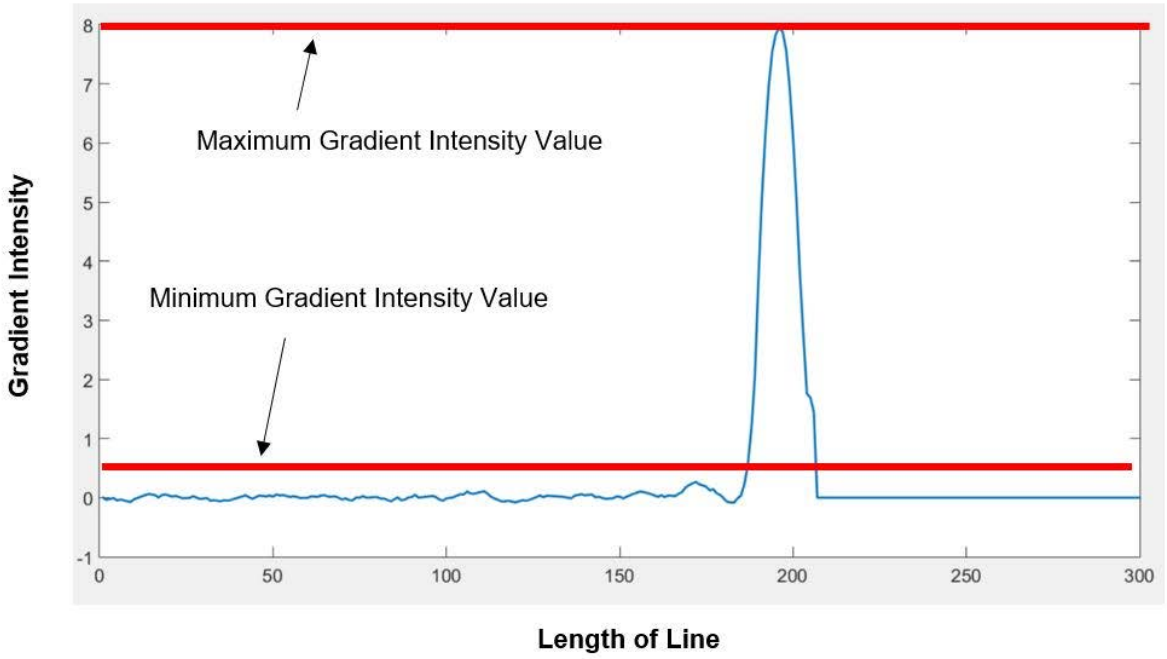

Figure 4-5: Graph showing gradient pixel intensity of one line

The method to obtain the gradient pixel intensity made use of a small gradient size window (GSW) beginning from the start of the line. The pixel intensity values along a small subset of the line, gradient size window (GSW) were fit to a linear function using the MATLAB polyfit function. The slope of this line was taken as the pixel intensity gradient. By incrementing the subset along the line, a relatively smooth output for the pixel intensity gradient was obtained. The range between the maximum and minimum gradient intensity values was chosen as the gradient thresholding as in equation (4.3) for the intensity values:

$$\text{Minimum gradient intensity value} < \text{Gradient thresholding points} < \text{Maximum gradient intensity value} \quad (4.4)$$

From Figure 4-5, the minimum and maximum gradient intensity values were 0.5 and 8 respectively.

With the maximum and minimum gradient and pixel intensities known, a series of tests was conducted to determine how the intensity and gradient threshold values would affect the accuracy of edge detection. It should be noted that the first point where both the intensity and gradient thresholds was met was chosen as the edge point.

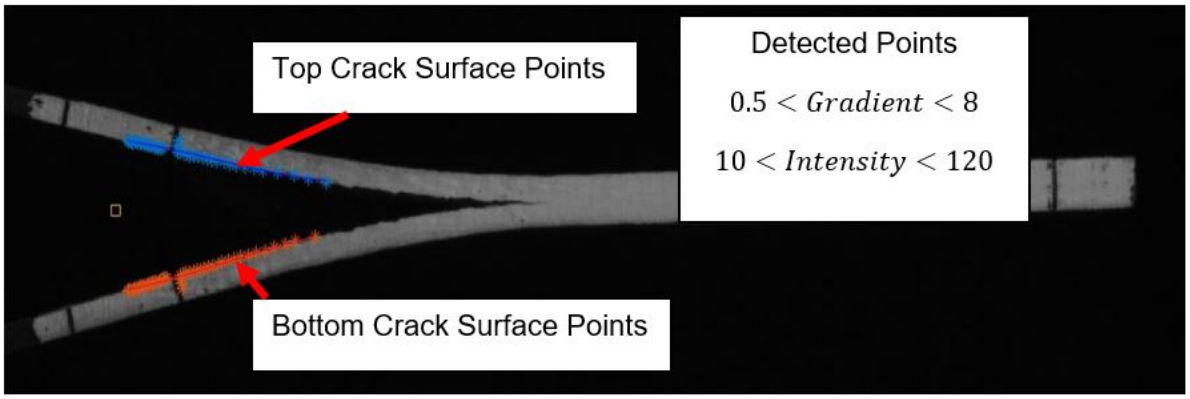

Figure 4-6: Detected edge points using maximum and minimum gradient and intensity values

Figure 4-6 shows a sample image of the detected surface edge points using the respective maximum and minimum gradient and intensity values. Figure 4-7 shows what happens when the maximum gradient intensity values are lowered, and the minimum intensity values increases. With the change in values, the algorithm picks up the edge points within an acceptable range. Minimum change was picked up compared to Figure 4-6.

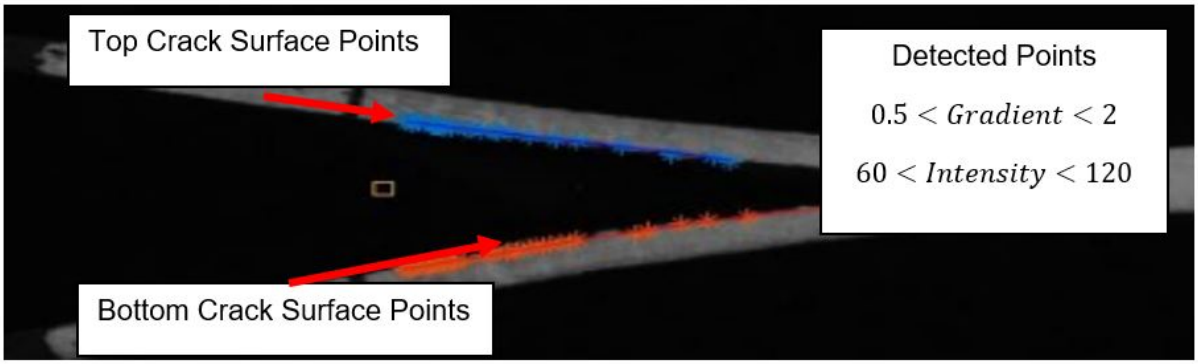

Figure 4-7: Decreasing maximum gradient value and increasing minimum intensity value

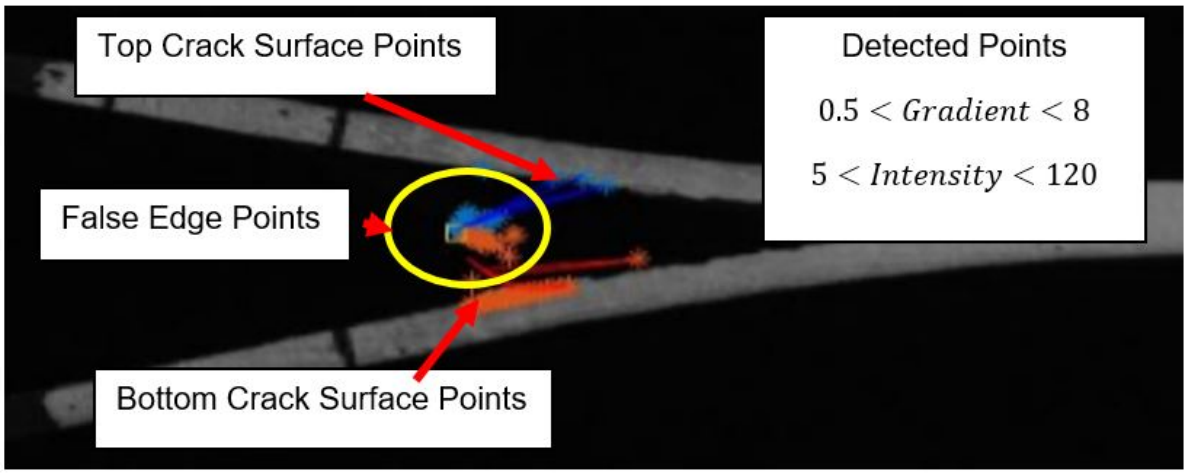

Figure 4-8: False detection edge points when lowering the minimum intensity value

False edge detection is picked up if we lower the minimum and maximum intensity values, as seen from Figure 4-8 and Figure 4-9.

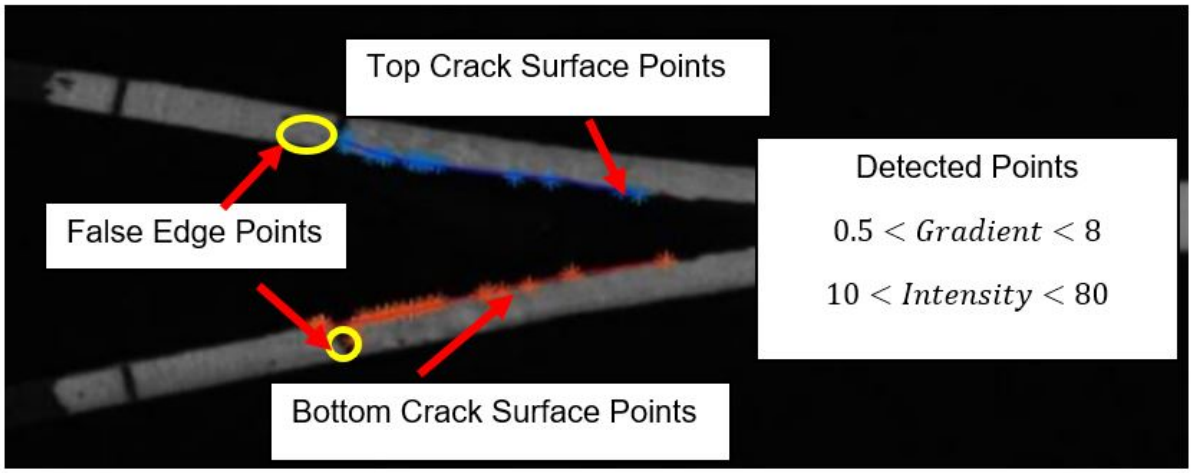

Figure 4-9: False detection edge points when lowering maximum intensity value

Based on Figure 4-8 and Figure 4-9, the intensity thresholding value is critical in correctly predicting the crack surface points as it is more sensitive to changes compared to the gradient threshold. Thus, to correctly detect the surface edge points, the gradient and intensity criteria was chosen to be between its minimum and maximum values.

Although the intensity value correctly predicted the crack tip for the current instant. Based on the literature as seen in sections 2.5.2 and Figure 2-16 it can be seen it is based on some kind of gradient operator. The detection method was refined In sections 4.3 by choosing the limiting case as the change in intensity (a form of gradient operator).

Although this method could correctly detect the edges, it would only assign them correctly as the top or bottom crack edges if the start point was located on the horizontal line midway through the specimen thickness. Referring to Figure 4-10, the midway of the specimen does not line up with the mid way between the hinge blocks.

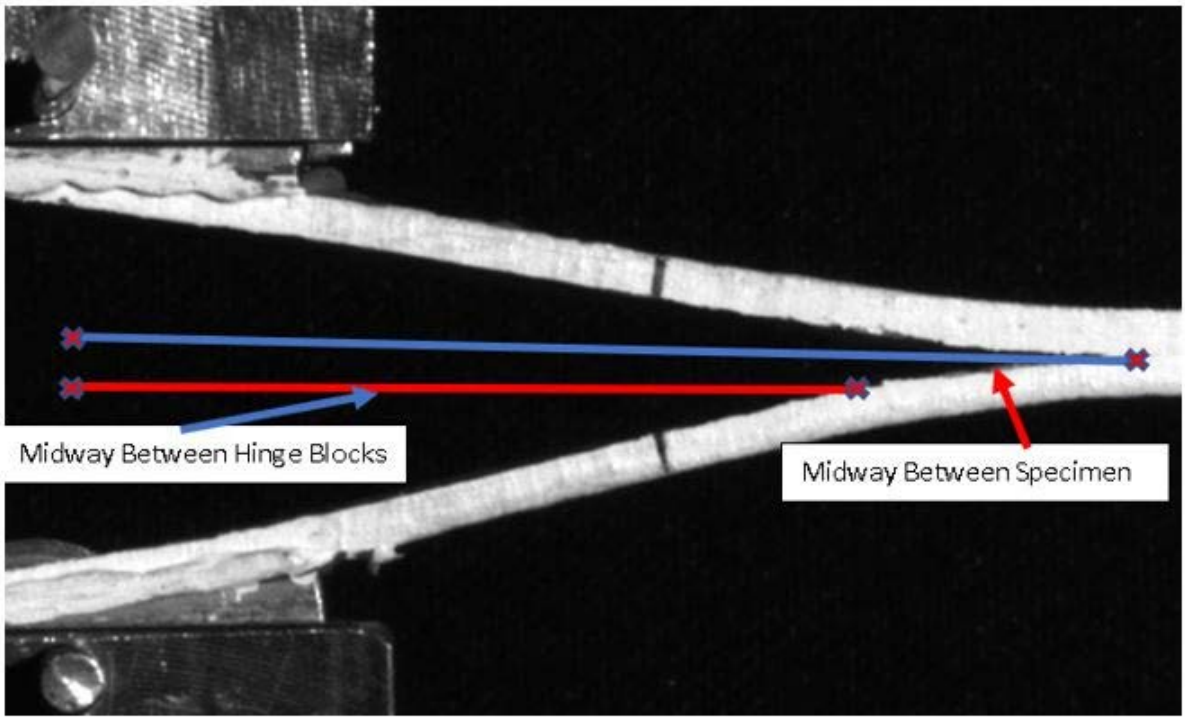

Figure 4-10: Specimen not symmetrical about mid plane

It should be noted that the midway between the hinge blocks coincides with x_0 from the starting value and the horizontal green line as shown in Figure 4-3. Due to them not lining up, the sweeping of the lines does not always assign edge points correctly to the top or bottom crack edge, as seen from Figure 4-11).

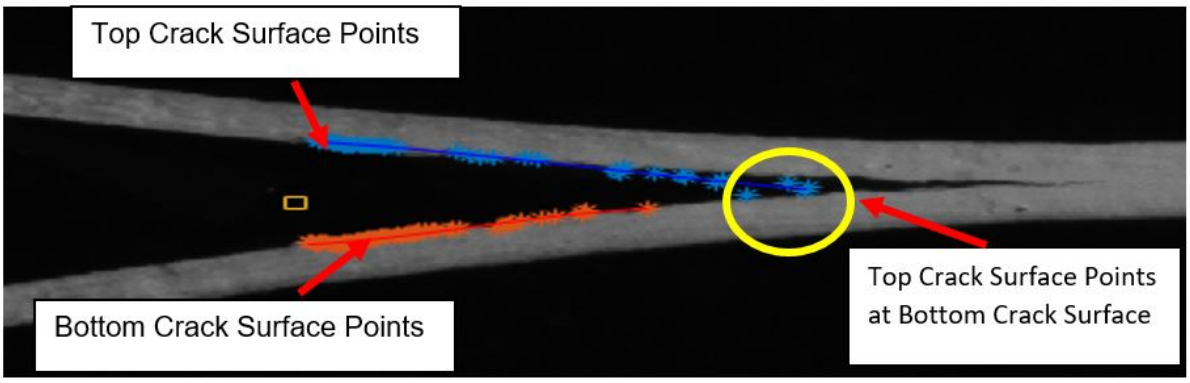

Figure 4-11: Error regarding sweeping method

Refer to Appendix F.1 for the MATLAB script file for the sweeping method detection algorithm.

4.2. Vertical Line method

In order to avoid errors in allocating edge points to the upper or lower surfaces incorrectly, sweeping along a vertical line rather than an angled line was investigated. Figure 4-13 shows a flow chart of the Vertical Line detection method.

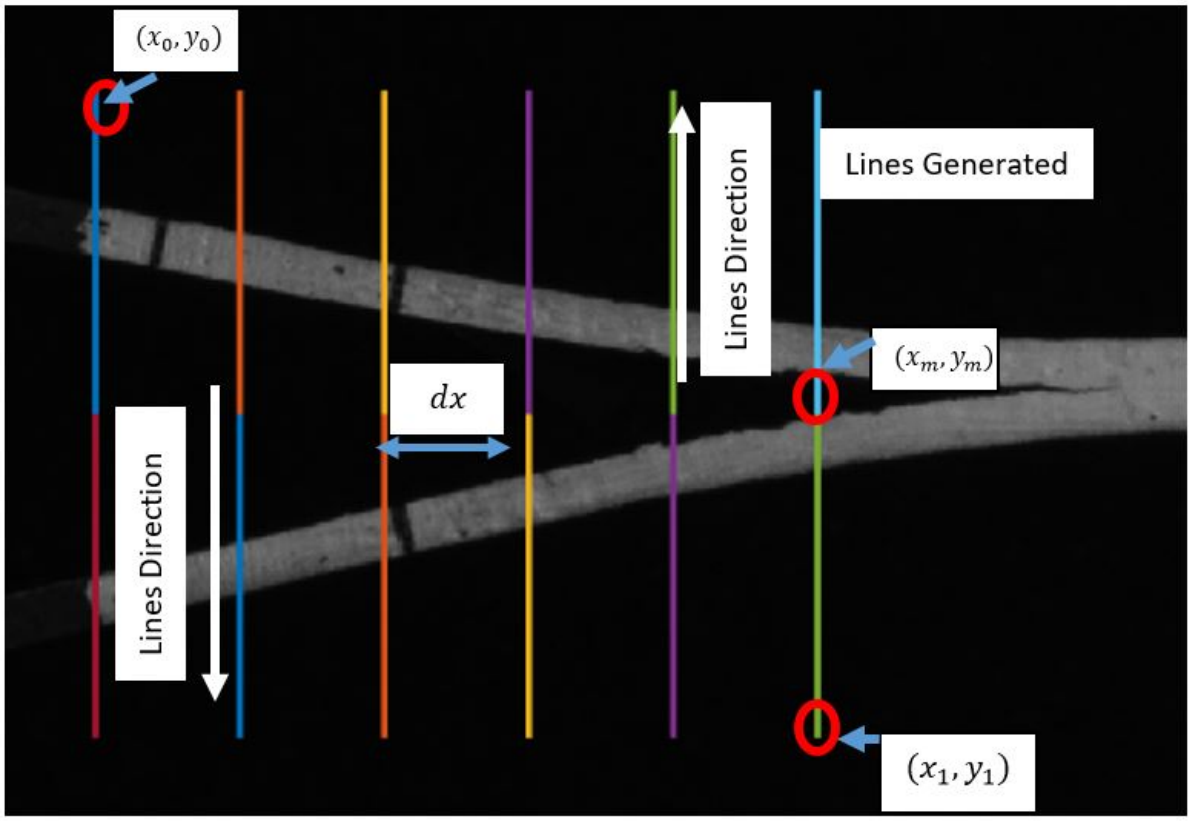

Figure 4-12: Line generation using the Vertical Line method

Rather than sweeping the lines at an angle as in section 4.1, vertical lines were used. The user inputs the start (x_0, y_0) and end points (x_1, y_1). Depending on the number of lines (N) chosen, dx (distance between adjacent lines) was chosen to produce lines such that all the lines go from x_0 to x_1.

The line ranges from: $y_1 \leq \text{Line range} \leq y_m$ for the top surfaces whereas the bottom surface ranges from: $y_0 \leq \text{Line Range} \leq y_m$, with L being the length of the line and $y_m = \frac{y_0 + y_1}{2}$

Just as in the sweeping method, the (x, y) pixel coordinate and intensity values were obtained using the "improfile" function. The gradient and pixel intensity along the length of the line was plotted (as in Figure 4-4 and Figure 4-5) to obtain the maximum and minimum intensity values.

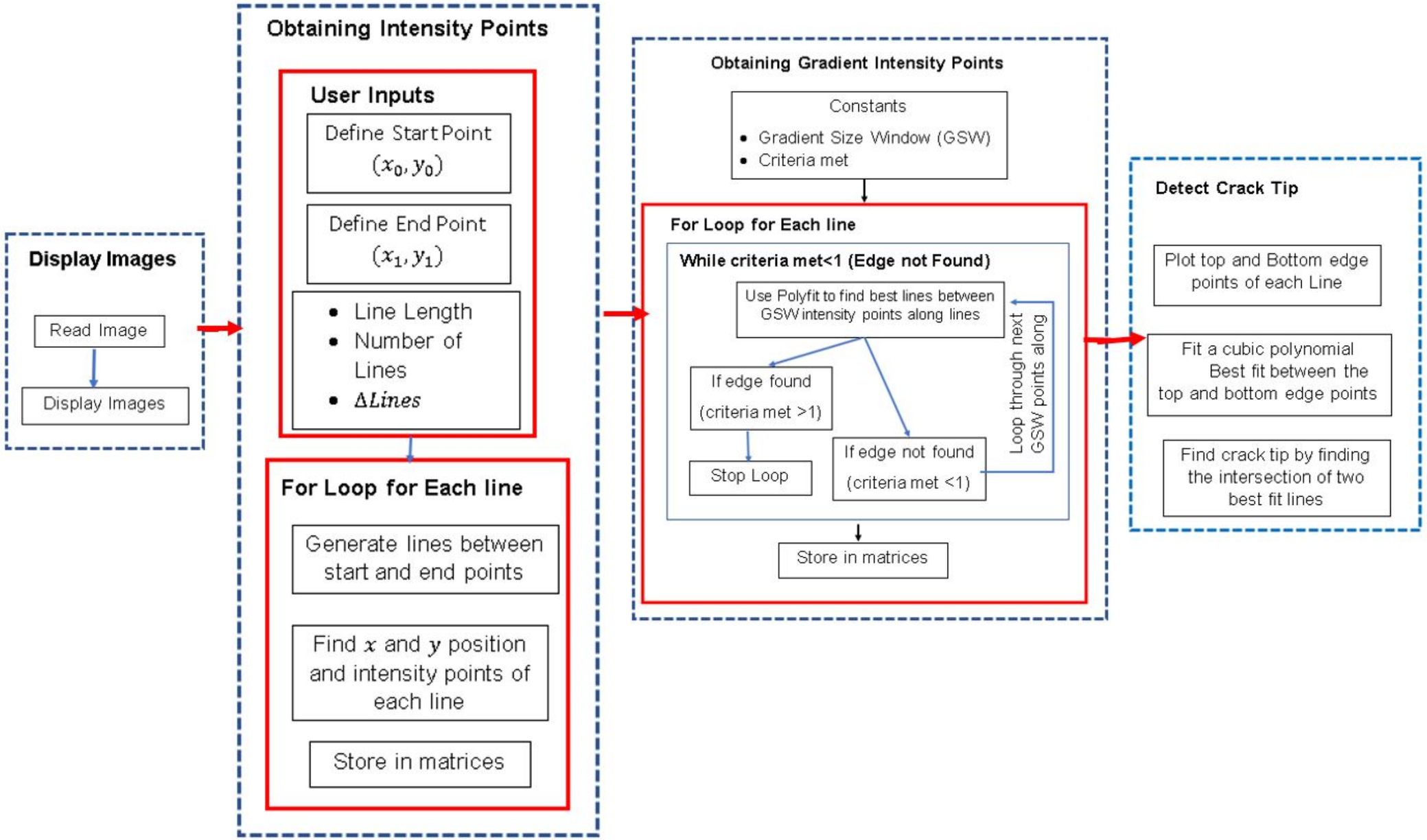

Figure 4-13: Flowchart showing the Vertical Line method

With the top and bottom surface points detected, the position of the crack tip was predicted using the intersection of polynomials fit to the upper and lower edge point sets. Figure 4-14 shows the predicted crack tip using a cubic curve fit. It should be noted that the “MATLAB detected crack point” is what the algorithm picked up as the crack tip and the “User identified crack point” is the position of the actual tip as seen by the author.

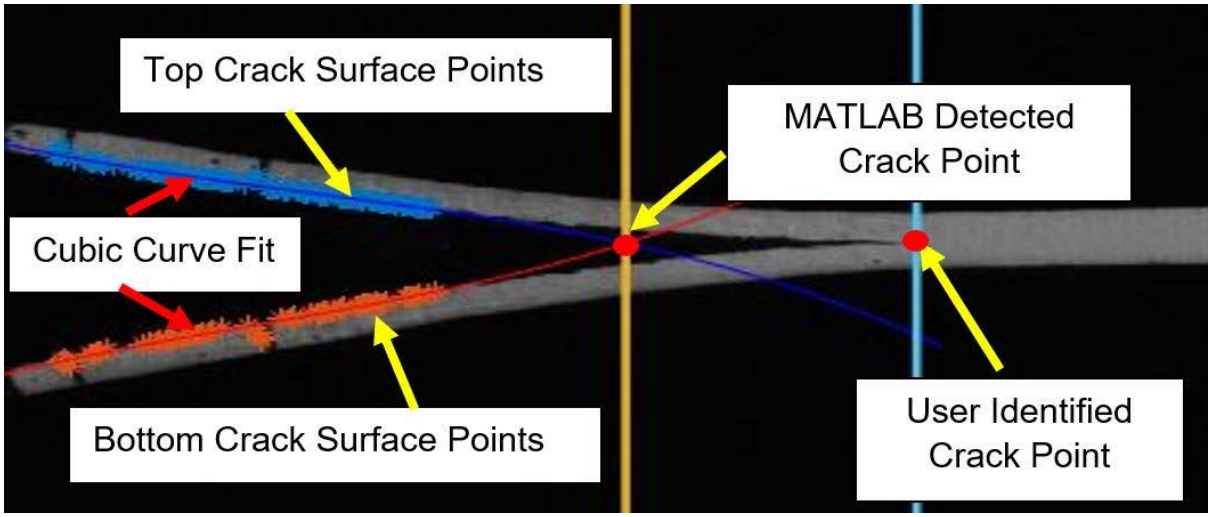

Figure 4-14: Error using cubic curve fit

Based on the data obtained from MATLAB, the error was approximately 23% of the actual crack tip, which is unacceptable. A parabolic (order 2 polynomial) and linear (order 1 polynomial) curve fitting was also chosen, and the results can be seen from Figure 4-15 and Figure 4-16 respectively.

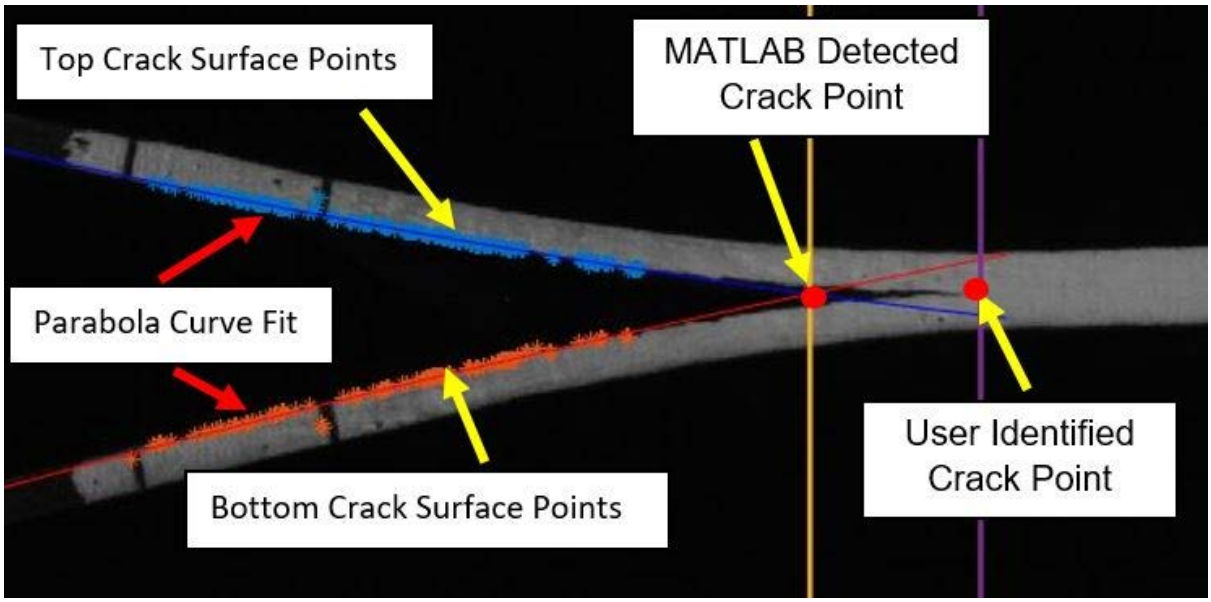

Figure 4-15: Error using parabolic curve fit

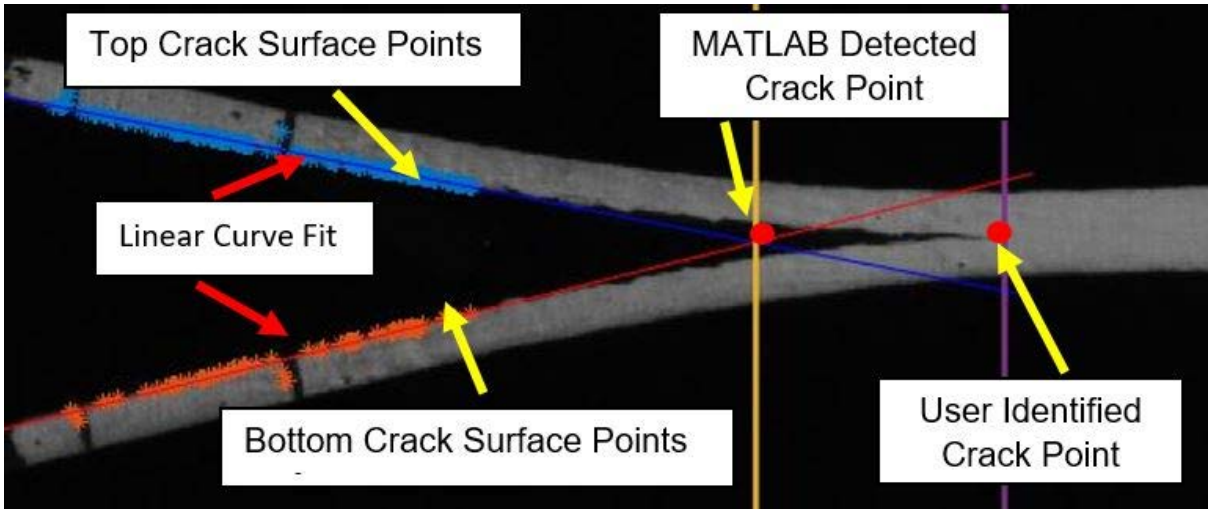

Figure 4-16: Error using linear curve fit

The error obtained for the parabolic and linear curve was approximately 13% and 18% respectively.

This strategy detected the edge points and allocated them to the upper or lower edge with very little error or spurious edge detection. However, the polynomial lines fitted to the edge point sets clearly do not intersect at the crack tip.

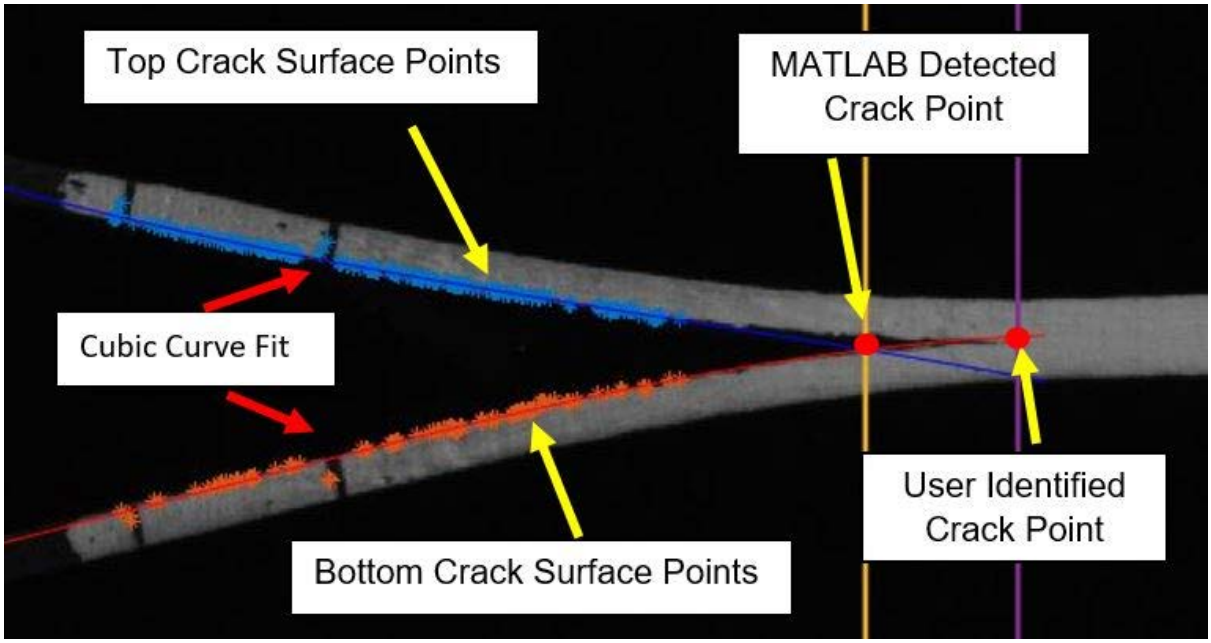

Figure 4-17: Error decreasing if more points are detected towards crack tip

Figure 4-17 shows how the error between detected and actual crack tip decreases if we move the end point (x_1, y_1) closer towards the crack position, effectively creating lines in a wider

range. The author believed that the crack tip detection would be more accurate, if the end point (x_1, y_1) could be brought closer to the crack tip.

With the current method, that was not possible as can be seen in Figure 4-18. The limitation of the Vertical Line Method occurred if we brought the (x_1, y_1) of the line towards the crack tip. The top edge points are misplaced to the bottom of the specimen, whereas there are no bottom surface edge points.

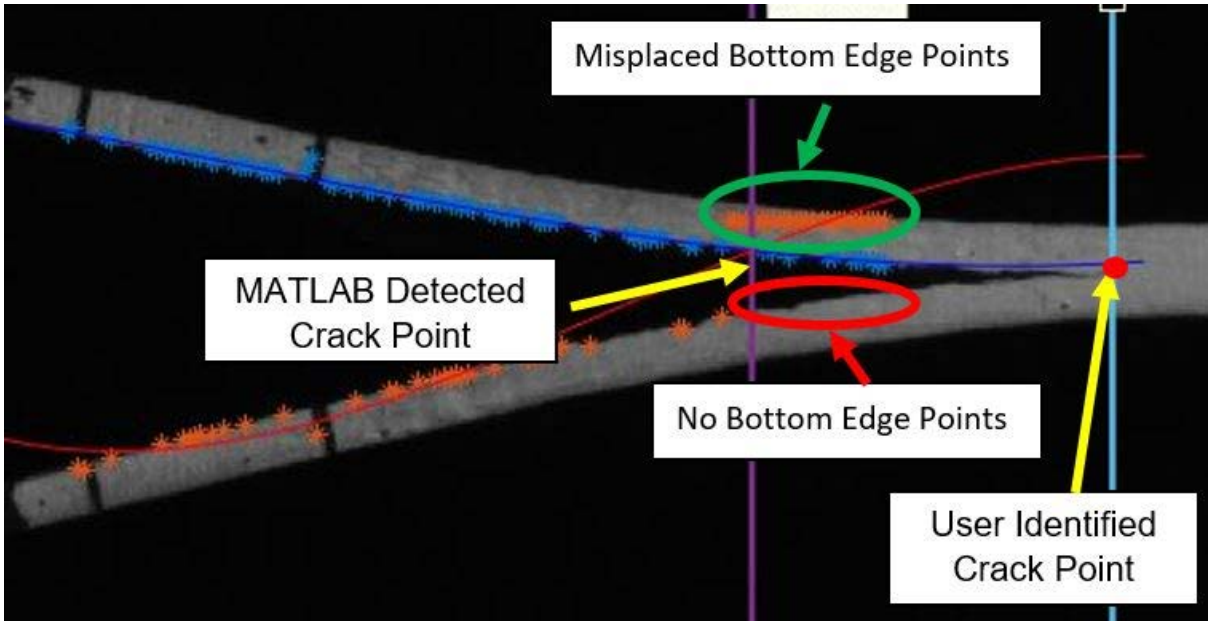

Figure 4-18: Misplaced edge points

Based on the start and end points, the y_m value may not necessarily coincide with the midplane of the specimen, thus effectively producing the same problem occurring for the sweeping method as shown in Figure 4-10.

Thus, a need arose to create a method that would accurately predict the top and bottom surface points as close as possible to the crack tip, regardless of how “asymmetrical” the specimens were opening as the crack propagate as stated in Figure 4-10.

The MATLAB script file for the Vertical Line detection algorithm can be seen in Appendix F.2.

4.3. Crossing Points method

The Crossing Points method aims to rectify the major deficiency of the previous two methods, namely the incorrect assignment of edge points to the top or bottom crack edge, when approaching the actual crack tip. Figure 4-19 shows a flow chart summarising the Crossing Point methodology

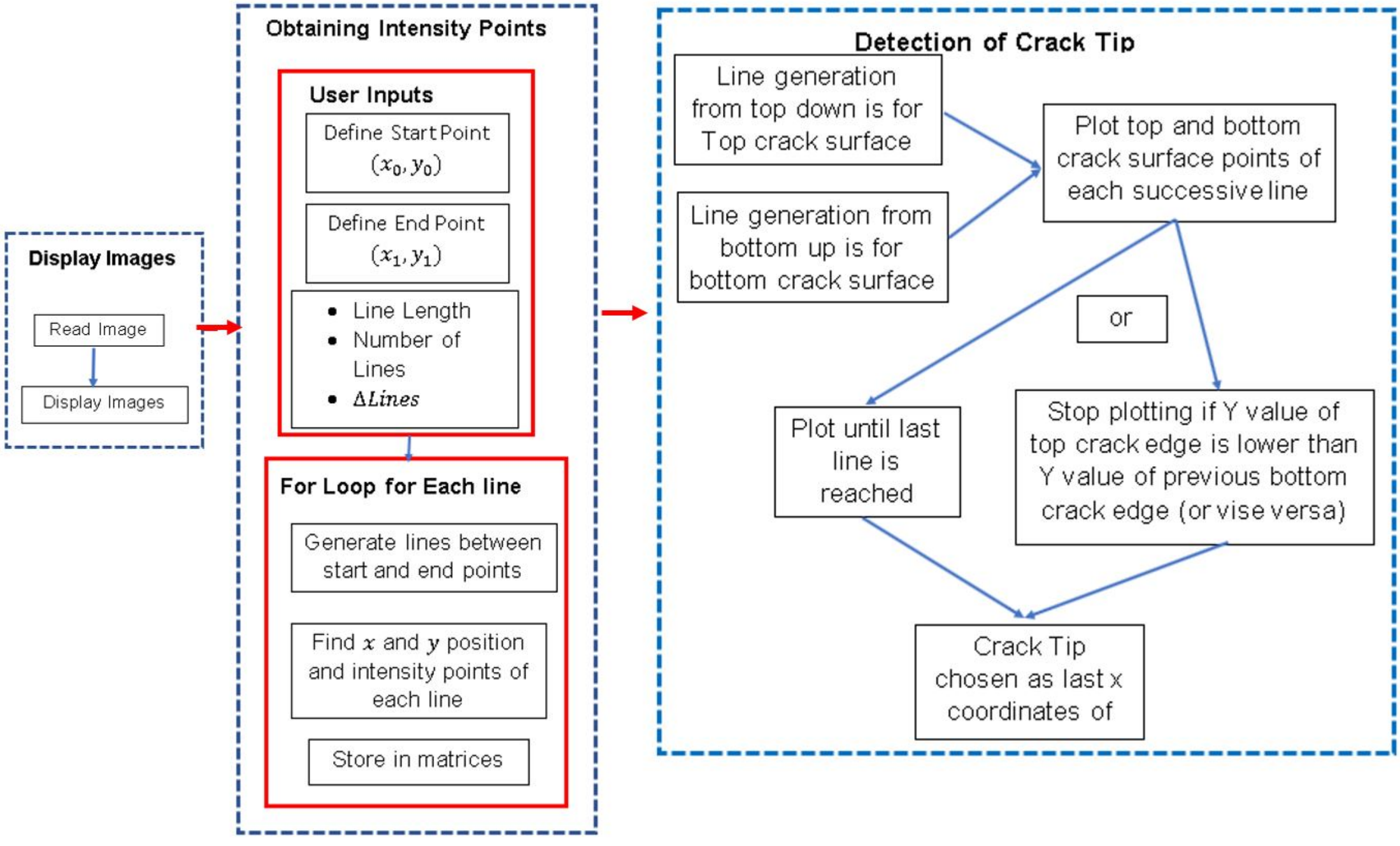

Figure 4-19: Flow chart of Crossing Point method

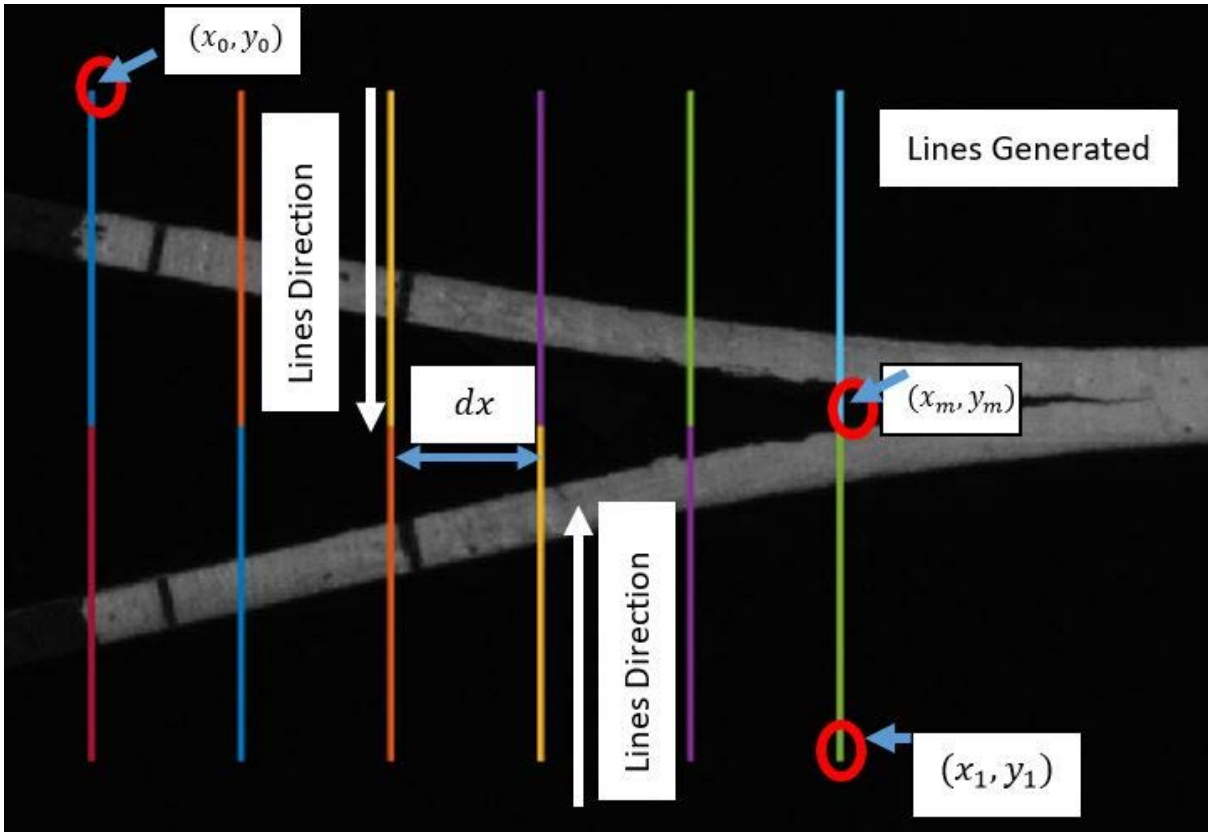

Figure 4-20: Lines generated using Crossing Point method

Figure 4-20 shows how the lines were generated using the Crossing Point method. It was very similar to that of the Vertical Line method in that there were two user input values $(\mathrm{x}_0, \mathrm{y}_0)$ and $(\mathrm{x}_1, \mathrm{y}_1)$ placed diagonally apart. The line range for the top surface edge points are $\mathrm{y}_0 \leq \text{Line range} \leq \frac{\mathrm{y}_0+\mathrm{y}_1}{2} + \text{ypixel}$ and $\frac{\mathrm{y}_0+\mathrm{y}_1}{2} + \text{ypixel} \leq \text{Line range} \leq \mathrm{y}_1$, where ypixel is an overlap length. Line direction stops just pass midway (due to the ypixel) between the two user input values. The overlap in upper and lower ranges is to cater for the midpoint not corresponding precisely to the horizontal plane of the crack tip.

To the left of the crack tip, this method will detect four edges, namely the top and bottom crack surface and the top and bottom specimen surface (as can be seen from Figure 4-21).

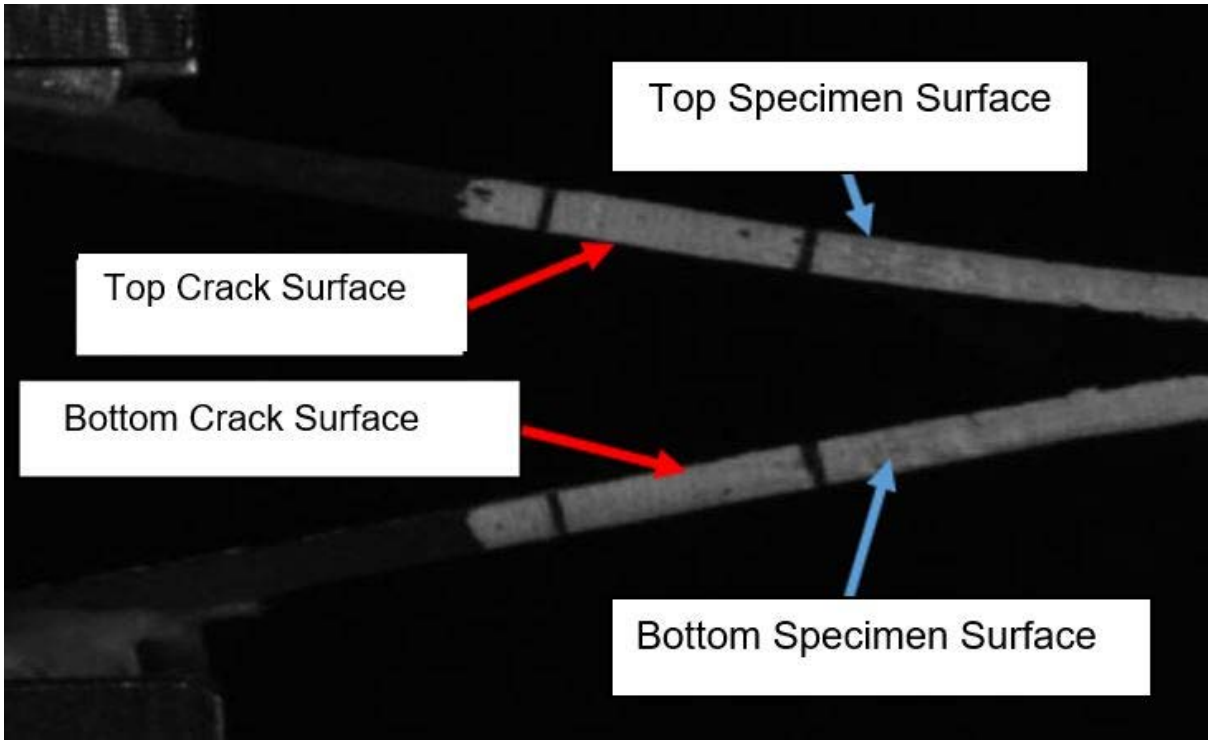

Figure 4-21: Specimen edges

It should be noted that (x_0, y_0) is above the top specimen surface. The line direction to obtain the top crack surface edges works from that point downwards. The (x_1, y_1) point is below the bottom surface point. The line direction to obtain the bottom crack surface edges works from that point upwards.

The intensity values along each element of a line was obtained. Based on the how the lines were generated, a sharp negative change (bright to dark) in intensity value is required to obtain the crack surface points. Figure 4-22 shows how the signs of the change in intensities of a top down and bottom up generated lines. The intended crack surface point is also shown for a sample line of both line types

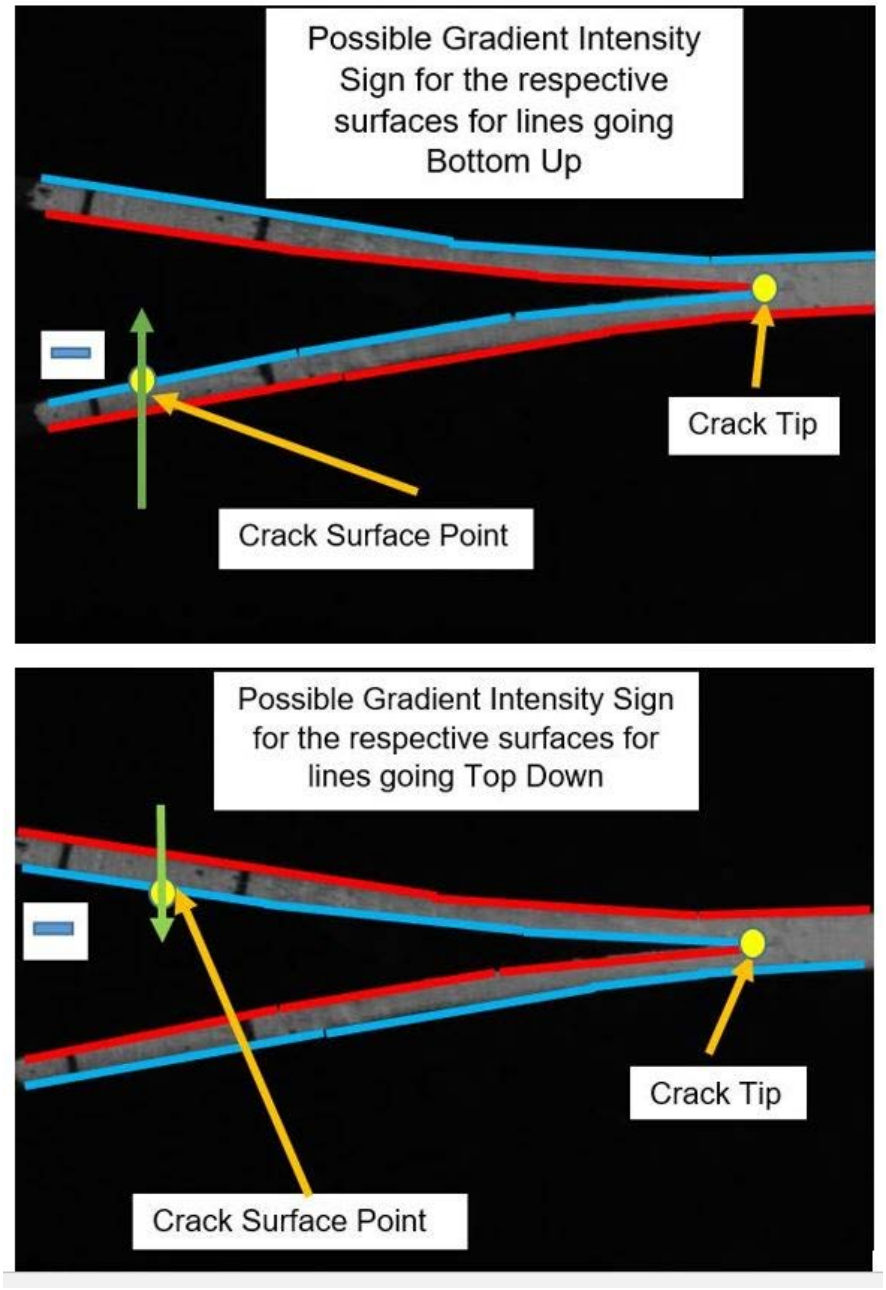

Figure 4-22: Edges detected for a positive intensity change (red) vs those for a negative intensity change (blue)

Based on Figure 4-22 it can be seen that when moving from bottom to top, the first negative intensity change corresponds to the bottom crack surface edge, prior to the crack tip. Conversely, when moving from top to bottom, the first negative intensity change corresponds to the top crack edge. The change in intensity values was found by using the MATLAB built-in “diff” function.

It should be noted that the line generations beyond the crack tip point, may detect the specimen surface points if the line exceeds the specimen and hence a negative change will be seen by the specimen surface edge as can be seen in Figure 4-23.

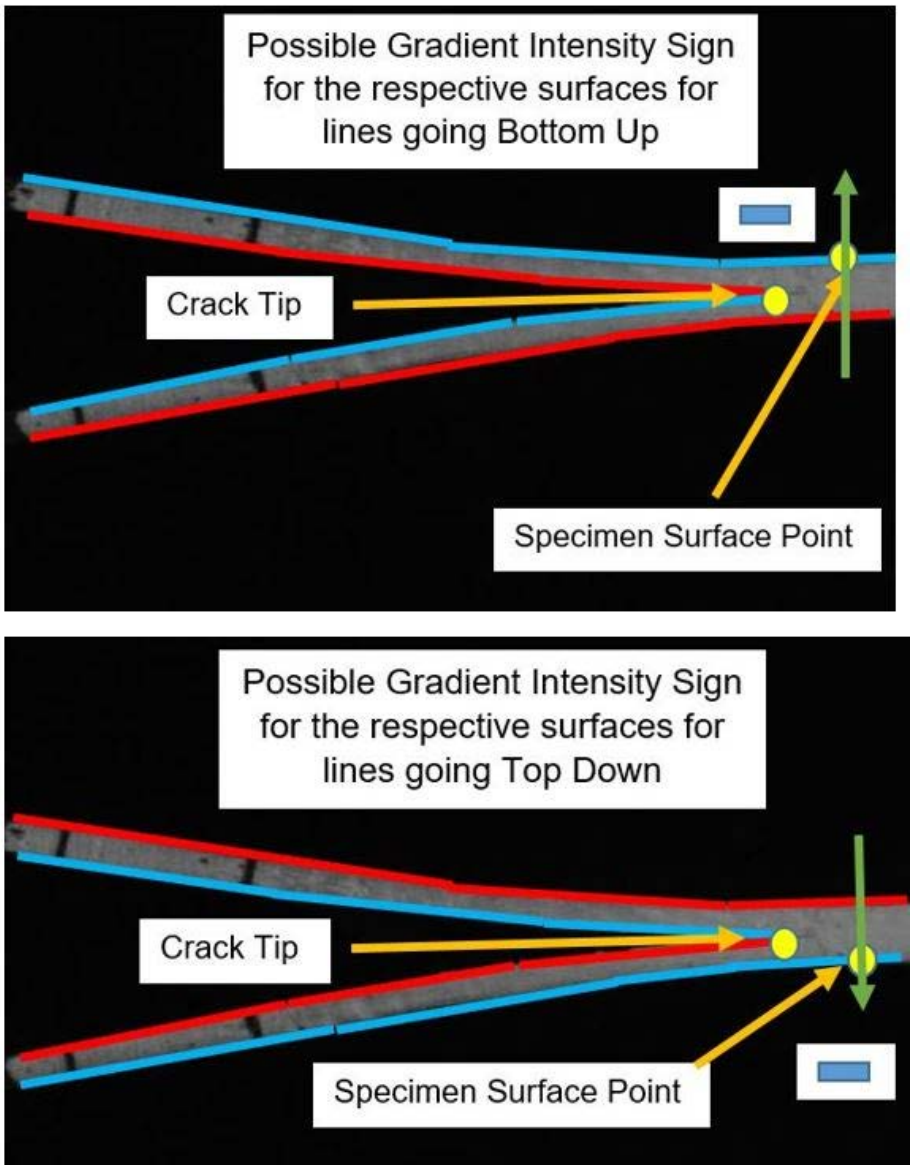

Figure 4-23: Sign of change in intensity for potential false crack (specimen) surfaces after the crack tip

If the line does not pass the specimen edge, then based on the criteria, no edge points will be found as it would not see a negative change. The detection algorithm for the lines is adapted to make sure that the line generation stops if the specimen edge is obtained for lines after the crack tip.

Figure 4-24 shows a plot of the difference in Intensity along the length of one line.

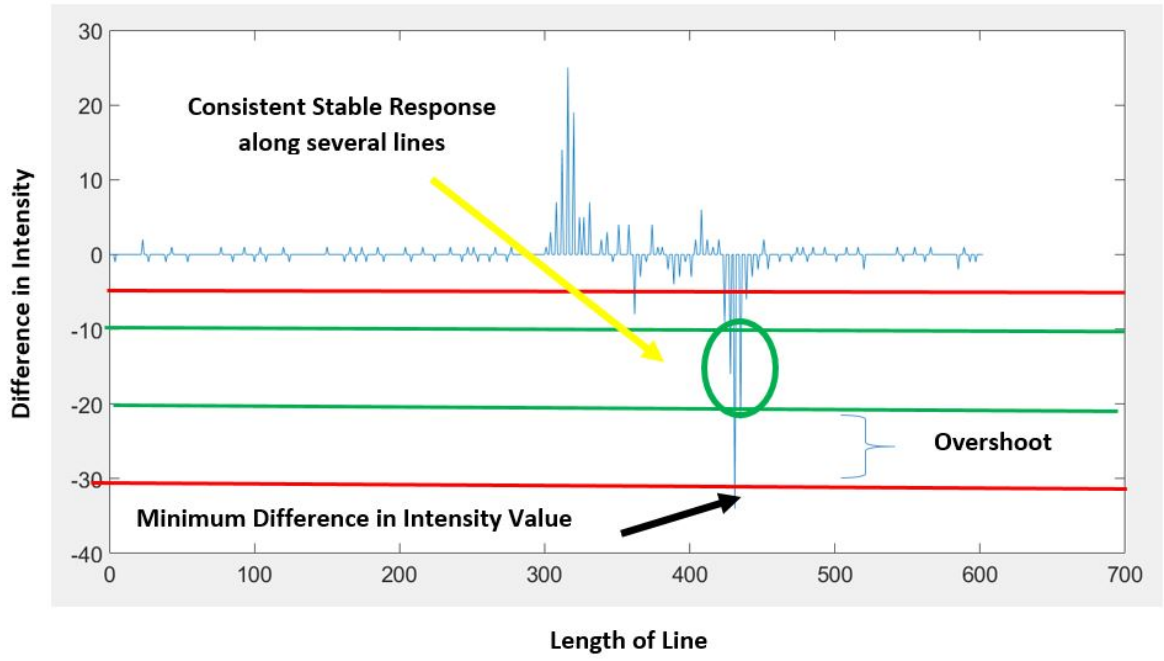

Figure 4-24: Graph showing difference in Intensity values

As shown Figure 4-24, the maximum negative change is approximately 30 $\frac{\Delta \mathrm{I}}{\Delta \mathrm{P}}$, whereby I is the intensity at a given point (x, y) and P is the pixels length.

Figure 4-25 shows the detection edge points for the change in intensity range of $0 < \Delta \mathrm{I} < 30$. There are misplaced top and bottom crack surface points and no actual crack surface points are detected.

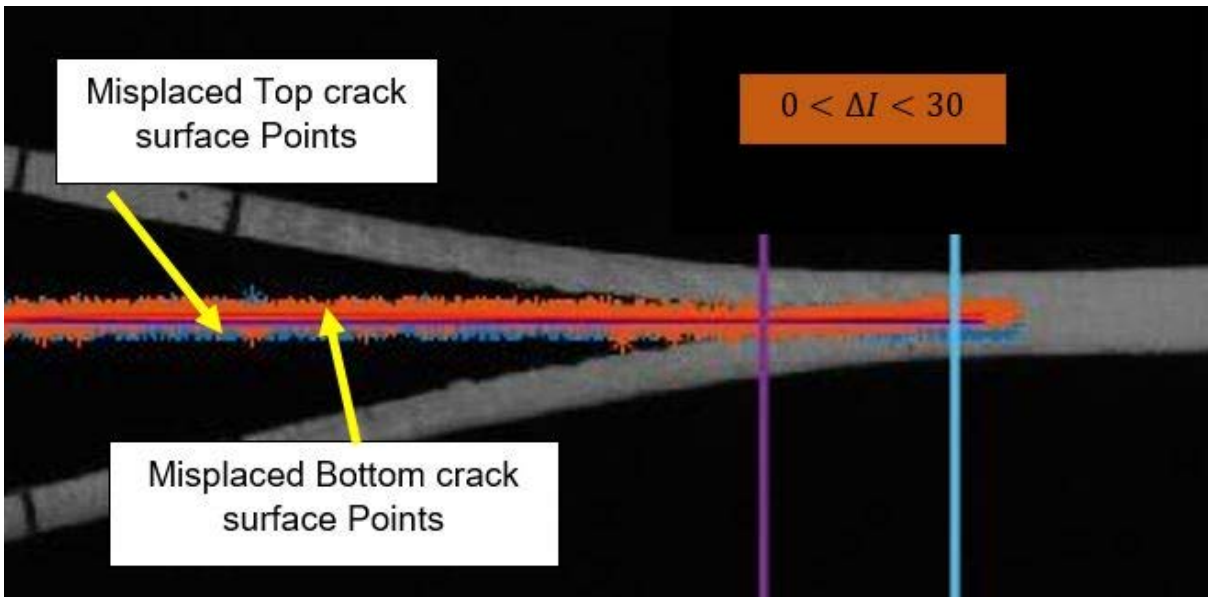

Figure 4-25: Detected edge points ($0 < \Delta I < 30$)

Figure 4-26 shows the detection edge points for change of intensity for the range of $5 < \Delta I < 30$. There are incorrect assignments of points to the top or bottom surface edges, but only after the actual crack tip has been passed. The edge points are always correctly assigned. The error in crack tip position is approximately 3%, which is a significant improvement on the previous methods.

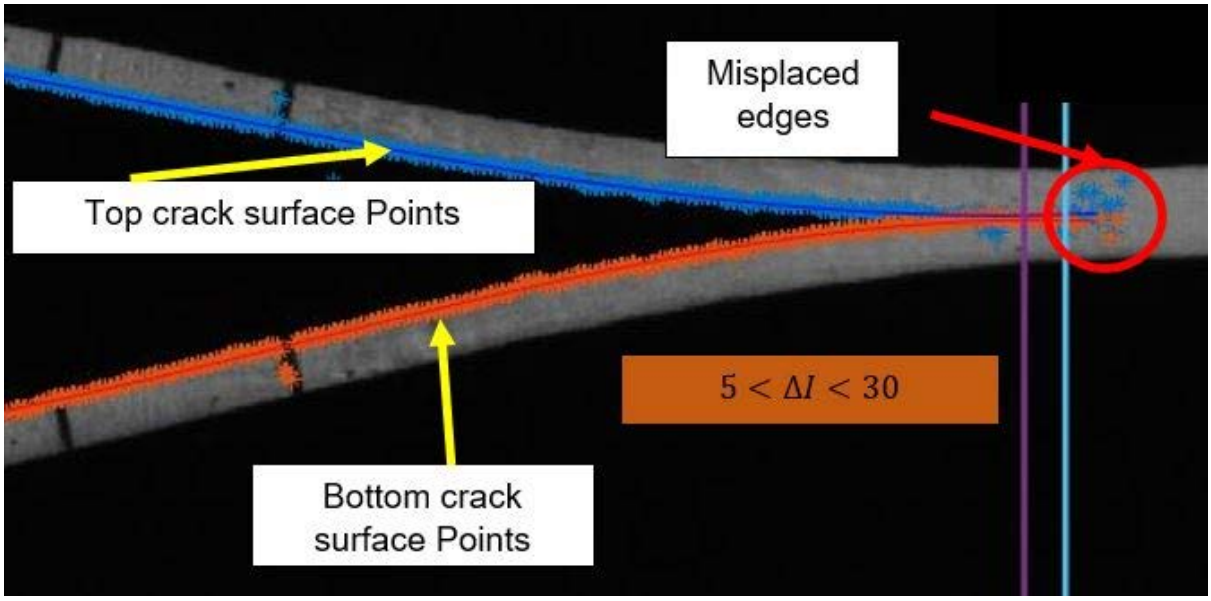

Figure 4-26: Detected edge points ($5 < \Delta I < 30$)

Figure 4-27 and Figure 4-28 shows the detection edge points for change in intensities from different minimum values of 10, 15 and 20 $\frac{\Delta I}{\Delta P}$.

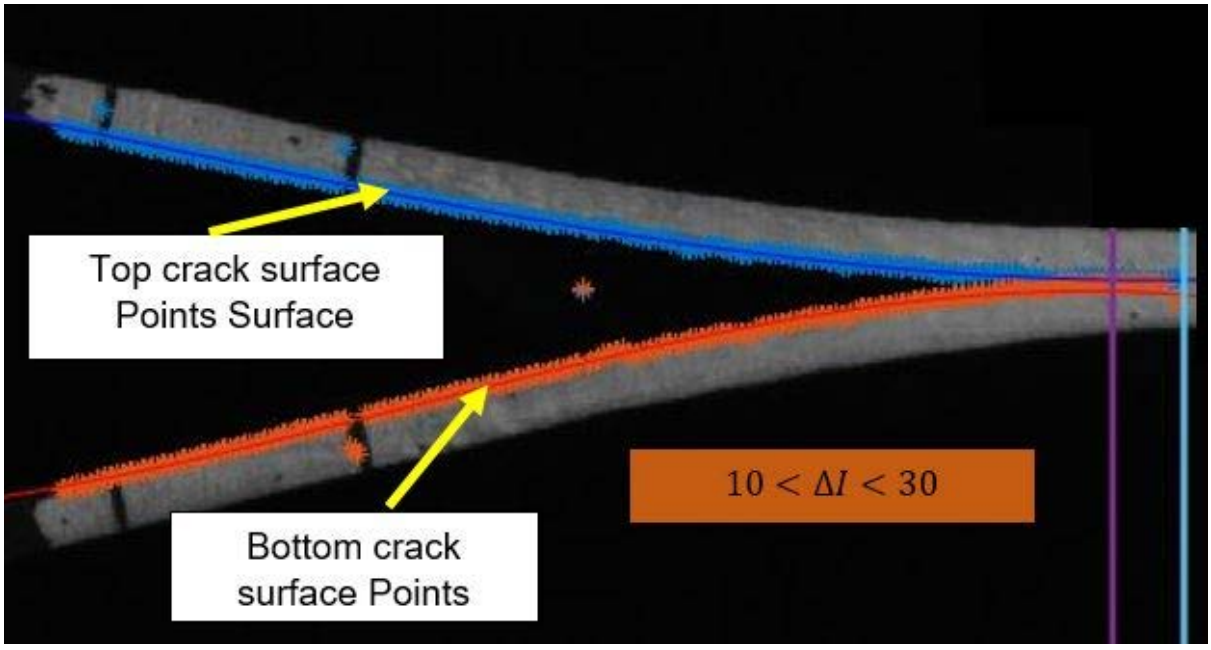

Figure 4-27: Detected edge points ($10 < \Delta I < 30$)

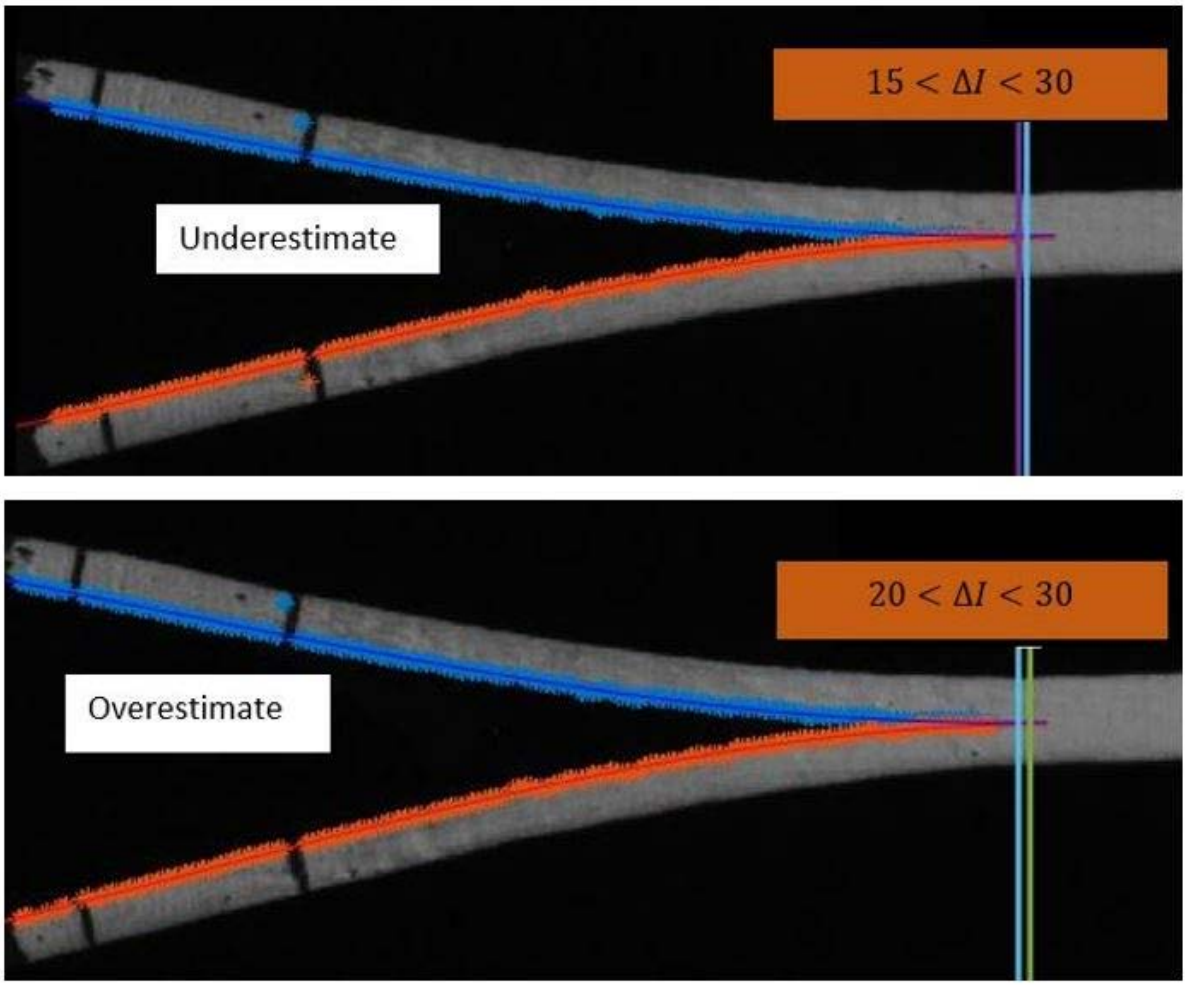

Figure 4-28: Detected edge points ($15 < \Delta I < 30$ & $15 < \Delta I < 30$)

For ΔI of 15, error in crack tip position is less than 1% and always underestimates the crack length. For ΔI of 20, the error in crack tip position is also less than 1% and overestimates the crack length. Hence a ΔI value of between 15 and 20 $\frac{\Delta I}{\Delta P}$ results in crack tip detection to within the desired tolerance.

It should be noted that no edge points were detected if the minimum change in intensity is more than 23 $\frac{\Delta I}{\Delta P}$. Based on these, the edge criteria was chosen as $15 < \frac{\Delta I}{\Delta P} < 20$. This would give an error in the algorithm of less than 1%.

5. Validation of crack detection algorithm

In the previous chapter, the "actual crack tip" was determined by the author's visual judgement. In order to properly validate the Crossing Point method, it must be compared to a more objective crack detection method. An Ultrasonic Thickness Tester is a reliable NDT device that shows a sudden change in thickness in the vicinity of a crack tip.

It would be extremely cumbersome to use the Ultrasonic Thickness Tester with a DCB specimen mounted in the Zwick testing machine (refer to section 6 for more information on the DCB set up), due to the space constraints. In order to replicate the opening of a DCB specimen to a desired static position, while allowing easy access for Ultrasonic thickness measurements, a Wedge device was designed and built to replicate the a DCB test outside from the Zwick.

The Ultrasound Thickness Tester along with a designed Wedge device was used to further check the reliability of the results obtained from detection algorithm.

5.1. Ultrasound Wedge device

The Wedge device simply drives a Wedge between the top and lower DCB arms to open the crack to a desired position. The specimen was clamped in the device prior to the usage of the Thickness Tester.

The device is made up of three parts, namely the Wedge Base, Specimen Holder and the Wedge. Figure 5-1 shows the assembled Wedge device along with the Ultrasonic (US) Probe and its holder. It should be noted that the Wedge Base is not featured in Figure 5-1.

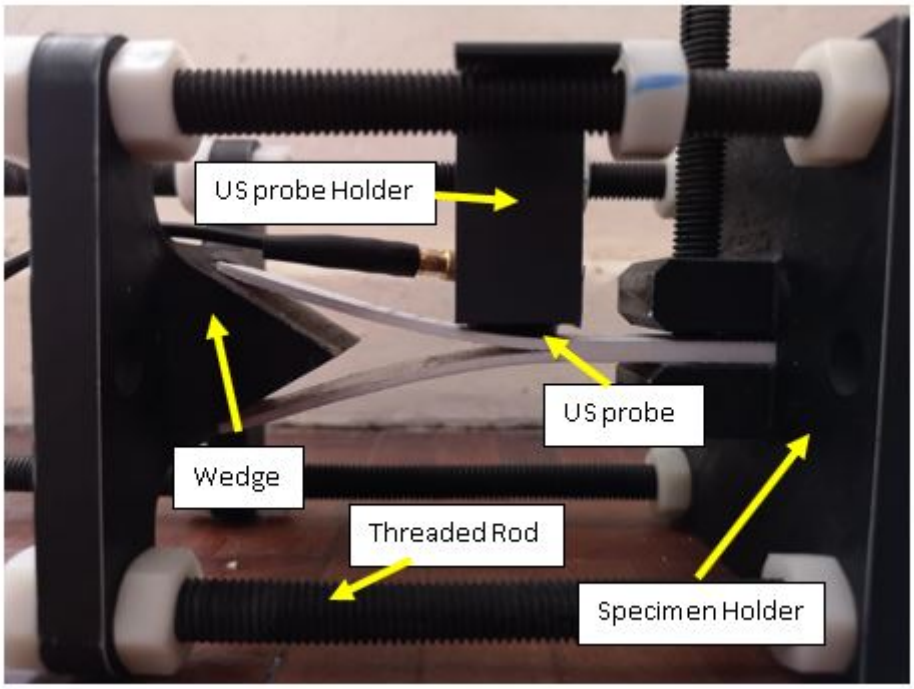

Figure 5-1: Ultrasound Wedge device

The Wedge Base and Specimen Holder are clamped to threaded rods with nuts on both ends of the parts. The specimen is clamped down using the same embedded nut technique used for the DCB jigs (Refer to section 3.2 and Appendix C). A threaded rod is threaded through an embedded nut and attached to the Wedge. As the thread rod is turned, the Wedge will drive forward which will allow the crack of the specimen to propagate and replicate a DCB test. Refer to Appendix G for full instructions on how to assemble the Wedge device.

5.2. Ultrasound Thickness Tester

An Ultrasound Thickness Tester measures the thickness of a part at the probe position, by measuring the transit time for an ultrasonic wave to travel from the probe, reflect off the far surface and return to the probe. If the ultrasonic probe is moved along a line on the specimen's upper surface (probe points), it will detect a change from the nominal thickness in the uncracked region, to approximately half this thickness when past the crack tip ,as can be seen Figure 5-2 .

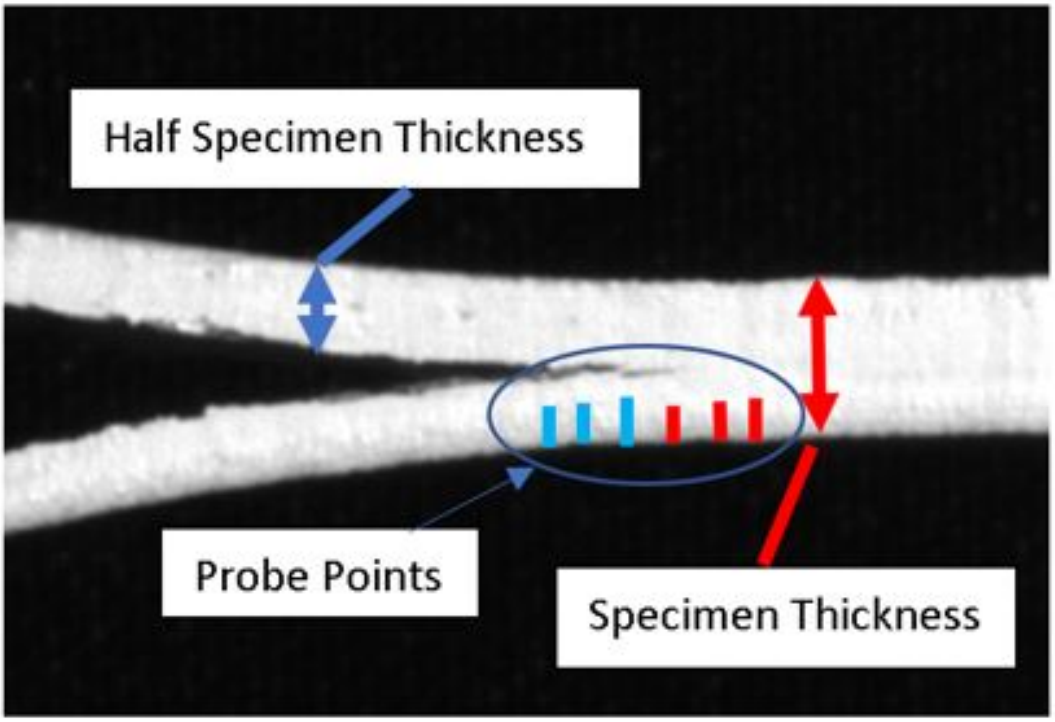

Figure 5-2: Explanation of the Thickness Tester in DCB specimen

Hence the crack tip position may be determined by an independent method, to verify the accuracy of the image-based detection algorithm.

The Model of the Thickness Tester used was the GE Inspection Technology CL - 5, with the 20mm probe Model number of CA211A. A coupling agent was also used to aid transmission of the ultrasonic wave between probe and specimen, by filling any air gaps.

Before clamping the specimen into the Wedge device, the specimen is first marked off with probe marks 5mm apart, starting from 30mm from one edge as can be seen in Figure 5-3.

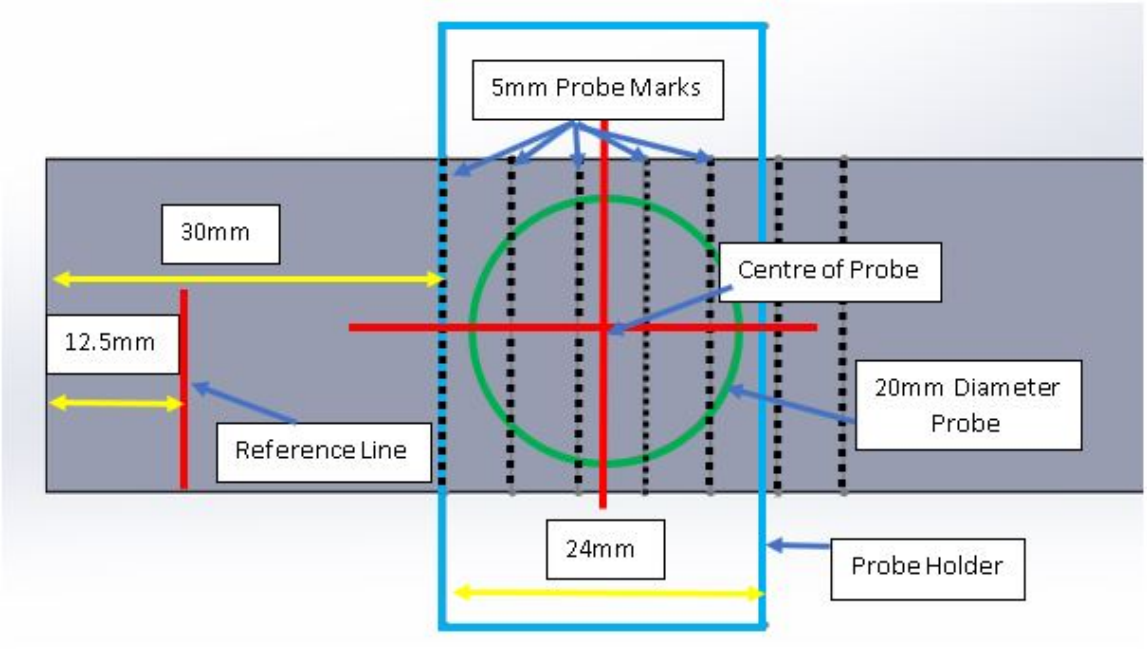

Figure 5-3: Top view of specimen showing probe points

The probe will then be placed within a probe holder of 24mm in width. Thus, if the left of the probe holder is on the 30mm marker, then the centre of the probe will read $30 + \frac{24}{2} = 42\text{mm}$. The crack length is taken to be the position from the reference line to the centre of the probe. The reference line was taken as 12.5mm. This would coincide with the midway of the Hinge Blocks of a DCB specimen.

After the specimen is marked, it is clamped into the Wedge device, with the Wedge driven to the desired position. The Thickness Tester probe is then placed into the probe holder. The probe holder is located by M10 nylon hex nuts. The M10 thread has a pitch of 1.5mm. The nuts were divided in 4 (or at 90° apart) with permanent markers. Thus, for each quarter turn on the nuts, the probe holder would be moved 0.375mm. Based on this method, we can obtain thickness from the Ultrasound Thickness Tester at every 0.375mm. This is referred to as the crack length range. Figure 5-4 shows an assembled Wedge device with the probe and probe holder.

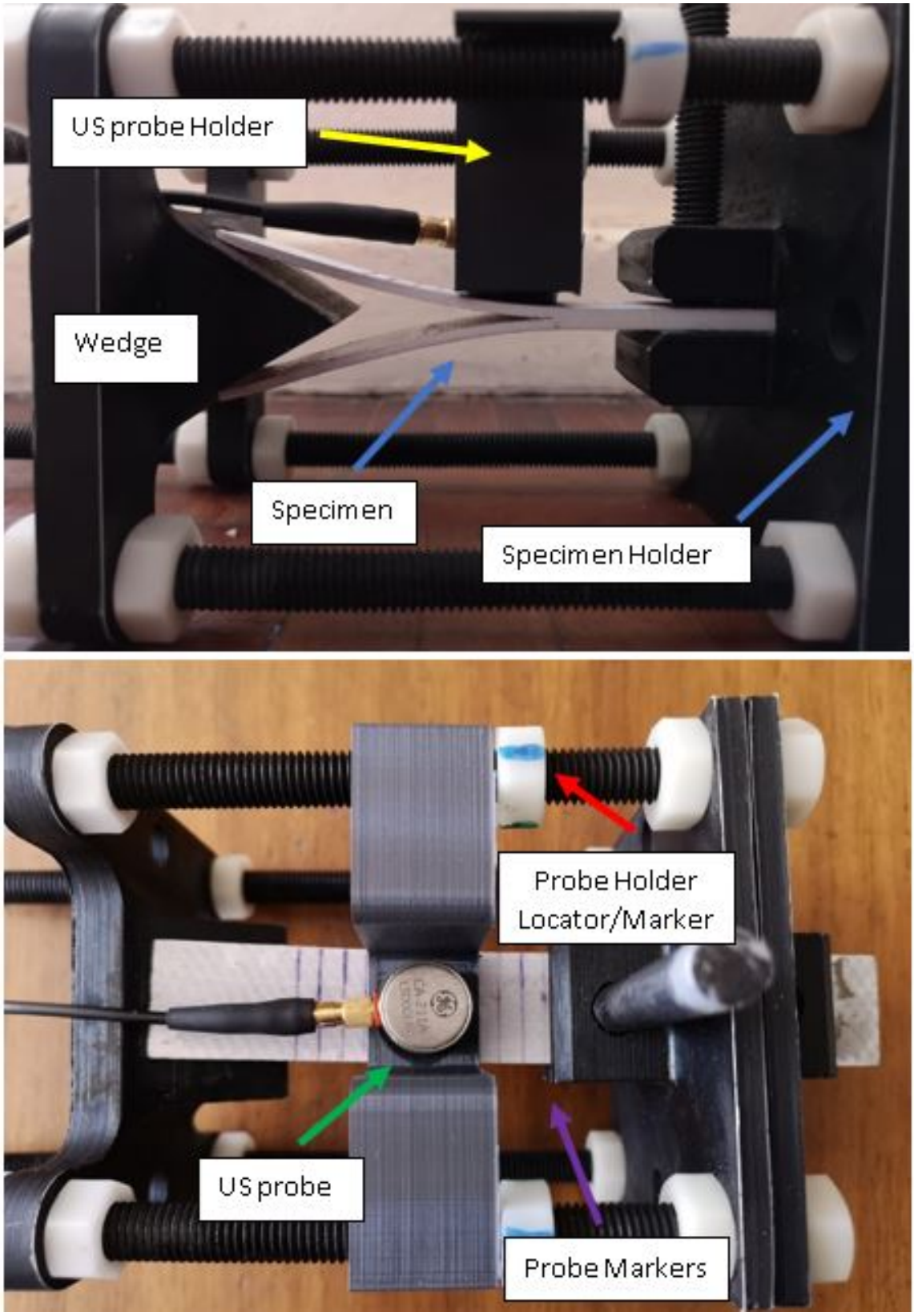

Figure 5-4: Assembling of Wedge device with US probe

5.3. Image-based crack measurements with Wedge device

5.3.1. Calibration of images.

With the images of Wedge device taken, the image is then loaded into the MATLAB detection algorithm as described in section 4.3. In order to compare the crack tip positions obtained from the ultrasonic and image-based methods, it is necessary to convert the image pixel coordinates to real world coordinates in mm. A known millimetre length within the image was taken. The same measurement was obtained in pixel space using the MATLAB “imtool” and or the data cursor points. This provided the factor to convert image distances in pixels to real world distances in mm, in the appropriate plane of the DCB specimen lateral face.

5.3.2. Crack length detection

The chosen Crossing Point detection algorithm was adjusted to allow for the pixel conversion and the origin to be defined. Figure 5-5 shows the flow chart of the Wedge detection

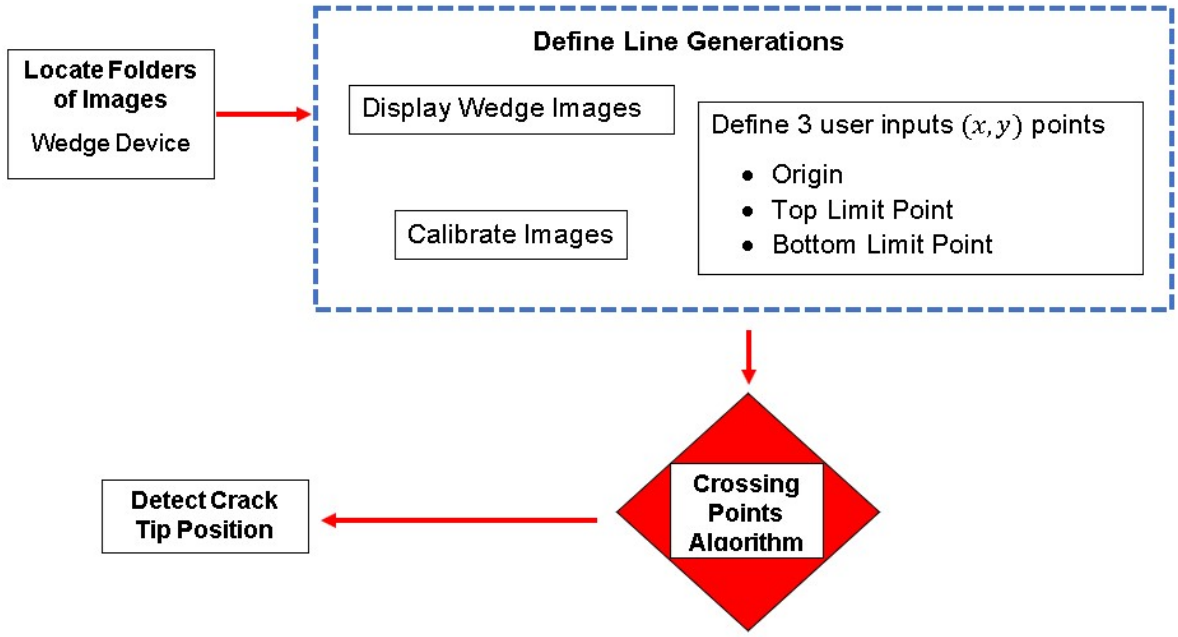

Figure 5-5: Flow chart showing method of Wedge detection

Figure 5-6 shows whereabout the origin, the top and bottom limit points are defined. The top limit point must be chosen above the top hinge block whereas the bottom limit point must be chosen below the bottom hinge block. The line generations for the detection algorithm will run between the x distance from the top to the bottom limit lines.

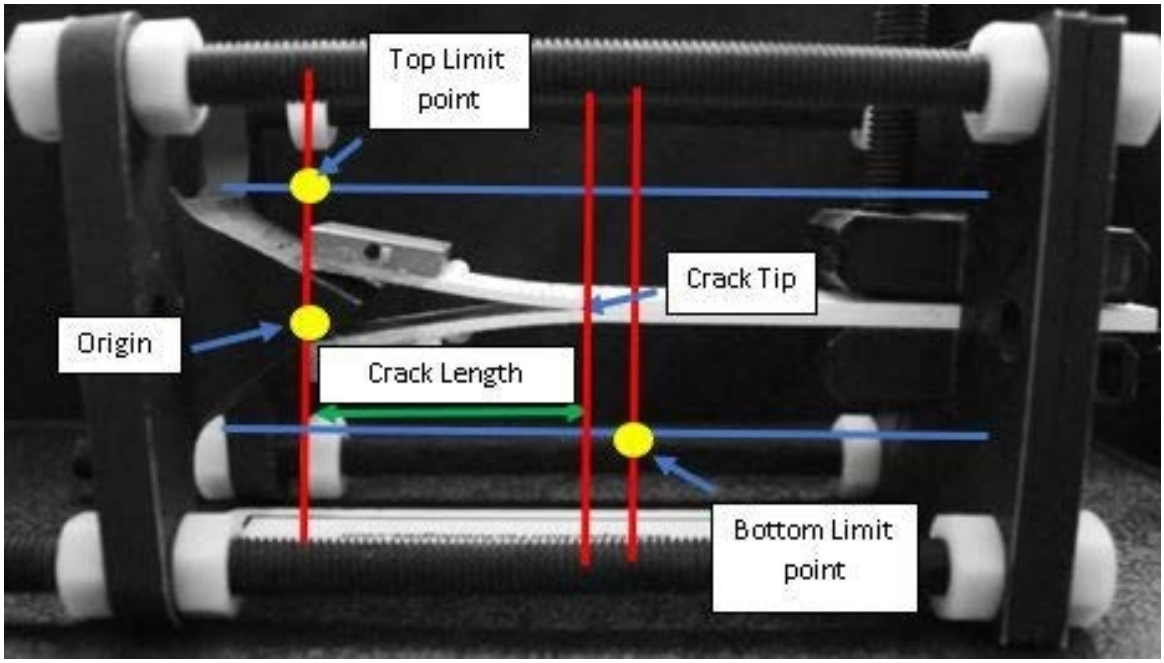

Figure 5-6: Wedge detection defined points

The crack length is taken as the horizontal length from the origin to the detected crack tip.

5.4. NDT Wedge and Thickness Tester results

The ultrasonic crack tip detection was repeated for four different Wedge experiments. Thus, four US probe crack length range was obtained by plotting the graphs of thickness vs crack length to see where the US Thickness Tester reading has doubled in length.

It should be noted that for each experiment, three different crack lengths were determined, namely:

- as determined using the Ultrasonic Thickness Tester, termed the US probe crack length
- as identified by the author by selecting the crack tip visually in the image loaded in MATLAB, termed User identified crack tip
- as identified using the Crossing Point method in MATLAB, termed MATLAB detected crack tip.

The US probe crack length will naturally occur somewhere within the vicinity of the crack length region of $\text{US probe lower limit} < \text{US probe crack length} < \text{US probe upper limit}$. Since its not known exactly where the crack length lies, the author is taking the crack length to be midway between the two specimen marking limits. The crack length range between the limits is 0.375mm, which corresponds to a quarter rotation of the nut for the US probe holder. With the US crack length determined, the User identified crack length and MATLAB detected crack

length was determined using the Crossing Point algorithm. An acceptable tolerance range for the Thickness Tester was taken to be one quarter rotation of the nut from either side of the US probe crack length. An uncertainty in the crack length of 0.5mm is deemed acceptable according to ASTM D5528.

Figure 5-7 shows a sample figure of thickness vs crack length of experiment 1 along with position of the three crack lengths.

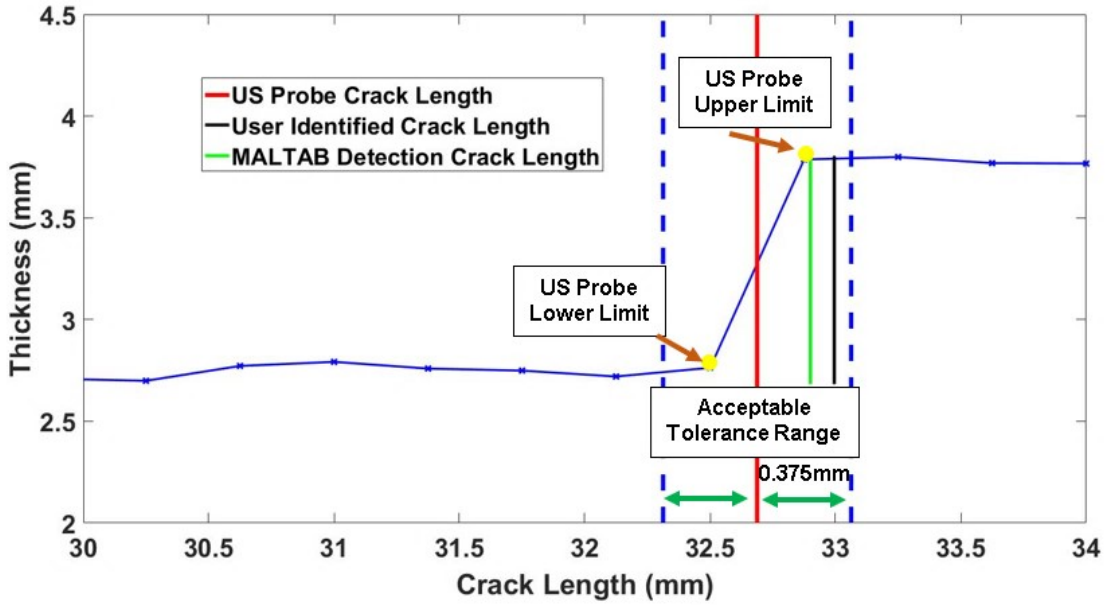

Figure 5-7: Thickness vs crack length of experiment 1

From Figure 5-7, the upper (32.50mm) and lower limit (32.375mm) of the US probe crack length can be seen from the blue and red vertical line. Both the MATLAB detection crack length value of 32.9mm and user identified crack length value of 33.995mm can be seen to lie outside of the US probe crack length limits. It does however fall within the acceptable tolerance range of one quarter nut rotation of 0.375mm. Using the US probe crack length as the reference, the error for the user identified crack length is 0.212mm or 0.65% and the error for the MATLAB detection error is 0.308mm or 0.94%. Using the User Identified crack length as the reference, the with respect to the Crossing Point algorithm is less than 0.1%, which corresponds to what has been stated in section 4.3.

The graphs of thickness vs crack length for experiment 2 through 4 can be seen in Appendix I.1., as well as Tables of thickness vs crack lengths of all four experiments in Appendix I.2.

All the three raw data (US probe, MATLAB detection and the user identified crack lengths) along with the errors with respect to the US probe crack length and the Crossing Point algorithm in both mm and % is summarised in Table 5-1.

Table 5-1: Table showing raw data of the Ultrasonic Wedge device

Experiment Number	US Probe (mm)			MATLAB Detection Crack Length (mm)	User Identified Crack Length (mm)	Error referenced to US Probe Crack length				Error of Crossing Point Algorithm with referenced to the User identified crack tip	
						Error for MATLAB detection		Error for User			
	Lower Limit	Upper Limit	Crack Length			(mm)	(%)	(mm)	(%)	(mm)	(%)
1	32.500	32.875	32.688	32.900	32.995	0.212	0.65	0.308	0.94	0.096	0.29
2	44.375	44.750	44.563	44.746	44.845	0.184	0.41	0.282	0.63	0.099	0.22
3	51.000	51.375	51.188	50.564	50.854	0.624	1.22	0.334	0.65	0.290	0.57
4	55.625	56.000	55.813	55.571	55.747	0.242	0.43	0.066	0.12	0.176	0.32

The red highlighted data are the values that do not fall within acceptable tolerance range.

The variation between the Crossing Point crack detection method and the US crack detection is less than 0.5mm (apart from error of the third experiment for the MATLAB detection), which is the requirement of ASTM D5528.

As the Crossing Point method only requires user inputs for one image in the test series, it requires far less user effort than the user identifying the crack tip in each image. Hence the Crossing Point method may be applied to reduce the cost of crack tip tracking for large experimental studies, without sacrificing accuracy. Thus, the Crossing Point algorithm was used for the DCB tests knowing that it can be deemed acceptable.

6. Double Cantilever Beam fracture toughness test

The DCB test is used to measure the Mode I fracture toughness, G_I and was conducted using the Zwick 1484 Universal Test Frame (referred to as 'the Zwick' from here). The Zwick makes use of a 10kN load cell which applies a tensile load to the specimens, which actively measures the force and cross head displacement. We assume that the fixtures and load cell are sufficiently rigid that the DCB opening displacement is the same as the cross-head displacement. These values (force and opening displacement) will be used in conjunction with the crack displacement values obtained from the image analysis to infer the G_I values.

It should be noted that each specimen's widths and thicknesses were measured. These values are summarised and can be seen in Appendix A.2

6.1. DCB Set-Up

Each DCB test utilises the following equipment:

- Zwick machine – to load specimen and measure force and opening displacement
- Camera – captures images of specimen for crack measurement.
  The following are the properties of the camera used
  - Model – Cannon EOS100D
  - Image Resolution – 1920x1080 pixels
  - Lens Data – $\phi 58\text{mm}$ Cannon Zoom Lens EF-S 18-55MM 1:3.5-5.6 IS
- PC linked to Zwick machine – configure Zwick and store force + displacement data
- Ring Lighting source – To illuminate room for ease of post processing results
- Black cloth – Black background to give sharp contrast with white specimen.

Figure 6-1 shows the camera set up of a DCB test.

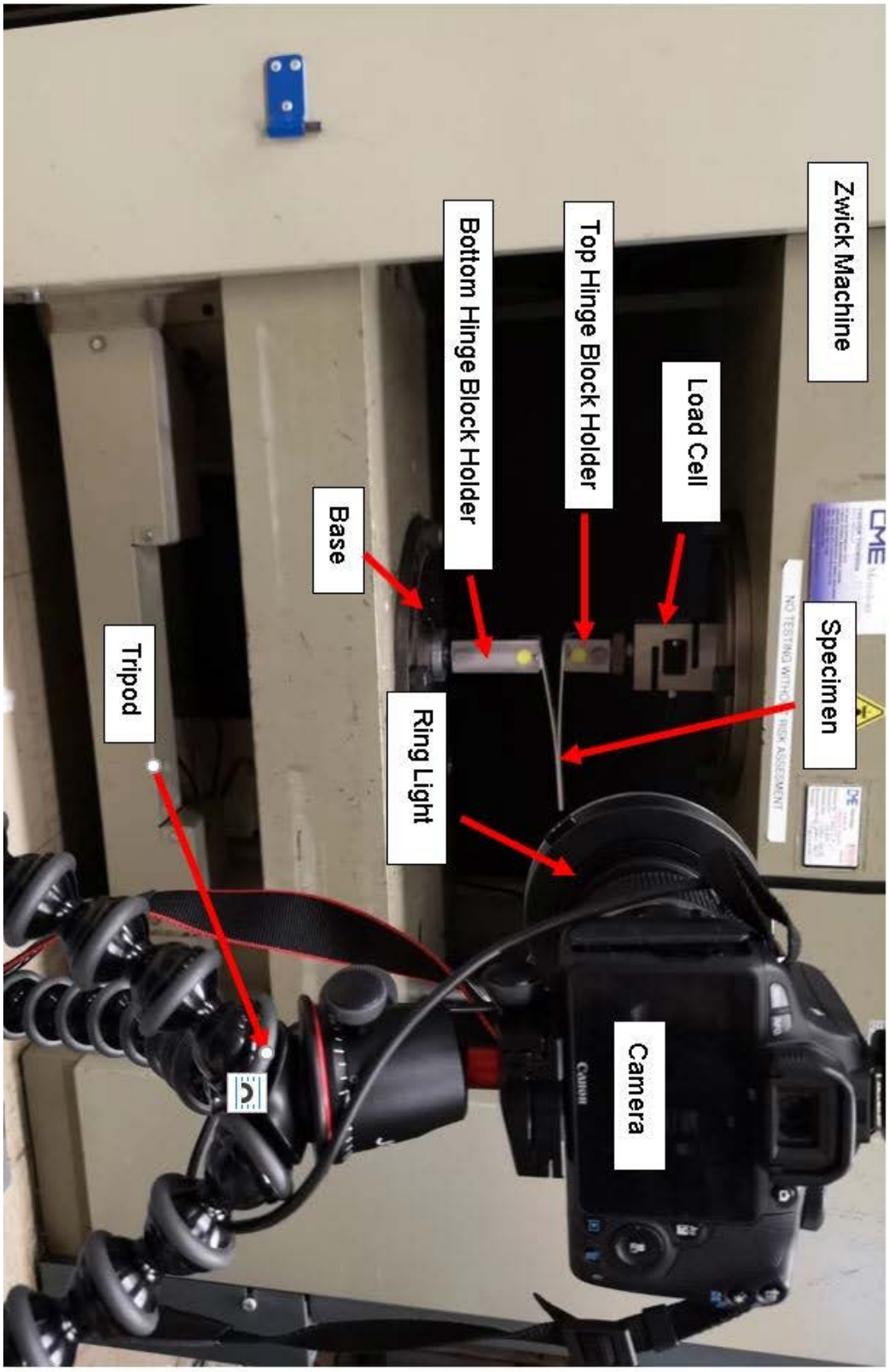

Figure 6-1: DCB camera set up

Before each DCB test, the DCB fixtures are pinned to the load cell and base respectively. The hinge blocks of the DCB specimen are then pinned through the DCB fixtures. The camera is then set up and placed on a tripod about 60 to 70 cm away from the front end of the Zwick machine where the specimen is placed. A lighting source (ring light) is attached to the camera lens. A black cloth is attached to the back of the Zwick machine to give a uniform black background. This will help aid to remove unnecessary visual background and effects. The Zwick machine needs to be configured to store all the raw data into a predestined folder for post processing.

Once the camera and Zwick machine are configured, the camera needs to be focused correctly onto the appropriate area.

Before the specimen is fixed to the Zwick machine, a 50mm mark is placed on the top of the specimen. The Zwick machine is then loaded until the crack propagates to the 50mm mark. This is a form of pre-cracking. According to ASTM D5528, specimen is loaded until the crack length is observed to be 3 to 5mm beyond the start crack position. Once satisfied, the cross head of the Zwick machine is lowered until the force is nominally zero, which is the starting position of the DCB test.

The camera starts recording the specimen before the Zwick machine starts the DCB test. The results of the test are stored and exported as an xls file for post processing. It should be noted according to the ASTM D5528, the cross-head speeds need to be 0.5mm/minute for loading the specimen until the crack reaches 50mm. After the speeds can be increased to 5mm/ minute. Based on the limitation of the camera, the video size for one recording has a maximum size of 4GB. Thus, the speed of the test needed to be increased to 10mm/minute avoid the video from splitting to two videos as the video size has been reduced due to the increased speed.

The DCB test was chosen to stop when the opening displacement reaches 50mm, effectively making each test 5 minutes long. The camera recording is stopped, and the video files are stored for further processing. According to the ASTM D5528, the test is to be stopped manually once the crack length has propagated to beyond 50mm. Due to nature of the author dealing with post processing, the tests was not stopped based on the length the crack has propagated.

6.2. Image Analysis of DCB Test

Since the camera recorded a video of each test, the video file needed to be converted into frames so that they could be processed using the Crossing Point detection algorithm.

6.2.1. Extraction of images

A command prompt programme called FFMPEG was used to convert each video file into grayscale images. A sample command used for one video file was **ffmpeg - i ./file_name.mov -vf fps=15 -pix_fmt gray - compression_algo raw. /Output Folder/IMG_%5d.tiff.** This command converts the input video to TIFF images in grayscale with no compression, at a rate of 15 frames per second.

The Zwick machine force and displacement was set at 15 data points per second. Thus, for consistency, the video file was extracted at 15 frames per second to keep the sample rate constant.

6.2.2. Calibration of images

The pixel to mm conversion factor is determined by measuring a known length within an image. This known length was taken to either be the width and height of the DCB fixtures, which are 30mm and 40mm respectively, as can be seen in Figure 6-2. The plane in which these edges were measured is offset 2mm from the plane of the specimen face. However, as the camera was located approximately 1m from the specimen, the effect of this offset on the distance conversion is negligible. The DCB fixtures are machined, and the edges may be considered perpendicular. However, due to camera positioning, the edges of the fixtures are rotated by 6º relative to the camera axes. This rotation is corrected by simply multiplying the camera coordinates by the planar rotation matrix:

$$\begin{bmatrix} x \\ y \end{bmatrix} = \begin{pmatrix} \cos\theta & -\sin\theta \\ \sin\theta & \cos\theta \end{pmatrix} \begin{bmatrix} p \\ q \end{bmatrix} \tag{6.1}$$

$$= \begin{pmatrix} \cos 6° & -\sin 6° \\ \sin 6° & \cos 6° \end{pmatrix} \begin{bmatrix} p \\ q \end{bmatrix}$$

$$= \begin{pmatrix} 0.995 & -0.105 \\ 0.105 & 0.995 \end{pmatrix} \begin{bmatrix} p \\ q \end{bmatrix}$$

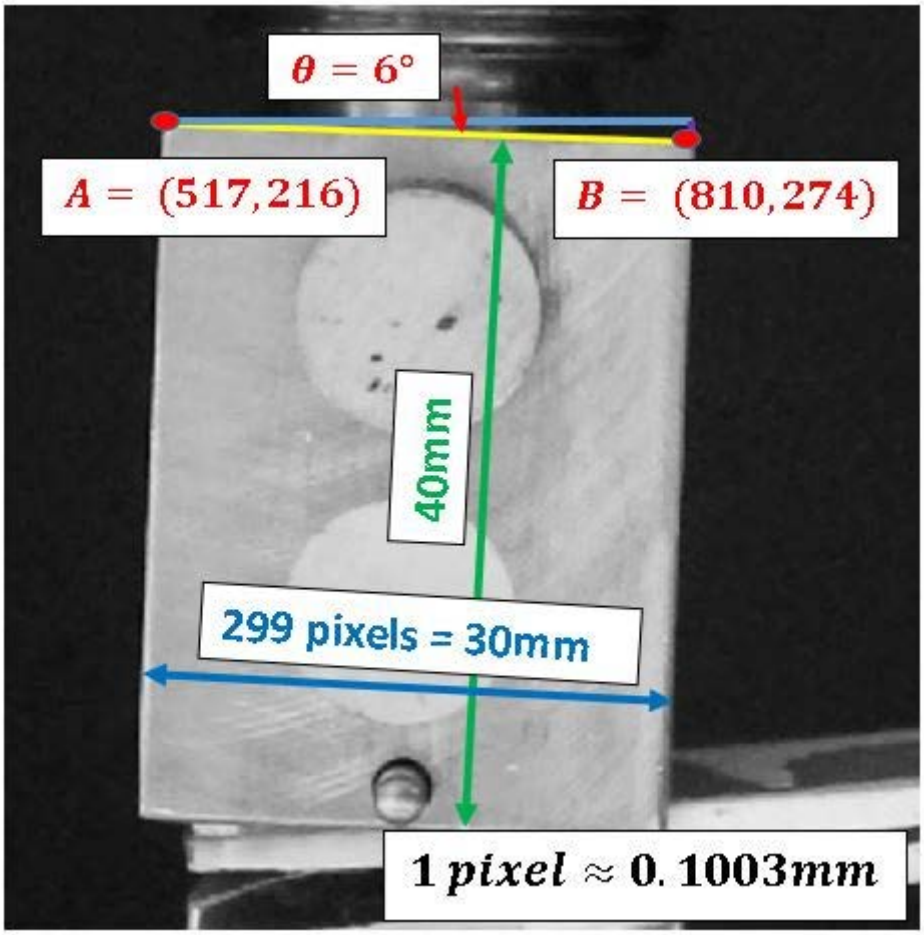

Figure 6-2: Calibration of DCB tests

An example was used with image coordinates of $A(p_1, q_1) = (517,216)$ and $B(p_2, q_2) = (810,274)$ as can be seen in Figure 6-2. This corresponds to 299 pixels.

After taking the rotation of 6° , the new coordinates are $A'(x_1, y_1) = (492,269)$ and $B'(x_2, y_2) = (777,358)$. This corresponds to 298.57 pixels. The error between the rotated and unrotated image is 0.43 pixels. Using the conversion factor this is effectively 0.043mm or 0.1%. According to ASTM 5528, an error of 0.5mm uncertainty of the crack length is deemed acceptable. Assuming that the error would be approximately the same for each DCB tests then as the crack propagates horizontally in a DCB specimen, the rotation correction may be considered minimum or and would be neglected.

6.2.3. Synchronising data sets

The position of the crack tip between each frame is needed along with the force and displacement values to calculate the G_I as per ASTM D5528 standards. The Crossing Point algorithm was used to determine the crack tip position in each frame.

Figure 6-3 shows how the Crossing Point algorithm was altered to accommodate to calculate the Mode I G_I value.

It should be noted that the DCB test started a couple of seconds after the video started recording.

Since there was a time delay between starting the camera and the DCB specimen beginning to load, it was necessary to synchronise the time frames for the images and force-displacement measurements. Thus, the image frame for the start of the test is required. The MATLB script file of the Crossing Point's algorithm was altered to automatically detect the start time of the test.

To achieve this, a circular sticker was applied to the moving specimen fixture, to track its displacement (refer to Figure 6-5). Built in MATLAB functions of "imfindcircles" and "visucircles" were used to show and locate the (x, y) pixel coordinates of the centre of the circle. This was done for approximately the first 550 to 700 frames, corresponding to approximately 35 to 45 seconds of the test. The crosshead displacement should have reached a constant speed by this time. The loading rate in the first few seconds of the test is not necessarily constant, as any clearance in test fixtures is taken up. The position data for the first 100 frames is fitted with a best fit horizontal line ($y = Xcrack1$). The position data for frames 500-700 is then fit with a best fit straight line ($\text{Constant loading rate line}$). The Zwick initially preloads the specimen at a slower rate (5mm /minute) till a force of 10 N is reached, then applies a constant cross head speed of 10 mm/ minute. Thus, the latter linear region is the best indication of the test having reached its steady state speed.

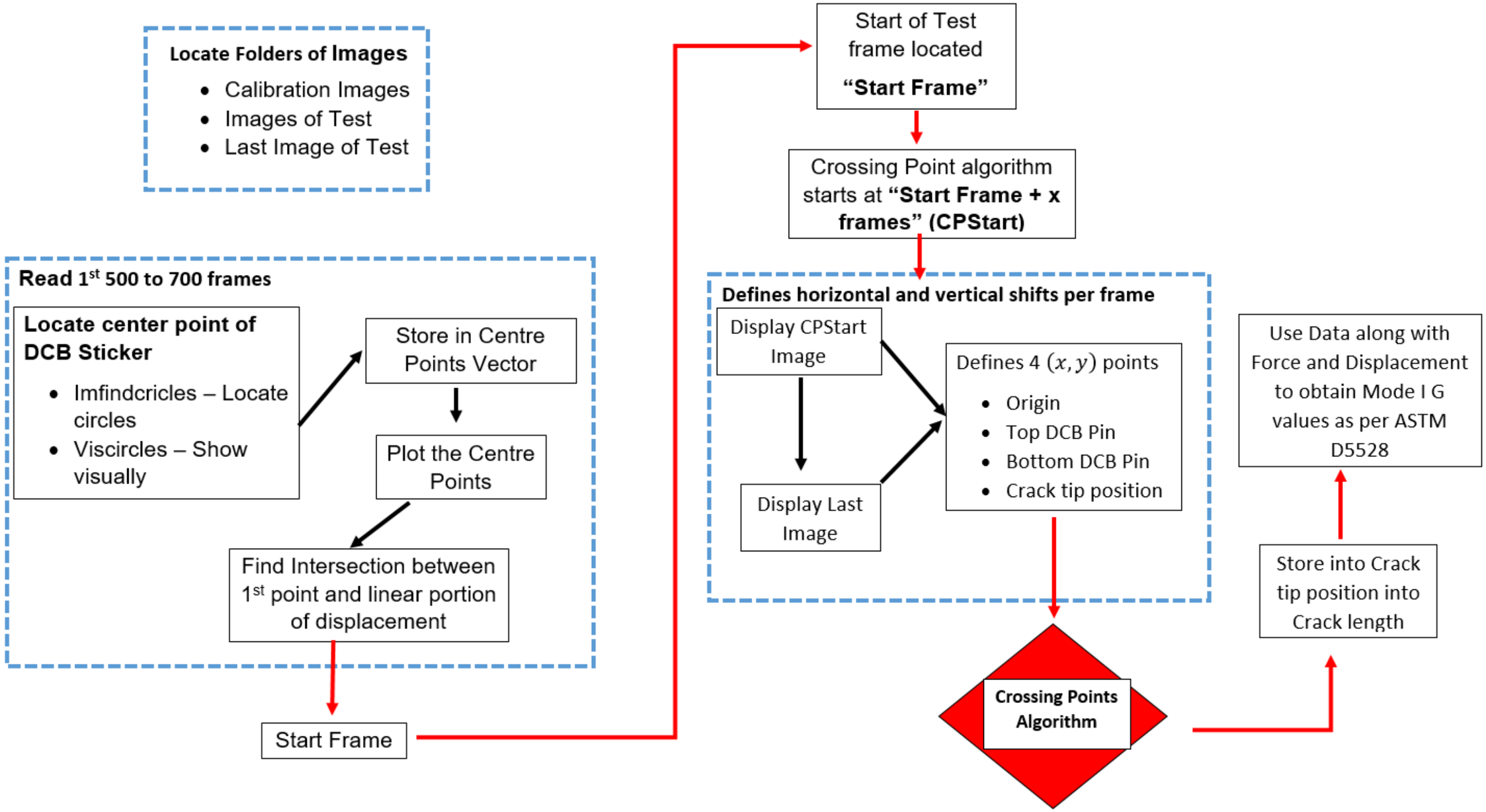

Figure 6-3: Flow chart showing how to obtain G_I

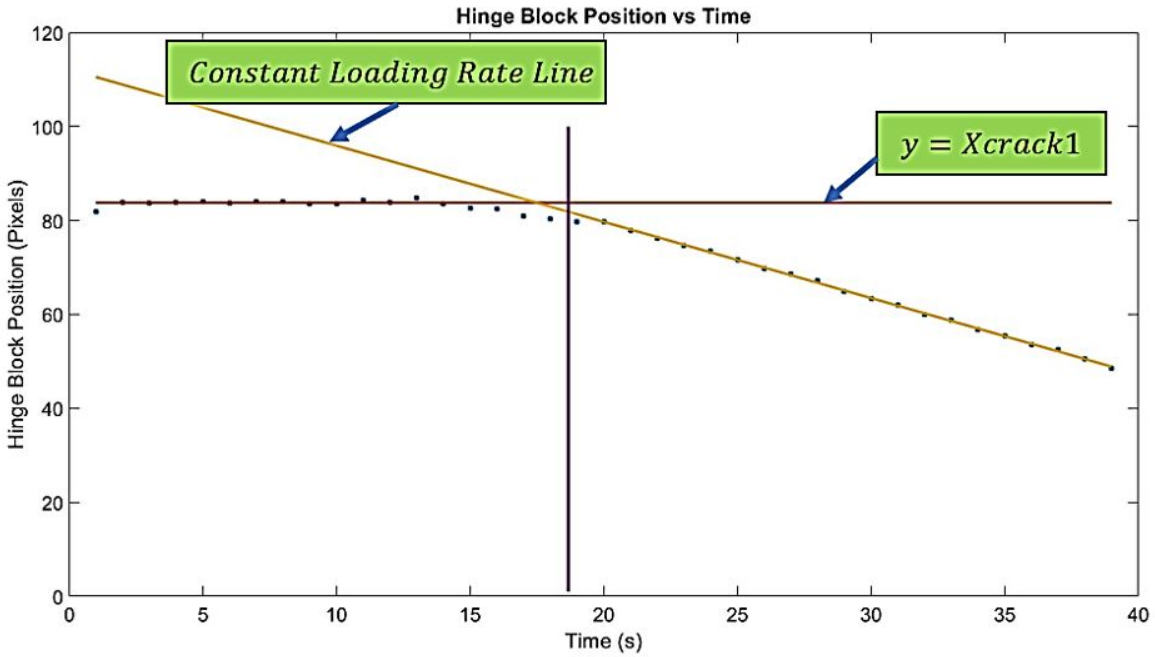

Figure 6-4: Graph showing how start frame is obtained

The start time is chosen as the x position of the intersection of these two curves as can be seen from Figure 6-4

Figure 6-5: Circle displacement locator

With start test frame known, the detection algorithm can start. The start frame and last image frame of a test were located and displayed. User inputs are used to define the pixel coordinates of the top and bottom pin and the crack tip as can be seen in Figure 6-6. This will give a range of values between which the specimen crack propagates. With these values known, a rough

estimate of the propagation can be determined for each frame. These are used within the script as an initial guess to predict the position of the crack tip within each frame as well as used to define generated lines as per Figure 4-20.

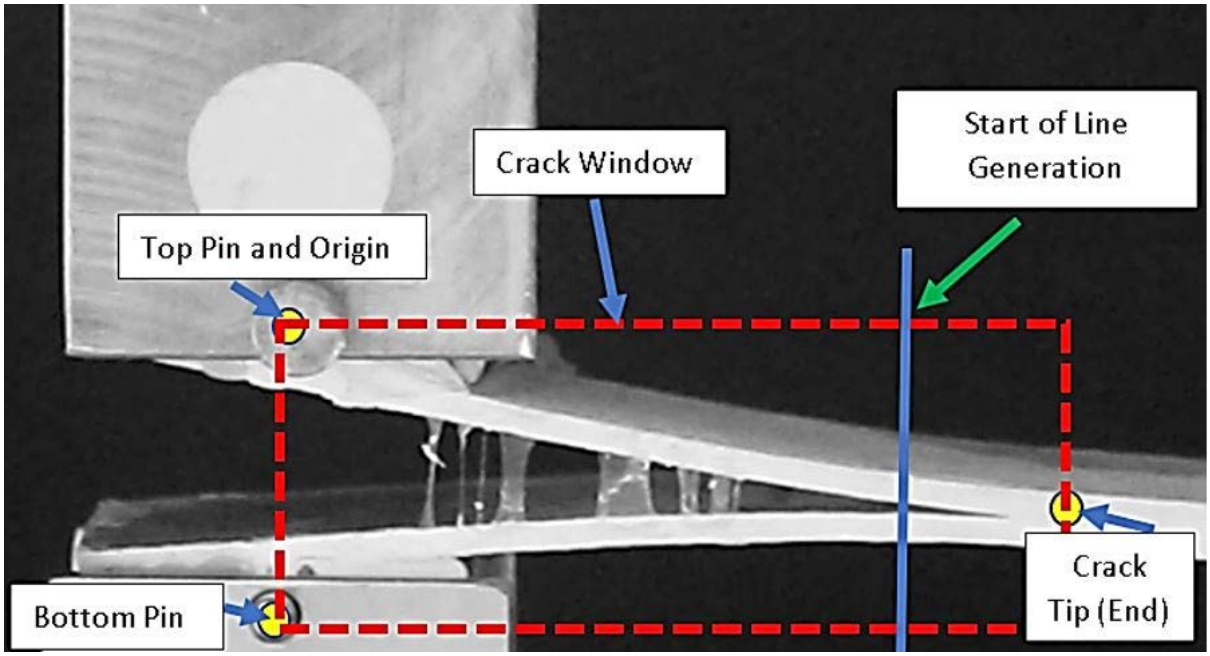

Figure 6-6: User defined points for DCB algorithm

The crack length is the horizontal distance from the crack tip, to the vertical line joining the top and bottom pin. To reduce computational speed, the line generation was started approximately 80 to 100 pixels to the left of crack Tip (End). The same process is repeated for the last image. Thus, the crack window was adjusted in such a way that the size remains the same but shifts to the region where the crack tip is expected to be as the test progresses.

The Crossing Point algorithm as shown in Figure 4-19 is used to detect the position of the crack tip. According to ASTM D5528, only 25mm of crack prorogation is required. For the purpose of this experiment, the crack length was recorded for the full duration of the test to check the behaviour of the crack beyond the 25mm length as well.

It should be noted that the crack length is only plotted from 400 frames (approximately 25s) after the determined starting frame. The grip opening displacement is less than 5mm at the beginning of the test, and the crack should only begin propagating approximately 25 seconds later after the test has started. An additional reason for this is to allow for the specimen to open towards the initiation point. Figure 6-7 shows a sample start frame before the “frame jump” where the specimen is considered “closed” within the crack region. Due to the specimen being closed, the Crossing Point algorithm does not accurately predict the crack tip for very small opening displacement of the specimen.

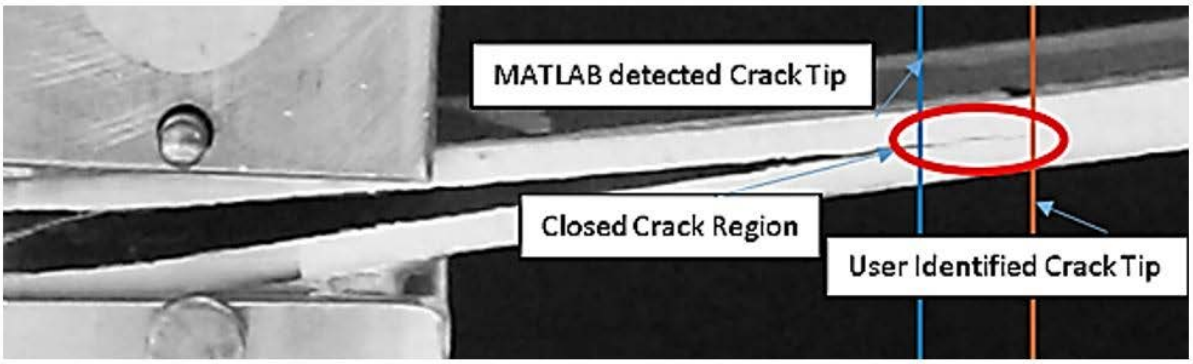

Figure 6-7: Underestimated detected crack tip for start frame of a sample test

From Figure 6-7, It can be seen that with the closed region, the MATLAB Crossing Point algorithm underestimates the user identified crack tip. The error for small opening in this case is approximately 10%. Thus, with the frame jump, this error can be minimised by increasing the crack jump to at least 400 frames. The 400-frame jump for each test forces the crack initiation point of the detection algorithm to correspond to 48s of when the camera starts recording, or 25s after when the test starts.

The force and displacement data obtained from the Zwick machine are loaded into the script file. These files were truncated to the length of the vector of crack length. Using these 3 points, the critical energy release rate for Mode I (G_I) can be calculated.

7. Results and Discussion

The raw measurements (force and crack length histories) are presented for all specimens for the three different weave patterns. After eliminating outliers, the calculated Mode I fracture toughness (G_I) is presented.

7.1. Force and crack length vs time

Figure 7-1 shows the force and crack length histories for Specimen 1 of the UD batch, which is representative of the general UD response.

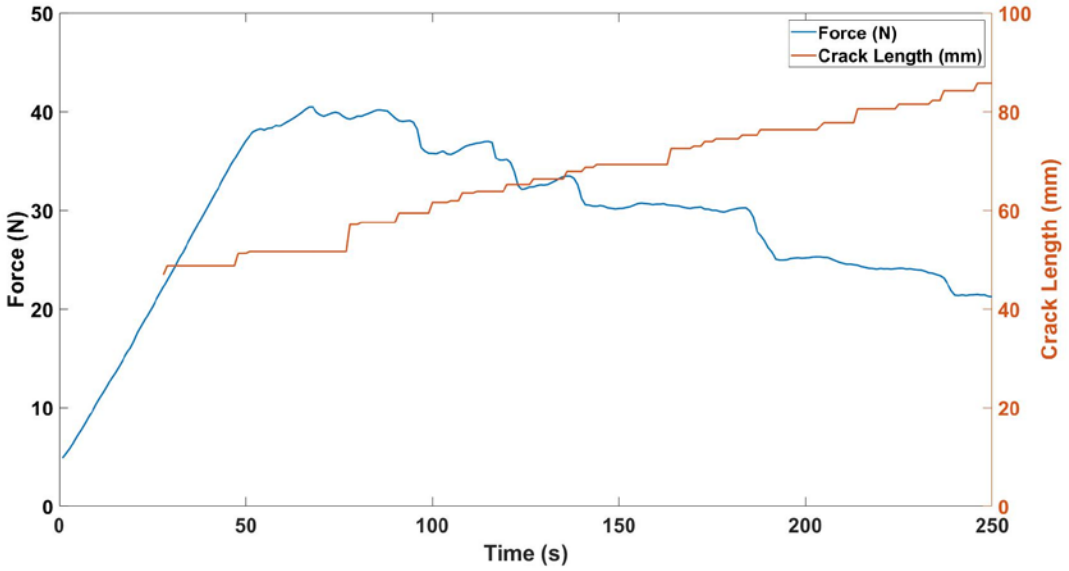

Figure 7-1: Graph of force and crack length vs time of UD 1

As explained in section 6.2.3, the initiation time in Figure 7-1 can be seen to be $48s$. The force at initiation is $35.8N$, whereas the crack initiation is $51.3mm$. The maximum force is $40.5N$ whereas the crack length at maximum force is $51.7mm$.

The force and crack length vs time of the remaining specimens of UD, Twill and Plain can be seen in Appendix K. A summary of all the forces at initiation and maximum force along with the crack lengths at initiation and at maximum force for all the remaining specimens and weave patterns can be seen in Appendix J.1.

Figure 7-2 and Figure 7-3 show the graphs of force vs time and crack length vs time respectively for 6 of the UD specimens.

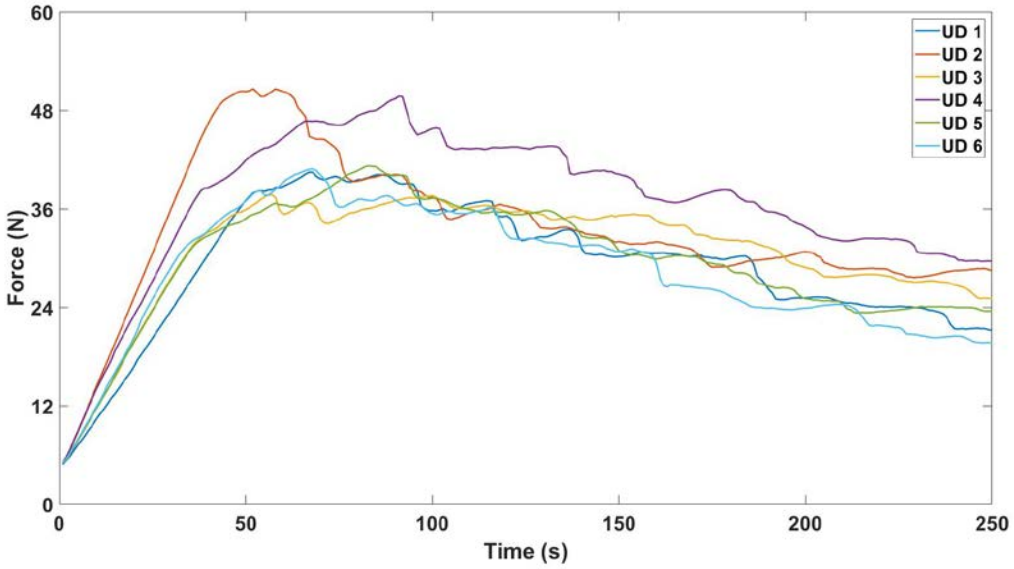

Figure 7-2:Graph of force vs time of all UD weave specimens

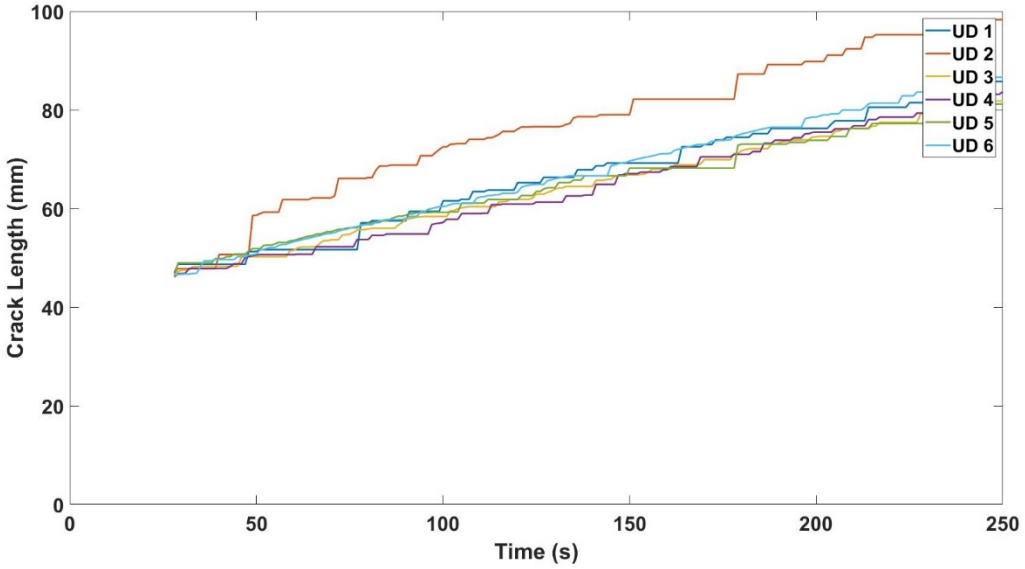

Figure 7-3: Graph of crack length vs time of all UD weave specimens

The crack length of UD 2 initially follows the same trend as the other specimens, before making a noticeable jump at approximately 50 seconds, which is a clear outlier. The maximum force of UD 2 is also higher than the other five UD specimens. Hence UD 2 is excluded from the fracture toughness calculations. The force vs time and crack length vs time of the 5 remaining UD specimens all follow a similar trend. For the first $40\,\text{to}\,50\text{s}$ the force applied to the specimens is linear. When the peak force of between $40\,\text{to}\,50\text{N}$ is reached, the response of the force applied to the specimens decreases to a range of $20\,\text{to}\,35\text{N}$. The crack initiation is considered as the crack length which corresponds to the approximately 50mm. The crack

length response at initiation is approximately $48s$ of the DCB tests. This corresponds to the first deviation point from linearity of the force vs time response. The DCB tests lasts about 5 minutes whereby the crack of the UD specimen propagates to approximately 85mm

Figure 7-4 and Figure 7-5 show the graphs of force vs time and crack length vs time respectively for the Twill weave specimens.

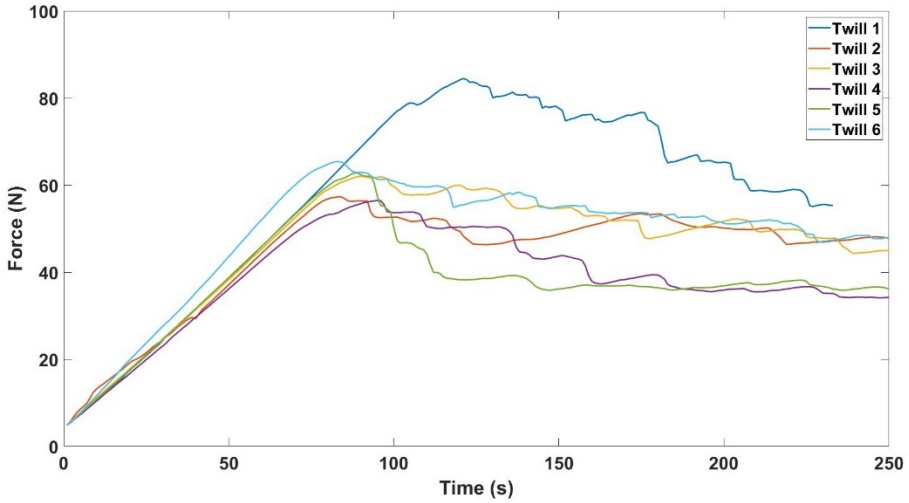

Figure 7-4: Graph of force vs time of all Twill weave pattern

Twill weave pattern 1 could be considered as an outlier as the maximum force is approximately 80N. The resulting force is considerably larger than the other five specimens, which all peak within a range of $50 \text{ to } 60 \text{ N}$. Once the peak force is reached the force decreases to approximately $35 \text{ to } 50\text{N}$ as seen in Figure 7-4.

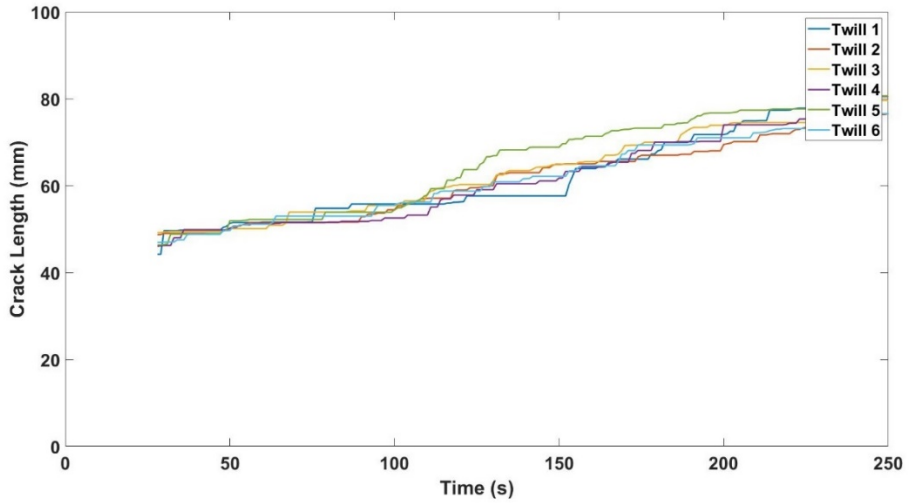

Figure 7-5: Graph of crack length vs time of all Twill weave pattern

The trend of the force and crack length vs time is similar between all the Twill weave specimens. The crack length of the Twill weave propagates from the initiation length of 50mm to approximately 80mm.

Figure 7-6 and Figure 7-7 show the graphs of force vs time and crack length vs time respectively for all 6 of the Plain weave patterns.

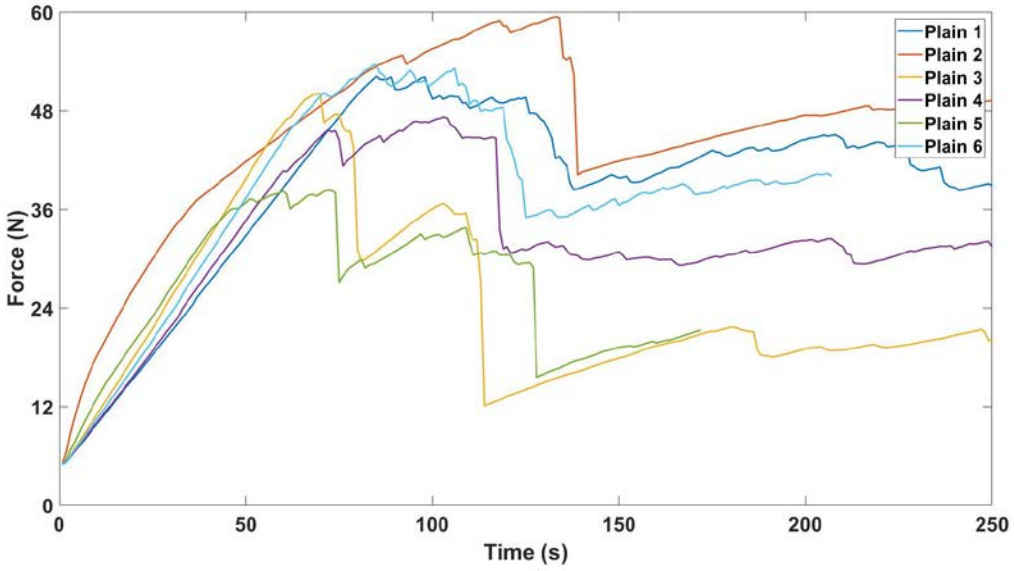

Figure 7-6: Graph of force vs time of all Plain weave pattern

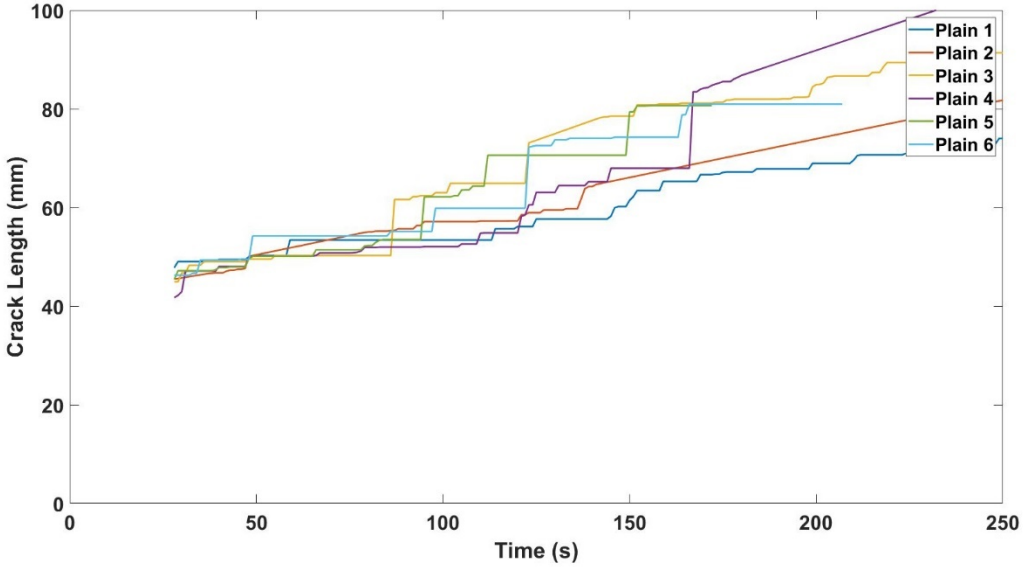

Figure 7-7:Graph of crack length vs time of all Plain weave pattern

The Plain weave specimens show a linear response for the first 70 seconds. When the peak force is reached, the crack growth is non-uniform with several large jumps in crack length. The crack resistance of the Plain weave specimens does not appear to be as uniform as the other weave patterns.

The averages of the crack initiation, crack length at maximum force, maximum force and force at initiation of each specimen types calculated. These are summarised in **Error! Reference source not found.** through to **Error! Reference source not found.** in Appendix J.1.

Figure 7-8 shows the average force at crack initiation, while Figure 7-9 shows the average maximum force, for all three weave patterns. The error bars represent the maximum and minimum values of the respective force values.

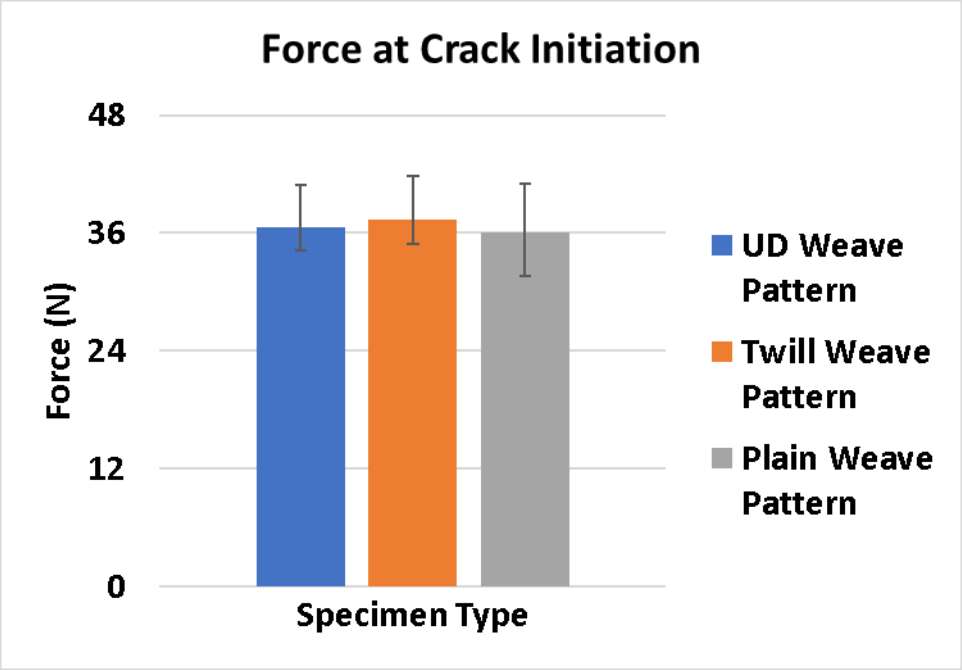

Figure 7-8: Bar graph of force at crack initiation for each specimen type

Based on Figure 7-8, it is difficult to draw any reasonable conclusions as the variations between the upper and lower bounds for any pattern is much larger than the variation in the averages between the patterns.

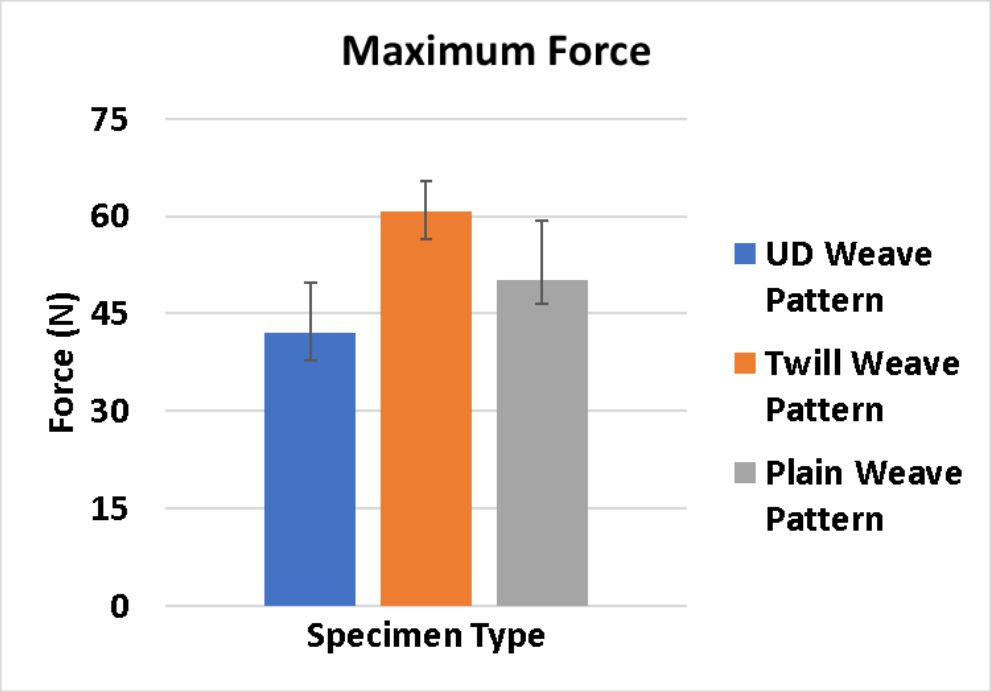

Figure 7-9: Bar graph of maximum force for each specimen type

Once the crack initiation is reached, the average force response increases until the maximum force is reached. Figure 7-9 shows that the lowest force is required to propagate the UD specimen after the crack initiation whereas the highest force is required to propagate the Twill weave specimens.

The average maximum force between the different weave patterns follows in the range of $\text{Twill} > \text{Plain} > \text{UD}$ for the different specimen types. The upper and lower limits for the maximum force of the different weave patterns follow the same trend as the average maximum forces. With the force at initiation varying between the averages and upper bounds, it shows that there is a greater uncertainty of the force readings at the start of the DCB tests.

The average crack at initiation for each specimen types is approximately $50 \pm 1\ \text{mm}$, This is due to the pre-cracking of the DCB specimens before the DCB tests were conducted.

Figure 7-10 shows the bar graph of the crack length at maximum force for each specimen weave type.

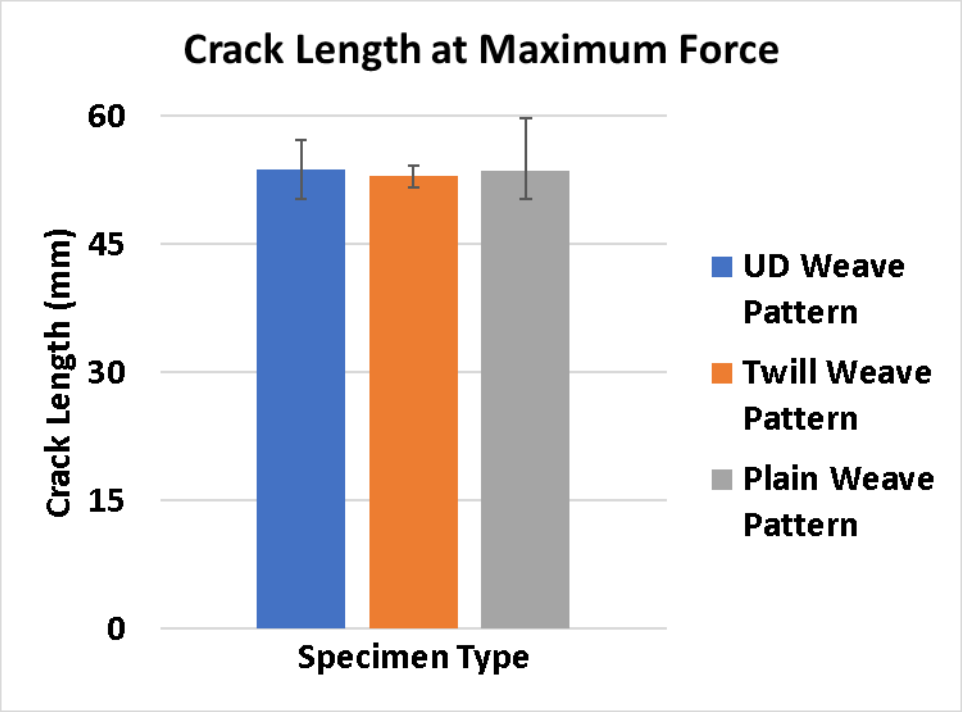

Figure 7-10: Bar graph of crack length at maximum force for each specimen type

From Figure 7-10 the results show a variation in the rate at which the crack propagates between the specimen types. There is also variation in the average crack lengths at maximum force. The average crack length values range from $\text{Plain} > \text{UD} > \text{Twill}$. The upper and lower bounds follow the same trend as the averages. It should be noted that the Plain weave pattern displayed large error bars. This is due to the large fluctuations of the force vs time between the different Plain weave specimens.

The force and crack length data were averaged and down-sampled for each weave type, in order to highlight their different responses. The down-sampling allowed for 20 points to be plotted for each specimen. The upper and lower bounds for each data set are shown as error bars, and the down sampled data is plotted for clarity. These graphs were then overlaid with each other where the average down-sampled force vs time can be seen in Figure 7-11.The average down-sampled crack length vs time can be seen in Figure 7-12.

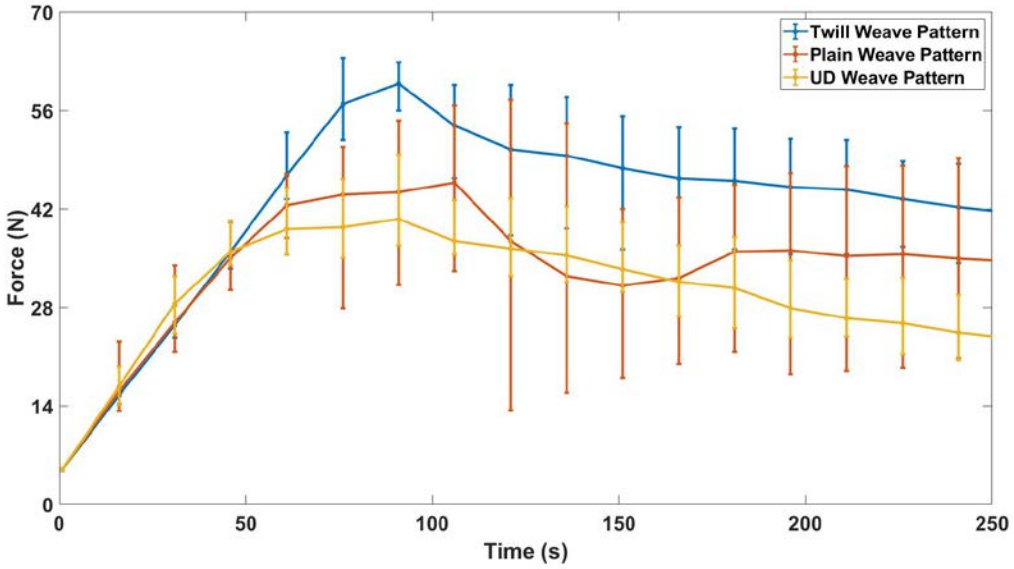

Figure 7-11: Graph of average down-sampled force vs time of all values

From Figure 7-11, it is clear that more force is required during crack propagation for the Twill weave, with the UD weave generally requiring the least force. The fluctuations in force for the Plain weave as can be seen by the error bars are larger than for the other two weave patterns.

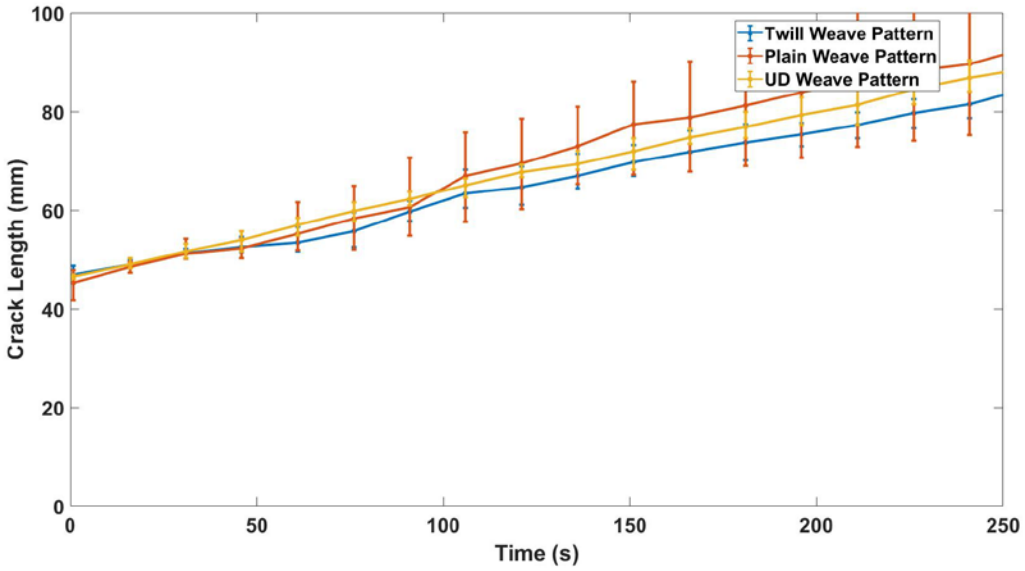

Figure 7-12: Graph of average down-sampled crack length vs time

From Figure 7-12 , there is very little variation in crack propagation rate for the first 50 seconds of loading. Between 50 and 100 seconds, the UD specimens have a faster crack growth on average. After 100 seconds the Plain weave specimens have the fastest crack growth.

7.2. Fracture toughness (G_I) vs crack length.

With the measured force, opening displacement and crack length known, the Mode I fracture toughness was calculated using the Modified Beam Theory as described in Section 2.3.2.

Figure 7-13 shows the G_I vs crack length (the resistance curve or R-curve) for the first UD specimen, with the fracture toughness values at initiation and maximum force highlighted. It should be noted that this graph was generated using the force, displacement and crack length data at the as sampled rate (15 points / second).

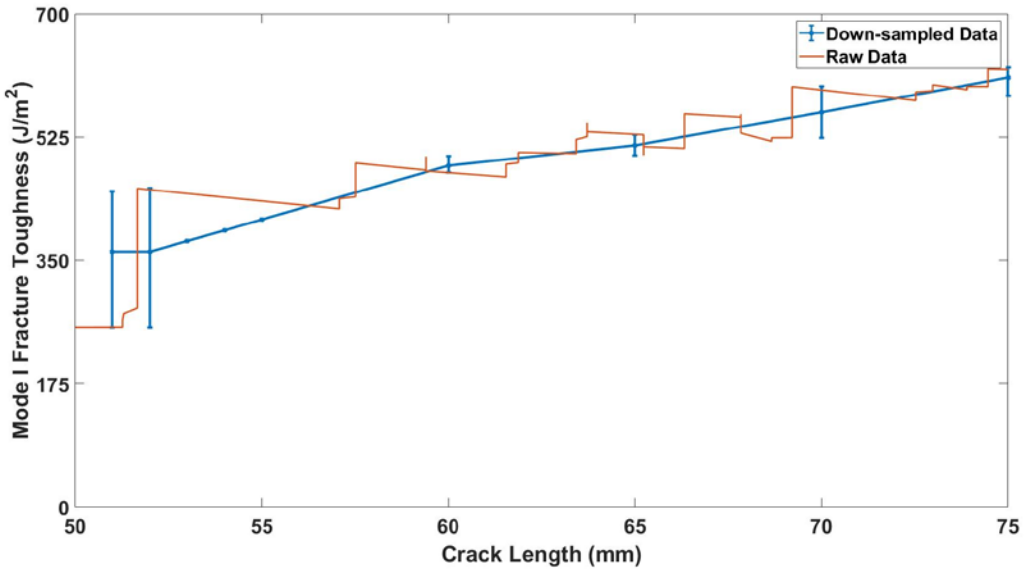

Figure 7-13: Graph of Mode I fracture toughness vs crack length of UD 1

From Figure 7-13 the fracture at initiation is approximately $250\,\mathrm{J.m^{-2}}$ and the fracture at maximum force is approximately $400\,\mathrm{J.m^{-2}}$. The R -curve for the UD 1 has large jumps across the length of the specimens.

The R-curves for all specimens of a weave pattern are overlaid for comparison. Figure 7-14 shows all five retained R-curves for UD specimens.

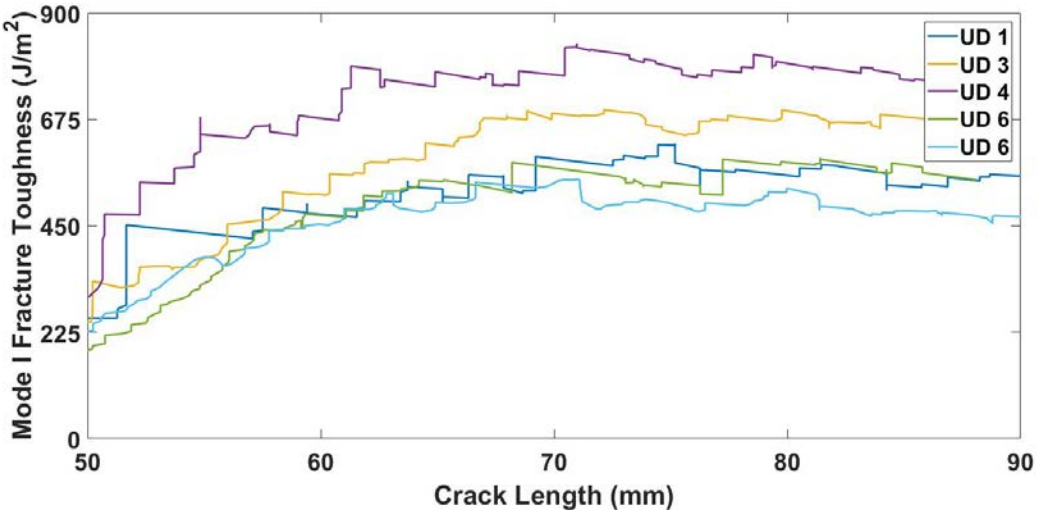

Figure 7-14: Graph of Mode I fracture toughness vs crack length of UD Specimens

Figure 7-15 shows all five retained R-curves for the Twill weave pattern and Figure 7-16 shows all the Plain pattern.

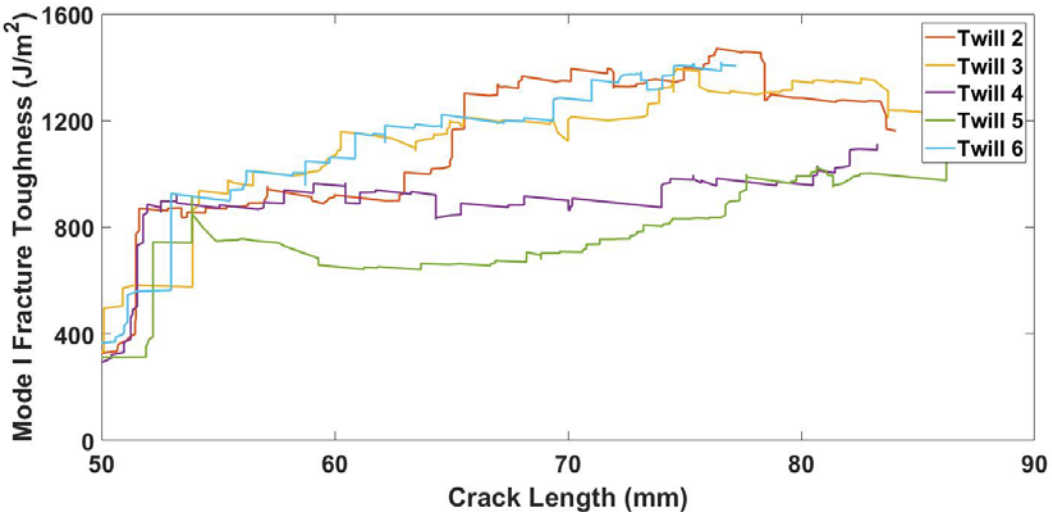

Figure 7-15: Graph of Mode I fracture toughness vs crack length of Twill weave pattern

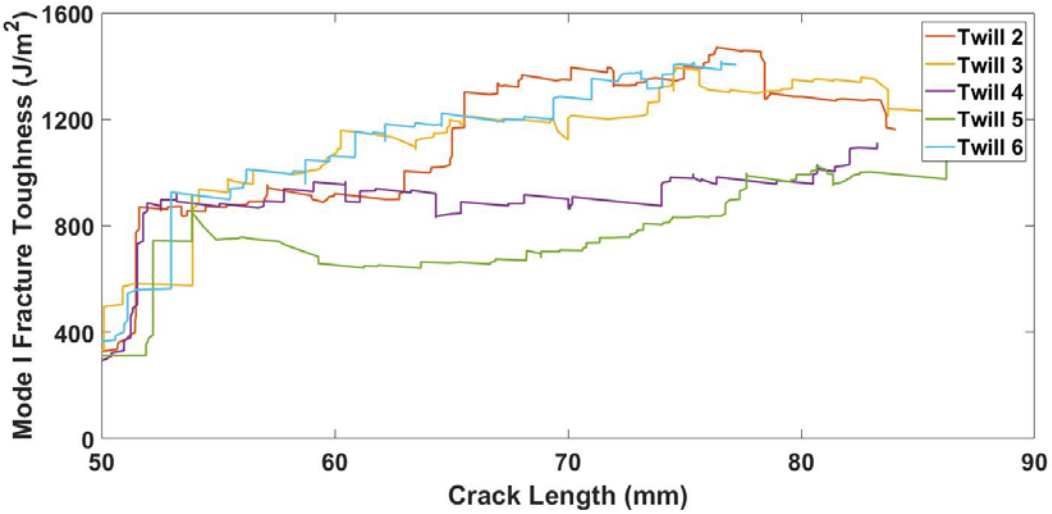

Figure 7-16: Graph of Mode I fracture toughness vs crack length of Plain weave pattern

From the R -curves in Figure 7-14, Figure 7-15 and Figure 7-16, there are large fluctuations in the fracture toughness values among the same specimen type. The G_I value was calculated at the same sampling rate as the force, displacement and crack length (15 points / second) and are very sensitive to small changes in force or crack length.

To clean up the R-curves, the G_I data was smoothed and down sampled to obtain the 10 points required by ASTM D5528 to generate the R-curve of one specimen type. These 10 points correspond to every 1 mm from the 50mm mark through 55mm of crack length from the reference line. The next five points correspond to 5mm spacings, namely from 55mm to 75mm, as can be seen in Figure 7-17.

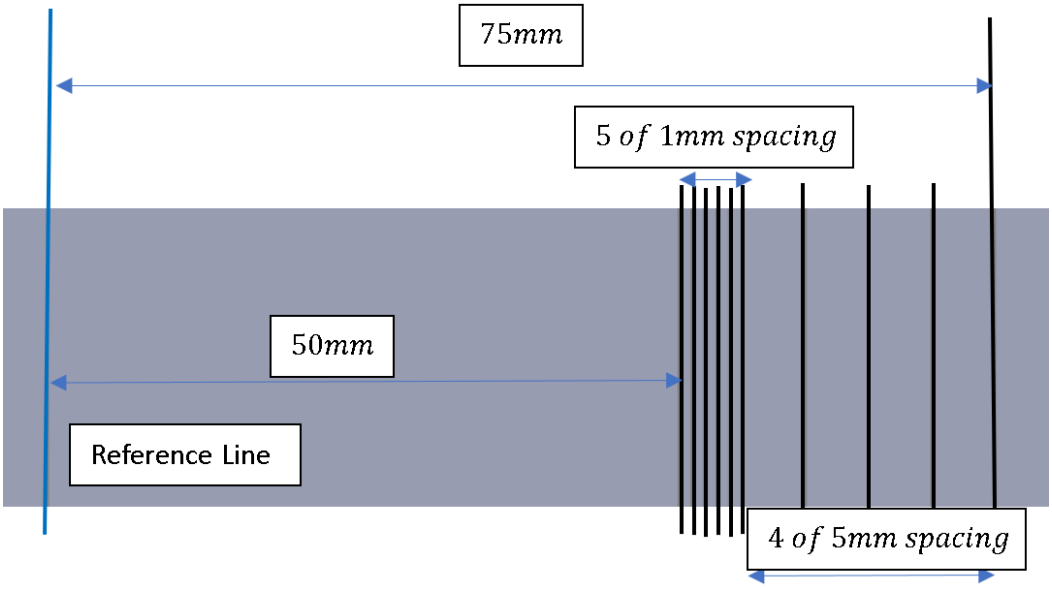

Figure 7-17: Fracture toughness data points as per ASTM standards

The G data for a given specimen was smoothed by averaging in the close vicinity of each of the crack lengths shown in Figure 7-17. The G value plotted at a crack length of 50mm is the average of G between 49.5 and 50.5mm.

Figure 7-18 shows the down-sampled cleaned up version of fracture toughness vs crack length overlaid with the original fracture toughness of the first UD specimen. The upper and lower bounds of the error bars correspond to the maximum and minimum fracture values of the raw data which falls within each crack length bandwidth as accordance to the ASTM standards.

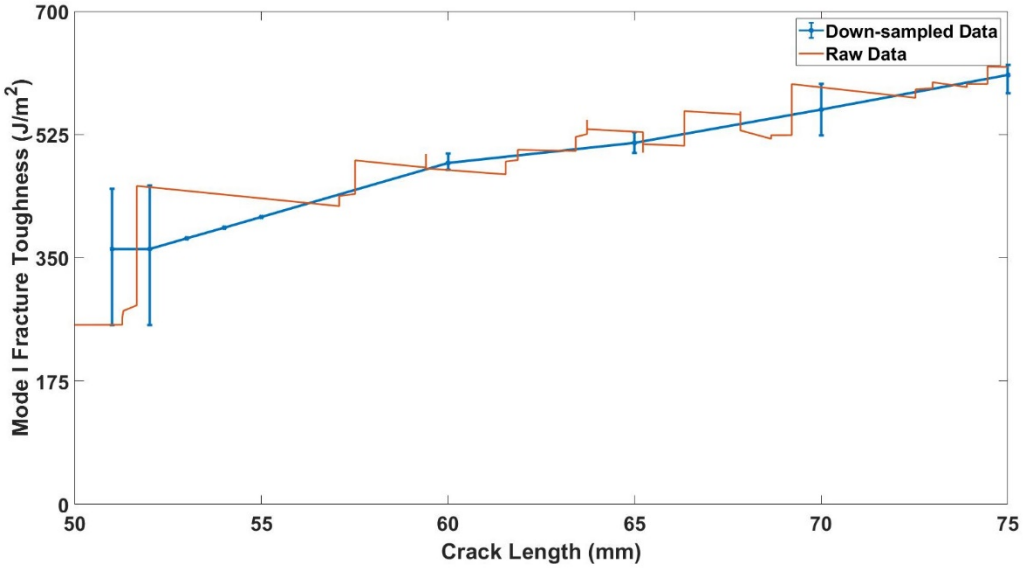

Figure 7-18: Graph of down-sample and Mode I fracture toughness vs crack length of UD 1

The rest of the R curves can be seen in Appendix K.2, **Error! Reference source not found.** through **Error! Reference source not found.**.

All the cleaned-up UD specimens fracture toughness vs crack length can be seen in Figure 7-19. The Twill and Plain weave specimens can be seen in Figure 7-20 and Figure 7-21 respectively.

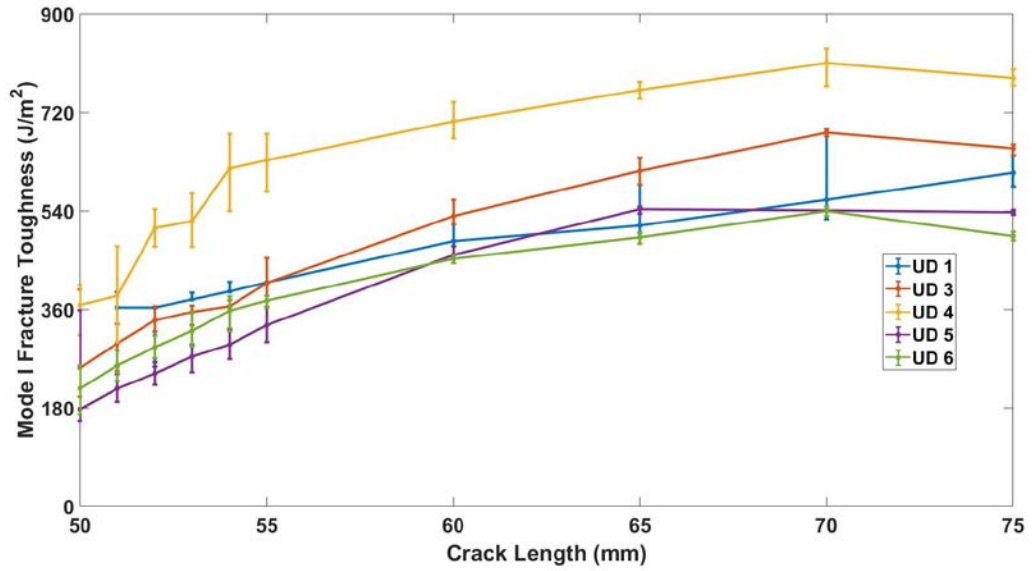

Figure 7-19: Graph of down-sampled Mode I fracture toughness vs crack length of all UD specimens

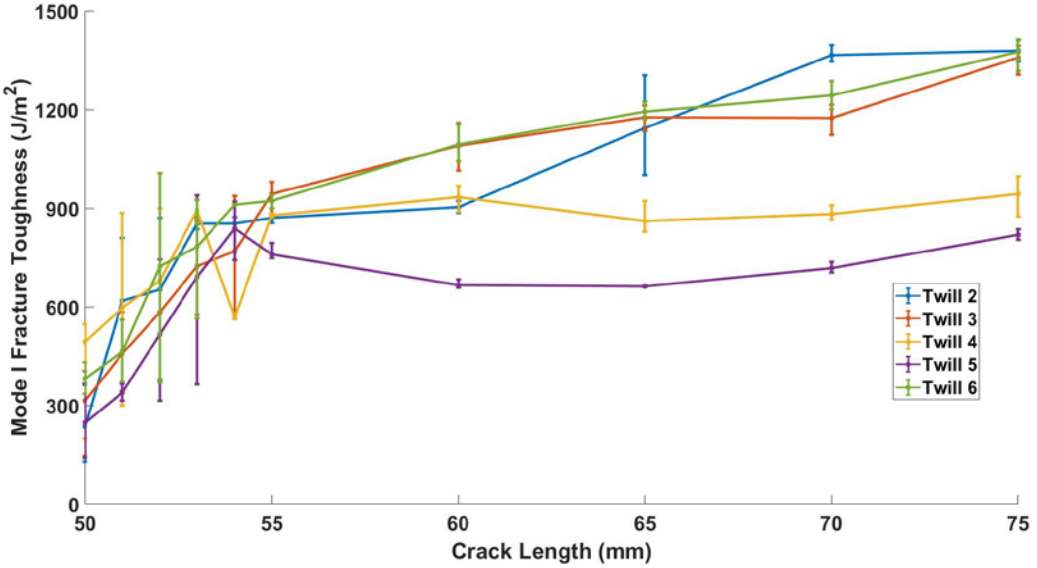

Figure 7-20: Graph of down-sampled Mode I fracture toughness vs crack length of all Twill weave pattern

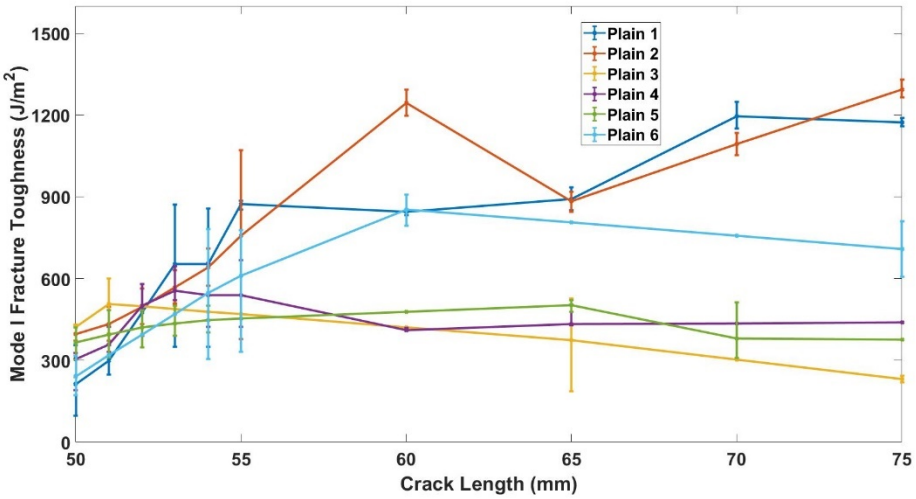

Figure 7-21: Graph of down-sampled Mode I fracture toughness vs crack length of all Plain weave pattern

Based on Figure 7-19 , Figure 7-20 and Figure 7-21, evens with the data cleaned up, the variations between the same specimen types are large. Thus, it is difficult to make a reliable conclusion about these experiments of the same specimen type.

The averages of each specimen type was determined and overlaid as seen in Figure 7-22.

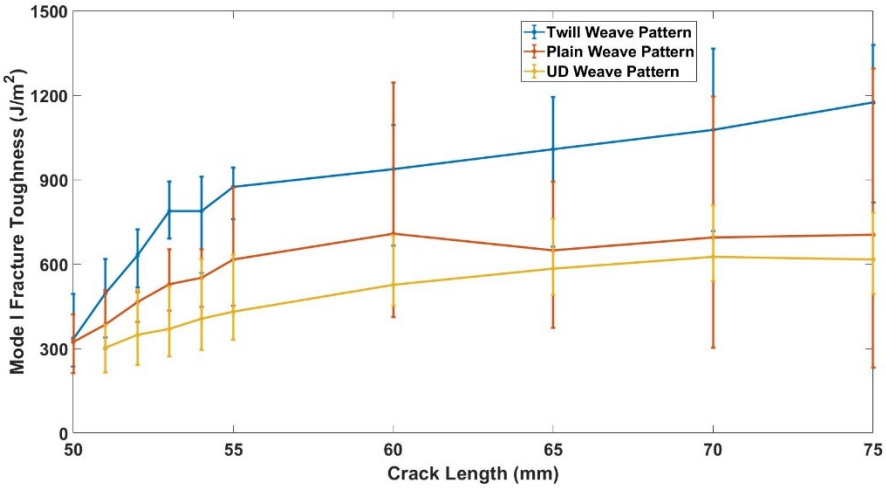

Figure 7-22: Graph of average down sampled Mode I fracture toughness vs crack length of all weave pattern

Figure 7-22 shows the average down sampled Mode I fracture toughness vs crack length. It can be seen that the Twill resistance to fracture is the largest whereas the resistance to fracture of the UD weave pattern is the least. The Twill weave pattern resistance increases as the crack propagates.

Of the three-specimen types, only the UD pattern comes to a plateau of approximately $600\ \mathrm{J.m^{-2}}$ from an initiation point of slightly above $200\ \mathrm{J.m^{-2}}$.

The Plain weave pattern resistance increases to approximately $700\ \mathrm{J.m^{-2}}$ at 60mm crack length from fracture initiation of $300\ \mathrm{J.m^{-2}}$. The resistance then decreases to $600\ \mathrm{J.m^{-2}}$ at 65mm and then the crack resistance increases for the duration of the tests. This implies that the bonding of the Plain weave pattern may not be uniform which could suggest why the resistance to crack fluctuates.

Thus, Twill weave pattern can be considered the weave pattern with the highest resistance to delamination, from initiation through to larger crack length. The UD specimen can be considered the weakest.

The fracture toughness (referred to from here as $\mathrm{G_I}$) at initiation and maximum force is explored further and these values are summarised in Appendix J.2.

Figure 7-23 and Figure 7-24 show the bar graph of the average $\mathrm{G_I}$ at initiation and at maximum force of the different weave patterns. The error bars are the upper and lower bounds of the $\mathrm{G_I}$ at initiation,$\mathrm{G_{Ic}}$, of all the specimens of the same type.

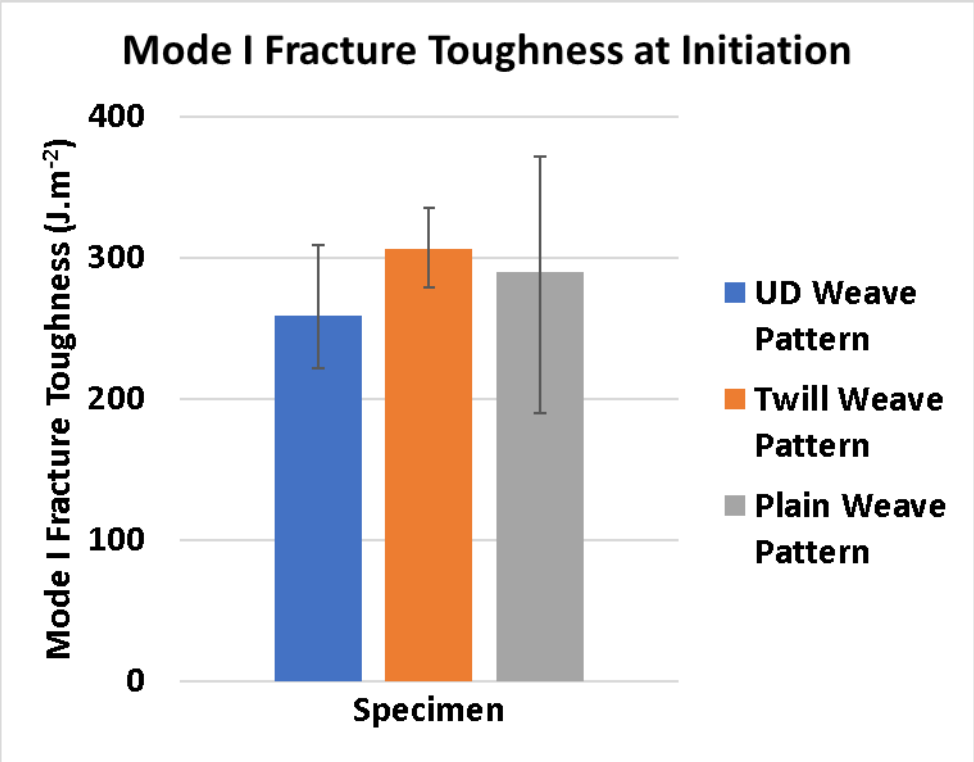

Figure 7-23: Bar graph of Mode I fracture toughness at initiation of each specimen type

From Figure 7-23, the average $\mathrm{G_I}$ is in the range of $\mathrm{Twill} > \mathrm{Plain} > \mathrm{UD}$. This shows that the resistance to fracture at initiation varies between the different specimen types. The upper

bound limit follows the same trend as the average G_I whereas the lower bound limits follows the range of $Twill > UD > Plain$. With the force response of the Plain weave having large fluctuations between them (refer to Figure 7-6), it is expected that the G_{Ic} values would contain some uncertainty as can be seen from the large error bars from both Figure 7-23 and Figure 7-24. Thus, it's difficult to make a sensible conclusion for the Plain weave patterns due to the large variations within the specimens

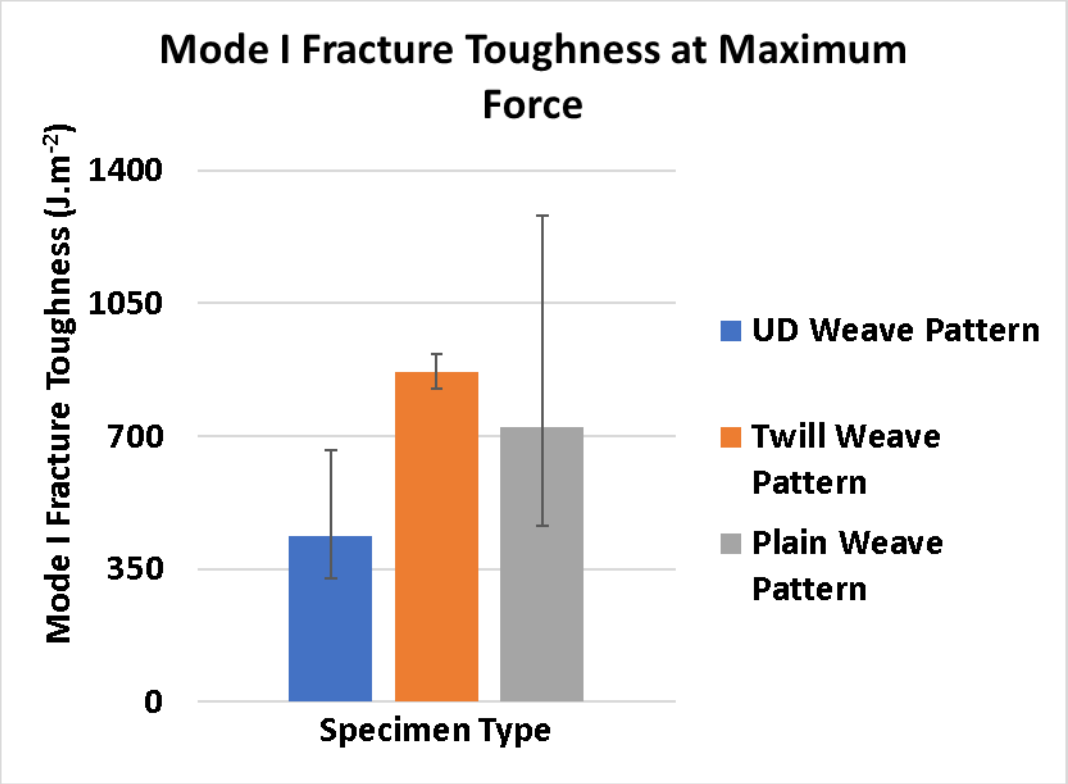

Figure 7-24: Bar graph showing Mode I fracture toughness at maximum force of each specimen type

From Figure 7-24, the Twill weave has the highest average G_I values for the maximum force. The lower bounds follow the same trend as the average G_I of $Twill > Plain > UD$. The average G_I values for the initiation and at maximum force follows the same trend. The upper bounds for the Plain weave are the largest due to the large fluctuations and uncertainties of the force response.

Based on Figure 7-23 and Figure 7-24 it can be considered that the Twill weave has the highest resistance to crack growth and the UD specimen has the least crack resistance. These conclusions confirm what has been found from Figure 7-22.

8. Conclusions

The vacuum infusion moulding process was used to manufacture FRP of Unidirectional, Twill and Plain weave panels, incorporating insert film as a starter for delamination testing. Rectangular specimens of size 160x25x4mm were cut from the panel using a waterjet cutter. The actual thickness is dependent on the panel's thickness which is dependent on the manufacturing batch. Due to a total of 12 manufacturing batches made, the thicknesses of the specimens of the same type were different which in turn may affect the specimen stiffness.

The DCB tests were conducted on the Zwick Universal Testing Machine, which measured the force and opening displacement. The DCB test was recorded using a digital camera in order to obtain the crack length measurements post-test. It should be noted that based on the camera used, the video file was restricted to 4GB. To make sure that the entire test was recorded, the speed of the DCB test was increased to a higher rate than what's stated in the ASTM standards.

One camera was used to film the test and was nominally perpendicular to the specimen face. It was thus essential to calibrate the conversion from pixel coordinates to world coordinates in mm, using calibration points as close to the plane of the specimen face as possible. This was achieved using the corners of the DCB specimen fixture, which were known lengths and very close to the plane of the specimen face. However, the corners were selected by user input (which carries a small error) and in initial calibration, the rotation of the holder wasn't considered. While these errors were small, it would be preferable to use a more robust calibration method that avoids user error and directly corrects for rotation.

The crack length was determined using an image-based method, which used the frames from the video as input. Using edge detection, a series of algorithms for identifying the crack upper and lower surfaces, and hence the crack tip, were investigated. These were iteratively improved until the algorithm was able to locate the crack tip to within an acceptable error. The process was repeated for all images to obtain the crack length. It should be noted that the chosen algorithm has difficulties detecting the crack tip for small opening displacements. The algorithm was adapted to start after these "small openings" and with these alterations, the detection algorithm was deemed acceptable as the error was less than 0.5mm. It should be noted that once an acceptable method was reached, the algorithm was not optimised for speed.

In order to validate the detection algorithm, an Ultrasonic Wedge device was designed to replicate a DCB test in a static case. The Wedge device was used in conjunction with an Ultrasound Thickness Tester. The probe diameter was 20mm, which made it difficult to accurately determine the distance from the probe center to the reference point. Thus, the author devised a means of positioning the probe using a holder running on threaded rods, located with nuts. This allowed the probe position to be accurately controlled. Comparison of the crack length measurements from the ultrasound measurements and the image-based algorithm showed the error of the Crossing Point algorithm to be less than 0.25mm. As the ASTM standard requires crack measurement to within 0.5mm, the image-based measurements were sufficiently accurate. Thus, the algorithm was deemed suitable to detect the position of the crack length automatically.

Force and crack length vs time graphs were generated of all 3 weave patterns. The force at crack initiation and the maximum force were highlighted from the force vs time graphs. The crack length at maximum force was also determined. There was very little variation in the force at crack initiation, for the three different weave patterns. However, once the crack has propagated, there are noticeable differences in the force history and the speed of crack propagation. Twill weave pattern requires the most force to propagate the crack whereas the UD pattern requires the least force to propagate the crack.

The Mode I fracture toughness vs crack length graphs, i.e. R-curves, of the specimens was also generated. It should be noted that these R-curves were very noisy and had large fluctuations between the specimens of the same type. To clean up the R-curves, the force, displacement and crack length data were down-sampled so that G values were only calculated at the crack lengths required by the ASTM standard (rather than as continuous data). Even with down-sampling, there was significant variation in fracture toughness at crack initiation, both within one weave pattern and when comparing difference weave patterns. The variation seems to decrease as the crack begins to propagate.

When considering the R-curves for longer crack lengths, we can conclude that the Twill weave pattern showed the most resistance to delamination, while the UD showed the lowest delamination resistance. These are consistent with the results obtained from the force vs time and crack vs time results.

It should be noted that the Plain weave pattern had larger fluctuation in the results compared to the other patterns and thus the results could not be deemed acceptable. The crack length measurements were sufficiently accurate to observe different crack propagation rates for the different weave patterns, which correlated with the fracture toughness values calculated.

9. Recommendations

Based on the results and findings, the following recommendations can be made:

The thickness of a given panel is dependent not only on the layers thickness but also on how the vacuum compacts the dry fibres, the temperature etc. Thus, the thickness of each panel will differ from manufacturing batch to batch. It is recommended that rather than manufacturing several small panels for each weave pattern, that a single larger panel is manufactured, that is sufficient for all specimens of that weave pattern. This would ensure that the thickness of the one type of panel will be the same within a reasonable uncertainty. This will reduce the variation between specimens, and hence reduce uncertainty in the results. This was not entirely the case for this dissertation as can be seen from the specimen dimensions in Appendix A.2.

In order to conduct some tests at the cross-head speed specified in the ASTM standard, it would be advisable to set up a system that captures still images at slower rates than 15 fps. This would avoid the video file size limit and would reduce the need to extract a large number of frames from the video unnecessarily.

Two cameras can be used to increase the calibration accuracy of the images. Although minimal in this case, the effect of rotation when dealing with calibration can be considered to improve the calibration of the image results. Using two cameras allows us to track 3D displacements, which means we avoid the assumption around planar motion. However, calibrating the system for two cameras isn't trivial!

The detection algorithm can be altered to cater for small opening displacement as the results of experiments will hold greater credibility. Coding of the algorithm to improve processing speed should also be considered.

This dissertation served as a base to conduct DCB testing at the UCT facility. Thus, with all the necessary equipment made, and an acceptable working detection algorithm, the doors of exploring and investigating more weave patterns can be looked into. An option of looking into more types of pattern of the same type can also be explored. Extensive studies of Modes II and Mixed mode can also be explored to give more credibility to the results obtained.

Reference Lists

[1] P. K. Malick, Fiber-reinforced composites: materials, manufacturing, and design, Third. CRC Press, 2007.

[2] M. M. Shokrieh and M. Heidari-Rarani, “Effect of stacking sequence on R-curve behavior of glass/epoxy DCB laminates with 0°//0° crack interface,” Mater. Sci. Eng. A, 2011.

[3] M. Kenane, “Delamination Growth In Unidirectional Glass/Epoxy Composite Under Static And Fatigue Loads,” Phys. Procedia, 2009.

[4] “Introduction to Fracture mechanics.” [Online]. Available: https://www.slideshare.net/HarshalPatil7/introduction-to-fracture-mechanics. [Accessed: 22-Apr-2019].

[5] M. L. Benzeggagh and M. Kenane, “Measurement of mixed-mode delamination fracture toughness of unidirectional glass/epoxy composites with mixed-mode bending apparatus,” Compos. Sci. Technol., vol. 56, no. 4, pp. 439–449, 1996.

[6] G. S. Langdon, D. Karagiozova, C. J. Von Klemperer, G. N. Nurick, A. Ozinsky, and E. G. Pickering, “The air-blast response of sandwich panels with composite face sheets and polymer foam cores: Experiments and predictions,” Int. J. Impact Eng., 2013.

[7] Z. W. Guan, A. Aktas, P. Potluri, W. J. Cantwell, G. Langdon, and G. N. Nurick, “The blast resistance of stitched sandwich panels,” Int. J. Impact Eng., 2014.

[8] G. M. Sinclair, “The response of singly curved fibre reinforced sandwich and laminate composite panels subjected to localised blast loads,” 2014.

[9] I. B. Ghoor, “The response of concave singly curved fibre reinforced moulded sandwich and laminated composite panels to blast loading,” 2018.

[10] G. S. Langdon, C. J. von Klemperer, B. K. Rowland, and G. N. Nurick, “The response of sandwich structures with composite face sheets and polymer foam cores to air-blast loading: Preliminary experiments,” Eng. Struct., 2012.

[11] Y. T. Obaidat, S. Heyden, O. Dahlblom, G. Abu-Farsakh, and Y. Abdel-Jawad, “Retrofitting of reinforced concrete beams using composite laminates,” Construction and Building Materials, vol. 25, no. 2. pp. 591–597, 2011.

[12] “BBC - GCSE Bitesize: Woven fabrics.” [Online]. Available:

http://www.bbc.co.uk/schools/gcsebitesize/design/textiles/fabricsrev1.shtml. [Accessed: 04-Mar-2018].

[13] “Fibre Glast Developments Corp. | Fiberglass & Composite Materials.” [Online]. Available: https://www.fibreglast.com/. [Accessed: 04-Mar-2018].

[14] David Cripps, “Composite materials guide: Reinforcements - Woven Fabrics,” NetComposites. [Online]. Available: https://netcomposites.com/guide-tools/guide/reinforcements/woven-fabrics/. [Accessed: 04-Mar-2018].

[15] D. Cripps, “Composite materials guide: Manufacturing - Wet/Hand Lay-up | NetComposites,” NetComposites. [Online]. Available: https://netcomposites.com/guide-tools/guide/manufacturing/wethand-lay-up/. [Accessed: 01-May-2016].

[16] M. Elkington, D. Bloom, C. Ward, A. Chatzimichali, and K. Potter, “Hand layup: understanding the manual process,” Adv. Manuf. Polym. Compos. Sci., vol. 1, no. 3, pp. 138–151, Jul. 2015.

[17] W. J. Stuart, “Composite Materials Layup Lab,” 2010.

[18] Fibre Glast, “Vacuum Infusion Equipment and Methods - Part One - Fibre Glast.” [Online]. Available: https://www.fibreglast.com/product/vacuum-infusion-Guide/Learning_Center. [Accessed: 16-Apr-2019].

[19] “Composite materials guide: Manufacturing - Infusion Processes | NetComposites.” [Online]. Available: https://netcomposites.com/guide-tools/guide/manufacturing/infusion-processes/. [Accessed: 01-May-2016].

[20] David Roylance, “Introduction to Fracture Mechanics,” 2001. [Online]. Available: https://ocw.mit.edu/courses/materials-science-and-engineering/3-11-mechanics-of-materials-fall-1999/modules/MIT3_11F99_frac.pdf. [Accessed: 24-Dec-2018].

[21] ASTM International, “ASTM D5528 - 13 Standard Test Method for Mode I Interlaminar Fracture Toughness of Unidirectional Fiber-Reinforced Polymer Matrix Composites.”

[22] M. M. Shokrieh, A. Zeinedini, and S. M. Ghoreishi, “On the mixed mode I/II delamination R-curve of E-glass/epoxy laminated composites,” Compos. Struct., vol. 171, pp. 19–31, 2017.

[23] P. Davies, B. R. K. Blackman, and A. J. Brunner, “Standard Test Methods for Delamination Resistance of Composite Materials: Current Status,” Appl. Compos. Mater., vol. 5, no. 6, pp. 345–364, 1998.

[24] A. J. Brunner, B. R. K. Blackman, and P. Davies, “A status report on delamination resistance testing of polymer-matrix composites,” Eng. Fract. Mech., vol. 75, no. 9, pp. 2779–2794, 2008.

[25] ASTM International, “ASTM D7905-14. Standard Test Method for Determination of the Mode II Interlaminar Fracture Toughness of Unidirectional Fiber-Reinforced Polymer Matrix Composites.”

[26] “Vizebh Compositech Pvt. Ltd.” [Online]. Available: http://www.vctech.co/services/testing. [Accessed: 03-Mar-2018].

[27] A. D6671M, “ASTM D6671 - Standard Test Method for Mixed Mode I-Mode II Interlaminar Fracture Toughness of Unidirectional Fiber Reinforced Polymer Matrix Composites.”

[28] “Determining the Energy Release Rate (G) with ZwickRoell Testing Equipment.” [Online]. Available: https://www.zwickroell.com/en/composites/other-tests/energy-release-rate-g. [Accessed: 03-Mar-2018].

[29] A. B. De Morais, M. F. De Moura, J. P. M. Gonçalves, and P. P. Camanho, “Analysis of crack propagation in double cantilever beam tests of multidirectional laminates,” Mech. Mater., vol. 35, no. 7, pp. 641–652, 2003.

[30] R. Velmurugan and S. Solaimurugan, “Improvements in Mode I interlaminar fracture toughness and in-plane mechanical properties of stitched glass/polyester composites,” Compos. Sci. Technol., vol. 67, no. 1, pp. 61–69, 2007.

[31] F. Ducept, P. Davies, and D. Gamby, “An experimental study to validate tests used to determine mixed mode failure criteria of glass/epoxy composites,” Compos. Part A Appl. Sci. Manuf., vol. 28, no. 8, pp. 719–729, 1997.

[32] M. M. Shokrieh, M. Salamat-talab, and M. Heidari-Rarani, “Effect of initial crack length on the measured bridging law of unidirectional E-glass/epoxy double cantilever beam specimens,” Mater. Des., vol. 55, pp. 605–611, 2014.

[33] M. Kenane and M. L. Benzeggagh, “Mixed-mode delamination fracture toughness of unidirectional glass/epoxy composites under fatigue loading,” Compos. Sci. Technol., vol. 57, no. 5, pp. 597–605, 1997.

[34] A. B. De Morais, “A new fibre bridging based analysis of the Double Cantilever Beam (DCB) test,” Compos. Part A Appl. Sci. Manuf., vol. 42, no. 10, pp. 1361–1368, 2011.

[35] K. Saravanakumar, N. Farouk, and V. Arumugam, “Effect of fiber orientation on Mode-

I delamination resistance of glass/epoxy laminates incorporated with milled glass fiber fillers," Eng. Fract. Mech., vol. 199, pp. 61–70, 2018.

[36] J. D. Gunderson, J. F. Brueck, and A. J. Paris, "Alternative test method for interlaminar fracture toughness of composites," Int. J. Fract., vol. 143, no. 3, pp. 273–276, 2007.

[37] E. Triki, B. Zouari, and F. Dammak, "Dependence of the interlaminar fracture toughness of E-Glass/Polyester woven fabric composites laminates on ply orientation," Eng. Fract. Mech., vol. 159, pp. 63–78, 2016.

[38] F. Dharmawan, G. Simpson, I. Herszberg, and S. John, "Mixed mode fracture toughness of GFRP composites," Compos. Struct., vol. 75, no. 1–4, pp. 328–338, 2006.

[39] S. L. Bazhenov, "Interlaminar and intralaminar fracture modes in 0/90 cross-ply glass/epoxy laminate," Composites, vol. 26, no. 2, pp. 125–133, 1995.

[40] B. Krull, J. Patrick, K. Hart, S. White, and N. Sottos, "Automatic Optical Crack Tracking for Double Cantilever Beam Specimens," Exp. Tech., vol. 40, no. 3, pp. 937–945, 2016.

[41] TWI, "Manual Ultrasonic Testing - NDT inspection | TWI," The welding Institute, 2017. [Online]. Available: http://www.twi-global.com/capabilities/integrity-management/non-destructive-testing/ndt-techniques/manual-ultrasonic-testing/. [Accessed: 23-Aug-2016].

[42] S. Gholizadeh, "A review of non-destructive testing methods of composite materials," Procedia Struct. Integr., vol. 1, pp. 50–57, 2016.

[43] ASTM International, "ASTM E2533-09 Standard Guide for Nondestructive Testing of Polymer Matrix Composites Used in Aerospace Applications."

[44] V. Richter-Trummer, E. A. Marques, F. J. P. Chaves, J. M. R. S. Tavares, L. F. M. Da Silva, and P. M. S. T. De Castro, "Analysis of crack growth behavior in a double cantilever beam adhesive fracture test by different digital image processing techniques," Materwiss. Werksttech., vol. 42, no. 5, pp. 452–459, 2011.

[45] F. C. Mayrhofer, F. H. Ooe, E. Gmbh, K. Niel, and S. Gmbh, "Optical Crack Detection of Refractory Bricks," 2006.

[46] A. Mohan and S. Poobal, "Crack detection using image processing: A critical review and analysis," Alexandria Eng. J., vol. 57, no. 2, pp. 787–798, 2018.

[47] J. Corso, “Linear Filters and Image Processing,” College of Engineering - University of Michigan, 2014. [Online]. Available: https://web.eecs.umich.edu/~jjcorso/t/598F14/files/lecture_0924_filtering.pdf. [Accessed: 24-Dec-2018].

[48] A. M. A. Talab, Z. Huang, F. Xi, and L. Haiming, “Detection crack in image using Otsu method and multiple filtering in image processing techniques,” Optik (Stuttg)., vol. 127, no. 3, pp. 1030–1033, 2016.

[49] “Chapter 3 FILTERS,” Image (Rochester, N.Y.). [Online]. Available: http://www.bioss.ac.uk/people/chris/ch3.pdf. [Accessed: 24-Dec-2018].

[50] MATLAB, “What Is Image Filtering in the Spatial Domain? - MATLAB &amp,” MathWorks & Simulink Documentation. [Online]. Available: https://www.mathworks.com/help/images/what-is-image-filtering-in-the-spatial-domain.html. [Accessed: 21-Feb-2018].

[51] H. Elbehiery, A. Hefnawy, M. Elewa, and Aaa, “Surface Defects Detection for Ceramic Tiles Using Image Processing and Morphological Techniques,” Proc. World Acad. Sci. Eng. Technol. Vol 5, vol. 1, no. 5, pp. 1488–1492, 2007.

[52] D. M. Pound, “Finding the Edges (Sobel Operator) - Computerphile - YouTube.” [Online]. Available: https://www.youtube.com/watch?v=uihBwtPIBxM. [Accessed: 23-Feb-2018].

[53] D. Ray, “Edge Detection in Digital Image Processing,” University of Washington: Department of Mathematics, 2013. [Online]. Available: https://sites.math.washington.edu/~morrow/336_13/papers/debosmit.pdf. [Accessed: 24-Dec-2018].

[54] D. M. Pound, “Canny Edge Detector - Computerphile - YouTube.” [Online]. Available: https://www.youtube.com/watch?v=sRFM5IEqR2w. [Accessed: 23-Feb-2018].

[55] “Canny Edge Detection - Walk Through,” 2009. [Online]. Available: http://www.cse.iitd.ernet.in/~pkalra/col783-2017/canny.pdf. [Accessed: 24-Dec-2018].

[56] “OpenCV: Canny Edge Detection.” [Online]. Available: https://docs.opencv.org/3.1.0/da/d22/tutorial_py_canny.html. [Accessed: 24-Sep-2018].

[57] “Products | AMT Composites.” [Online]. Available: https://www.amtcomposites.co.za/products. [Accessed: 30-Dec-2017].

[58] “Spabond 340LV EPOXY ADHESIVE SYSTEM.” [Online]. Available: http://www.amtcomposites.co.za/sites/default/files/media/data-sheets/Spabond 340LV_v14.pdf. [Accessed: 29-Apr-2018].

[59] Gurit, “Prime 20LV Epoxy Infusion System,” 2015. [Online]. Available: https://www.amtcomposites.co.za/sites/default/files/media/data-sheets/PRIME 20LV_v12.pdf. [Accessed: 24-Dec-2018].

[60] “PRIME™ 20LV Resin.” [Online]. Available: www.Gurit.com. [Accessed: 09-Feb-2019].

Appendices

Appendix A **Measurements**

The following are a summary of various measurements used through this project.

Appendix A.1 Manufacturing materials dimensions

Table A-1: Dimensions used for the materials of manufacturing process

Materials	Quantity/Mould	Dimensions(mm)/Mould
200 GSM Plain Weave Fibre Glass	24	580X230
250 GSM Unidirectional Fibre Glass	20	500X230
280 GSM Twill Weave Fibre Glass	18	580X230
Green Flow (UD)	2	500X310
Green Flow (Twill & Plain)	2	580X310
Peel Ply (UD)	2	560X380
Peel Ply (Twill & Plain)	2	640X380
Vacuum Bag	1	1000X750
Tacky Tape	N/A	700X490
Spiral Feed Pipes	2	500
Feed Pipes	2	1500

Appendix A.2 DCB specimen dimensions

Table A-2: Table showing the thickness of specimen of the final DCB measurements

Final DCB Measurements						
Weave Pattern	**Specimen Number**	**Thickness**				
		25mm	**80mm**	**135mm**	**Chosen Thickness (mm)**	**Thickness Average (mm)**
UD	1	3.6	3.6	3.7	3.63	3.65
	2	3.64	3.62	3.62	3.63	
	3	3.6	3.62	3.62	3.61	
	4	3.66	3.7	3.68	3.68	
	5	3.7	3.72	3.7	3.71	
	6	3.7	3.7	3.7	3.70	
Plain	1	4.82	4.82	4.84	4.83	4.74
	2	4.88	4.92	4.9	4.90	
	3	4.54	4.56	4.6	4.57	
	4	4.88	4.9	4.88	4.89	
	5	4.42	4.62	4.58	4.54	
	6	4.9	4.92	4.9	4.91	
Twill	1	4.3	4.3	4.32	4.31	4.31
	2	4.3	4.34	4.32	4.32	
	3	4.32	4.34	4.36	4.34	
	4	4.28	4.3	4.32	4.30	
	5	4.3	4.32	4.32	4.31	
	6	4.3	4.3	4.3	4.30	

Table A-3: Table showing the width of specimen of the final DCB measurements

Final DCB Measurements						
Weave Pattern	**Specimen Number**	**Width**				
		25mm	**80mm**	**135mm**	**Chosen Width (mm)**	**Average Width (mm)**
UD	1	25	25	25	25.00	24.97
	2	25.02	25	25.02	25.01	
	3	25	24.98	25	24.99	
	4	24.94	24.9	24.98	24.94	
	5	24.92	24.9	24.92	24.91	
	6	24.92	24.94	24.96	24.94	
PLAIN	1	24.92	24.92	24.9	24.91	24.90
	2	24.92	24.88	24.9	24.90	
	3	24.74	24.8	24.76	24.77	
	4	24.9	24.92	24.9	24.91	
	5	25	25.1	25	25.03	
	6	24.96	25	24.98	24.98	
Twill	1	25	25.02	25.04	25.02	24.69
	2	25.02	25	24.98	25.00	
	3	24.96	25	24.98	24.98	
	4	24.08	24.06	24.08	24.07	
	5	24.04	24.06	24.06	24.05	
	6	25	25.02	25.02	25.01	

The thickness and widths from Table A-2 and Table A-3 are recorded at 3 different lengths of the specimen using a vernier calliper. The average of these three values are used for the thickness and widths for that specimen. The average of the 6 specimens was also recorded.

Appendix B **Mould lay-up and resin infusion**

Appendix B.1 Preparation before resin infusion

The process of laying up and manufacturing the panels was the same for all three weave patterns, with only the reinforcing fabric being changed.

The materials described in Table 3-2, Figure 3-1 and Figure 3-2 were cut to size with a pair of scissors. The details of the 12 steps of manufacturing lay-up is described in Appendix B.5 and summarised in Appendix B.1through to Appendix B.4.

Before starting the layup, the mould table is thoroughly cleaned and coated with multiple layers of mould release agent (ram wax), to ensure easy removal of the infused panel.

After the waxing process, the sizing of mould is defined using tacky tape as can be seen by the light blue arrow in Figure 3-3. The first layer of the green flow layer is taped down to the table. The first layer of peel ply is then placed over the green flow and taped onto the table. The 12 layers of fibre glass were individually layered over the peel ply. Thereafter, the Teflon insert was placed at the desired location on the fibres. This was followed by another 12 layers of glass fabric and a second peel ply layer. This is taped down to the first peel ply layer and over the glass fibres. The second green flow layer is then added on the peel ply. This is taped down to the first green flow layer. The resin spiral feed pipe is taped down onto the green flow layers and the vacuum spiral feed pipe is taped down onto the peel ply layers. The vacuum and resin feed pipes are attached to their respective spiral pipes. Lastly, the vacuum bag is taped down onto the tacky tape. Care is needed to ensure the bag is correctly sealed to prevent any leaks from occurring when the vacuum is switched on. The vacuum pump is switched on to check for any leaks. Once satisfied that no leaks are present, the vacuum pump is switched off so the preparation for the resin mixture can take place.

Figure B-1 shows the different layers of the infusion process in application:

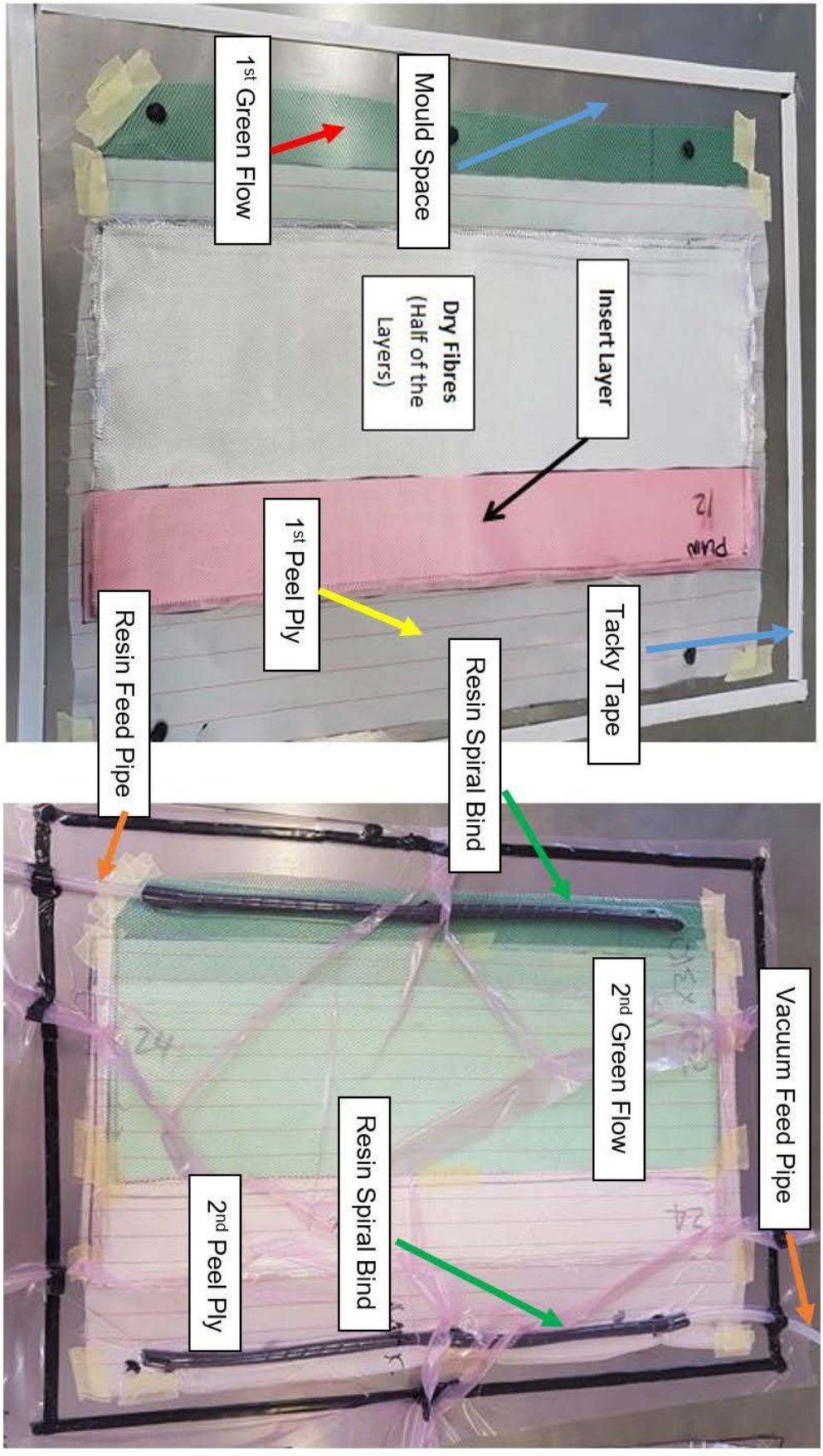

Figure B-1: Materials used in application of infusion process

Appendix B.2 Preparation for mixing the resin with hardener

The Gurit PRIME^{TM} 20LV epoxy resin was mixed with PRIME^{TM} 20 fast hardener, in the ratio of 100:26 by mass [59]. A total mass of resin equal to 1.1 times the mass of dry fibres was prepared for each panel. Once the total amount of resin and hardener for a given panel was established, the amount was divided into smaller quantities. In order to avoid wastage, the quantities were mixed as the need arose.

Appendix B.3 Infusion process

Prior to the start of the mixing process, the vacuum pump is switched on to check for leakage. Once satisfied that there is no leakage, the mixing of the first batch begins. To ensure that the infusion process is complete before the resin gels (pot life), the start of the mixing time is noted. The resin and hardener are manually mixed using a disposable wooden strip for three minutes, regularly scraping the container sides and bottom, to ensure thorough mixing.

Following a successful first batch, the second batch is mixed in a similar way as the first batch. Thereafter, the infusion process begins, and a third batch is prepared if required. The preparation of the third batch is dependent on how the resin flows through the part. If required, more batches of resin/ hardener are added. However, if the part becomes fully infused then no additional batches are required.

To start the infusion process, one inserts the resin feed pipe into the first batch mixture. This will allow the resin mixture to flow into the part. Once the bucket is almost empty, the subsequent batches of resin mixture were poured into the first bucket as required.

During the infusion process, the vacuum bag compressed all the material together. Therefore, the resin mixture flowed in the compressed part by the least spaces available. Once the part is completely infused, the resin feed pipe needs to be clamped off. This will prevent any resin mixture from flowing into the part.

The epoxy-hardener reaction is exothermic and thus heats up as time passes. One needs to be attentive of the resin mixture, to ensure that the mixture does not overheat. If overheating occurs, the resin bucket is placed in a container of water to cool it down.

Once the resin has completely gelled, the part was kept under vacuum for 24 hours. This is to allow for the part to be completely cured and ready for de-moulding. Once the part is de-moulded, the peel ply and green flow are removed.

Note: The gelling time and pot life of the epoxy resin changes depending on the current temperature of the infusion process. These times can be found on the in the PRIME^{TM} 20LV Material Safety Data Sheet (MSDS) [60].

Appendix B.4 Post curing

Once the panels peel ply and green flow layers have been removed, the panels are ready to be post cured. To achieve maximum material properties of the FRP, the parts were post cured at 50℃ in a controlled oven for 16 hours [59].

Appendix B.5 Material Lay-Up for infusion Process

The following is the manufacturing process of one Infusion Process.

Step 1:- Weigh the dry fibres

Figure B-2 shows the mould space on the stainless steel table, bounded using tacky tape

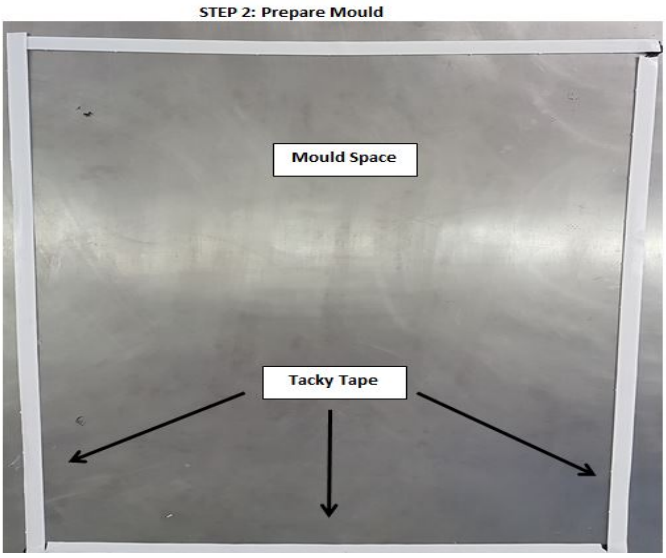

Figure B-2: Area bounded by the tacky tape

The first layer of green flow material, which promotes flow of resin, is then placed on the moulded area, shown in Figure B-3.

STEP 3: Add 1st Layer of Green Flow

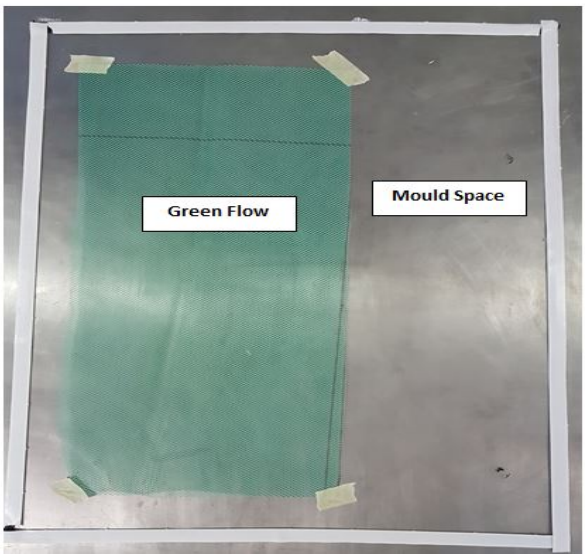

Figure B-3: First layer of green flow

Masking tape was used to attach the green flow to the table.

The first layer of peel ply is then placed onto the layer of green flow and mould area, and secured with masking tape as shown in Figure B-4.

STEP 4: Add 1st Layer of Peel Ply

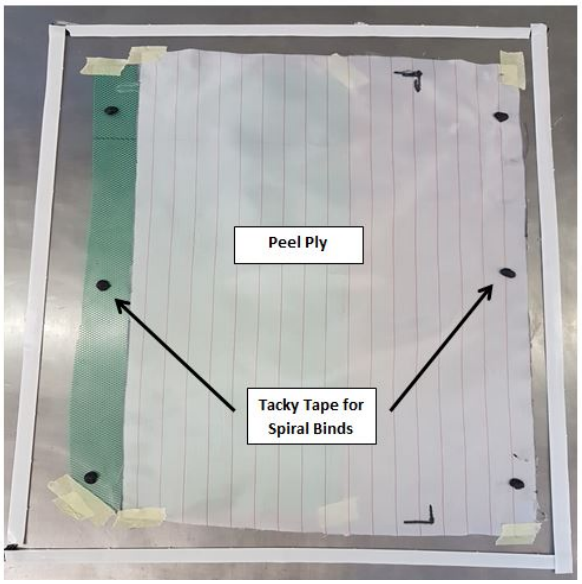

Figure B-4:First layer of peel ply

Masking tape is again used to tie down the peel ply layer. Also visible in Figure B-4 are the tacky tapes for the spiral binds. These are for stability purposes to keep the binds from lifting.

Half of the number of dry fibre plies are placed onto the peel ply layer. The Teflon insert is then placed on one of the corners of the dried fibre stack, as shown in Figure B-5.

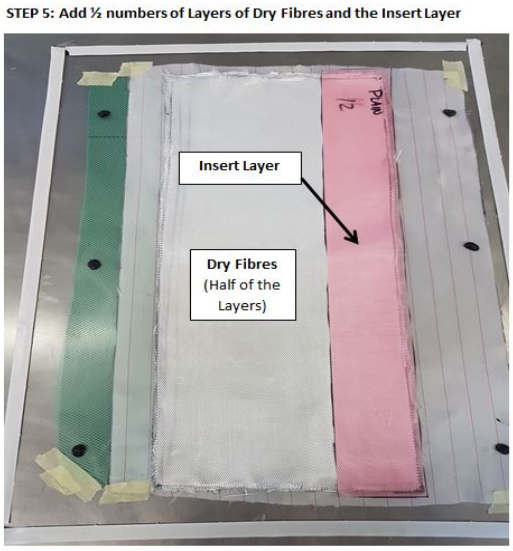

Figure B-5: Inserted teflon

The second half of the dried fibres are then stacked on top of the layers, and covered with the second peel ply layer shown in Figure B-6 and Figure B-7.

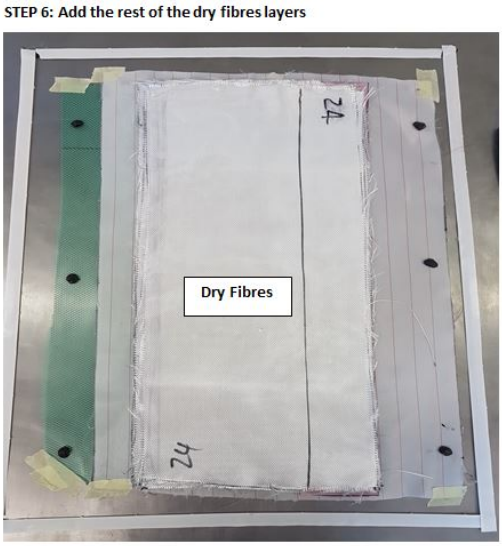

Figure B-6: Dry fibres

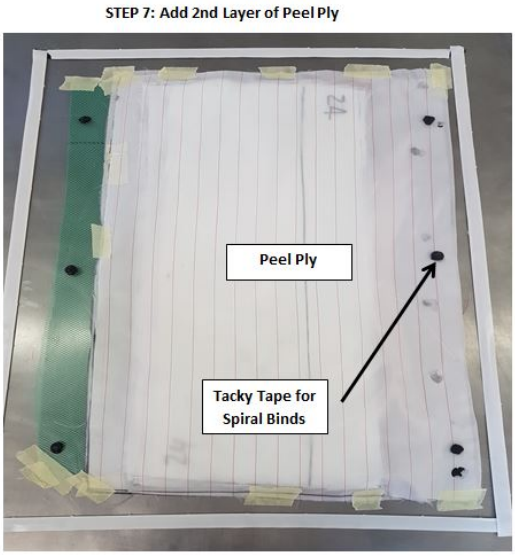

Figure B-7: Second layer of peel ply

Masking tape was again used to tie down the peel ply layer. The tacky tapes for the spiral binds are again visible. These were placed directly on top of the pieces on the first peel ply layer.

The second layer of green flow is then placed onto the peel play layer and secured with masking tape as shown in Figure B-8.

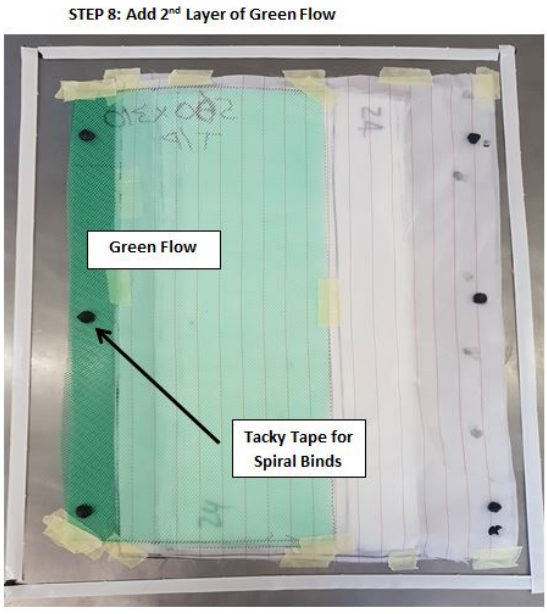

Figure B-8: Second layer of green flow

The spiral binds, which aid even distribution of the resin are then placed onto the tacky tape pieces, as shown in Figure B-9.

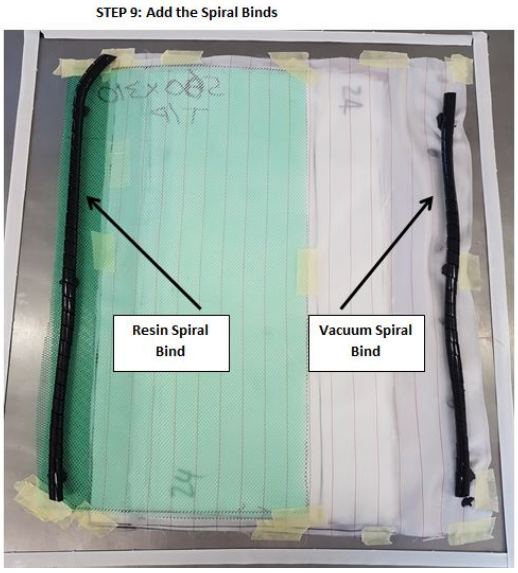

Figure B-9: Spiral binds

The resin and vacuum feed pipes are then inserted into the spiral binds at opposite ends, shown in Figure B-10.

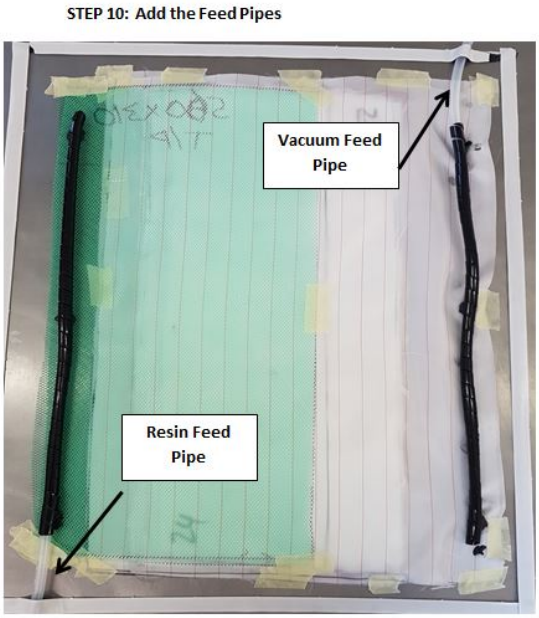

Figure B-10: Feed pipes

The non-stick strips on the tacky tapes are then removed and the vacuum bag is then placed onto the sticky side of the tape. This is done to seal the vacuum bag as can be seen in Figure B-11.

STEP 11: Add Vacuum Bag

Figure B-11: Vacuum Bag

The bag is tested to make sure there are no leaks. The vacuum is drawn and clamped off as can be seen in Figure B-12.

If bag remains tight against the table after 30 minutes, the vacuum bag has a sufficient seal. If the bag loosens, this indicates leaks, which are traced and sealed.

STEP 12: Draw Vacuum from Pump

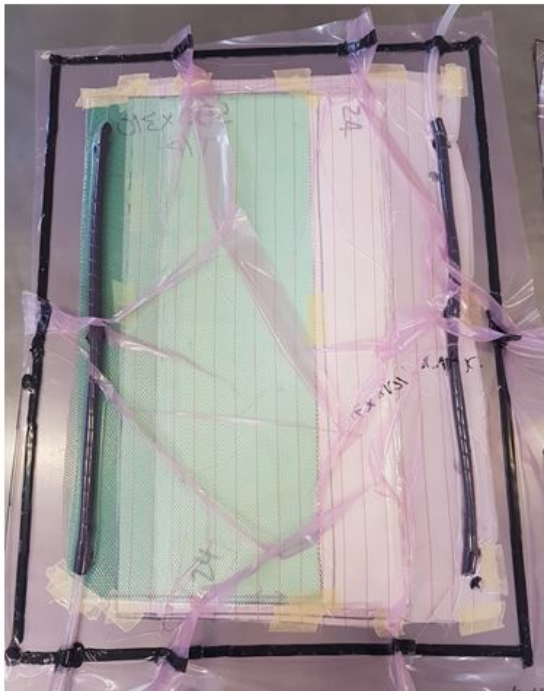

Figure B-12: Draw Vacuum

Appendix C **Assembling the DCB Clamping Jig**

Appendix C.1 First iteration

The assembling of the DCB Clamping Jig can be considered as an assembly three sub-assemblies: The Base sub-assembly, the Tail sub-assembly and the pin sub-assembly

Appendix C.1.1 Base sub-assembly

The Base sub-assembly for one DCB Clamping Jig consists of:

- 1 x Base
- 2 x M5 hexagonal nuts
- 2 x M5 bolts

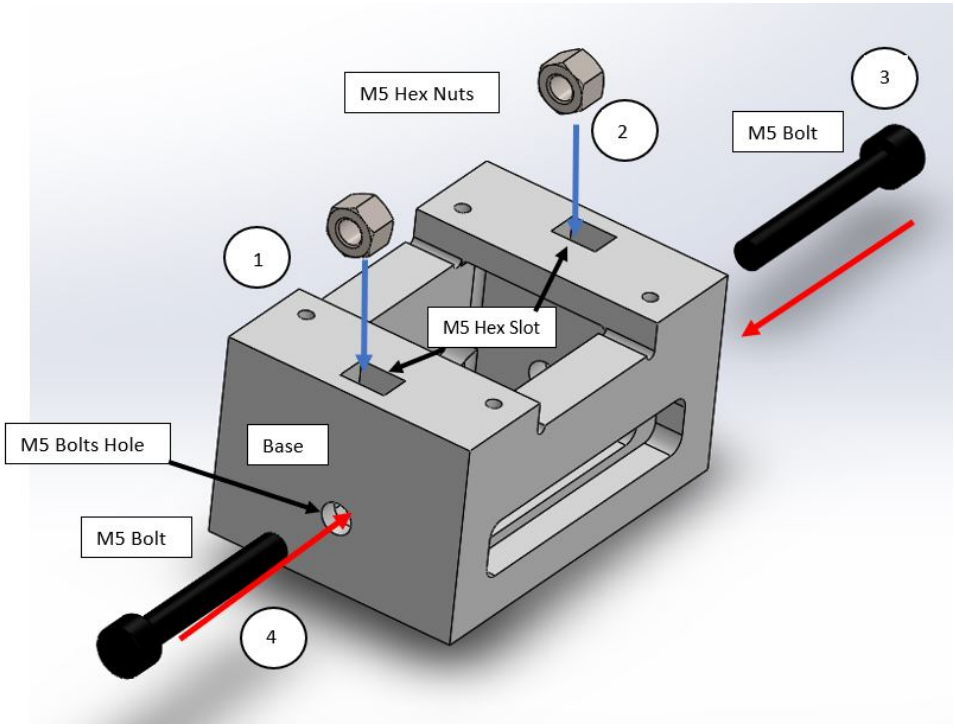

Figure C-1: Assembling of Base sub-assembly

Figure C-1 shows an image of how the Base sub-assembly is assembled. The blue arrows (Number 1 and 2) indicate that the M5 hex nuts are inserted into the seat of the hexagonal slots. The red arrows (Number 3 and 4) indicates the M5 bolts, which are inserted into the M5 bolt holes. It should be noted that the thread of the bolt will be threaded into the M5 hex nut, since the Base component does not contain any thread.

Appendix C.1.2 Tail sub-assembly

The Tail sub-assembly for one DCB Clamping Jig consists of:

- 1 x Tail
- 2 x M5 hexagonal nuts
- 2 x M5 bolts

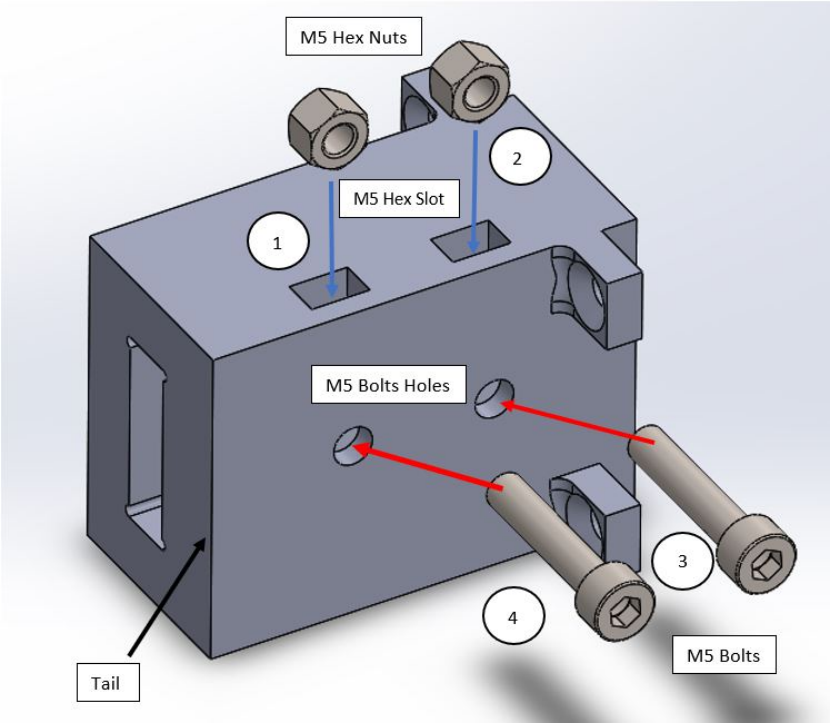

Figure C-2: Assembling of Tail sub-assembly

Figure C-2 shows an image of how the Tail sub-assembly is assembled. It can be seen from the blue arrows (Number 1 and 2) that the M5 hex nuts are to be slotted into the seat of the hexagonal slots. The red arrows (Number 3 and 4) show that the M5 Bolts are to be inserted into the M5 bolt holes. It should be noted that the thread of the bolt will be threaded into the thread on the M5 hex nut since the Tail component does not contain any thread.

Appendix C.1.3 Pin Slider sub-assembly

The Pin Slider sub-assembly for one DCB Clamping Jig consists of:

- 1 x Pin Slider
- 1 x M3 Hexagonal Nuts

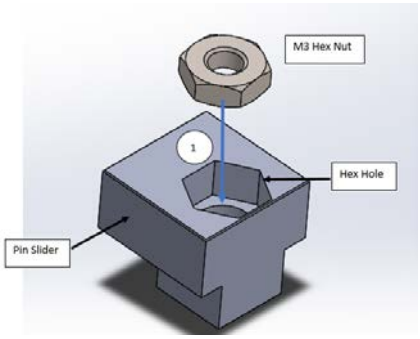

Figure C-3: Assembling of Pin Slider sub-assembly

Figure C-3 shows how the one Pin Slider sub-assembly is assembled. The blue arrow (Number 1) shows how the M3 hex nut needs to be placed to the seat of the hex hole of the Pin Slider. It should be noted that 4 pin slider sub-assemblies are needed for one DCB Clamping Jig.

Appendix C.1.4 DCB Clamping Jig

One Base sub-assembly, one Tail sub-assembly and 4 Pin Slider sub-assembly can be easily assembled to form one DCB Clamping Jig:

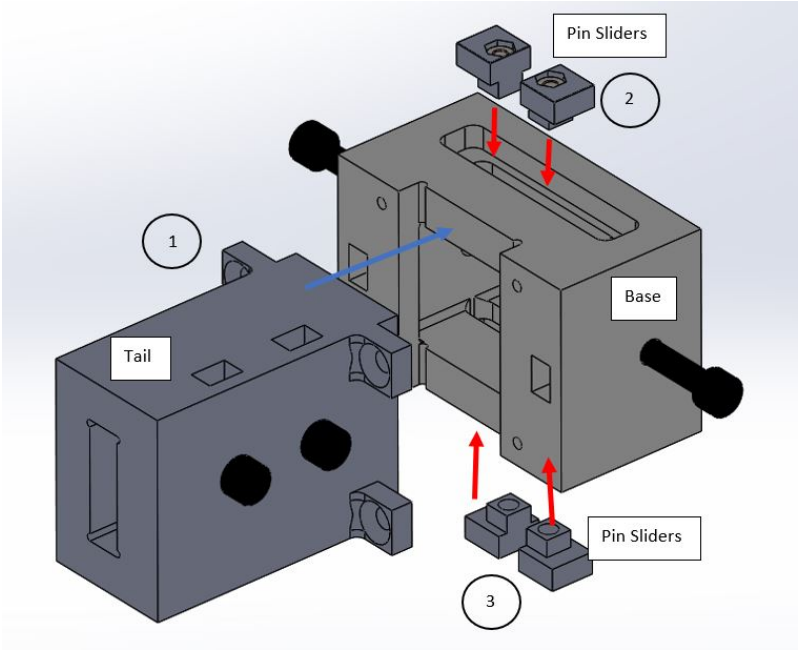

Figure C-4: Assembling of DCB Clamping Jig

Figure C-4 shows an image of how the DCB jig can be assembled. It can be seen from the blue arrow (Number 1) that the Tail component of the Tail sub-assembly is inserted into the Base component of the Base sub-assembly. It should be noted that the screw holes on the Tail are to line up with the pilot holes on the Base. A M4 screw (not shown in figure) is screwed into the holes to join the two components. The Pin Sliders sub-assemblies are inserted into the Pin Slider slots of the Base component as can be seen from the red arrows (Number 2 and 3).

Appendix C.2 Second iteration

The second iteration of the gluing jig was designed to improve the bonding of hinge blocks efficiency.

The design consists of a Base and 2 Pin Sliders. Threaded rods, washers and nuts are used to secure all the components together. Bolts are used to secure the hinge blocks to the specimen.

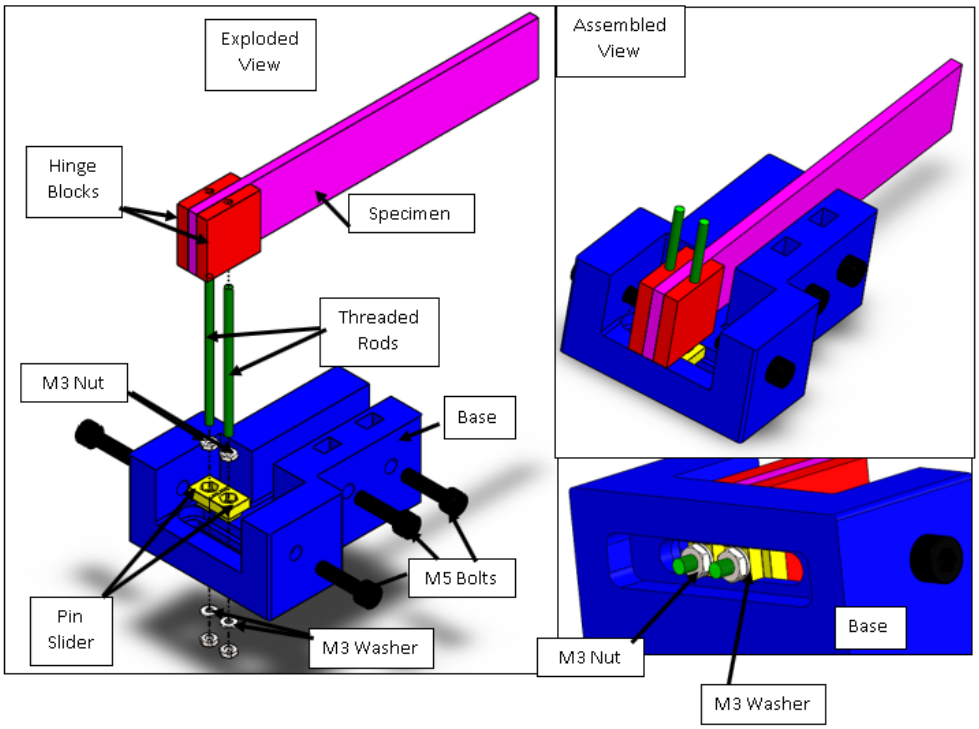

Figure C-5: Second Iteration of DCB Clamping Jig

Figure C-5 shows an exploded and assembled view of the second iteration of the DCB Clamping Jig. The two Pin Sliders with an embedded nut in its seat (as in the case of the First iteration) is inserted into the slot on top of the Base. The threaded rods are threaded through the embedded nut. Washers and nuts are used to secure the threaded rod from sliding out from the bottom of the Base.

Appendix D Gluing of the Hinge Blocks

Appendix D.1 First Design Iteration

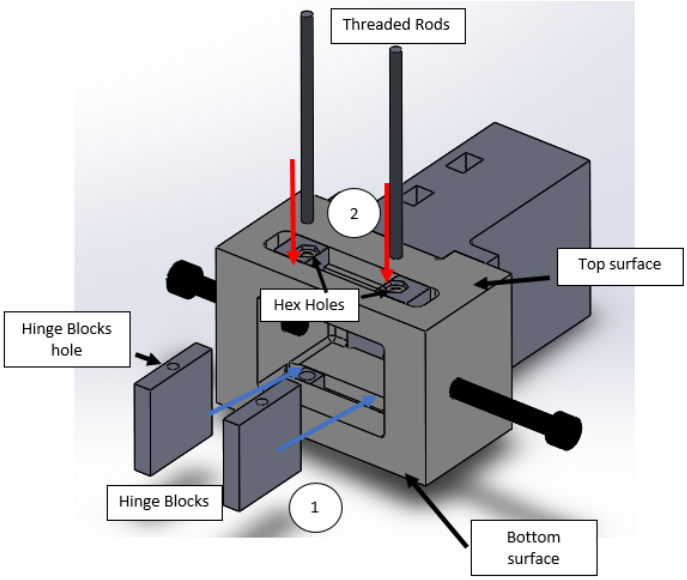

Figure D-1: Hinge Blocks being added to the DCB jigs

Figure D-1 shows an image of how the hinge blocks are being added to the DCB jig. Firstly, the Hinge Blocks are lined up such a way that the Hinge Block hole is aligned with the hex nut hole of the Pin Slider sub-assembly (Indicated by Number 1 and the two blue arrows). The threaded rod is then threaded through the top surface hex hole of the Pin Slider and then through the Hinge Block hole and finally the hex hole of the bottom surface (Indicated by number 2 and the 2 red arrows).

The Figure D-2 shows an image of the completed DCB jig and hinge blocks without the specimen inserted.

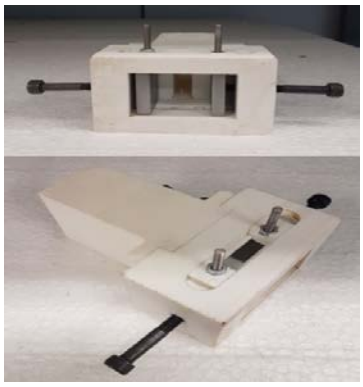

Figure D-2: DCB Clamping Jig with Hinge Blocks

The specimen is then inserted through the specimen slot protruding about 40mm out from the Base component side, exposing the specimen bonding area.

The Spa Bond epoxy resin and hardener are mixed together following the manufactures instructions.

Once the resin/hardener mixture has been mixed, the epoxy mixture was applied to the bonding area and the specimen was placed back in line with hinge blocks. The bolts are used to tighten the hinge blocks and specimen into place. Once completed then to achieve the best mechanical properties for the spa bond adhesive, the DCB jigs are placed in an oven to be cured at $45°$ for approximately one hour [17]

Once the part is cured the specimen is then removed from the DCB jigs.

Appendix D.2 Second design iteration

The gluing of the hinge blocks for the second iteration of the DCB Cluing Jig is done in a similar way as to that of the first design iteration (Refer to Appendix D.1).

The difference being that the design of the Base was that of an open top to allow the specimen and hinge blocks to slide easily into the Base and threaded rods respectively (Refer to Appendix C.2 to see how the second design of the jig was assembled)

Appendix E **CAD of DCB fixtures**

Appendix E.1 DCB Top Hinge Block Holders

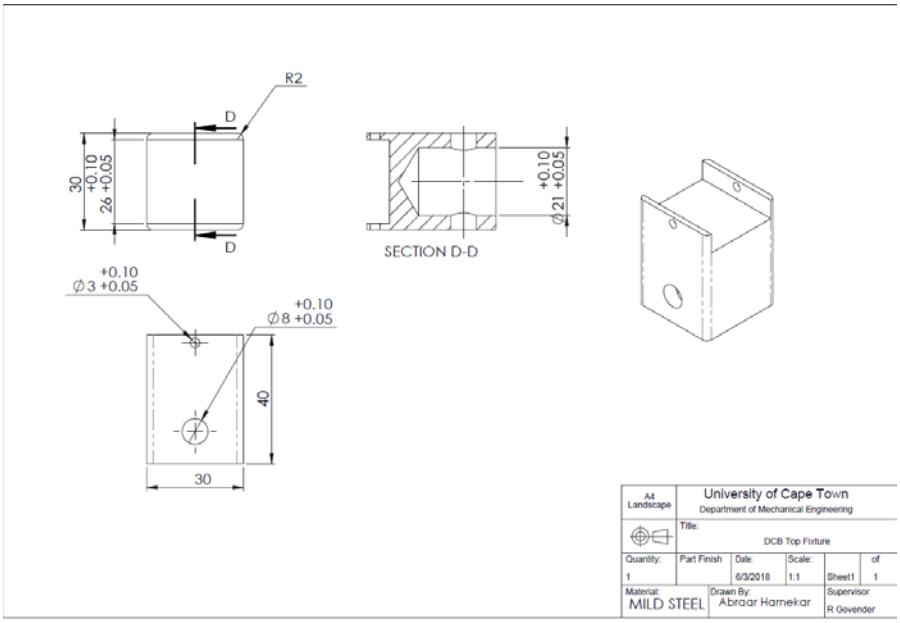

Figure E-1: DCB Top Hinge Block Holder

Appendix E.2 DCB Bottom Hinge Block Holders

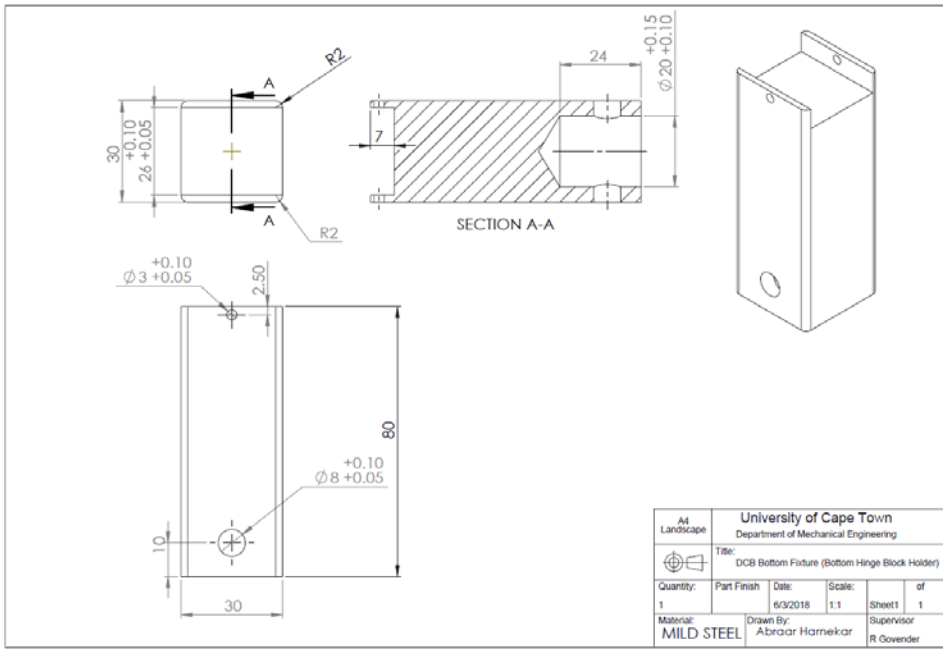

Figure E-2: DCB Bottom Hinge Block Holder

Appendix F **MATLAB script files**

Appendix F.1 Angular Sweeping method

The following is a script file to generate the edge points of the top specimen surface.

```
% Detection Algorithm for Sweeping Method
 % Insert Images
 I= imread('sample image.tiff');           % Read Sample Image
 figure, imshow(I)              % Show Smaple Image
 hold on
 % Obtaining Pixel Intensities
 % Constants
 [x0, y0] = getpts ;            % User Define start point
 lines = 100;                   % Number of Lines
 thetasT = -80*pi/180;          % Sweep Angle for Top surface
 thetasB = -1*thetasT;          % Sweep Angle for Bottom surface
 dtheta = ((1*thetasT)/(lines)); % Change in Angle
 L =300;                        % Length of Line


 % Initialising Vectors
 Vt = zeros(L,1);      % Sizing Top Surface Intensity (x,y pixel co-oordinates)
 Vb = zeros(L,1);      % Sizing Bottom Surface Intensity (x,y pixel co-oordinates)
 V_intt = zeros(L,1);  % Sizing Top Surface Intensity of each line (Pixel Intensity)
 V_intb = zeros(L,1);  % Sizing Bottom Surface Intensity of each line (Pixel Intensity)


 % Loop Between Lines
 %Intensity Top Surfaces
 for i = 0:lines                          % Number of Lines
    theta = thetasT - i*dtheta ;
```

```
    xct = x0 + sqrt((L^2)/((tan(theta))^2+1));  % End x coordinate
    yct = (xct - x0)*tan(theta)+y0;             % End y coordinates
    plot([x0,xct],[y0,yct],'LineWidth',2);     % Plot each line
    [Vxt, Vyt, VIt] = improfile(I,[x0,xct],[y0,yct],L); % Generating x,y and intensity
    Vt = [Vt, Vxt, Vyt];
    V_intt(:,i+1) = VIt; % Pixel Intesity
 end
 Vt = Vt(:, 2:end);       % x and y pixel coo-dinates
% Obtaining Gradient Intensity Values
a = zeros(length(VIt),1);  % Creating Column values as x-axis
for i = 1:length(VIt)
   s = 0;
   a(i)= s+i;
end
GSW = 15;
BFgt = zeros(length(VIt),1);
BFgb = zeros(length(VIt),1);
Least_Best_Fit_Grad = 8;
Best_Fit_Diff = 5;
for i = 1:lines  % Generating gradients of best fit lines (Top Surface)
j = 1;
criteriamet = 0;
while criteriamet < 1 && j < length(VIt)-GSW
t(j,i+1) = j;
BFt = polyfit(a(j:j+GSW-1),V_intt(j:j+GSW-1,i+1),1);
BFgt(j+1,i+1)=BFt(1,1);
   if  j >10
```

```
        GC_Previous = BFgt(j-5,i+1);

        GC  = BFgt(j+1,i+1);

        if GC > GC_Previous && GC > Least_Best_Fit_Grad && (GC-GC_Previous)>
Best_Fit_Diff

            criteriamet =0;

        end

        if  GC < GC_Previous  && GC < Least_Best_Fit_Grad  && (GC-GC_Previous)< -
Best_Fit_Diff

            criteriamet =1;

        end

    end

    j = j+1;

end

end
%% Plotting Correct Intensity Point

% Top Surfaces

xyt = [0,0];

maxgrad = 25;

mingrad = 0;

maxVI = 250;

minVI = 60;


for i = 1:lines

 xyppost = find(((BFgt(:,i)>mingrad) & (BFgt(:,i)<maxgrad) & V_intt(1:end,i)>minVI)&
(V_intt(1:end,i)<maxVI));

if ~isempty(xyppost)

    xynowt =  [Vt(xyppost(1), (2*i-1)),Vt(xyppost(1), (2*i))];

    xyt = [xyt; xynowt];
```

```
end
end
figure,imshow(I)
hold on
plot(xyt(:,1),xyt(:,2),'*')
plot(xyb(:,1),xyb(:,2),'*')
plot(x0, y0, 's')

 % Polynomial Curve Fitting
    p1 = polyfit(xyt(2:end,1),xyt(2:end,2),3);
    yfit1 = polyval(p1,xyt(2:end,1));
    hold on
    b1 = plot(xyt(2:end,1),yfit1,'b-');

    p2 = polyfit(xyb(2:end,1),xyb(2:end,2),3);
    yfit2 = polyval(p2,xyb(2:end,1));
    hold on
    b2 = plot(xyb(2:end,1),yfit2,'r-');
 % Intersection of Curve
 ypic= 0:1:1000;
c = p1 - p2;
roots = roots(c);
x = roots(:,1);
figure,imshow(I);
hold on
plot(x*ones(size(ypic)), ypic, 'LineWidth', 2);
 CrackTip = x
```

The bottom surface edge points can be found in a similar way as the top surface edge points.

Appendix F.2 Vertical Line method

The following is a script file to generate the edge points of the top specimen surface for the vertical line method.

```
%Detection Algorithm for Vertical Line Method

% Insert Images

Ic= imread('t.tiff');

figure,imshow(Ic);

hold on

[x0, y0] = getpts ;                    % User Define start point

[x1, y1] = getpts ;                    % User Define end point

[cx,cy] = getpts;

lines = 250;                           % Number of Lines

dlines = (x1 - x0)/lines;              % Distance Between Lines

L = 200;                               % Length of Lines


Vt = zeros(L,1);               % Sizing Top Surface Intenisty (x,y pixel co-ordinates)

Vb = zeros(L,1);               % Sizing Bottom Surface Intenisty (x,y pixel co-ordinates)

V_intt = zeros(L,1);           % Sizing Top Surface Intenisty Values of Each Line (Pixel
Intensity)

V_intb = zeros(L,1);       % Sizing Top Surface Intenisty Values of Each Line (Pixel Intensity)


%% Loop Between Lines

%Intensity Top Surfaces

for i = 0:lines

xi = x0 + i*dlines;

 %plot([xi,xi],[y0,y0+L],'LineWidth',2);

[Vxt, Vyt, VIt] = improfile(Ic,[xi, xi],[y0+L, y0],L);
```

```
Vt = [Vt, Vxt, Vyt];

V_intt(:,i+1) = VIt;

end

Vt = Vt(:, 2:end); % x and y pixel co-ordinates
```

The script file for the Vertical Line detection method for the rest of the code is similar to the Angular Sweeping method algorithm as in Appendix F.1

Appendix F.3 Crossing Point method

The following is a script file to generate the edge points of the top specimen surface of the Crossing Point algorithm.

```
%% Load Images & Constants

% Crossing Point Detection Algorithm

I = imread('3.tiff');

figure,imshow(I)

hold on

[xs,ys]=getpts;

[xe,ye]=getpts;

nLines = 300

dx = (xe-xs)/nLines;

Pixel_Add = 5;

V_intt = zeros(round((ye+ys)/2+Pixel_Add),1);

Vt = zeros(round((ye+ys)/2)+Pixel_Add,1);

V_intb = zeros(round((ye+ys)/2+Pixel_Add),1);

Vb = zeros(round((ye+ys)/2+Pixel_Add),1);


for i = 1:nLines

    xi = xs + i*dx;
```

```
    plot([xi,xi],[ys, (ye+ys)/2+Pixel_Add],'LineWidth',2);
    plot([xi,xi],[ye, (ye+ys)/2-Pixel_Add],'LineWidth',2);
    [Vxt, Vyt, VIt] = improfile(I,[xi, xi],[ys, (ye+ys)/2+Pixel_Add],round((ye+ys)/2+Pixel_Add));
    Vt = [Vt, Vxt, Vyt];
    V_intt(:,i) = VIt;

    [Vxb, Vyb, VIb] = improfile(I,[xi, xi],[ye, (ye+ys)/2-Pixel_Add],round((ye+ys)/2+Pixel_Add));
    Vb = [Vb, Vxb, Vyb];
    V_intb(:,i) = VIb;
end
Vt = Vt(:, 2:end);
Vb = Vb(:, 2:end);
AveVIdifft = diff(V_intt);
AveVIdiffb = diff(V_intb);
figure,plot(AveVIdifft(:,4));
figure,plot(AveVIdiffb(:,4));
edgepos = zeros(2,nLines);
edgeneg = zeros(2,nLines);
xyt = [0,0];
xy2 = [0,0];
xyb = [0,0];
xy4 = [0,0];

StartJ = 2;
V_intDifft = 20;
V_intDiffb = 20;
JLookBack = 1;
for i = 1:nLines
```

```
n = 1;
c = 1;
for j = 1:length(V_intt(:,i))
    if j > StartJ
        if V_intt(j,i)-V_intt(j-JLookBack,i)< - V_intDifft
            edgepos(n,i) = V_intt(j,i);
            if n == 1
            xynowt =  [Vt(j, (2*i-1)),Vt(j, (2*i))];
            end
        end
        if V_intb(j,i)-V_intb(j-JLookBack,i)< - V_intDiffb
            edgeneg(c,i) = V_intb(j,i);
            if c ==1
            xynowb =  [Vb(j, (2*i-1)),Vb(j, (2*i))];
            end
        end
    end
end
 xyt = [xyt; xynowt];  % xy position of Top outer surface edge
 xyb = [xyb; xynowb];  % xy position of Top inner surface edge
end
```

The script file for the Crossing Point's detection method for the rest of the code is similar to the Sweeping method algorithm as in Appendix F.1

Appendix G Assembling of Ultrasound Wedge Device

Assembling of the Ultrasound Wedge Device consists of components being assembled along with two sub-assemblies namely:

- Wedge Base sub-assembly
- Specimen Holder sub-assembly

Appendix G.1 Wedge Base sub-assembly

The Wedge Base sub-assembly consists of a M10 by 70mm threaded rod, 1 M10 Plastic nut and the Wedge Base. Figure G-1 shows how the Wedge Base sub-assembly is assembled.

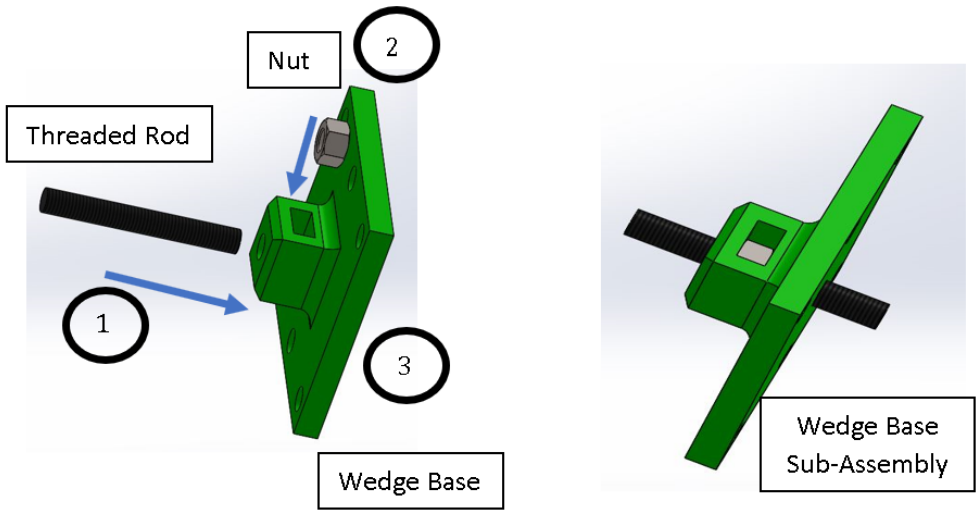

Figure G-1: Wedge Base sub-assembly

The hex nut (item 2) is embedded into the slot of the Wedge Base (item 3). The threaded rod (item 1) then threaded through the embedded nut.

Appendix G.2 Specimen Holder sub-assembly

The Specimen Holder sub-assembly consists of two plastic hex nuts, two plastic hex bolts and the Specimen Holder. Figure G-2 shows how the Specimen Holder sub-assembly is assembled. The hex nut is embedded into the Specimen Holder. The bolts are then threaded through the embedded nut.

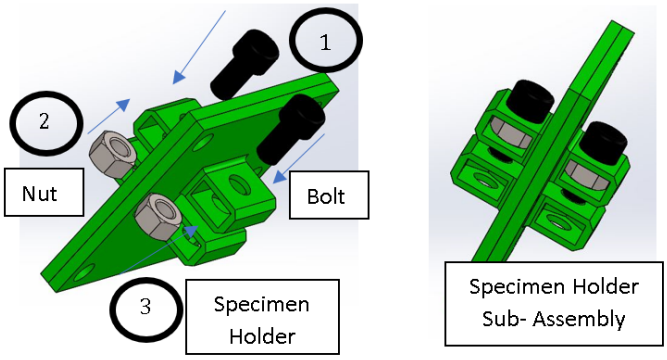

Figure G-2: Specimen Holder sub-assembly

To begin the assembling of the Wedge device, the Specimen Holder sub-assembly needs to be located. This done by placing a M10 nut (item 4) at each of the end of 4 M10 threaded rods (item 1) on either side of the Specimen Holder sub-assembly (item 2). A specimen (item 3) is then clamped onto the Specimen Holder via the two bolts. Figure G-3 shows how the specimen and its holder is clamped onto the threaded rod.

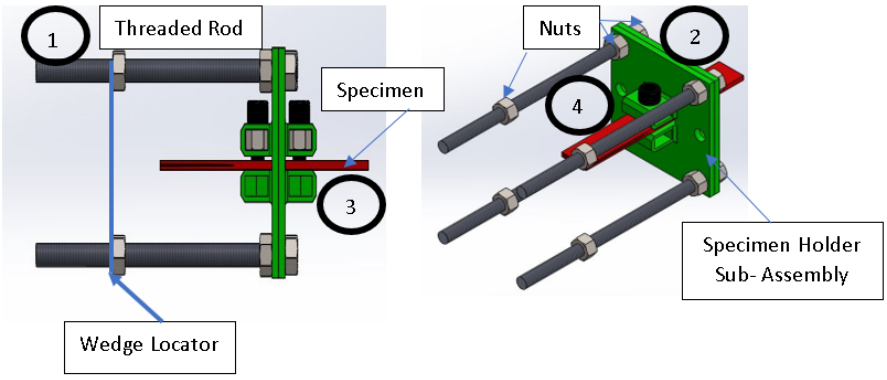

Figure G-3: Specimen Holder sub-assembly location

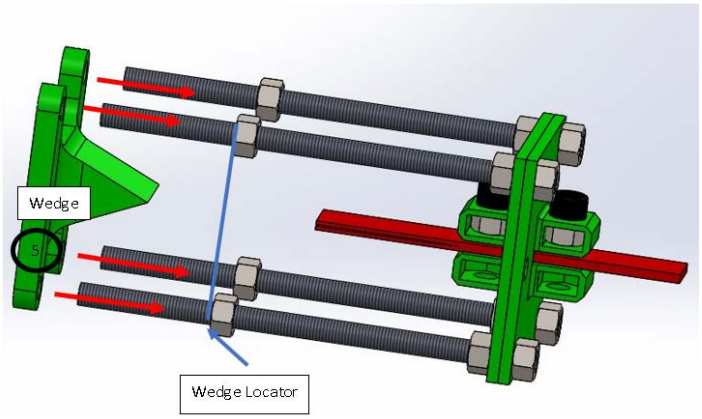

Figure G-4: Wedge location

Figure G-3 and Figure G-4 shows the Wedge locator as 4 additional M10 hex nuts. The Wedge component is then slide along the rods against the Wedge locating nuts.

An additional 4 M10 hex nuts are used as the Wedge locator 2 as seen in Figure G-5, to fully locate the Wedge (item 5) onto the rod (indicated by the red arrow). Four extra nuts are again used to locate the Wedge Base component (blue arrow). Figure G-5 shows how the wedge Base device (item 6) is assembled and located. The threaded rod is inserted into the slot of the Wedge (yellow arrow).

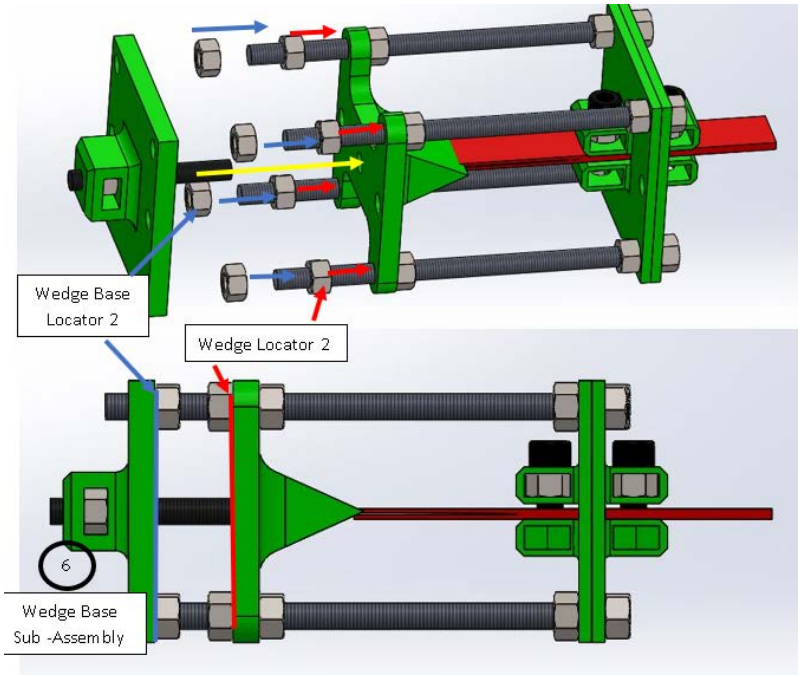

Figure G-5: Location of Wedge Base sub-assembly

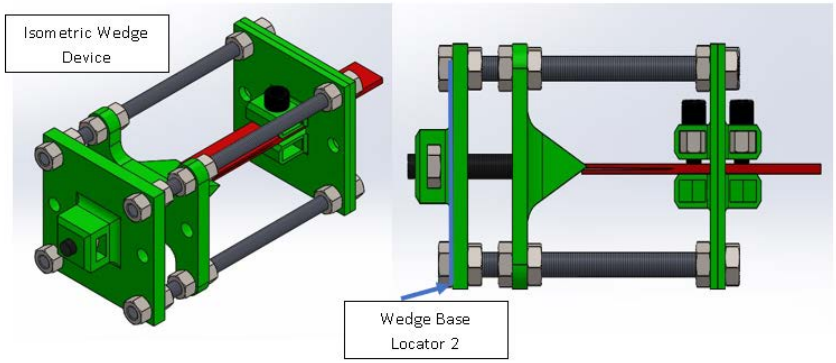

Figure G-6: Isometric view of Wedge device

Figure G-6 shows how the completed assembled Wedge device.

Appendix H Assembling of Test fixtures and specimen onto Zwick DCB machine

The following is the assembly instruction for the Zwick to conduct a DCB test. Assembling of the Zwick machine consists of:

- Load cell
- 12 x M16X2 bolts
- 2 x 8mm pin
- 2 x 3mm pin
- 2 Hinge Block Holders
- Specimen with two Hinge Blocks attached.

Figure H-1 how the load cell (item 2) is attached to the top (cross-head) of the Zwick machine (item 3). The load cell has a capacity of 10kN and is assembled using 6 M16 bolts (item 1).

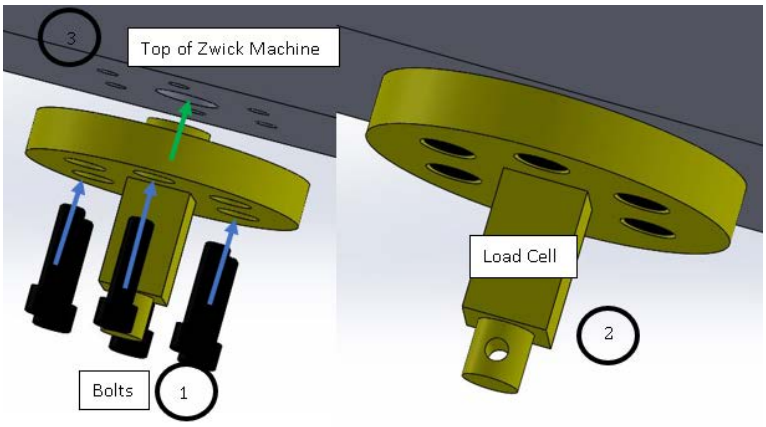

Figure H-1: Load cell assembling

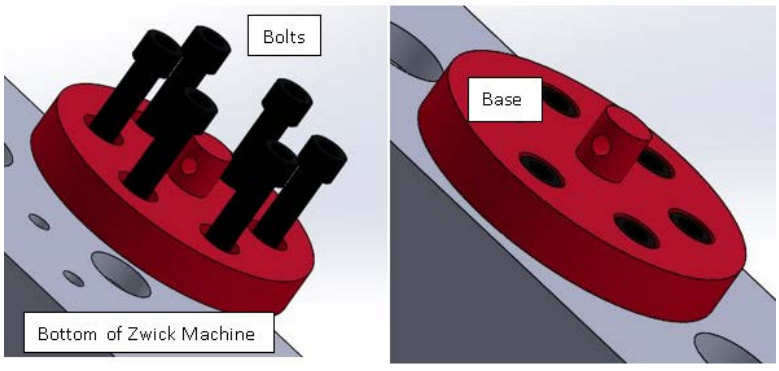

Figure H-2: Base assembling

Figure H-2 shows how the Base is assembled to the bottom of the Zwick machine. The Base is assembled in a similar manner to the load cell.

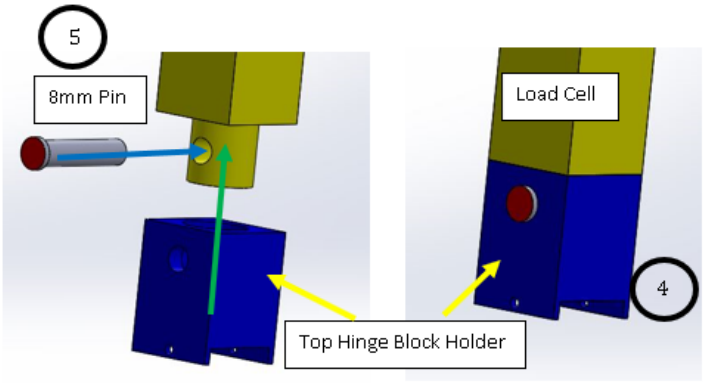

Figure H-3: Assembling of the Top Hinge Block

The Top Hinge Block Holder (item 4) is attached to the load cell using an 8mm pin (item 5) as seen in Figure H-3 and the Bottom Hinge Block Holder is attached to the Base using another 8mm pin as can be seen in Figure H-4

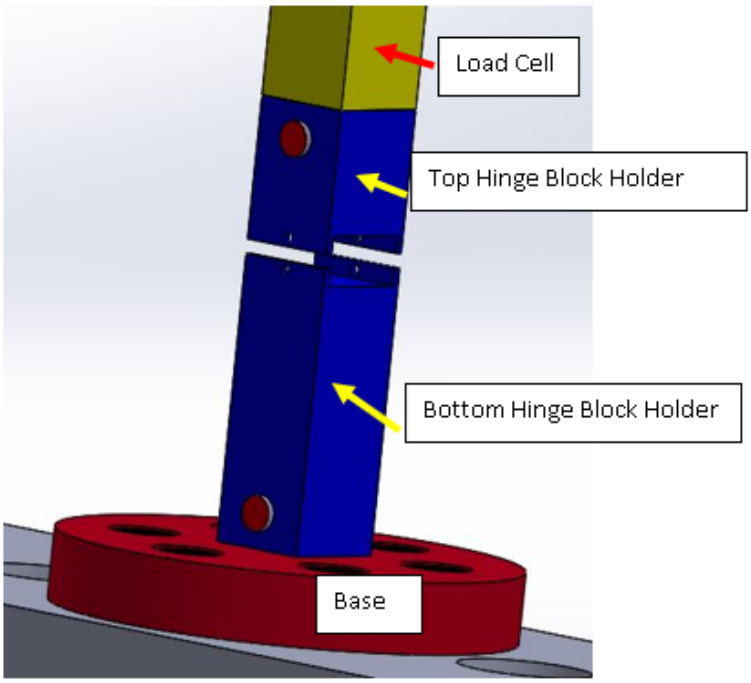

Figure H-4: Assembling of the Bottom Hinge Block

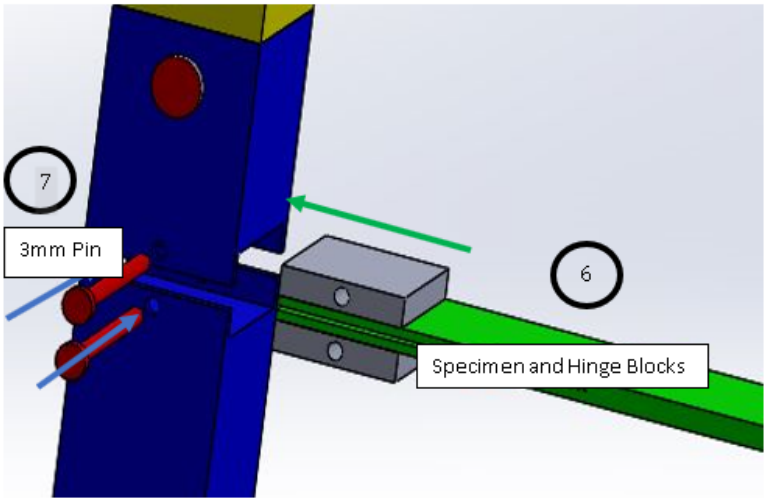

Figure H-5: Assembling of specimen

The specimen with the bonded hinge blocks (item 6) is then slide into the slots of the hinge blocks Holders. The specimen is assembled using two 3mm pin, one each for the Top and Bottom Hinge block Holders as can be seen Figure H-5

Figure H-6 shows the how the DCB set up is assembled on the Zwick machine.

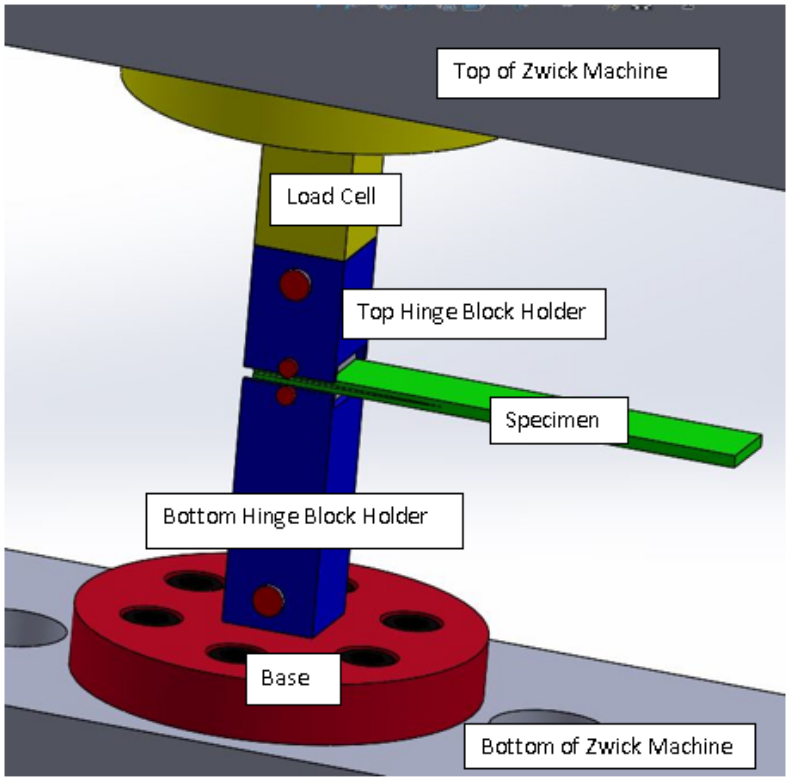

Figure H-6: Assembling of DCB test fixtures on Zwick

Appendix I **Ultrasound Wedge device results**

The data for all Ultrasound Wedge device are presented in this appendix.

Appendix I.1 Graph of thickness vs crack length

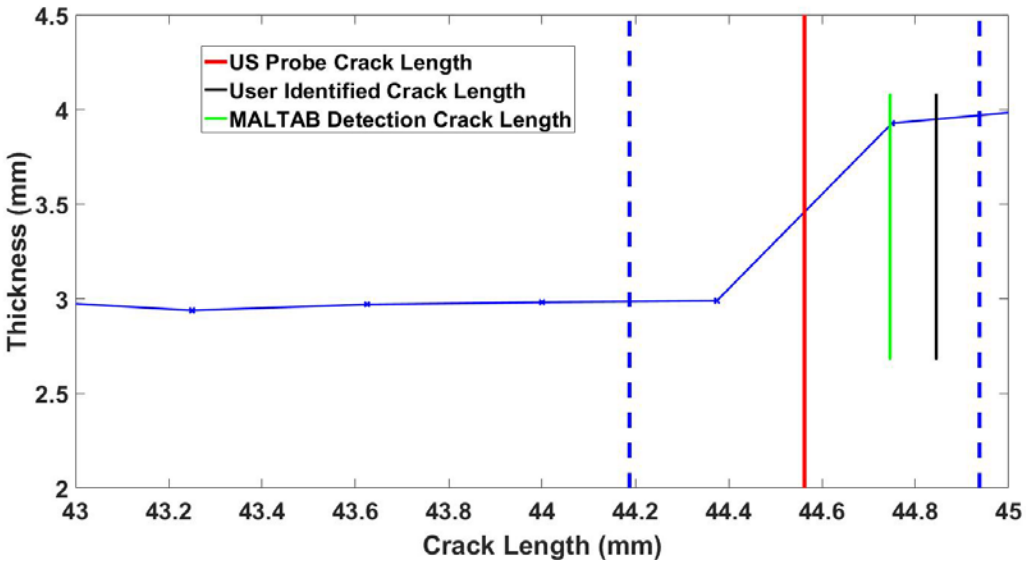

Figure I-1: Thickness vs crack length of experiment 2

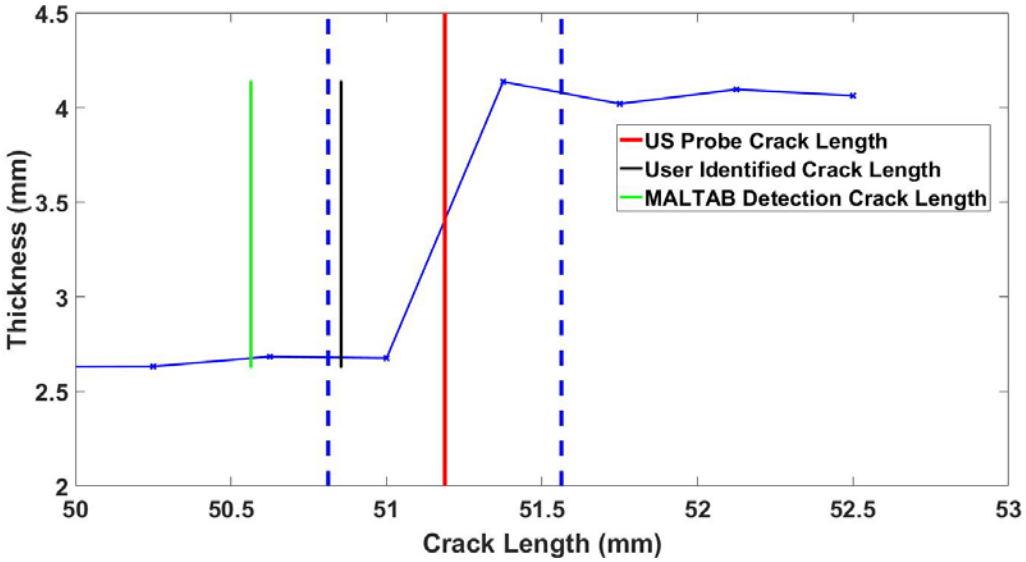

Figure I-2: Thickness vs crack length of experiment 3

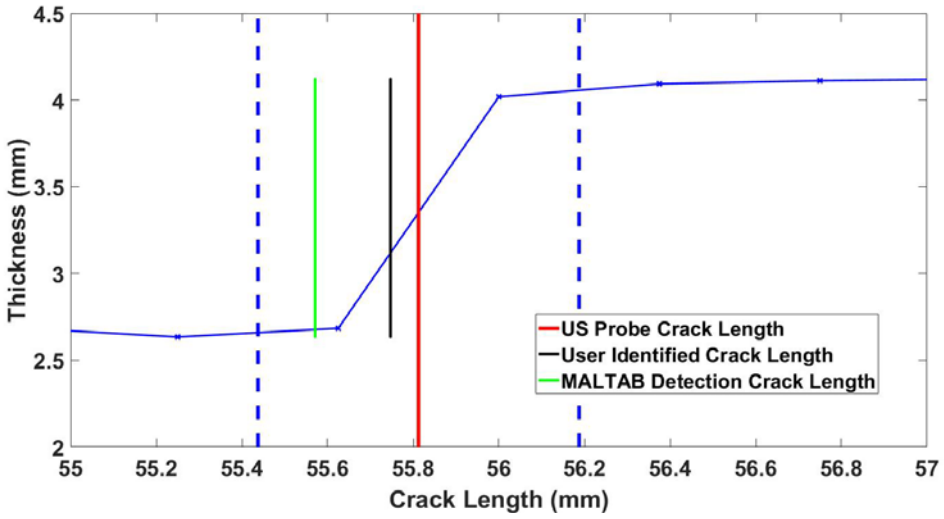

Figure I-3: Thickness vs crack length of experiment 4

Appendix I.2 Tables of thickness vs crack length

The following Table I-1 to Table I-4 are a summary of the thickness recorded from the Thickness Tester for experiment 1 through 4.

Table I-1: Crack length vs thickness of experiment 1

Experiment 1	
crack length (mm)	**Thickness (mm)**
29.500	2.682
29.875	2.709
30.250	2.699
30.625	2.772
31.000	2.792
31.375	2.759
31.750	2.749
32.125	2.720
32.500	**2.763**
32.875	**3.787**
33.250	3.799
33.625	3.769
34.000	3.767
US Probe crack length (mm)	**32.688**
US crack length Range (mm)	**0.375**

Table I-2: Crack length vs thickness of experiment 2

Experiment 2	
crack lengths (mm)	**Thickness (mm)**
39.500	2.869
39.875	2.873
40.250	2.912
40.625	2.776
41.000	2.782
41.375	2.683
41.750	2.977
42.125	2.957
42.500	2.932
42.875	2.992
43.250	2.938
43.625	2.970
44.000	2.982
44.375	**2.99**
44.750	**3.927**
45.125	4.012
45.500	4.083
US Probe crack length (mm)	**44.5625**
US crack length Range (mm)	**0.375**

Table I-3: Crack length vs thickness of experiment 3

Experiment 3	
crack lengths (mm)	**Thickness (mm)**
49.500	2.867
49.875	2.630
50.250	2.632
50.625	2.683
51.000	**2.675**
51.375	**4.136**
51.750	4.019
52.125	4.095
52.500	4.062
US Probe crack length (mm)	**51.1875**
US crack length Range (mm)	**0.375**

Table I-4: Crack length vs thickness of experiment 4

crack lengths (mm)	Thickness (mm)
54.500	2.645
54.875	2.687
55.250	2.634
55.625	**2.684**
56.000	**4.018**
56.375	4.092
56.750	4.110
57.125	4.120
57.500	4.086
US Probe crack length (mm)	**55.8125**
US crack length Range (mm)	**0.375**

Appendix J **DCB test results**

Appendix J.1 Force and crack length summaries

The following tables are raw data obtained for the force at initiation and maximum force as well as the crack length at initiation and crack length at maximum force. The red highlighted values are the outliers.

Table J-1: Summary of force of UD weave pattern

Force (N)				
UD	**Force at Initiation**	**Average**	**Maximum force**	**Average**
1	35.81	36.53	40.45	41.98
2	50.25		50.62	
3	35.54		37.69	
4	40.93		49.7	
5	34.26		41.22	
6	36.13		40.86	

Table J-2: Summary of force of Twill weave pattern

Force (N)				
Twill	**Force at Initiation**	**Average**	**Maximum force**	**Average**
1	37.17	37.31	84.47	60.79
2	35.64		57.31	
3	36.89		61.98	
4	34.84		56.45	
5	37.3		62.8	
6	41.86		65.4	

Table J-3: Summary of force of Plain weave pattern

Force (N)				
Plain	**Force at Initiation**	**Average**	**maximum force**	**Average**
1	31.66	36.01	52.19	50.12
2	41.05		59.38	
3	38.02		50.08	
4	33.3		47.2	
5	36.08		38.31	
6	35.92		53.55	

Table J-4: Summary of crack length of UD weave pattern

Crack length (mm)				
UD	**Crack length at Initiation**	**Average**	**Crack length maximum force**	**Average**
1	51.27	50.76	51.66	53.73
2	51.34		59.26	
3	50.21		50.22	
4	50.25		54.84	
5	51.47		57.19	
6	50.58		54.72	

Table J-5: Summary of crack length of Twill weave pattern

Crack length (mm)				
Twill	**Crack length at Initiation**	**Average**	**Crack length maximum force (mm)**	**Average (mm)**
1	50.4	49.65	56.33	52.92
2	49.66		51.61	
3	49.74		54.17	
4	49.72		51.96	
5	49.56		53.88	
6	49.56		52.98	

Table J-6: Summary of crack length of Plain weave pattern

Crack length (mm)				
Plain	**crack length at Initiation (mm)**	**Average (mm)**	**crack length maximum force (mm)**	**Average (mm)**
1	50.01	49.80	53.4	53.52
2	50.01		59.73	
3	49.54		50.26	
4	50.1		52.06	
5	49.63		51.43	
6	49.5		54.23	

Appendix J.2 Fracture toughness summaries

It should be noted that specimens that are highlighted in red was omitted due to them being outliers

Table J-7: Summary of Mode I fracture toughness of UD weave pattern

Mode I fracture toughness $(\mathbf{J.m^{-2}})$				
UD	**G_I at Initiation**	**Average**	**G_I at maximum force**	**Average**
1	254.97	259.18	394.88	436.88
2	358.48		343.54	
3	261		323.99	
4	308.95		662.02	
5	221.76		428.19	
6	249.22		375.34	

Table J-8: Summary of Mode I fracture toughness of Twill weave pattern

Mode I fracture toughness $(\mathbf{J.m^{-2}})$				
Twill	**G_I at Initiation**	**Average**	**G_I at maximum force**	**Average**
1	315.6	306.21	1650.83	868.52
2	302.71		824.6	
3	312.81		915.81	
4	279.29		866.35	
5	301.22		878.83	
6	335.02		857	

Table J-9: Summary of Mode I fracture toughness of Plain weave pattern

Mode I fracture toughness $(\mathbf{J.m^{-2}})$				
Plain	**G_I at Initiation**	**Average**	**G_I at maximum force**	**Average**
1	247.76	289.92	681.89	724.09
2	371.41		1278.99	
3	309.77		581	
4	189.58		565.05	
5	303.23		464.74	
6	317.79		772.89	

Appendix K **Graphs from results sections**

Appendix K.1 Force and crack length vs time

The following figures show the graphs of force and crack lengths of the UD, Twill and Plain weave.

Appendix K.1.1 UD weave pattern

Figure K-1 through Figure K-5 show the graphs of the force and crack vs time of UD 2 through UD 6 specimens.

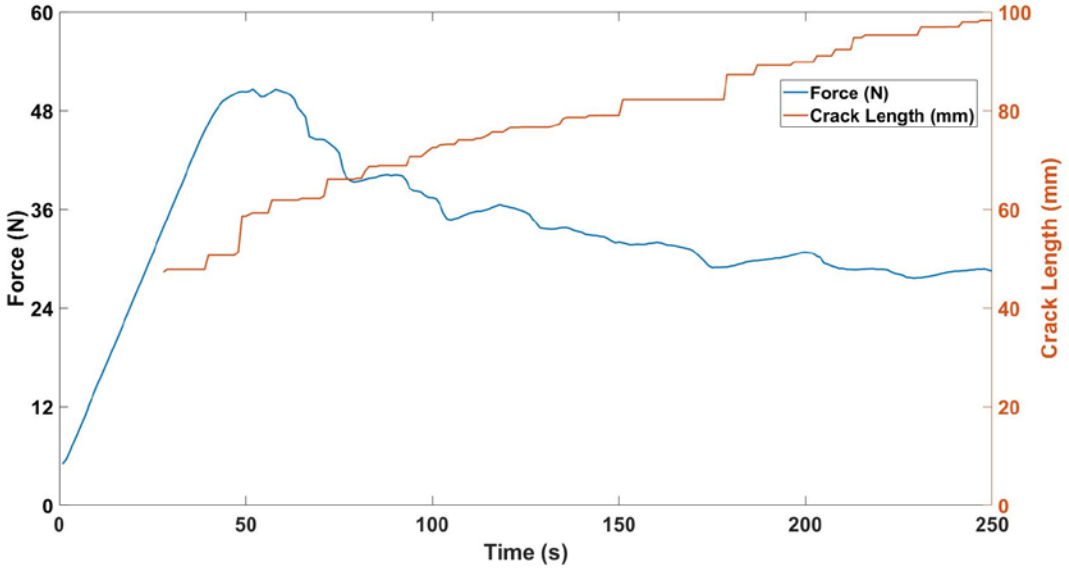

Figure K-1: Graph of force and crack length vs time of UD 2

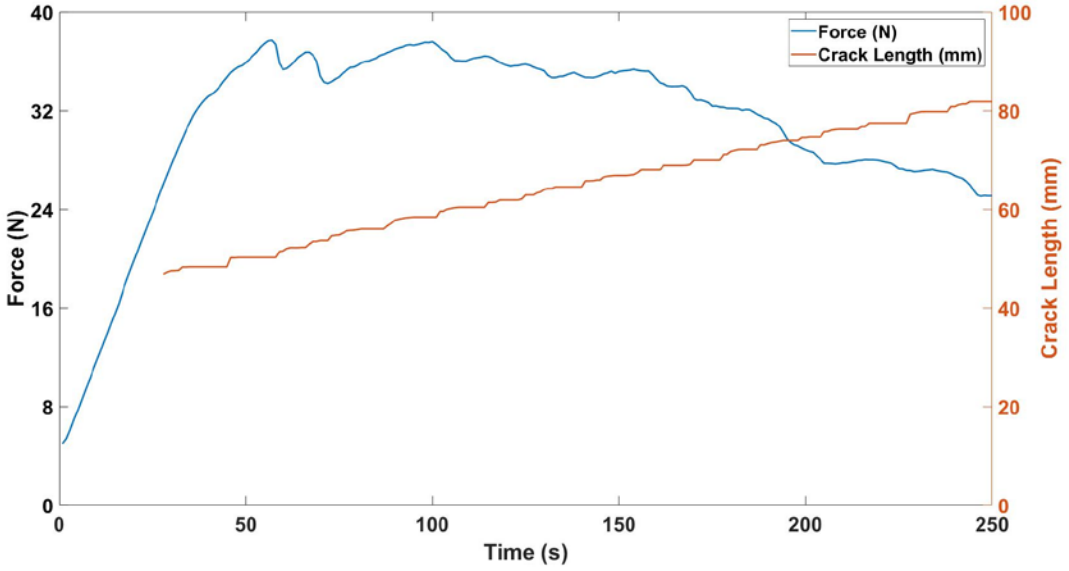

Figure K-2: Graph of force and crack length vs time of UD 3

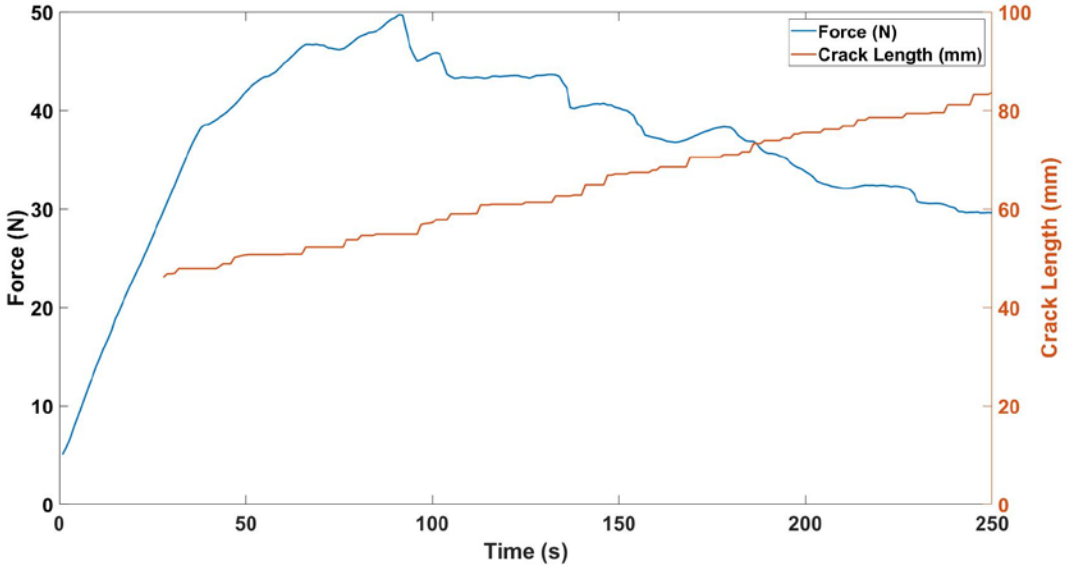

Figure K-3: Graph of force and crack length vs time of UD 4

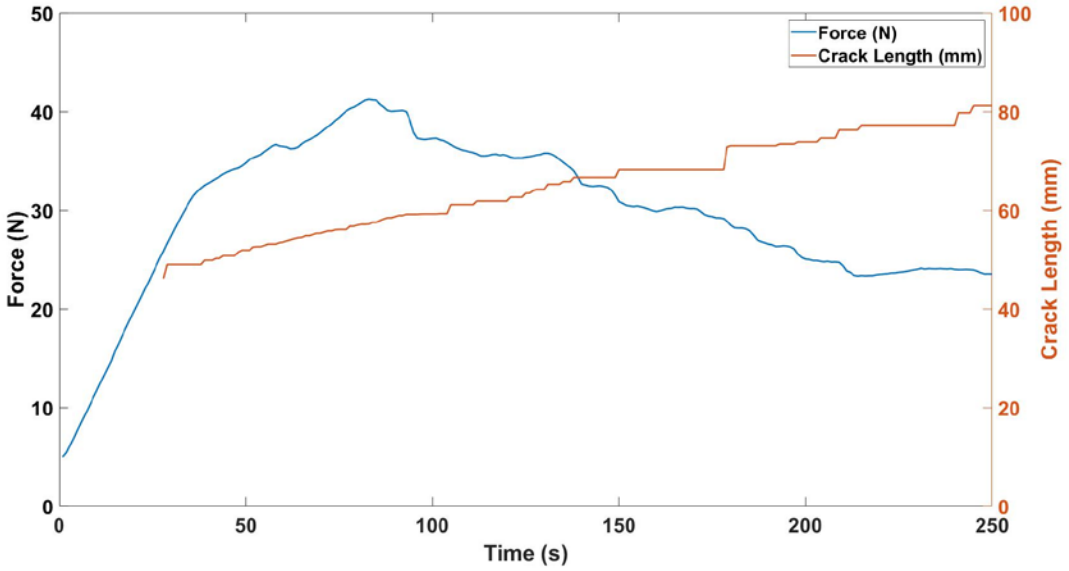

Figure K-4: Graph of force and crack length vs time of UD 5

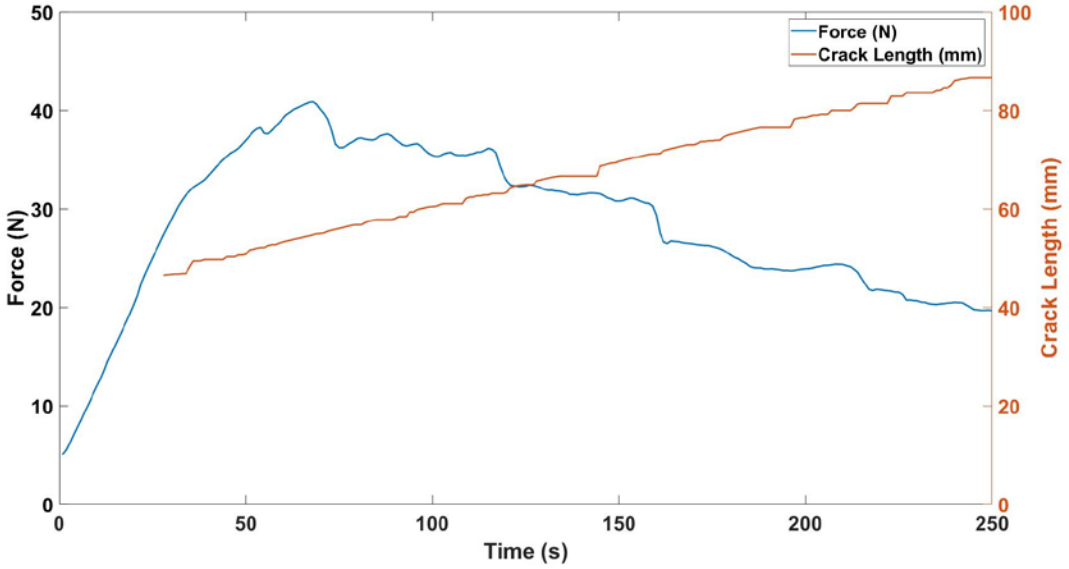

Figure K-5: Graph of force and crack length vs time of UD 6

Appendix K.1.2 Twill weave pattern

Figure K-6 through Figure K-11 show the graphs of the force and crack vs time of 6 Twill weave pattern

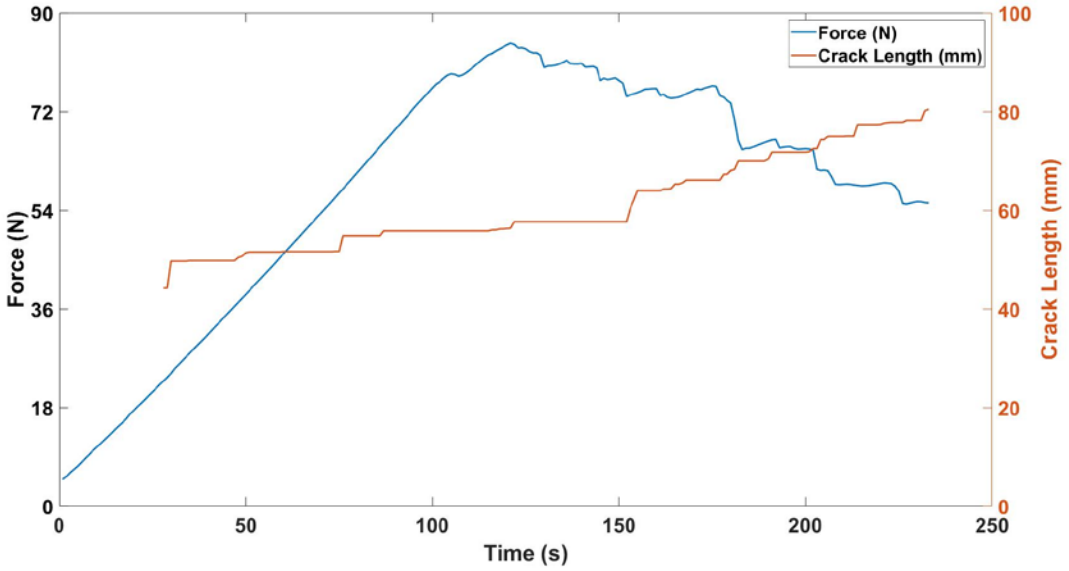

Figure K-6: Graph of force and crack length vs time of Twill 1

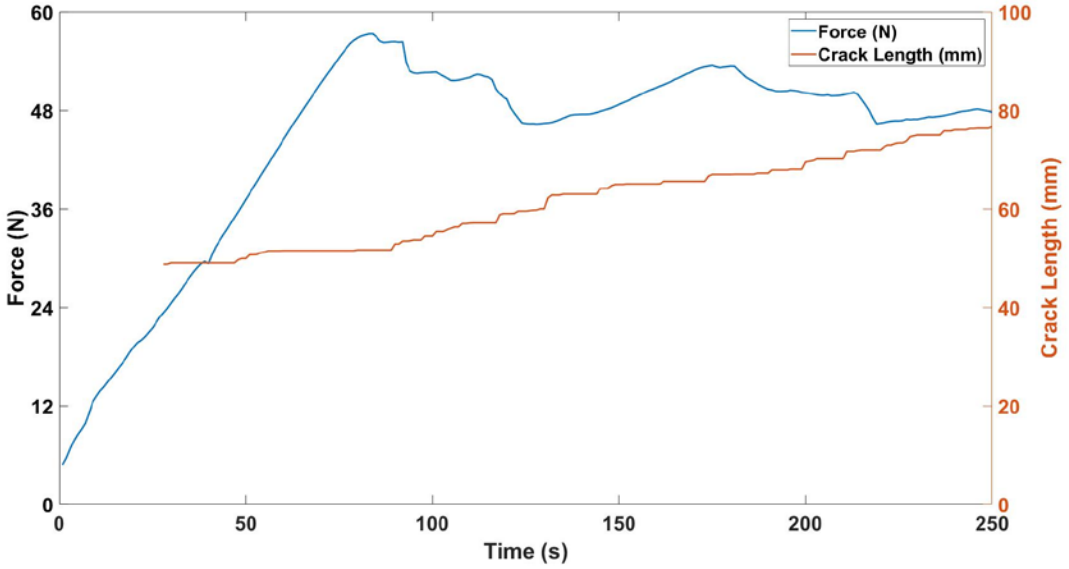

Figure K-7: Graph of force and crack length vs time of Twill 2

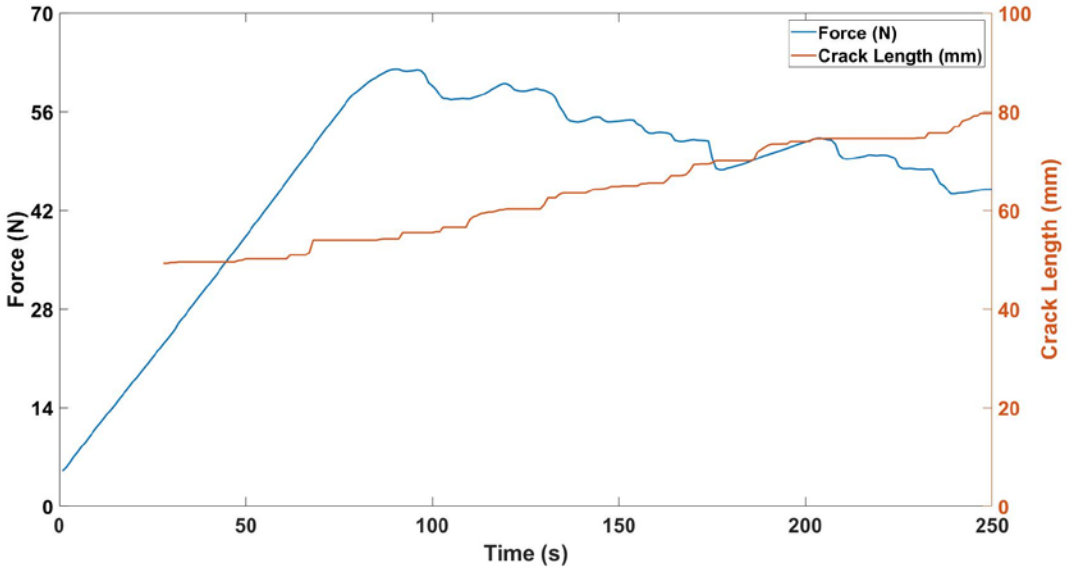

Figure K-8: Graph of force and crack length vs time of Twill 3

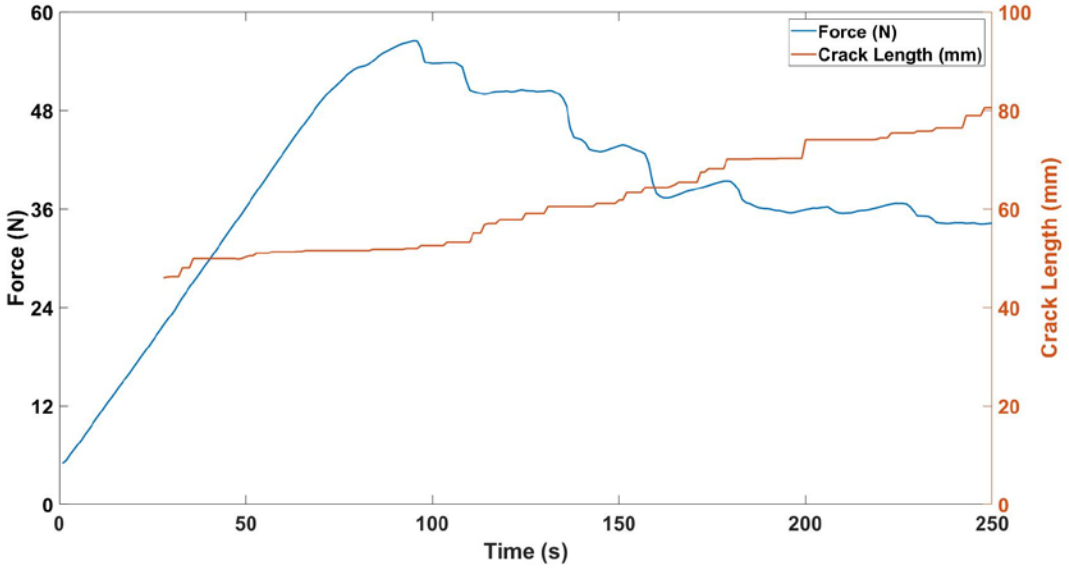

Figure K-9: Graph of force and crack length vs time of Twill 4

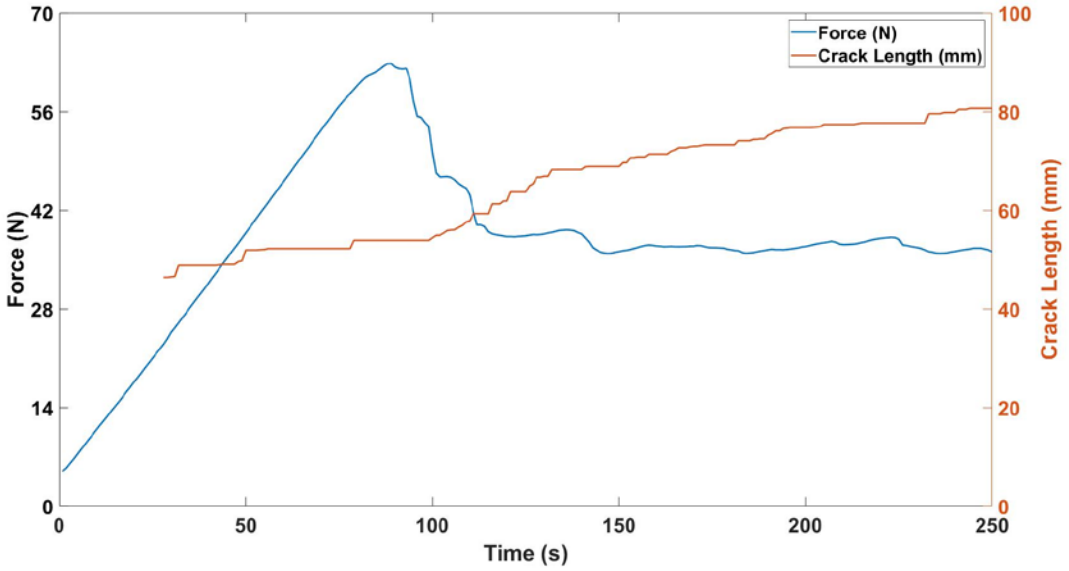

Figure K-10: Graph of force and crack length vs time of Twill 5

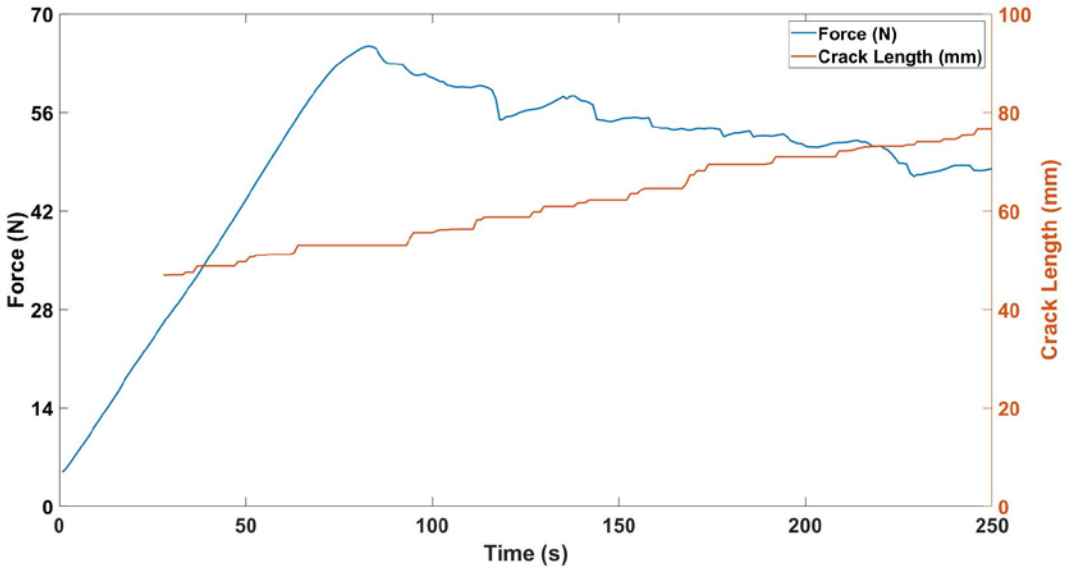

Figure K-11: Graph of force and crack length vs time of Twill 6

Appendix K.1.3 Plain weave pattern

Figure K-12 through Figure K-17 show the graphs of the force and crack vs time of all 6 Plain weave pattern

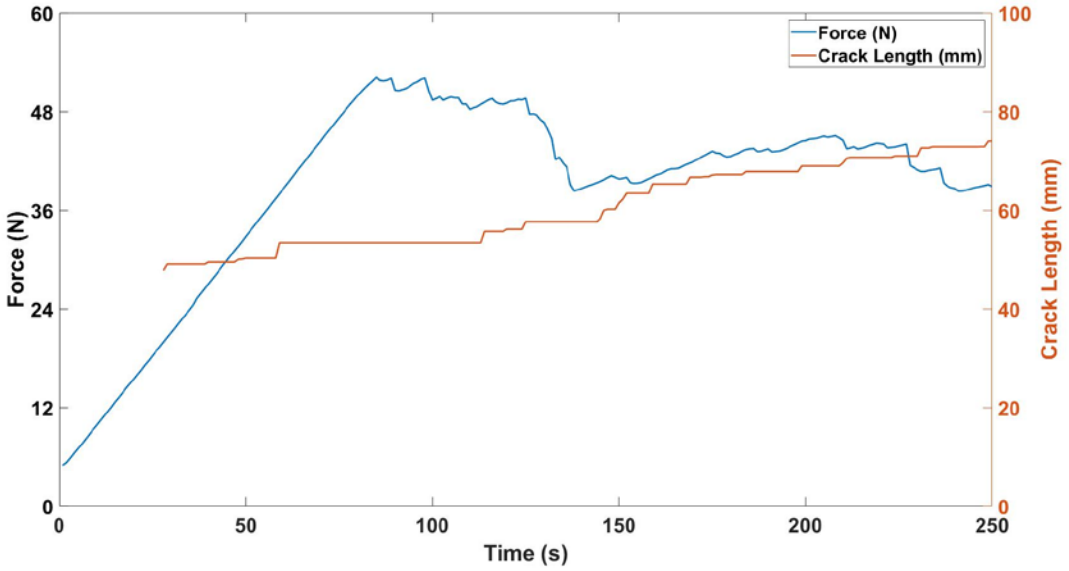

Figure K-12: Graph of force and crack length vs time of Plain 1

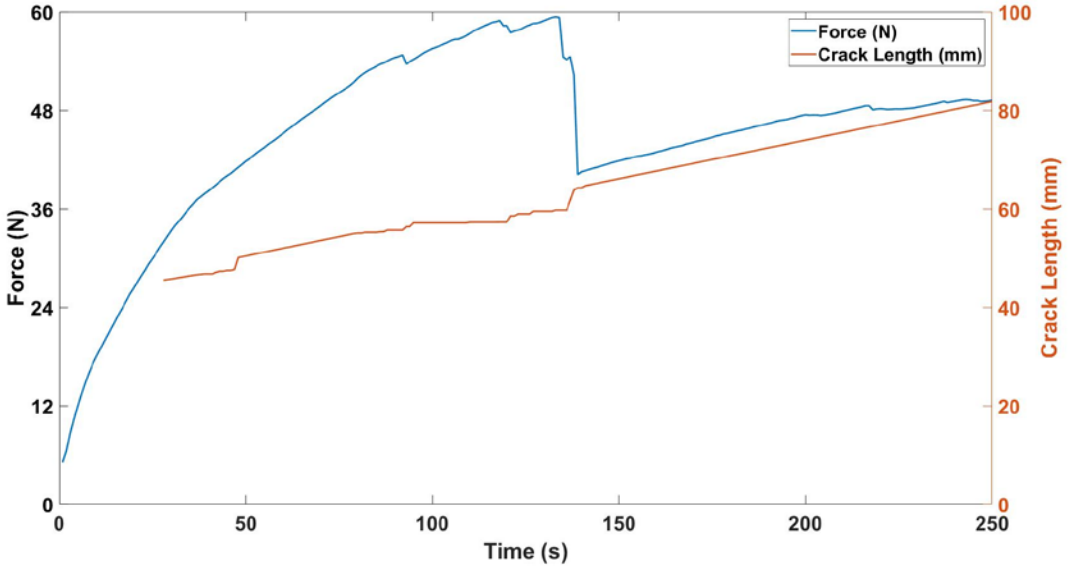

Figure K-13: Graph of force and crack length vs time of Plain 2

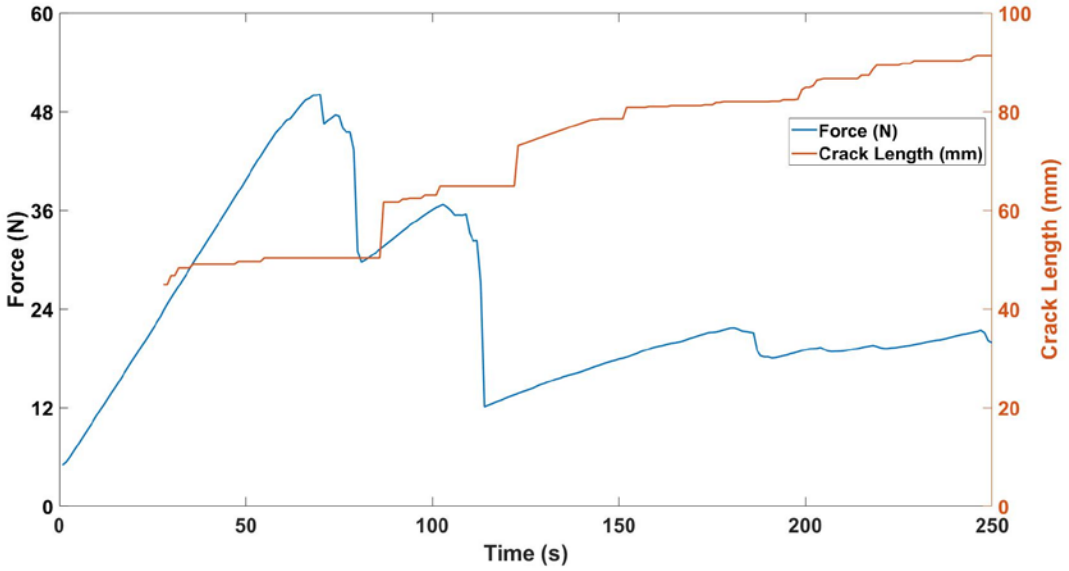

Figure K-14: Graph of force and crack length vs time of Plain 3

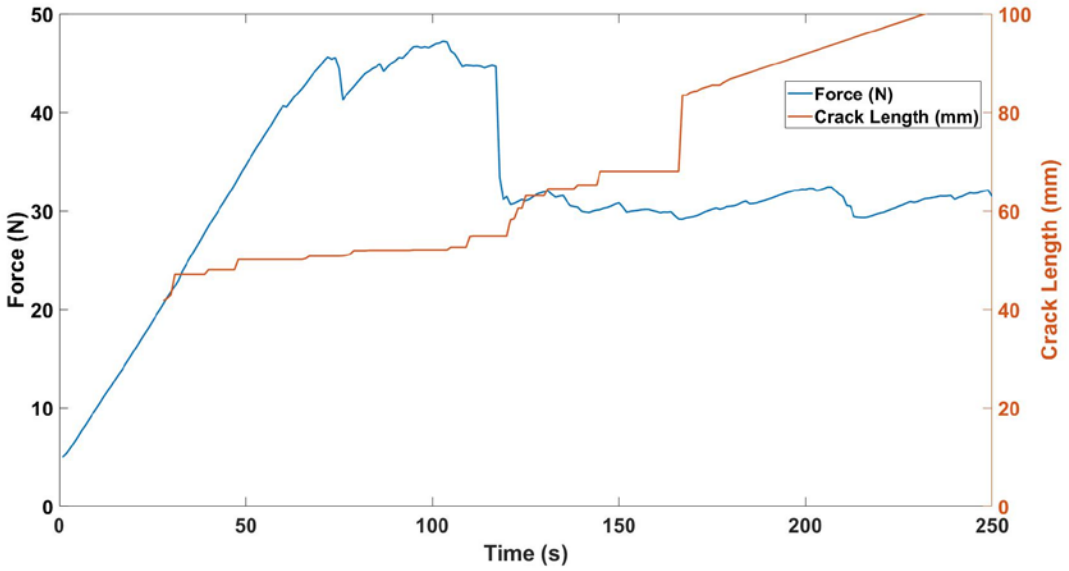

Figure K-15: Graph of force and crack length vs time of Plain 4

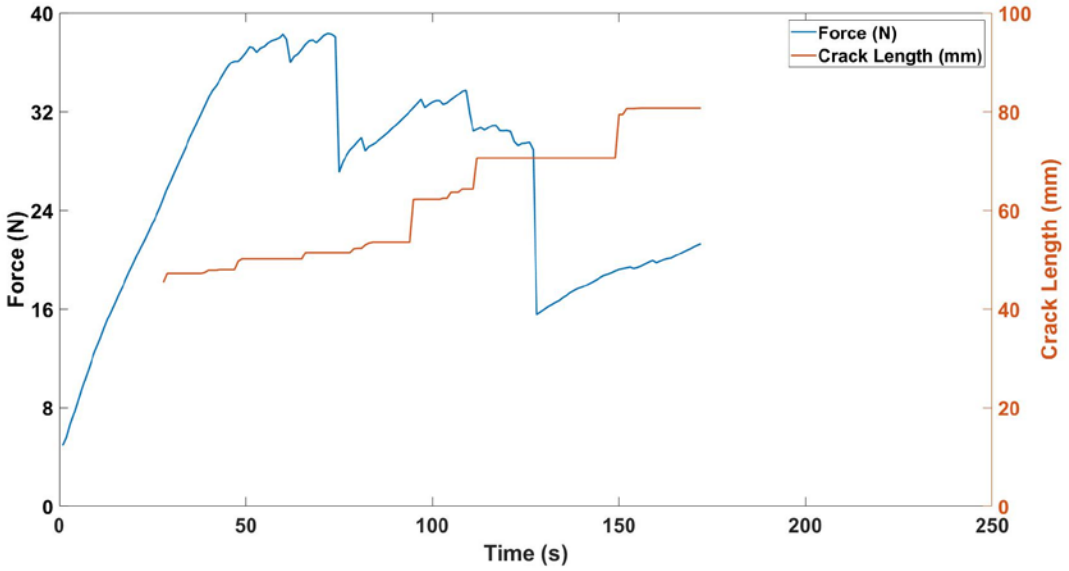

Figure K-16: Graph of force and crack length vs time of Plain 5

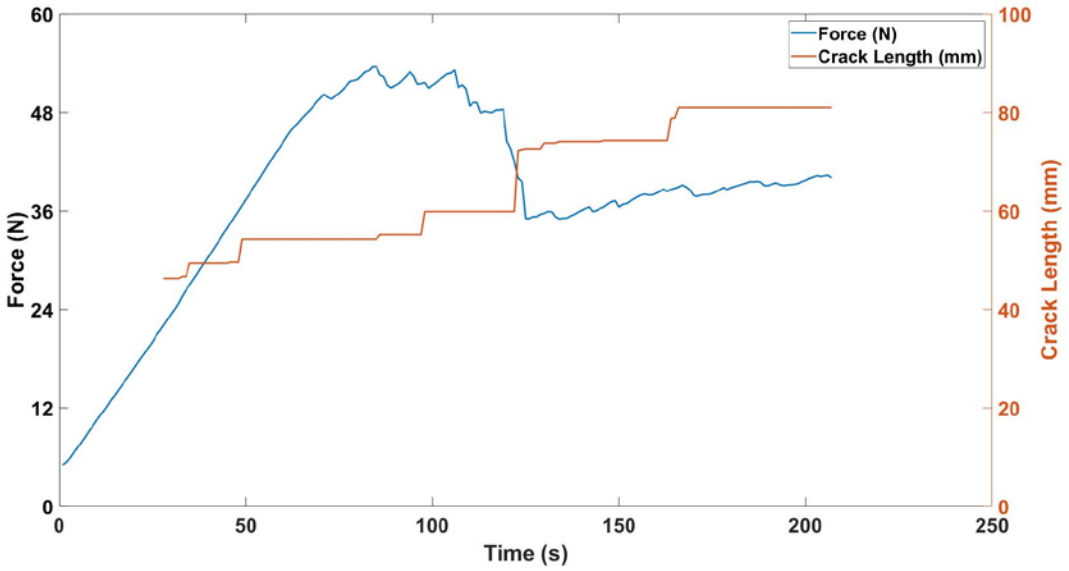

Figure K-17: Graph of force and crack length vs time of Plain 6

Appendix K.2 Mode I fracture toughness vs crack length

The following figures show the graphs of Mode I fracture toughness vs crack lengths of the UD, Twill and Plain weave.

Appendix K.2.1 UD specimens

Figure K-18 through Figure K-22 show the graphs of Mode I fracture toughness vs crack lengths of Specimens UD 2 through UD 6

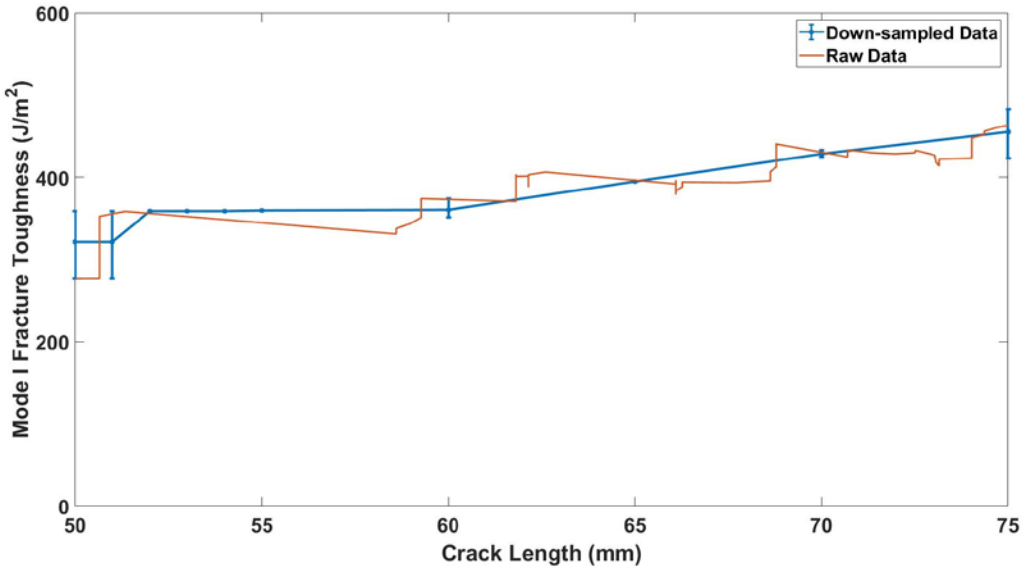

Figure K-18: Graph of Mode I fracture toughness vs crack length of UD 2

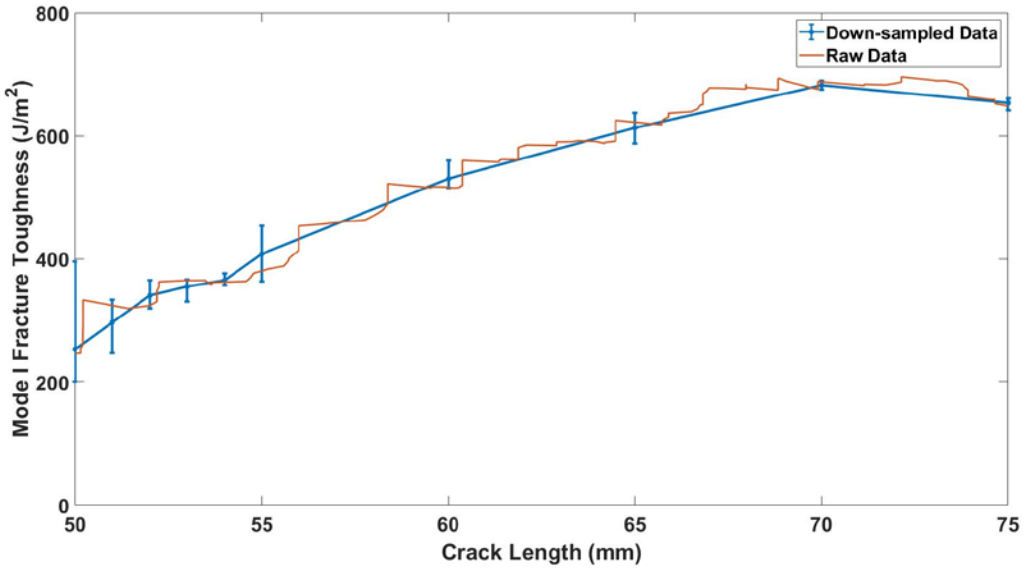

Figure K-19: Graph of Mode I fracture toughness vs crack length of UD 3

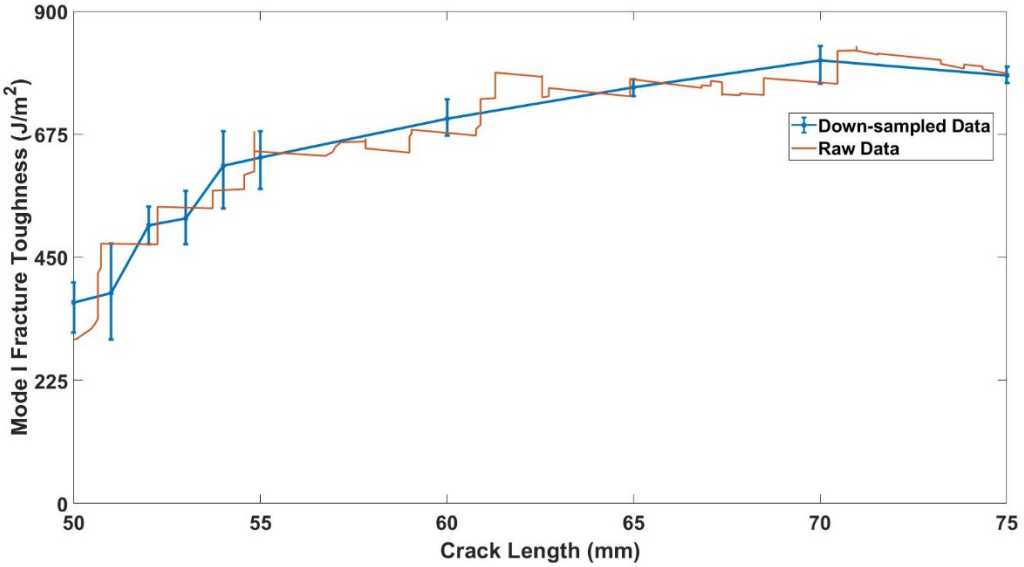

Figure K-20: Graph of Mode I fracture toughness vs crack length of UD 4

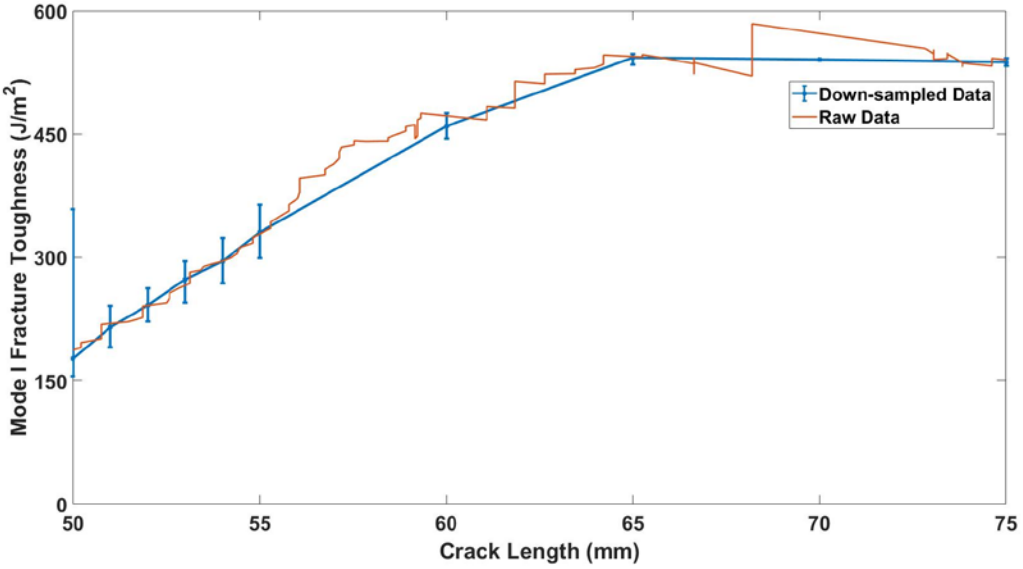

Figure K-21: Graph of Mode I fracture toughness vs crack length of UD 5

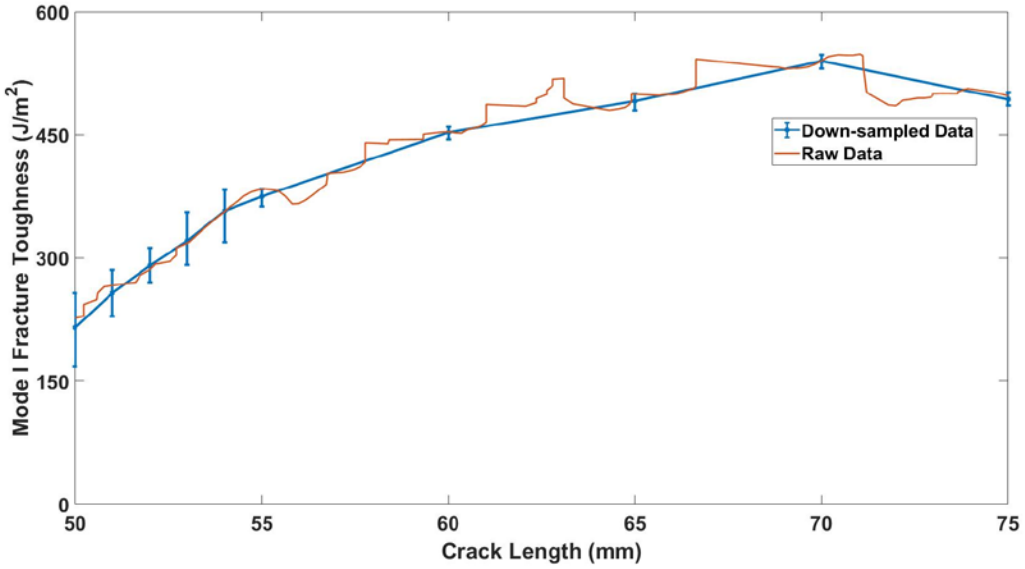

Figure K-22: Graph of Mode I fracture toughness vs crack length of UD 6

Appendix K.2.2 Twill weave pattern

Figure K-23 through Figure K-28 show the graphs of Mode I fracture toughness vs crack lengths of all 6 of the Twill weave specimens. **Error! Reference source not found.**

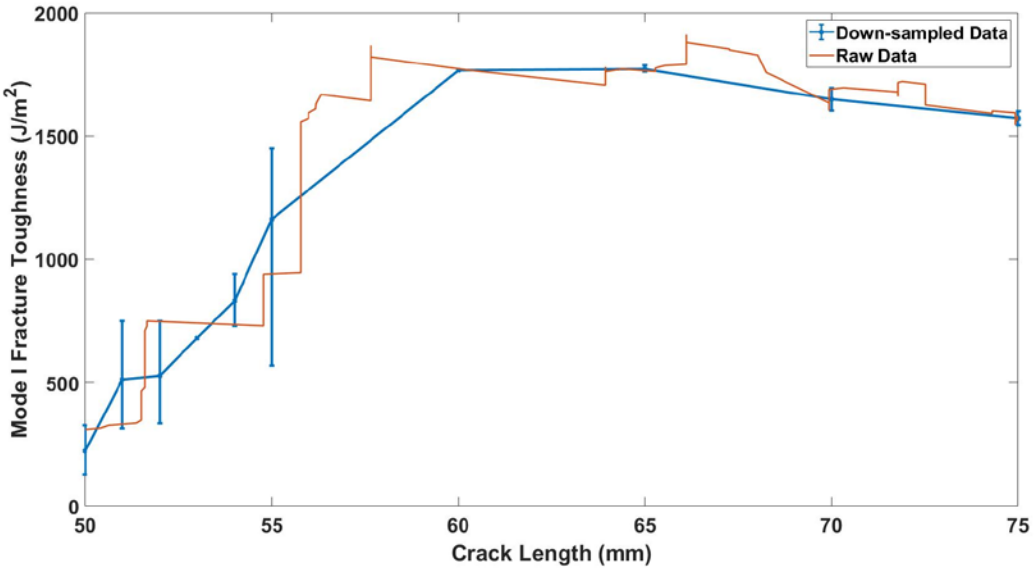

Figure K-23: Mode I fracture toughness vs crack length of Twill 1

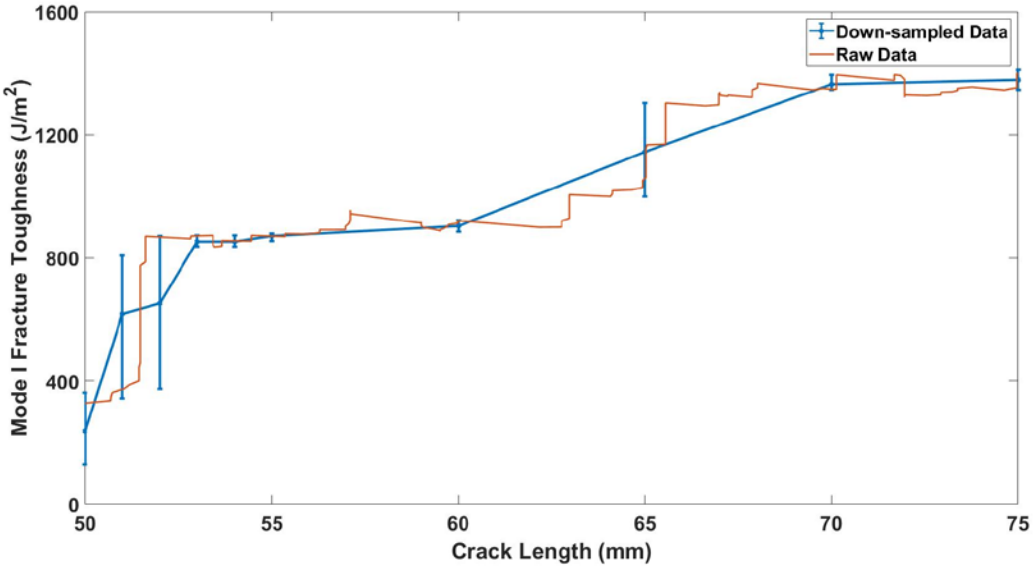

Figure K-24: Graph of Mode I fracture toughness vs crack length of Twill 2

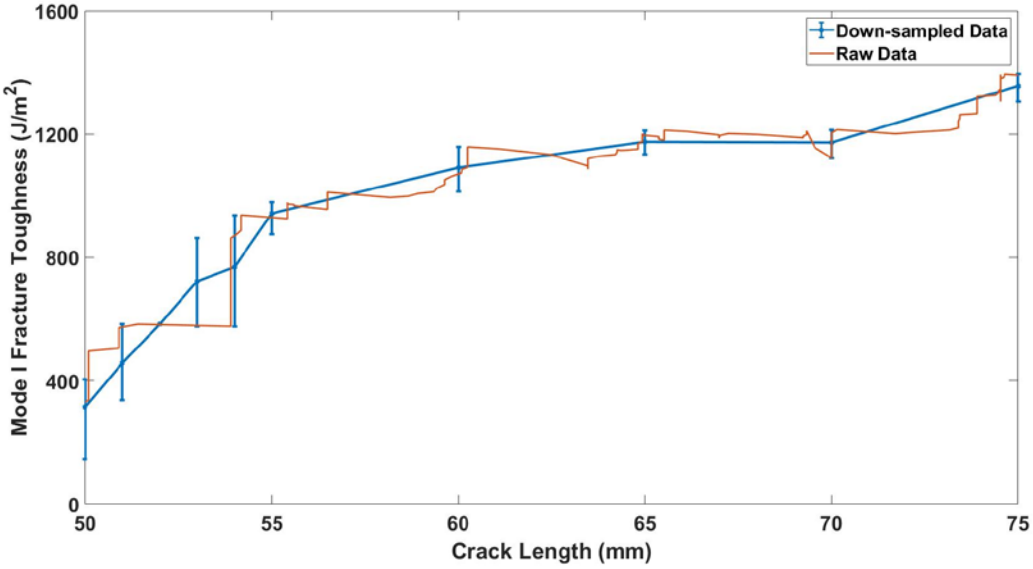

Figure K-25: Graph of Mode I fracture toughness vs crack length of Twill 3

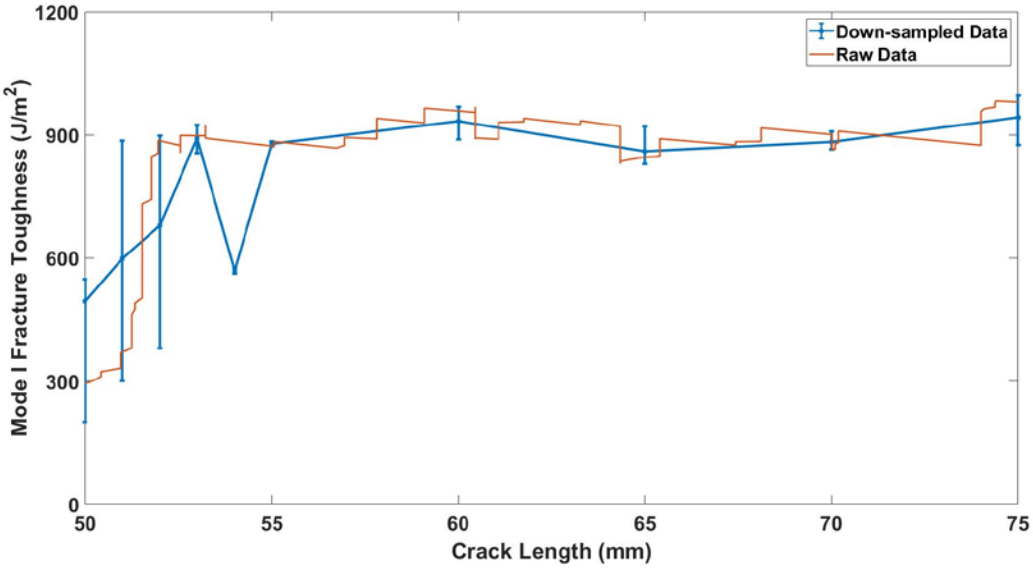

Figure K-26: Graph of Mode I fracture toughness vs crack length of Twill 4

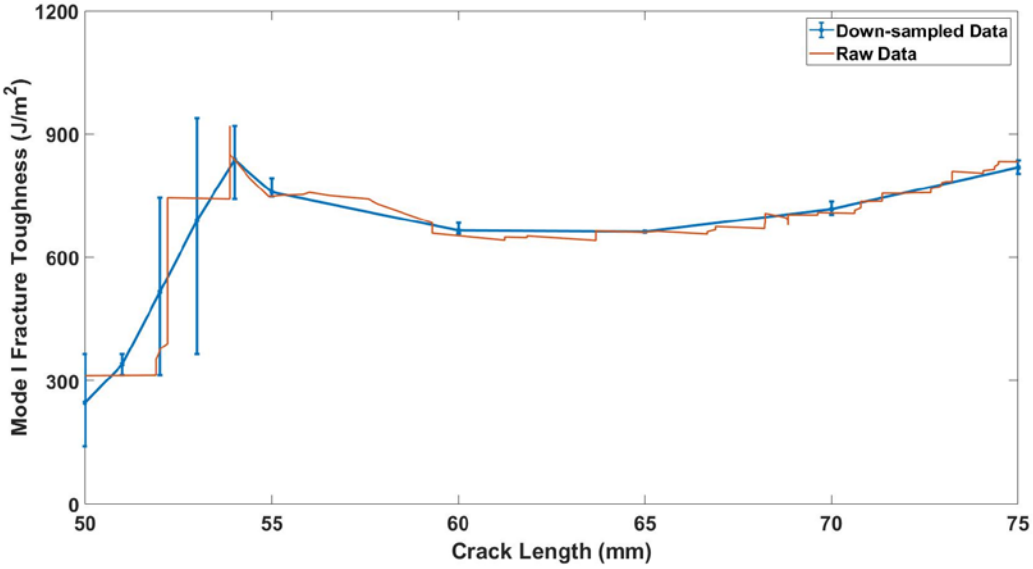

Figure K-27: Graph of Mode I fracture toughness vs crack length of Twill 5

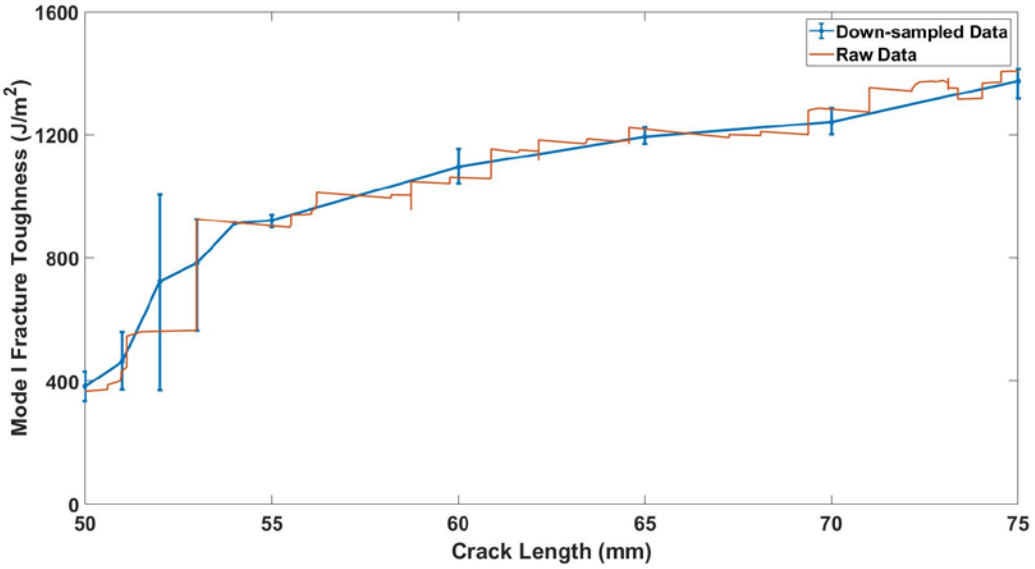

Figure K-28: Graph of Mode I fracture toughness vs crack length of Twill 6

Appendix K.2.3 Plain weave pattern

Figure K-29 through **Error! Reference source not found.** show the graphs of Mode I fracture toughness vs crack lengths of all 6 of the Plain weave specimens

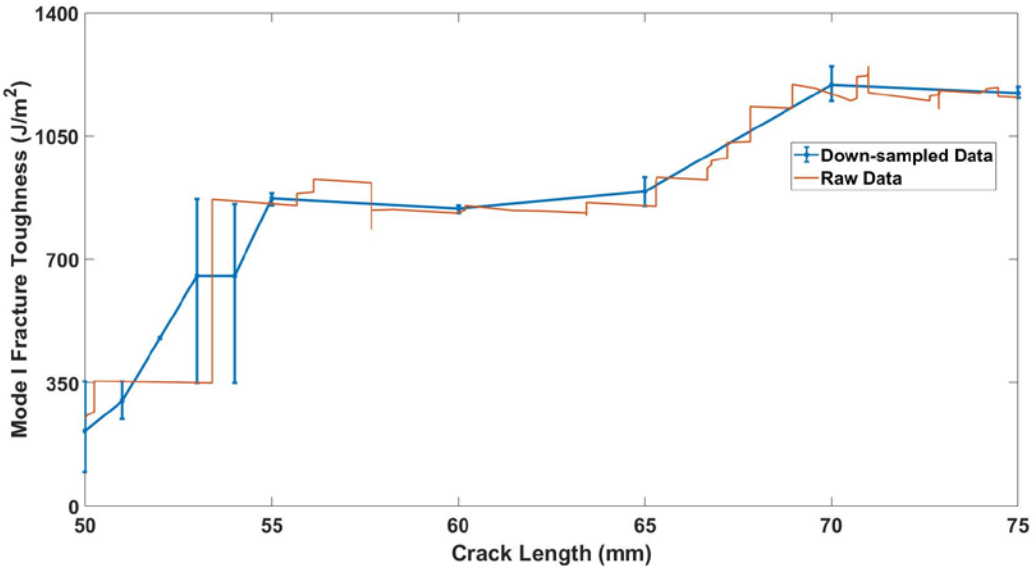

Figure K-29: Graph of Mode I fracture toughness vs crack length of Plain 1

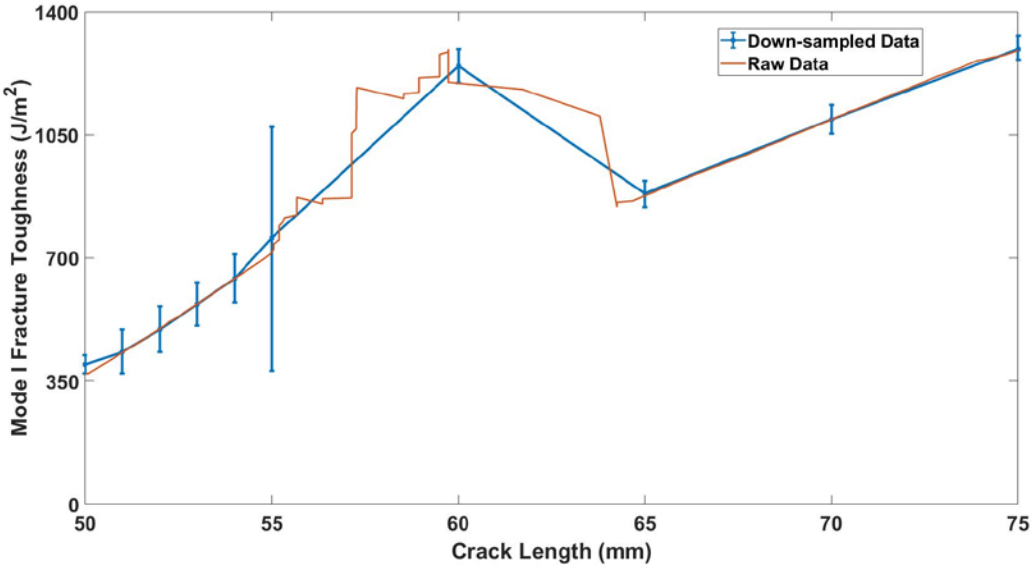

Figure K-30: Graph of Mode I fracture toughness vs crack length of Plain 2

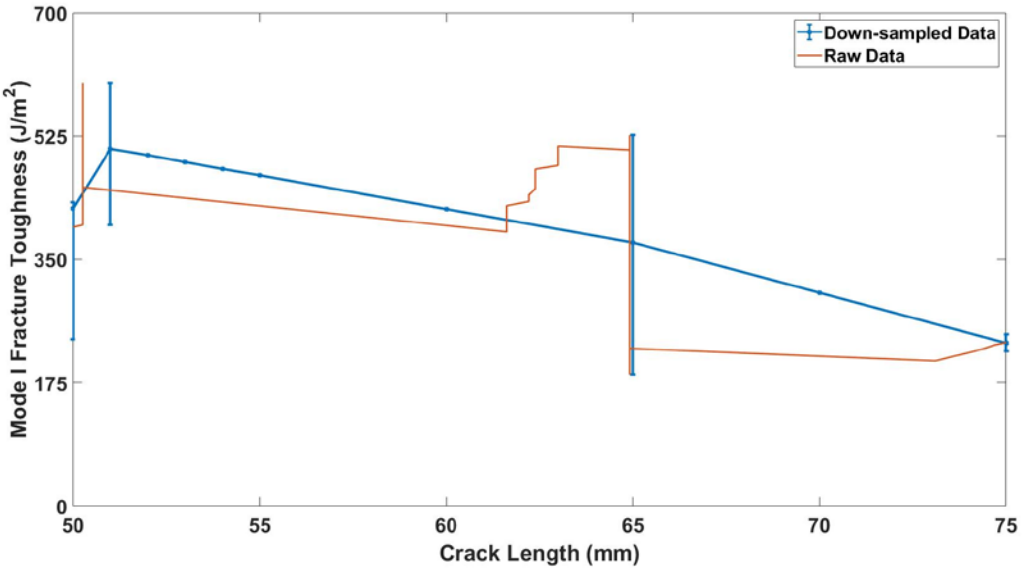

Figure K-31: Graph of Mode I fracture toughness vs crack length of Plain 3

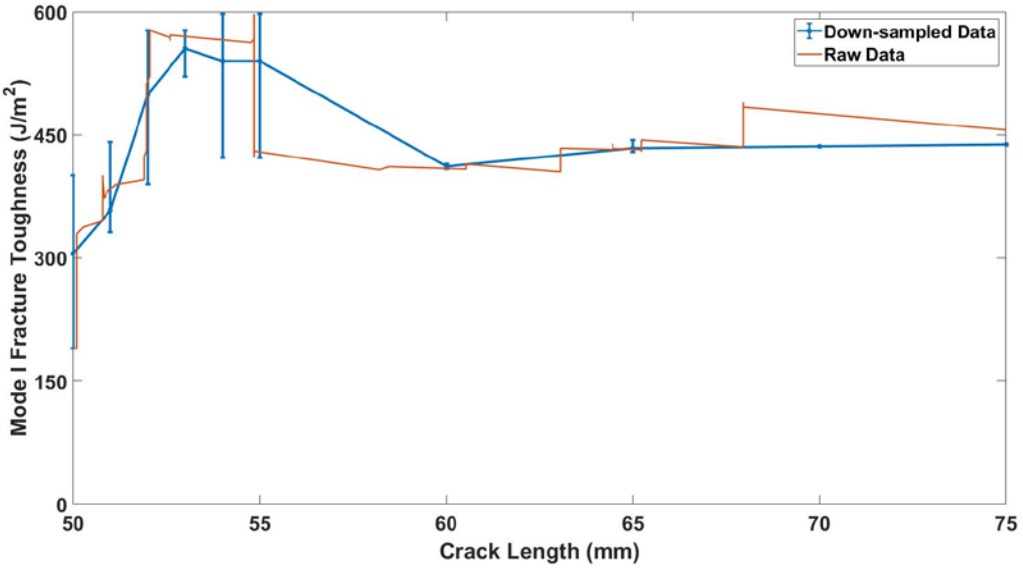

Figure K-32: Graph of Mode I fracture toughness vs crack length of Plain 4

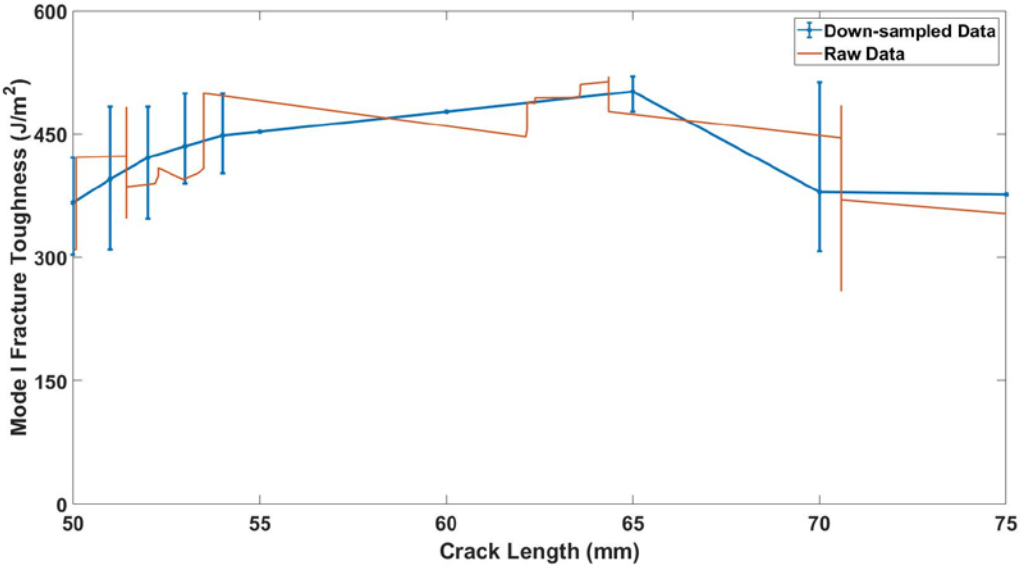

Figure K-33: Graph of Mode I fracture toughness vs crack length of Plain 5

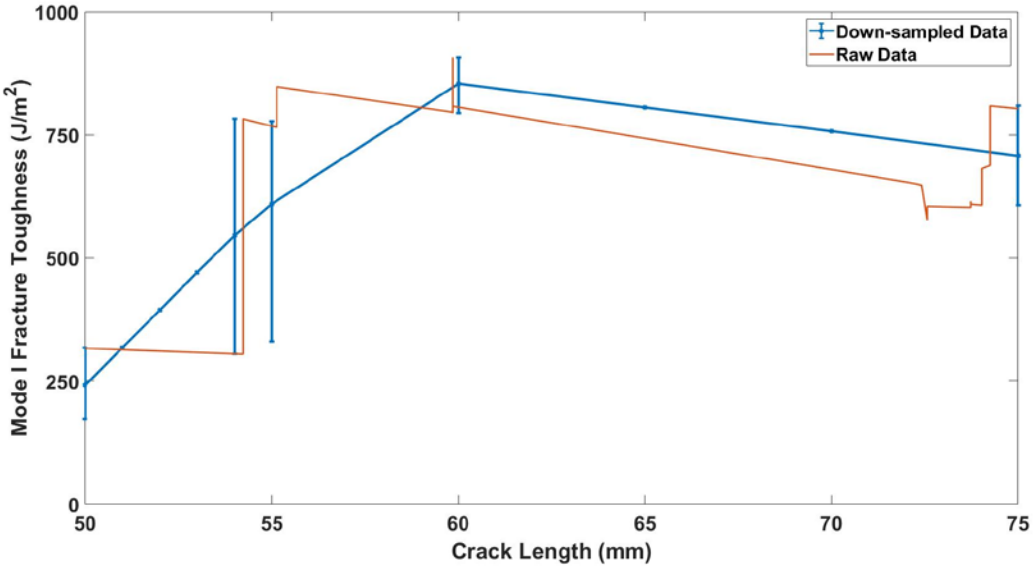

Figure K-34: Graph of Mode I fracture toughness vs crack length of Plain 6